



Vehicles, pedestrians and flood risk: a focus on the incipient motion due to the mean flow

Dissertation

submitted to and approved by the

Department of Architecture, Civil Engineering and Environmental Sciences
University of Braunschweig – Institute of Technology

and the

Department of Civil and Environmental Engineering
University of Florence

in candidacy for the degree of a

Doktor-Ingenieur (Dr.-Ing.) /

In Civil and Environmental Engineering

by

Chiara Arrighi

born 09/03/1986

in Fiesole (FI), Italy

Submitted on 1st March 2016

Oral examination on 9th May 2016

Professorial advisors Prof. Fabio Castelli
Prof. Hocine Oumeraci

2016

UNIVERSITY OF FLORENCE

Abstract

Faculty of Engineering
Department of Civil and Environmental Engineering

Doctor of Philosophy

Vehicles, pedestrians and flood risk: a focus on incipient motion due to the mean flow

by Chiara ARRIGHI

Floods are overflowing of water onto land, which is normally dry and are one of the costliest natural hazards. According to global scale reports, in the last decade floods affected the largest number of people with respect to other hazards such as earthquakes or droughts. Beside the damages to structures and infrastructures, floods also cause many fatalities and injuries. It has been demonstrated that the majority of fatalities occurs as a consequence of inappropriate high-risk behaviours like driving and walking in floodwaters. In fact, vehicles can lose stability also for very low water depths and may turn into deadly traps. For flood risk managers, people safety is the primary objective, but although vehicles are so crucial, very little is known about the critical conditions in which the onset of motion occurs. Besides, the existing instability criteria for pedestrians under water flow suffer from the large scatter of experimental pairs of critical water depth and velocity. As a matter of fact, the instability conditions of both vehicles and pedestrians are affected not only by flood parameters (i.e. water depth and velocity), but also by geometric and physical properties of the object. The main aim of this PhD research project is to better understand the instability mechanisms for pedestrians and vehicles, which are responsible for most of the casualties in order to introduce new hazard criteria capable of accounting for both flood and object characteristics. For this purpose, a comprehensive analysis of the current knowledge is firstly presented. Secondly, the forces acting on a partly immersed vehicle and human subject are examined and two dimensionless mobility parameters are introduced. The existing experimental data on vehicles and people instability are used to identify a dimensionless critical threshold of incipient motion. Thirdly, a 3D numerical model in the OpenFOAM framework is adopted to clarify the role of hydrodynamic forces and determine relevant dimensionless parameters and scaling numbers involved in the instability mechanisms, considering the mean flow properties. Then, the results of the numerical simulations for a selected vehicle, which reproduce a set of existing experiments, are analysed and discussed. Finally, two case studies are presented in order to demonstrate the applicability of the mobility parameters to the field scale and the advantages of hazard maps implemented with the proposed method. The results show that the scatter of existing experimental data can be overcome using a dimensionless approach, which accounts for both floods and objects properties. Since the critical thresholds are dimensionless, the instability conditions for people and vehicles can be easily compared in order to develop behavioural rules, management strategies and support people education. The numerical model hints the importance of flow regimes for the hydrodynamic effects and clarifies the contribution of drag and lift forces. The application of the mobility parameters to inundation maps demonstrates the applicability of the method to the field scale. The qualitative comparison between the reconstructed inundation maps and the georeferenced pictures taken after the 2014 flood event in Genoa shows a very good accordance, thus the method appears promising and provides an improved basis for flood hazard and risk mapping.

Acknowledgements

The present PhD research has been conducted thanks to a PhD scholarship given by the University of Florence (Italy) which is greatly acknowledged. I would like to express my special gratitude to Prof. Dr. Ing Hocine Oumeraci and Prof. Dr. Ing Fabio Castelli for allowing me to conduct the PhD study under their supervision in the Leichtweiss-Institut Hydraulic Engineering and Water Resources (LWI), Braunschweig, Germany and in the Department of Civil and Environmental Engineering, Florence (Italy) and for encouraging my research with their valuable suggestions. The support from Prof. Dr. Ing. Federico Domenichini (University of Florence) and Prof. Dr. Ing. Abdellatif Ouhasine (UTC, Compiègne) during the PhD research is acknowledged. A special thanks to Dr. Simone Gabellani (CIMA Research Foundation, Italy) and to Ing. Patrick Chassé (CEREMA, France) for providing the inundation model datasets. The laboratory Lasis at the University of Florence is acknowledged for having provided the 3D numerical geometry of the simulated car model. I would also like to thank my colleague Juan Carlos Alcèrrec-Huerta for his friendship, guidance and assistance during my stay in Braunschweig.

Contents

Abstract	i
Acknowledgements	iii
1 Introduction	1
1.1 Motivation	1
1.2 Objectives	2
1.3 Methodology	2
1.4 Expected results and impacts	2
2 Current state of knowledge and modelling	5
2.1 Flood risk in urban areas	5
2.1.1 Impacts of floods	5
2.1.2 Flood risk definition and European legislation	6
2.1.3 Hazard modelling	8
2.1.4 Damage assessment	11
2.1.5 Risk assessment	12
2.1.6 People fatalities	13
2.2 Experimental data on vehicles and people	14
2.2.1 Experiments on incipient motion of small scale vehicle models	14
2.2.2 Experiments on people instability in flood flows	19
2.3 Numerical modelling	23
2.3.1 Effects of an obstacle in a fluid flow	23
2.3.2 CFD numerical modelling	24
2.3.3 CFD codes	25
2.4 Summary and implications for the research	27
2.5 Specification of objectives and methodology	27
2.5.1 Specification of objectives	28
2.5.2 Specification of methodology	28
3 Incipient motion of parked cars and pedestrians under water flow	33
3.1 Incipient motion of parked cars	33
3.1.1 Mobility parameter of parked cars	33
3.1.2 Application of the mobility parameter to available experimental data	36
3.1.3 Effect of flow orientation on the mobility parameter	38
3.1.4 Sensitivity analysis of θ_V to uncertainties in H and U	42
3.2 Incipient motion of pedestrians standing in floodwaters	43
3.2.1 Mobility parameter of pedestrians	43
3.2.2 Application of the mobility parameter to existing experimental data	47
3.3 Comparison between mobility parameters for vehicles and people	48
3.4 Summary of key results and implications	49

4	Numerical model set-up in OpenFOAM	53
4.1	The OpenFOAM framework	53
4.2	Governing equations of the CFD model	55
4.3	Numerical model set up	56
4.3.1	Structure of a simulation in OpenFOAM	56
4.3.2	Solver	56
4.3.3	Mesh generation	57
4.3.4	Relaxation zones, boundary and initial conditions	61
4.3.5	Control of the simulation and forces calculation	61
4.4	Sensitivity analysis to the applied mesh size and turbulence model	62
4.4.1	Sensitivity of the results to the mesh size	62
4.4.2	Sensitivity of the results to the turbulence model	64
4.5	Test programme for the parameter study	65
4.5.1	Test programme for the Ford Focus	65
4.5.2	Test programme for human subjects	65
4.6	Applicability and limitations of the CFD simulations	69
4.7	Summary of the chapter	70
5	Numerical results and data analysis	73
5.1	Numerical results of the simulations of the Ford Focus car	73
5.1.1	Flow around the Ford Focus	73
5.1.2	Forces and force coefficients for scale and prototype Ford Focus for angles of flow incidence $\beta = 0^\circ$ and $\beta = 180^\circ$	75
5.1.3	Comparison of numerical results with experiments	82
5.1.4	Discussion of the assumptions "rigid body and constant friction coefficient"	83
5.1.5	Effect of the angle of flow incidence	85
5.1.6	Forces and forces coefficients for different angles of flow incidence	86
5.1.7	Summary of the numerical results of the Ford Focus	89
5.2	Numerical results of the simulations of pedestrians	92
5.2.1	Flow characteristics around an upright standing human body	92
5.2.2	Forces and force coefficients	93
5.2.3	Identification of motion mechanisms	97
5.2.4	Comparison with experimental data and discussion	99
5.2.5	Summary and discussion of the results of the numerical simulations of people	100
5.3	Summary of the chapter	102
6	Application to two case studies	105
6.1	Definition of hazard criteria	105
6.1.1	Hazard criteria for vehicles	105
6.1.2	Hazard criteria for pedestrians	106
6.2	The TELEMAC-MASCARET suite	107
6.3	The case study of Ajaccio in Corsica (France)	108
6.3.1	Case study description	108
6.3.2	Inundation characteristics and hazard maps for vehicles and pedestrians	109
6.4	The case study of Genova (Italy)	113
6.4.1	Case study description	113
6.4.2	Inundation characteristics and hazard maps for vehicles and pedestrians	114

6.4.3	Comparison of proposed hazard criteria with photos of the flood event	116
6.5	Summary	120
7	Summary, conclusions and outlook	123
7.1	General summary	123
7.2	Mobility parameters and numerical modelling	123
7.3	Limitations of the results	125
7.4	Outlook	127

List of Figures

1.1	An episode of flash flood in Athens (left panel, source: www.timesofmalta.com) and the aftermath of the 2011 flood in Genova (right panel, source: www.adnkronos.com).	1
2.1	Human impacts by disaster type in the decade 2002-2012 (EM-DAT, 2012)	6
2.2	Hazard, vulnerability and exposure (from Merz et al., 2004).	7
2.3	Standard flow chart for flood risk assessment based on flood depth maps and socio-economic data (from Arrighi et al., 2013).	8
2.4	The 2013 flash flood in Athens (source: http://www.timesofmalta.com).	14
2.5	The aftermath of Genoa 2011 flood event (source: http://www.italia45-45.it/alluvioni).	15
2.6	Experiments on fully (a) and partially (b) submerged Mitsubishi Pajero (1:18) (from Xia et al., 2011).	17
2.7	Critical threshold values of hydraulic instability for vehicles (Teo et al. 2012)	19
2.8	Experiments on human instability: water depth 1.07 m and velocity 1.0 m/s (from Karvonen et al., 2000)	21
2.9	Human model (scale 1:5.54) tested by Xia et al. 2014	22
2.10	Proposed hazard regimes for people (from Russo et al., 2013)	22
2.11	Summary of the topics described in the review of the current knowledge.	30
2.12	Methodology of the research and structure of the PhD thesis.	31
3.1	Forces acting on a parked vehicle under water flow.	33
3.2	Definition of geometric parameters of the vehicle and water flow parameters.	34
3.3	Mobility parameter θ_V versus Froude number Fr of undisturbed flow using the experimental data of Xia et al. (2011) and Shu et al. (2011).	36
3.4	Experimental data by Shu et al. 2011 (left panel) and by Xia et al. 2011 (right panel) scaled to prototype values.	37
3.5	Mobility parameter θ_V versus Froude number Fr_v of the vehicle using the experimental data of Xia et al. (2011) and Shu et al. (2011).	38
3.6	Plan view of the surfaces affected by drag force according to the angle of flow incidence.	39
3.7	Geometric scheme for a vehicle with angle of flow incidence β .	39
3.8	Mobility parameter accounting for the angle of flow incidence (experiments with 90° angle represented with diamonds, Xia et al., 2013)	41
3.9	Effect of addition of a small random noise to the pairs (H, V) on the mobility parameter.	44
3.10	Effect of addition of a large random noise to the pairs (H, V) on the mobility parameter.	44
3.11	Mobilising and resisting forces on a human body in floodwater (a) lateral view, frontal view (b).	45
3.12	Mobility parameter θ_P versus Froude number Fr for the experiments from published selected studies.	47

3.13	Instability diagram “water depth H versus flow velocity U ” scaled to prototype for vehicles (Xia et al., 2011; Shu et al., 2011; Xia et al., 2013) and people (Foster and Cox, 1973; Karvonen et al., 2000; Jonkman et al., 2008; Xia et al. 2014).	48
3.14	Dimensionless instability diagram as mobility parameter versus Froude number for vehicles and people.	49
3.15	Graphical summary of chapter 3.	51
4.1	OpenFoam Structure (OpenFOAM User Guide, 2013)	54
4.2	File structure of OpenFOAM cases (OpenFOAM, 2013)	56
4.3	Mesh generation procedure in OpenFOAM (exemplarily for a car).	58
4.4	Triangulated surface .stl of the car Opel Astra used for the mesh generation	59
4.5	Triangulated surface .stl of a human body used for the mesh generation	60
4.6	Instantaneous values of drag coefficient C_D for the three analysed meshes	63
4.7	Computational mesh for the simulation of a car: 3D view of the whole mesh (a), longitudinal cross section (b) and detail of the mesh around the car surface (c).	63
4.8	Computational mesh for the simulation of a human body: cross section (a) and detail of the legs (b) and of the feet (c)	64
4.9	Graphical summary of the chapter	71
5.1	Streamlines, flow velocity and pressures around the car for super-critical flow conditions with 0.4 m water depth and 2.7 m/s velocity (angle of flow incidence $\beta = 0^\circ$).	74
5.2	Flow around the Ford Focus for sub-critical flow conditions, 0.5 m water depth and 0.8 m/s velocity (angle of flow incidence $\beta = 0^\circ$).	74
5.3	Streamlines for 0.5 m water depth and 0.8 m/s velocity, angle of flow incidence $\beta = 0^\circ$	75
5.4	Pressure distribution on the Ford Focus surface for sub-critical (top) and super-critical (bottom) flow conditions (angle of flow incidence $\beta = 0^\circ$).	76
5.5	Drag coefficient versus Froude number for incipient motion conditions of a Ford Focus in scale 1:18 and prototype subject to incoming flow with angles of incidence $\beta = 0^\circ$ and $\beta = 180^\circ$	77
5.6	Lift coefficient versus Froude number for incipient motion conditions of a Ford Focus in scale 1:18 and prototype subject to incoming flow with angles of incidence $\beta = 0^\circ$ and $\beta = 180^\circ$	78
5.7	Drag coefficient against lift coefficient for scale 1:18 and prototype ($\beta = 0^\circ$ and $\beta = 180^\circ$).	79
5.8	Drag and lift forces for prototype (top panel) and scale 1:18 Ford Focus (bottom panel).	80
5.9	Drag coefficient versus Reynolds number for prototype and 1:18 scaled Ford Focus (top left and top right panels) and lift coefficient versus Reynolds number for prototype and 1:18 scaled Ford Focus (bottom left and bottom right panels).	81
5.10	Comparison between numerical results and mobility parameter evaluated from the experiments of Shu et al. (2011)	83
5.11	Vertical scaling of the Ford Focus to reproduce the suspension travel (a) and detail of the stretched tyre (b).	84
5.12	Vertical scaling of the Ford Focus to reproduce the suspension travel (a) and detail of the stretched tyre (b).	85

5.13	Friction coefficient versus suspension travel for water depth 0.23 m and velocity 5.06 m/s.	86
5.14	Flow velocity for a prototype Ford Focus with 0.23 m water depth and 5.09 m/s velocity, $\beta = 0^\circ$	87
5.15	Pressure for a prototype Ford Focus with 0.23 m water depth and 5.09 m/s velocity $\beta = 90^\circ$	87
5.16	Comparison of drag coefficient for all the investigated angles of flow incidence.	88
5.17	Comparison of the lift coefficients for all the investigated angles of flow incidence, $\beta = 90^\circ$, $\beta = 65^\circ$ and $\beta = 0^\circ$, $\beta = 180^\circ$ in the left and right panel respectively.	89
5.18	Drag force versus Froude number for the analysed flow orientations	90
5.19	Lift force versus Froude number for the analysed flow orientations	90
5.20	Ratio between resisting and drag forces for $\beta = 65^\circ$ and $\beta = 0^\circ$, values of the ratio R above 1 represent stable conditions	91
5.21	Streamlines around human body for subject 4 considered by Karvonen et al. (2000) at 0.87 m elevation for H=1.0 m and U=0.8 m/s	92
5.22	Streamlines around human body for subject 4 considered by Karvonen et al. (2000) at 0.62 m elevation for H=1.0 m and U=0.8 m/s.	93
5.23	Splashing effect for super-critical flows shown as flow velocity (a), streamlines (c) and inset view parallel to flow direction upstream-oriented (b), for the subject considered by Jonkman & Penning-Rowse (2008), H=0.35 m, U=2.40 m/s.	94
5.24	Drag (top panel) and lift (bottom panel) coefficients versus Froude number for the four human subjects considered in (Karvonen et al., 2000; Jonkman & Penning-Rowse, 2008) and the human body model considered in (Xia et al., 2014). Reference area A_{ref} for both force coefficients shown in Tab. 5.5	95
5.25	Drag (top panel) and lift (bottom panel) coefficients versus relative submergence H/H_P for the four human subjects considered in (Karvonen et al., 2000; Jonkman & Penning-Rowse, 2008) and the human body model considered in (Xia et al., 2014).Reference area A_{ref} for both force coefficients shown in Tab. 5.5	96
5.26	Drag force versus Froude number for the four human subjects considered in Karvonen et al., 2000; Jonkman & Penning-Rowse, 2008 and the human body model considered in Xia et al., 2014.	98
5.27	Lift force versus Froude number for the four human subjects considered in Karvonen et al., 2000; Jonkman & Penning-Rowse, 2008 and the human body model considered in Xia et al., 2014.	98
5.28	Normalized moment against Froude number for the four human subjects (Karvonen et al., 2000; Jonkman & Penning-Rowse, 2008) and the human body model considered in Xia et al., 2014.	99
5.29	Comparison between experiments in terms of mobility parameter and numerical results for all the simulated human subjects and human body model defined in Table 5.5.	100
5.30	Comparison between experiments in terms of mobility parameter and numerical results separating the human subjects (circles) and human model (triangles).	101
5.31	Graphical summary of the chapter.	103
6.1	Detail of les Cannes district in the eastern part of Ajaccio (violet polygon on the left) (Sogreah, 2006).	108

6.2	Temporal maximum of water depth during the flood simulation in the district les Cannes for 100 years recurrence interval (Sogreah, 2006)	109
6.3	Temporal maximum of flow velocity during the flood simulation in the district les Cannes for 100 years recurrence interval (Sogreah, 2006)	110
6.4	Hazard to vehicles for the 100 years scenario and relevant streets and buildings in Les Cannes district based on the proposed Hazard criterion (see Eq. 6.1)	111
6.5	Hazard to pedestrians for the 100 years scenario and relevant streets and buildings in Les Cannes district based on the proposed Hazard criterion (see Eq. 6.2)	112
6.6	City of Genova (a) Location in Italy (www.wikipedia.it) and (b) port area (Google Maps) with indication of the Bisagno creek and the inundated area in 2014.	113
6.7	Maximum simulated water depth for the 2014 Genova flood (Dolia, 2015).	114
6.8	Maximum Froude number for the 2014 Genova flood.	115
6.9	A detail of hazard to people (temporal maximum) close to Brignole station for the reconstructed 2014 Genova flood event	115
6.10	A detail of hazard to vehicles (temporal maximum) close to Brignole station for the reconstructed 2014 Genova flood event.	116
6.11	Hazard to vehicles and locations a, b, c, d of the photos in Figs. 6.12, 6.13, 6.14, 6.15 taken during and after the 2014 Genova flood event. Location where the body of A. Campanella was found (e), Fig. 6.16	117
6.12	The day after the flood, photo taken at location a (Figure 6.11, from: www.ilsecoloXIX.it).	117
6.13	The day after the flood, photo taken at location b (Figure 6.11, from: www.ilsecoloXIX.it).	118
6.14	The night of the flood, photo taken at location c (Figure 6.11, courtesy of S. Gabellani, CIMA Research Foundation).	119
6.15	The night of the flood, photo taken at location d (Figure 6.11, from: www.adnkronos.it).	119
6.16	The night of the flood, photo taken at location d (Figure 6.11, from: www.meteoweb.eu./2014)	120
6.17	Graphical summary of chapter 6.	121
7.1	Graphical summary of the thesis.	124

List of Tables

2.1	International risk criteria in urban drainage based on water depth H and flow velocity U (Russo et al. 2005)	16
3.1	Characteristics and mobility parameter of the car models for different submergence $H/H_V = 0.25 - 1.0$	37
3.2	Characteristics of Honda Accord (prototype and scale 1:14)(Xia et al., 2013)	40
3.3	RMSE of the perturbed data over the original regression obtained with different multipliers for the standard deviation of the noise	42
3.4	Determination coefficient R^2 of the perturbed data over the original regression obtained with different multipliers for the standard deviation of the noise	43
4.1	Characteristics of Honda Accord (prototype and scale 1:14)(Xia et al., 2013)	59
4.2	Total number of cells and execution time for 1 s of simulation for the three analysed meshes (one core)	62
4.3	Percent variation of the estimated force coefficients for the three analyzed meshes	62
4.4	Percent variation of the force coefficient with the three tested turbulence model for subcritical ($Fr < 1$) and supercritical ($Fr > 1$) flow conditions.	65
4.5	Simulated pairs of water depth H and flow velocity U for prototype and scale 1:18 model for the frontal impact (0°)	66
4.6	Simulated pairs of water depth H and flow velocity U for prototype and scale 1:18 model for the rear impact (0°)	66
4.7	Simulated pairs of water depth H and flow velocity U for angle of flow incidence 90° and 65°	66
4.8	Simulated pairs of water depth and flow velocity for Subject 2 tested by Karvonen et al. (2000)	67
4.9	Simulated pairs of water depth and flow velocity for Subject 4 tested by Karvonen et al. (2000)	67
4.10	Simulated pairs of water depth and flow velocity for Subject 5 tested by Karvonen et al. (2000)	67
4.11	Simulated pairs of water depth and flow velocity for the stuntman tested by Jonkman and Penning-Rowsell et al. (2008)	67
4.12	. Simulated pairs of water depth and velocity (scaled to prototype) for the human model tested by Xia et al. (2014) classified as sliding instability . .	68
4.13	Simulated pairs of water depth and velocity (scaled to prototype) for the human model tested by Xia et al. (2014) classified as toppling instability .	68
5.1	Drag and lift coefficients for Ford Focus at prototype scale (1:1) and at scale 1:18 for angle of flow incidence $\beta = 0^\circ$	79
5.2	Drag and lift coefficients for Ford Focus at prototype scale (1:1) and at scale 1:18 for angle of flow incidence $\beta = 180^\circ$	80
5.3	Partial correlation of x over y , given z	82

5.4	Effect of the suspension travel on the forces exerted by water for 0.23 m water depth and 5.09 m/s velocity.	84
5.5	Reference frontal areas A_{ref} , height and weight of the human subjects and human body model considered for force coefficient calculation.	93
6.1	Color scale for hazard classification and mapping	106

List of Symbols

α	phase fraction	—
A	cross sectional flow area	m^2
A_{ref}	reference areas for force coefficients	m^2
A_D	reference areas for drag coefficient	m^2
A_L	reference areas for lift coefficient	m^2
B	buoyancy force	N
β	angle of flow incidence	°
C_D	drag coefficient	—
C_L	lift coefficient	—
C	group of force coefficients	—
C_s	group of force coefficients for pedestrians sliding	—
C_t	group of force coefficients for pedestrians toppling	—
D	drag force	N
$D_{\text{€tot}}$	monetary damage	€
d	length of the foot	m
EAD	expected annual damage	€ · year ⁻¹
Fr	Froude number	—
Fr_V	Froude number of the vehicle	—
g	acceleration of gravity	$m \cdot s^{-2}$
γ	water density	$N \cdot m^{-3}$
γ_c	car density	$N \cdot m^{-3}$
H, h	water depth	m
H_V	Height of the vehicle	m
H_P	Height of the person	m
h_c	Height of the planform	m
Haz_V	flood hazard for vehicles	—
Haz_P	flood hazard for pedestrians	—
L	length of the vehicle	m
Li	Lift force	N
l	width of the vehicle/person	m
m	mass	kg
n	Manning's coefficient	$s \cdot m^{-1/3}$
μ	friction coefficient	—
ν	kinematic viscosity	$m^2 \cdot s^{-1}$
p	pressure	Pa
Q	discharge	$m^3 \cdot s^{-1}$
R	ratio between resisting and drag forces	—
Re	Reynolds number	—
ρ	water density	$kg \cdot m^{-3}$
ρ_P	person density	$kg \cdot m^{-3}$
ρ_c	vehicle bulk density	$kg \cdot m^{-3}$
S_0	bed slope	—
S_f	friction slope	—

t	time	s
T_R	return period of an event	years
θ_P	mobility parameter for pedestrians	—
θ_V	mobility parameter for vehicles	—
θ_{Pcr}	critical mobility threshold for pedestrians	—
θ_{Vcr}	critical mobility threshold for vehicles	—
U	mean flow velocity	$\text{m} \cdot \text{s}^{-1}$
U_{max}	maximum flow velocity	$\text{m} \cdot \text{s}^{-1}$
U_c	critical flow velocity	$\text{m} \cdot \text{s}^{-1}$
U_{ref}	reference flow velocity for force coefficients	$\text{m} \cdot \text{s}^{-1}$
\mathbf{u}	flow velocity vector (u, v, w)	$\text{m} \cdot \text{s}^{-1}$
x, y, z	cartesian coordinates	—
W	weight	N
z_B	bed elevation	m

List of abbreviations

<i>CFD</i>	computational fluid dynamics
<i>DSM</i>	digital surface model
<i>DTM</i>	digital terrain model
<i>FE</i>	finite elements
<i>LiDAR</i>	Light Detection and Ranging
<i>RANS</i>	Reynolds averaged Navier-Stokes equation
<i>RMSE</i>	root mean square error
R^2	determination coefficient
<i>std</i>	standard deviation
<i>SWE</i>	shallow water equations
<i>VOF</i>	volume of fluid scheme

Chapter 1

Introduction

1.1 Motivation

Nowadays floods cause each year million euros of damages and affect a large number of people worldwide. The Flood Directive 60/2007/EC requires the European countries to implement flood hazard and flood risk maps in order to efficiently mitigate flood risks through structural and non-structural measures. Among the diversity of damages a flood can induce, the most crucial are loss of lives and injuries. Most of the fatalities in urban floods occurs in vehicles. The latter can be swept away by floodwaters even for low water depths and may turn into deadly trap for the driver and the passengers. The second cause of fatalities is associated with the high-risk behaviour of pedestrians trying to walk in floodwaters. Typical pictures taken during and after urban flood events are exemplarily shown in Figure 1.1. Usually, the recurring theme of photos representing the aftermath of a flood event is the consequence of this chain of events: vehicles are trapped by water, then float and are piled up into and on top of each other once the floodwaters subsides (Figure 1.1, right panel). Although people safety is the primary aim of any flood risk management strategy, the studies on vehicles and people instability under water flow are sparse and existing hazard criteria suffer from many drawbacks and are not reliable for the application to urban scale. In particular, a large scatter affects the existing experimental critical conditions, which lead to the instability. In fact, the loss of stability in floodwaters not only depends on flood characteristics (i.e. water depth and velocity) but also on the geometrical and other physical properties of the immersed object.



FIGURE 1.1: An episode of flash flood in Athens (left panel, source: www.timesofmalta.com) and the aftermath of the 2011 flood in Genova (right panel, source: www.adnkronos.com).

1.2 Objectives

Since a better understanding of the instability phenomenon is crucial for supporting education and flood risk management strategies, the aims of this research study are:

- Development of new hazard criteria for vehicles and pedestrians under water flow, which account for both flood and vehicle/human body characteristics and are more consistent in terms of reducing the scatter of existing experimental data.
- Identification of the most relevant parameters affecting the onset of motion and the different contribution of hydrodynamic forces for a wide range of flow regimes.
- Demonstration of the applicability of the new hazard criteria to real case studies of urban floods, showing the advantage of the hazard maps based on these new criteria for flood risk management, especially for non-structural mitigation measures.

A more detailed specification of the objectives as drawn from the implications of the identified knowledge gaps is provided in the concluding section of chapter 2 (sub-section 2.5.1).

1.3 Methodology

The method adopted in this research consists of four main work-packages:

- Review and analysis of the current knowledge including urban flood risk, reports on people fatalities, existing laboratory experiments on vehicles and people instability under water flow and available numerical tools.
- Dimensional analysis of the forces on partly immersed vehicles and human bodies and implementation of dimensionless instability diagrams.
- Reproduction of experiments on incipient motion of vehicles and people instability in flowing water using a 3D hydrodynamic model set up in OpenFOAM, with the aim of identifying of the most relevant dimensionless parameters, scaling numbers and effects of the mean flow regime for which experimental data are available from previous studies.
- Application of the findings to real case studies and qualitative validation through the comparison between resulting hazard maps and available documents (e.g. videos and pictures) of a flood event.

A more detailed description of the methodology of the research is provided in the concluding section of chapter 2 (sub-section 2.5.2).

1.4 Expected results and impacts

The expected result of this research is the creation of a new perspective to understand and analyse the instability conditions of vehicles and pedestrians under water flow, in order to provide a consistent support for the implementation of non-structural risk mitigation measures. In engineering terms, the new perspective consists of a new dimensionless parametrization of the instability conditions for pedestrians and vehicles as a basis for new hazard criteria easily applicable to the current inundation maps as required by the European Floods Directive. Since a reduction of the number of fatalities can be achieved

just through education (appropriate behaviour in flood), the results of this research may have significant impacts on the implementation of behavioural rules and emergency protocols.

Chapter 2

Current state of knowledge and modelling

The current knowledge on flood risk assessment in urban areas is reviewed and analysed in this chapter. The focus is put on the main causes of fatalities in urban floods and on the existing experimental data on the instability conditions for vehicles and people immersed in a fluid flow. Moreover, the numerical methods available to support flood risk assessment and hydrodynamic modelling are introduced. The impacts of floods and the current definition of flood risk according to the European legislative framework are first introduced (section 2.1.1). The methods to describe the propagation of an inundation as well as the techniques to assess the potential damages are summarized. The published reports on people casualties and loss of life models are analysed to highlight the main issues related to human-flood interaction. The experimental data about the critical instability conditions for vehicles and pedestrians are reviewed and discussed in section 2.2. The main existing instability criteria are described. Section 2.3 describes the role of the numerical modelling of hydrodynamic processes for a better understanding of the physical processes and their complementarity to the experiments in this respect. As a main result the literature study, the gaps of knowledge are identified and the implications for the present research are drawn, including a flow chart in Figure 2.11 summarizing the topics and the logical link followed in this chapter (section 2.4). Moreover, the objectives and methodology of the work are finally specified (section 2.5.1, 2.5.2).

2.1 Flood risk in urban areas

2.1.1 Impacts of floods

Floods represent one of the main natural disasters in terms of deadliest events and economic damages (Munich Re, 2015b). For instance, the 2011 flood in Thailand caused 40 billion dollars of overall damages (Munich Re, 2012), the 2014 flood affecting India and Pakistan caused 665 fatalities (EM-DAT, 2012; Munich Re, 2015a).

Figure 2.1 shows the human impact for different classes of disasters. Although the number of fatalities caused by floods is lower than other hazards (i.e. earthquakes), flood events affects the largest number of people. In the European Community (EC) countries, it has been estimated that the average annual flood loss in the period 1970-2006 was about 4 billion dollars (Barredo et al., 2009). In Europe many studies on the impact of the climate change show that some regions are prone to a rise in flood frequency such as northern and north-eastern Europe (Lehner et al. 2006; Lung et al. 2013) and at a continental level 18.7% of the territory is exposed to high flood hazard (Lugeri et al. 2006). Protection of densely populated areas against floods has always been a crucial issue, which is as old as many human settlements themselves. Indeed, most of the cities are located near river banks or on coasts, which offer favourable conditions for development, such as water

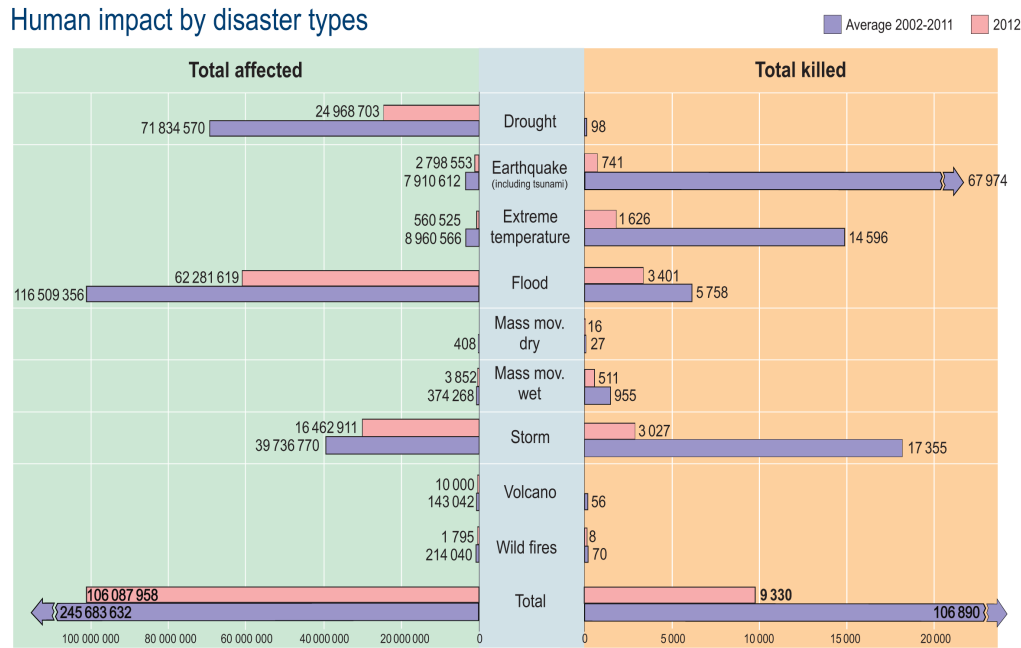


FIGURE 2.1: Human impacts by disaster type in the decade 2002-2012 (EM-DAT, 2012)

supply or the exploitation of fertile lands, but the cost for such favourable locations is an increased exposure to floods that leads to a rise in flood risk (World Meteorological Organization, 2008). According to global-scale reports (United Nations, 2015), around 2006 urban population exceeded for the first time in history the rural population and 60% of the global population is expected to live in cities by 2030. Given the above, it is expected that flood risk in urban areas will continue to rise as a consequence of changes in land use (e.g. due to increasing flood plain occupancy) and of socio-economic development (Elmer et al. 2012).

2.1.2 Flood risk definition and European legislation

The generally accepted definition of flood is the temporarily partial or complete inundation of normally dry land areas. Floods may be caused by the overflow of inland or tidal waters, the unusual and rapid accumulation or runoff of surface waters from any source, or mudflows or the collapse of shoreline land or dams. Flood risk is commonly defined as the product of hazard and subsequent damage, the latter depending on the vulnerability and exposure. Hazard is the occurrence probability of a flood in a certain time interval and location (e.g. a flood in every 100 years) (Ward et al. 2011). The vulnerability is the potential of being harmed by a flood (i.e. susceptibility) and exposure is the proximity to the inundated area for a given scenario (Figure 2.2)(Van Der Veen and Logtmeijer 2005; Messner et al. 2007; Merz et al. 2004). With economic damages estimated at any point for different return periods (e.g. different recurrence intervals), these values can be interpolated in the frequency domain to get a damage-frequency curve. This curve establishes the basis for the calculation of the risk measure, defined as the Expected Annual Damage (EAD). EAD is the sum of the damages caused by all the floods of any possible magnitude, weighted by their probability of occurrence in any one year. If T_R is the return period for which the total economic damage $D_{\epsilon, \text{tot}}$ is estimated, EAD (€/year) can be

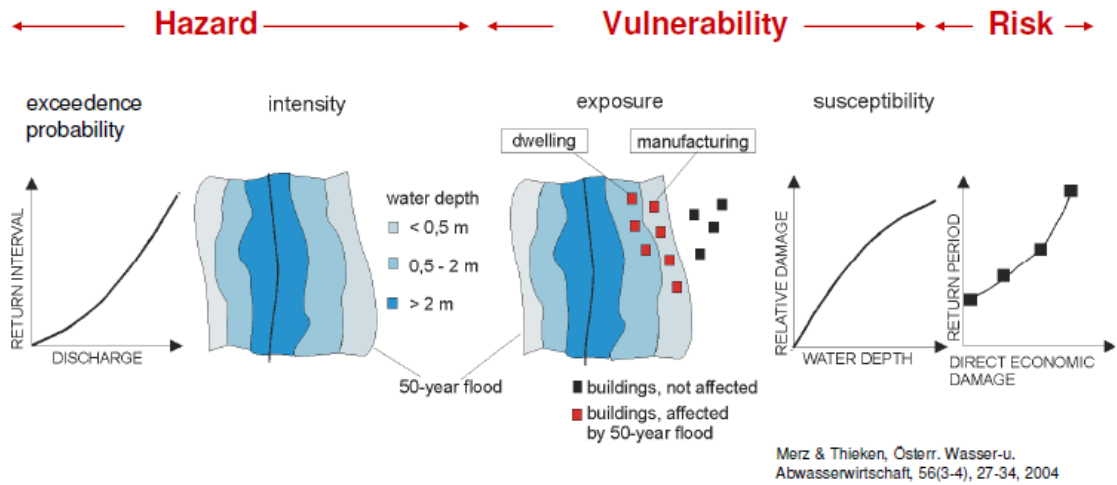


FIGURE 2.2: Hazard, vulnerability and exposure (from Merz et al., 2004).

computed as:

$$Risk = EAD = \int_0^1 D_{\epsilon_{tot}}(T_R) \cdot d\left(\frac{1}{T_R}\right) \quad (2.1)$$

Flood damages are commonly classified into direct and indirect ones (Merz et al. 2010). The direct damages are due to the physical impact of the water with people/objects, the indirect damages are induced by direct ones and occur outside of the flooded area. Indirect flood damages are damages caused by disruption of physical and economic linkages of the economy, and the extra costs of emergency and other actions taken to prevent flood damage and other losses. This includes, for example, the loss of production of companies affected by the flooding, induced production losses of their suppliers and customers, the costs of traffic disruption or the costs of emergency services. In recent years, flood management has shifted from the protection against floods to the management of the risk of floods (Oumeraci et al, 2015). In Europe, this shift is reflected in the Flood Risk Directive of October 2007. The Floods Directive (European Parliament, 2007) is the legislation of the European Parliament on the assessment and management of flood risks. It requires Member States to engage their government departments, agencies and other bodies to draw up a preliminary flood risk assessment. The information in this assessment is used to identify the areas at significant risk, which will then be modelled in order to produce flood hazard and risk maps. Flood Risk Management Plans have been worked out to communicate to policy makers, developers, and the public, the nature of the risks and the measures proposed to manage these risks. The management plans focus on prevention, protection and preparedness. As flooding can have devastating impacts, protecting the needs of the community is at the heart of the Floods Directive approach. The latter aims to manage the adverse consequences that flooding may have on human health, environment, cultural heritage and economic activities.

To satisfy the legislative requirements an interdisciplinary effort is needed to accomplish a chain of models (Figure 2.3), which starts from the hydrologic-hydraulic study (i.e. hazard) and ends up with a final risk map (section 2.1.5). Thus, according to flood risk definition (Eq. 2.1) the two main tasks are the hazard modelling (section 2.1.3) and the damage assessment (section 2.1.4).

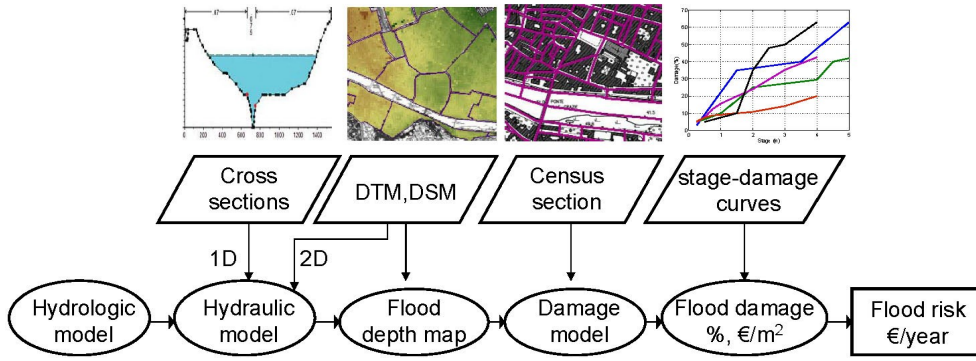


FIGURE 2.3: Standard flow chart for flood risk assessment based on flood depth maps and socio-economic data (from Arrighi et al., 2013).

2.1.3 Hazard modelling

The propagation of floodwaters through the affected area can be approximated using several methods. Simple hydraulic modelling methods may be sufficient for approximating propagation of flood peaks through river channels. More complex hydraulic analyses using advanced numerical models may be required to incorporate effects of infrastructure or complex overland flow in urban areas (Syme et al. 2004; Syme 2008). Advanced models are capable of modeling more detailed physical phenomena, but uncertainties still remain. Hydraulic models rely on topographic data for a consistent geometric representation of the study domain. The availability of high-resolution topographic data, for instance through LiDAR surveys (Yan et al. 2015; Cobby et al. 2001; Correia & Rego 1998), enables us to increase the spatial resolution of the computational mesh, which is generally required for heterogeneous areas such as dense urban settlements. Moreover, remote sensing and satellite images help in many cases to define flow parameters (e.g. roughness). The large use of different types of land data has revealed the role of Geographic Information System as an indispensable tool for a better data management before and after hydraulic simulations (Zerger & Wealands 2004; Deckers et al. 2010; Samarasinghe et al. 2010). The most widely used approach to modelling fluvial hydraulics has been 1D finite difference solutions of the full de Saint-Venant Equations (Horritt & Bates 2002; Gilles & Moore 2010; Finaud-Guyot et al. 2011; Helmiö 2002). The Saint-Venant equations are based on mass and momentum conservation equations, as respectively shown below for the 1D case:

$$\frac{\partial A}{\partial t} + \frac{\partial Q}{\partial x} = 0 \quad (2.2)$$

$$\frac{1}{A} \frac{\partial Q}{\partial t} + \frac{1}{A} \frac{\partial}{\partial x} \left(\frac{Q^2}{A} \right) + g \frac{\partial h}{\partial x} + g(S_0 - S_f) = 0 \quad (2.3)$$

Where Q is discharge (m^3/s), A is cross-sectional flow area (m^2), h is water depth (m), S_0 is the bed slope, and S_f the friction slope. 1D solutions of the full Saint-Venant equations are derived based on several assumptions: the water level across the section is horizontal, the streamline curvature is small and vertical accelerations are negligible, the effects of boundary friction and turbulence can be accounted for using resistance laws analogous to those for steady flow conditions, and the average channel bed slope is small so the cosine of the angle can be replaced by unity. Widely available software, such as HEC-RAS (USACE, 2010) use the general form of the depth-averaged Navier-Stokes

equations. The friction slope S_f in Eq. 4.2 is generally described by the Chézy or Manning formula, which relates the slope of hydraulic grade line to the roughness coefficient. For river reaches containing backwater areas or naturally occurring diversion channels, these assumptions are frequently violated. For out-of-bank flow, the interaction with the floodplain results in highly complex fluid motion with at least two-dimensional properties. The complex interaction of channel and floodplain flow fields make two-dimensional simulation codes more desirable than one-dimensional codes in many modelling situations (Cunge 1969; Horritt & Bates 2002). Continuous improvements in computational resources and affordability have also increased the implementation of 2D modelling. Most widely used 2D codes utilize depth-averaged Navier-Stokes equations, commonly called the Saint-Venant Shallow Water Equations (SWE):

$$\frac{\partial \mathbf{U}}{\partial t} + \frac{\partial}{\partial \mathbf{x}} (\mathbf{F} + \mathbf{F}_d) + \frac{\partial}{\partial y} (\mathbf{G} + \mathbf{G}_d) = \mathbf{H} + \mathbf{I} \quad (2.4)$$

where \mathbf{U} is the variables vector, \mathbf{F} and \mathbf{F}_d and \mathbf{G} and \mathbf{G}_d are the convective and diffusive fluxes vectors in the x and y directions, respectively (in the plane of movement). \mathbf{H} is the friction and slope source term vector and \mathbf{I} the infiltration source vector. The expressions for vectors \mathbf{U} , \mathbf{F} , \mathbf{G} above read:

$$\mathbf{U} = \begin{pmatrix} h \\ hu \\ hv \end{pmatrix}, \mathbf{F} = \begin{pmatrix} hu \\ hu^2 + gh^2/2 \\ huv \end{pmatrix}, \mathbf{G} = \begin{pmatrix} hv \\ huv \\ hv^2 + gh^2/2 \end{pmatrix} \quad (2.5)$$

where h is water depth, u and v are the averaged (over the depth and time in a turbulent flow) Cartesian velocity components, and g the acceleration of gravity. The corresponding expressions for the diffusive fluxes \mathbf{F}_d , \mathbf{G}_d can be written:

$$\mathbf{F}_d = \begin{pmatrix} 0 \\ -\varepsilon h \frac{\partial u}{\partial x} \\ -\varepsilon h \frac{\partial v}{\partial x} \end{pmatrix}, \mathbf{G}_d = \begin{pmatrix} 0 \\ -\varepsilon h \frac{\partial u}{\partial y} \\ -\varepsilon h \frac{\partial v}{\partial y} \end{pmatrix} \quad (2.6)$$

where ε is a viscosity coefficient that accounts for the fluid kinematic viscosity, the turbulent eddy viscosity and the apparent viscosity due to the velocity fluctuations about the vertical average. Finally \mathbf{H} and \mathbf{I} read:

$$\mathbf{H} = \begin{pmatrix} 0 \\ gh(S_{0x} - S_{fx}) \\ gh(S_{0y} - S_{fy}) \end{pmatrix}, \mathbf{I} = \begin{pmatrix} -i_r \\ -1/2 \cdot u \cdot i_r \\ -1/2 \cdot v \cdot i_r \end{pmatrix} \quad (2.7)$$

Here i_r is the infiltration rate into the ground/sinks, S_{0x} and S_{0y} are the bed slopes in the two Cartesian directions, which are assumed small:

$$S_{0x} = -\frac{\partial z_B}{\partial x}, S_{0y} = \frac{\partial z_B}{\partial y} \quad (2.8)$$

where z_B is the bottom elevation and S_{fx} , S_{fy} are the friction slopes, usually represented by means of empirical formulae such as Manning's formula:

$$S_{fx} = -\frac{n^2 u \sqrt{u^2 + v^2}}{h^{4/3}}, \quad S_{fy} = -\frac{n^2 v \sqrt{u^2 + v^2}}{h^{4/3}} \quad (2.9)$$

where n is the dimensional Manning's friction coefficient. However, the shallow water equations are not a true mathematical representation of the movement of water over the

earth surface (Alcrudo, 2004). Putting aside errors originated from a numerical integration of these equations, the following known shortcomings of this approximation stand:

- Vertical velocities are neglected (vertical acceleration are identically zero)
- The pressure field is assumed hydrostatic
- The bottom slope steepness is assumed to be very small
- A uniform horizontal velocity field over the entire water depth is assumed
- Turbulence effects are usually ignored
- Friction formulae are usually taken from uniform flow conditions

The use of 2D equations enables one to choose different levels of approximation with increasing complexity: kinematic, diffusive and full dynamic wave approximation (Hunter et al. 2007). The kinematic wave can be described by a simple partial differential equation with a single unknown field variable (e.g., the flow or wave height) in terms of the two independent variables time (t) and space (x) with some parameters describing the physics and geometry of the flow. This approximation is usually adopted in upstream and midstream steep channel reaches to avoid numerical instability when performing a flood forecast. When these assumptions can't be made, the diffusive wave approximation is considered as adequate for flood simulations (Hunter et al. 2008). The SWE system being of hyperbolic character in time, it represents an evolutionary problem in the form of propagating waves. Therefore a time marching procedure starting with a given initial condition in space, supplemented with boundary conditions along the time path is the proper mathematical conceptual treatment. The discretization of SWE can be made with different approaches: Finite Elements, Finite Volume and Finite Difference (Ferziger, J.H., Peric 2002). 2D models require topography/bathymetry data of the study area in order to generate a computational mesh of the domain. The resolution of the computational mesh varies, according to the scale of analysis, between 1 m (for dense urban areas) and 500 m for macro-scale studies (e.g. at a national or regional level) (Falter et al. 2013; Syme 2008; Hunter et al. 2008). The sustainable complexity of a model depends on the amount of available data and computational resources. Flood propagation in urban areas is clearly three-dimensional, with peculiar features that depend on the complex interaction between the flow and the streets/buildings pattern, especially when the urban texture is very dense as in many historic town centres (Arrighi et al. 2013). One of the challenges for the modeller is how to bring this 3D problem to a 2D model, for instance how to best to represent the roads, fences, houses and other features within the limitations and constraints. Even 2D solutions are very computationally intensive and it is not always practical to utilise a mesh of very fine elements. This requires approximations when representing the urban domain to represent the fences, buildings, and other obstructions. In some cases, 1D numerical models are considered as adequate for the estimation of flood-water levels in river with regular flow patterns and the preliminary identification of inundation zones (Apel et al. 2009; Messner et al. 2007). When there are more complex river geometries and inundation flow patterns are relevant for the precise mapping of local parameters, the use of 2D model becomes unavoidable (Galland et al. 1991; Hervouet et al. 2000; Büchele et al. 2006; Apel et al. 2009; Ernst et al. 2010). Diffusive full 2D models are potentially more accurate than 1D or quasi-2D models, but they are more difficult to apply systematically to large areas if only traditional elevation data are available. They require two crucial pieces of information to achieve their potential accuracy: the detailed

topography of the flow domain, including buildings and infrastructures and their representative roughness. LIDAR-based aerial survey generates high quality topographic data and enables to obtain a complete, high resolution (e.g. order of 1 m nominal spacing or even less) and up-to-date Digital Surface Model (DSM). Recently such tools has become increasingly available also for dense urban areas, so that the problem is no more the data availability, but rather the computational difficulties, resolution and structure of the computational grid, related to the streets/buildings pattern. The determination of roughness coefficients also needs an accurate and high resolution land use database, to be eventually augmented with the increase of friction due to irregular topography (Ernst et al. 2010; Syme 2008). The advantages of a 'classical' 2D model over a more parsimonious one can be strongly reduced if other simplifications are required for their practical implementation, such as a steady-state approximation (Ernst et al. 2010) or an upper bound to the computational nodes. 2D hydraulic models have usually been adopted in portions of sparse urban areas, providing reliable results after calibration studies (Mignot 2006; Apel et al. 2009; Ernst et al. 2010; de Moel et al. 2009; Schubert & Sanders 2012; Ma et al. 2015). For such a study in a dense urban environment, some problems arise in the set-up of a 2D model. First of all, the computational costs which is recognized as the major drawback of 2D models performed with a fine grid size (Begnudelli et al. 2008; Chen et al. 2012). A grid size of 1 or 2 m is generally considered as indispensable to describe the street pattern of many urban environments, especially when historic centres are included, and may lead to long simulations. The combination of a 1D model for the main river channel flow and a 2D model for the inundated areas is recognized as a good compromise between complexity, computation and accuracy. Shallow water equations or their diffusive wave approximation are theoretically optimal choices for the 2D part, but the use of storage cells (Bates & De Roo 2000; Huang et al. 2007; Horritt & Bates 2002) has been also proposed when the aforementioned difficulties arise. The final product of the hazard assessment is a hazard map for a given probability scenario. A GIS environment allows merging the inundation map with socio-economic data to proceed with the damage assessment phase and the risk assessment phase.

2.1.4 Damage assessment

Flood damages can be classified into direct and indirect damages. Direct damages are those that occur due to the physical contact of flood water with humans, property or any other objects. Indirect damages are induced by the direct impacts and occur, in space or time, outside the flood event. Both types of damages are further classified into tangible and intangible damages, depending on whether or not they can be assessed in monetary values (Smith 1994; Jonkman et al. 2008; Merz et al. 2010; Meyer et al. 2013; Thieken et al. 2006; Ward et al. 2011; ten Veldhuis 2011, Oumeraci et al, 2015). Tangible damages are damages to man-made capital or resource flows which can be easily specified in monetary terms, whereas intangible damage is damage to assets which are not traded in a market and are difficult to transfer to monetary values. Although the differentiation in direct and indirect, and tangible and intangible damage is commonplace, interpretations and delineations differ (Jonkman et al. 2008). The loss of life is classified as a direct intangible damage, damages to private buildings and contents or the business interruption are instead classified as direct tangible damages. Intangible damages are often related to damage categories, which are hardly monetizable such as human life or cultural heritage (Arrighi et al., 2016, Burzel et al., 2015). Therefore, the assessment methods for human losses differ from the common direct tangible damages estimation (Dassayanake et al., 2015). Usually direct tangible damages are evaluated by means of stage-damage functions. A stage-damage function is a relationship between flood depth

and potential damage. This does not mean that damages depend only on flood depth, other flood parameters play an important role (velocity, flood duration, preparedness) but are more rarely included in damage functions (Kreibich et al. 2009). Such functions are internationally accepted as the standard approach to assess urban flood loss (Smith 1994; Jonkman et al. 2008; Genovese 2006; Meyer et al. 2013; Luino et al. 2012; Arrighi et al. 2013; Scorzini & Frank 2015). Stage-damage functions can be drawn using existing damage data collected after occurred events (empirical functions) (Büchele et al. 2006; Apel et al. 2009) or synthetically by experts (Oliveri & Santoro 2000; Arrighi et al. 2013). The scale of analysis at which the risk study is carried out significantly affects the assessment of flood damages. The scale of analysis is strictly related to the available resources in terms of time, finance and data requirements. The choice of an appropriate method of damage evaluation depends on the size of the area under investigation. Three study types are usually distinguished. Firstly, national or even international studies may refer to a national coastline or a river basin of a transboundary river. Secondly, regional study areas are of medium size and relate, for instance, to a part of a big river or the catchment of a smaller river. Thirdly, local-sized study areas aim at examinations of municipalities, single cities or even single properties. The common classification of the scale of analysis is as follows:

- Micro-scale methods apply an object-oriented approach, i.e. damages are calculated for single properties, e.g. buildings (Oliveri & Santoro 2000; Apel et al. 2009; Ernst et al. 2010; Arrighi et al. 2013; Scorzini & Frank 2015)
- Meso-scale methods consider aggregated land use units, e.g. residential areas and industrial areas (Genovese 2006; Lindenschmidt et al. 2006)
- Macro-scale methods consider administrative units, e.g. municipalities or regions (Ward et al. 2013)

Recently, the direct economic losses due to flooding of an urban area in Hamburg has been assessed at a micro-scale level (buildings) and then aggregated to a meso-scale level by clustering similar buildings (Oumeraci et al. 2015). Although this approach required more data and efforts, it provided better results than the common meso-scale assessment. Moreover, it was also shown that direct economic losses alone cannot represent a sufficient indicator for the severity of the losses and for decision making related to risk mitigation measures. In addition, a consistent consideration of indirect economic losses and intangible losses as well as their consistent aggregation was found to be crucial for the outcomes of the integrated risk analysis (Oumeraci et al. 2015). Although performed at the same scale of analysis, flood risk assessments show large differences in terms of damage curves and economic evaluation, reflecting the adoption of different approaches and underlying hypothesis (de Moel et al. 2009).

2.1.5 Risk assessment

Once both hazard and damage assessment steps are accomplished, the risk can be evaluated according to Eq. 2.1. The risk measure, which normally is expressed as a monetary cost per year, is representative of the tangible damage categories. However, the assessment of flood risk for people, beside intangible damages, is required to understand the potential consequences of an inundation and support risk management practises. Flood fatality risk can be assessed both from an individual and societal point of view (Beckers & De Bruijn; de Bruijn et al. 2014; Tapsell et al. 2002). The individual flood fatality risk relates to the probability of a person dying as a result of a flood event at a certain location.

This perspective focuses on hazardous locations without taking into account the population density at those locations. Societal flood fatality risk is related to the probability of events with many fatalities. It is expressed by a curve, which gives the annual probability of an event with N or more fatalities (de Bruijn et al. 2014). It combines information on flood hazards, flood extents and population density in flood-prone areas. Research on loss of life in floods is sparse, and has been so far focusing on physical experiments (Abt et al. 1989; Karvonen et al. 2000; Jonkman & Penning-Rowsell 2008; Xia et al. 2014) or dam break catastrophes (Aboelata & Bowles 2008; Chakraborty et al. 2005). Most of loss of life models are based on the location of the population at risk measured by its distance from the dam and account for the depth of flooding, population distribution, and effectiveness of warning and evacuation processes (Aboelata & Bowles 2008; US Department of Homeland Security, 2011). Other models relate the mortality to past flood events, which may not be representative anymore of current situation (Jonkman et al. 2002). Brown and Graham (1988) have developed a loss of life model based on the analysis of 24 historic dam failures and flash floods. In developing the model, they included the statistical data on population at risk and warning time. An outline methodology and an operational framework for assessing and mapping the risk of death or serious harm to people from flooding at an intermediate or “community” scale has been presented by Penning-Rowsell et al. (2005). It covers death and physical injuries as a direct and immediate consequence of deep and/or fast flowing floodwaters (usually by drowning), and the risk of death and serious physical injuries associated with the flood event. The parameters for hazard rating are water depth, flow velocity and distance from the river/coast. However, the existing loss of life models suffer of many shortcomings. First, these models and the related criteria are empirical and second, they do not account for the actual causes of drowning. Thus, the examination of existing reports about people fatalities during floods is needed.

2.1.6 People fatalities

The characteristics of the flood and floodwater along with the characteristics and behaviour of the population determine the likelihood of a death due to flooding (Di Mauro et al. 2012). It is widely recognized that, in developed countries, the majority of flood-related fatalities occurs as a result of inexperienced people entering floodwater either in boats, vehicles or on foot (Franklin et al. 2014). Currently the vehicles instability in floodwaters is considered as the most aggravating factor of the flood risk in urban environment for people’s safety (Figure 2.4). Many studies (Jonkman & Kelman 2005; Maples & Tiefenbacher 2009; Fitzgerald et al. 2010; Meridith et al. 2010) have shown that the first cause of death during a flood event is related to roads and vehicles. The interaction between flood propagation and roads is crucial because roads are preferential channels and they allow floodwaters to move into the cities. Second, the flow in the streets may cause the instability of vehicles and street furniture, creating a temporary floating debris, which is deposited when floodwaters lose their energy.

Usually the pictures taken in the aftermath of a flood event in the newspapers show huge piles of vehicles swept away by floodwaters. Figure 2.5 shows a crossroad in Genoa after the 2011 flash flood. Beside the damages to the cars and danger for people, the stack of vehicles forms a barrier, which slows down the rescue and emergency activities.

Jonkman & Kelman (2005) reported that in the Netherlands the 33% of deaths for drowning occurs in a vehicle and the 25% as a pedestrian. Maples & Tiefenbacher (2009) show that a minimum of 216 deaths were caused by automobile immersion on flooded roadways in Texas during the study period 1950-2004. The deaths occurred in at least 140



FIGURE 2.4: The 2013 flash flood in Athens (source: <http://www.timesofmalta.com>).

separate incidents. A decadal examination shows an increasing frequency of roadway-drowning deaths in Texas. Fitzgerald et al. (2010) argue that the 48.5% fatalities is related to vehicle use and 26.5% fatalities occurred because of inappropriate or high-risk behaviour during floods (included driving in flooded streets). Therefore, it is clear that the circumstances of flood-related casualties are crucial to identify appropriate risk management strategies. Thus, the existing laboratory experiments (section 2.2) on vehicles/people instability in flood flows may provide a physical framework for hazard criteria.

Floods may have devastating impacts on the society, the environment and the economy. The Floods Directive promotes a risk management approach consisting in flood risk assessment and development of mitigation strategies. Assessing flood risk means to consider its components, namely hazard, vulnerability and exposure. People safety is the primary objective, but current hazard and risk maps do not allow to relate flood characteristics with the main causes of people fatalities, which are in order of importance driving and walking in water flows.

2.2 Experimental data on vehicles and people

2.2.1 Experiments on incipient motion of small scale vehicle models

Although the vehicles are so critical during floods in urban areas, a limited number of studies have been carried out on the behaviour of cars facing a flood flow. Buoyancy, lift and drag are recognized as the main hydrodynamic effects by which a stationary vehicle becomes unstable and floats or slides. Assuming that a car cannot be filled quickly by floodwater, its density is much smaller than water density and most of the weight is usually distributed in the lower front part (close to the engine in the majority of modern cars). The floating instability occurs when the buoyancy and lift effect exceed the weight



FIGURE 2.5: The aftermath of Genoa 2011 flood event (source: <http://www.italia45-45.it/alluvioni>).

of the car. The sliding instability occurs when the drag force exceeds the resistance force (i.e. tyre/road friction). Buoyancy and lift reduce the normal component of the weight thus promoting sliding conditions even for very low water depths. While for road safety purposes moving vehicles on a wet surface are considered (e.g. road-tyre adherence), for urban flood safety, parked vehicles are also considered. A common flooding situation is the one caused by failure of the street drainage system for intense rainfall, with flood depth up to 0.2 m and velocities up to 0.25 m/s. Much less studied is the vehicle interaction with flow conditions typical of river inundations or flash floods (Arrighi et al. 2015). Most of the existing studies have been performed for road safety purposes, including flume experiments in 1960's and early 1970's (e.g. Bonham & Hattersley, 1967; Gordon & Stone, 1973) as well as theoretical analyses in the early 1990's (e.g. Keller & Mitsch, 1993). However, substantial changes in vehicle design have been introduced since these early studies, especially in vehicle planform area, vehicle weight and ground clearance. Therefore, the results of these earlier studies may no longer be representative of contemporary vehicles (Cox & Shand 2010). In addition, some criteria, introduced for road drainage design, are empirical and completely neglect vehicle characteristics. Moreover, they mostly account for water depth H as a representative flood parameter. A review of existing road drainage design criteria related to road safety have been presented by Russo et al. (2005) and are summarized in Table 2.1.

Recently, some studies have been carried out to investigate, at the laboratory scale, the behaviour of parked vehicles in flooded streets (Shu et al. 2011; Xia et al. 2013; Xia, Teo, et al. 2011; Teo et al. 2012). In the study by Xia et al. (2011), a formula has been derived to predict the critical flow velocity for the incipient of flooded vehicles based on the sliding stability. A series of flume experiments were conducted using three types of scaled die-cast model vehicles, with two scales being tested for each type of vehicle (1:43 and 1:18). The three model vehicles were Mitsubishi Pajero, BMW M5 and Mini Cooper. Since the models were not waterproof, the density was assessed considering the amount

TABLE 2.1: International risk criteria in urban drainage based on water depth H and flow velocity U (Russo et al. 2005)

Hydraulic parameters Risk criteria by:	H (m)	U (m/s)	$H \cdot U$ (m ² /s)	$H^2 \cdot U$ (m ³ /s)
Denver (Wright-Mc Laughlin, 1969)	0.45	-	-	-
Mendoza (Nania, 1999)	0.3	-	-	-
Clark County (CCRFGD, 1999)	0.3	-	0.55	-
Austin (Austin Dep. Public Works, 1977)	Function of spread	-	-	-
Témez (Témez, 1992)	1.0	1.0	0.5	-
Abt (Abt et al., 1989)	-	-	0.5	-
Slide Stability (Nania, 1999)	-	-	-	1.0
Overtuning Stability (UPC, 2001)	-	-	0.45	-

of water filling the car. Each experiment consisted in gradually adjusting the velocity in the laboratory flume for a given water depth until the onset of motion of the vehicle model. Only a flow direction parallel to the longitudinal axis of the car was analysed during the flume experiments. The experimental data obtained for the small-scale model vehicles (1:43) were used to determine the two parameters α , β in the formula (Eq. 2.11) derived (Eq. 2.10) by Xia et al. (2011):

$$U_c = \alpha \cdot \left(\frac{H}{H_v} \right)^\beta \cdot \sqrt{2g \cdot \left(\frac{\rho_c - \rho}{\rho} \right) \cdot H_v} \quad (2.10)$$

where U_c (m/s) is the critical incipient motion velocity, H (m) is the water depth, H_c (m) is the vehicle height, ρ_c (kg/m³) is the vehicle density and ρ (kg/m³) is the water density. The parameter β is an empirical coefficient relating the near bed velocity and the average velocity according to the distance from the bottom of the channel and α is

$$\alpha = \frac{\sqrt{\frac{\mu a_v}{C_D \cdot a_d / a_h + \mu C_L}}}{(1 + m) a_b^\beta} \quad (2.11)$$

where C_D and C_L are the drag and lift coefficients respectively, μ is the friction coefficient, a_v is a coefficient representing the ratio between car volume and the volume of the rectangular prism with the same geometric dimensions. Then, a_h and a_d are empirical coefficient for calculating the area affected by lift and drag force respectively, a_b is a coefficient related to the height of the vehicle, m is not defined. The prediction accuracy of Eq. 2.10 was validated using the data obtained for the large-scale (1:18) model vehicles. Finally, the corresponding the critical flow velocities for incipient motion of the vehicles were computed for various incoming water depths using the formula for three prototype vehicles. It is found that for a specified vehicle, the value of the critical flow velocity for the onset of vehicle motion reaches its minimum as the incoming flow depth approaches the height of the vehicle and the smaller and lighter vehicle is the easiest to start sliding in floodwaters. Since the vehicle model can be filled by water, some fully submerged conditions of onset of motion are considered (Figure 2.6).

In the study by Shu et al. (2011), the experiments on the incipient sliding of the vehicle have been carried out using three different waterproof scale models (1:18). The vehicle models were Ford Focus (small passenger vehicle), Ford Transit (middle van) and Volvo XC90 (4WD vehicle). The models were filled with light foam in order to seal them. Thus, the experiments were conducted under partially submerged conditions. The density of

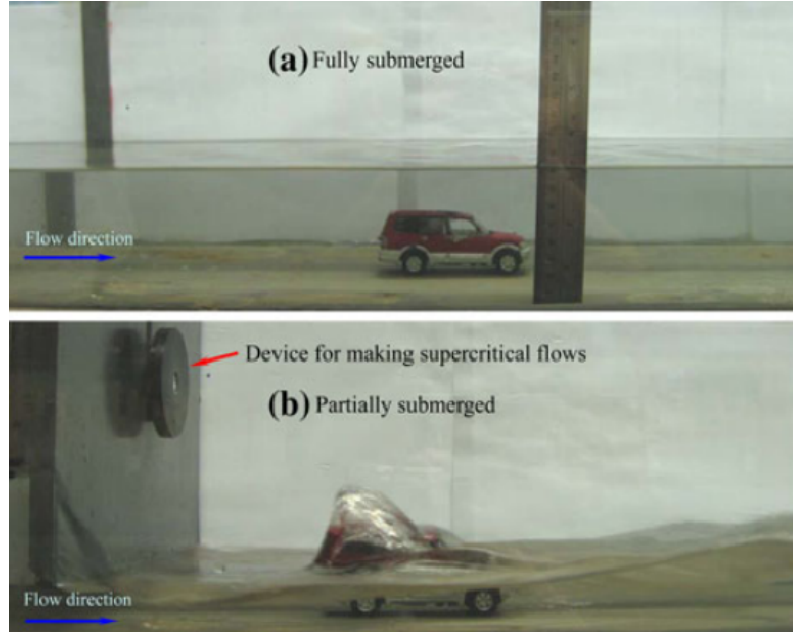


FIGURE 2.6: Experiments on fully (a) and partially (b) submerged Mitsubishi Pajero (1:18) (from Xia et al., 2011).

the model vehicle was approximately equal to that of the prototype vehicle. A formula to predict the flow velocity for incipient motion of vehicle was derived which accounts for the forces acting on the vehicle

$$U_c = \alpha \cdot \left(\frac{H}{H_v} \right)^\beta \cdot \sqrt{2gl_c \cdot \left(\frac{\rho_c}{\rho} \cdot \frac{H_v}{H} - R_f \right)} \quad (2.12)$$

where l_c (m) is the length of the vehicle and R_f is

$$R_f = \frac{H_v \cdot \gamma_c}{H_c \cdot \gamma} \quad (2.13)$$

with γ_c and γ as the specific weights of the car and the fluid, respectively and H_c is the critical depth at which the vehicle starts to float. Two vehicles orientation angles were considered. The orientation angle of 0° means that the front of a vehicle was facing the direction of the incoming flow, while the orientation angle of 180° means that the rear side was facing the incoming flow direction. The experimental results indicated that there was not a substantial difference in the conditions of incipient motion for these two vehicle orientation angles because the submerged area projected normal to the incoming flow for the case of 0° was virtually equivalent to that for the case of 180° for a partially submerged vehicle. The incipient velocity obtained in the experiments increased with the decrease in the incoming water depth for each vehicle. Similar relationships between H and U_c were obtained for orientation angles 0° and 180° . Under the same flow velocity, the depth at which the vehicle Volvo XC90 started to float was greater than the corresponding depth for the Ford Focus or the Ford Transit. Therefore, there exists a significant difference in the incipient motion conditions for various types of vehicles. The experimental results were used to assess the flow velocity for the incipient motion of prototype cars, based on scale ratios.

In the study by Teo et al. (2012), extensive investigations have been undertaken on

stationary scaled die cast model vehicles in laboratory hydraulics flumes by conducting a series of physical experimental studies on:

- the threshold of vehicle instability
- the effects of vehicle orientation
- the effects of ground surface gradient

The experimental studies were carried out on scaled die cast model including: a Mitsubishi Pajero, BMW M5, Mini Cooper, and a Ford Escort. The selected characteristics of the four vehicles differ in terms of size, design, shape, and weight: a new design of small size, a new design of medium size, a large size vehicle, and an old design of medium size. This range of vehicles was considered to provide a good coverage and comparison on how the size (i.e. small, medium, and large), design shape (i.e. new and old with aerodynamic considerations) and weight (i.e. light and heavy) of vehicles would affect the conditions for the threshold of instability in urban floodplains. Based on these experiments, the actual front and rear ends of the vehicles facing flows (i.e. 0° and 180°) resulted in higher values of both water depth and flow velocity for the threshold of instability. As a matter of fact, although the aerodynamic design of these vehicles plays a prominent role in hydraulic drag reduction, the smoothing front and rear ends of these vehicles facing flows reduces the extent and intensity of the high pressure. As a result, vehicles at these orientations to the flow require higher values of water depth and/or flow velocity to reach the threshold for incipient motion of the vehicles. On the other hand, the orientations for the side ends of vehicles facing the flow require smaller threshold values. The lateral orientations (60° and 90°) were recognized as one of the potential critical conditions to first trigger the motion of vehicles. Four different surface slopes of 1:100, 1:200, 1:300, and 1:1000 were tested in the laboratory flume. According to the experimental results for all the partially submerged model vehicles, the threshold velocity for incipient motion decreased with increasing channel slope. In fact, larger channel slopes decrease the horizontal weight component, which contributes to friction stability. The most interesting result by Teo et al. (2012) is the diagram of instability for the vehicles, that describes under which conditions of flood depth and velocity a vehicle becomes unstable (Figure 2.7). Two sets of linear relationships were observed for each type of vehicle during fully or partially submerged conditions, where the incoming water depth, was greater or smaller than the height of a vehicle.

Figure 2.7 shows clearly two contrasting relationships, with reference to the height of the vehicles. For the partially submerged vehicles (i.e. the incoming water depth is smaller than the height of a vehicle), the findings show that the downward force is countered by increased buoyancy, whereas an increase in the flow depth lead to a corresponding decrease of the flow velocity required to initiate vehicle motion. When vehicles are fully submerged, i.e. both the projected area of the vehicle and drag coefficient are larger, a lower threshold velocity was needed to induce a drag force large enough to overcome the friction force. The critical threshold velocity for vehicles under partially submerged conditions ranged from 2.0 to 8.0 m/s as compared to 2.0 -3.0 m/s under fully submerged conditions. The above described results were used for preliminary risk assessment to define the hazard to vehicles parked on flooded streets (Xia et al. 2011). Further results related to the influence of the flow orientation on the incipient motion of flooded vehicle has been recently published (Xia et al. 2013). Three orientation angles (0° , 180° and 90°) and two types of die-cast model vehicles (Honda Accord and Audi Q7) with two different scales (1:14 and 1:24) were tested in the laboratory. The test results indicated that there was not a substantial difference in the conditions of incipient motion for 0° and 180° ,

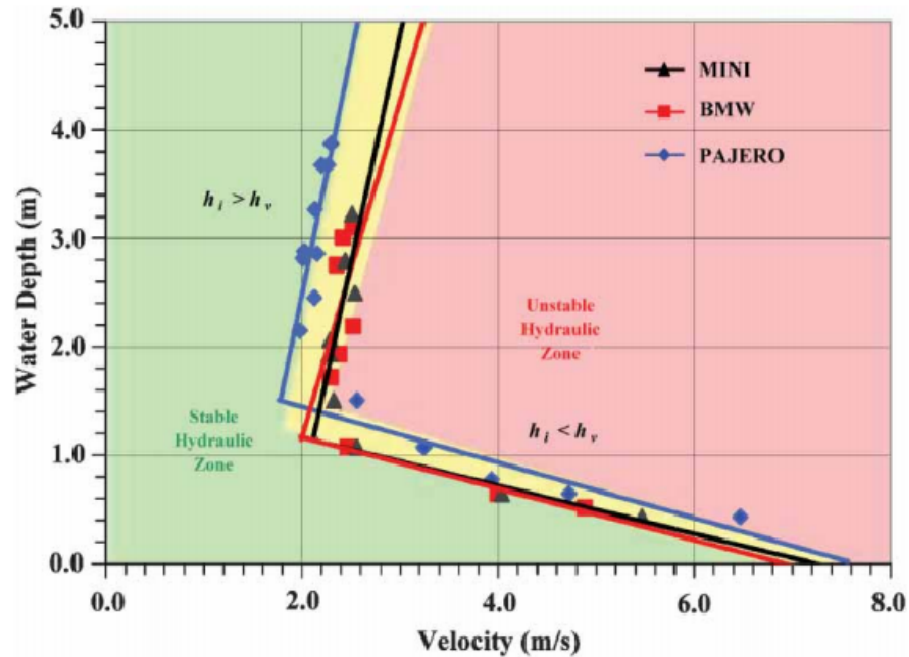


FIGURE 2.7: Critical threshold values of hydraulic instability for vehicles (Teo et al. 2012)

because the submerged area projected normal to the incoming flow for the former was virtually equivalent to that for the latter for a partially submerged vehicle. However, the test results for 90° evidently differ from those for 0° and 180° . The experiments with the Honda model show that for the same flow depth, the threshold velocity for 0° and 180° are slightly greater than that for the 90° orientation, due to the larger projected area, which contributes to increase the drag force. The available experiments on the onset of motion of modern vehicles (Shu et al. 2011; Xia et al. 2013; Xia, Teo, et al. 2011; Teo et al. 2012) have been carried out on small scale models, which may not be representatives of prototype cars. The experimental results have been used to calibrate some formulae describing the critical flow velocity for incipient motion of vehicles. However, drag and lift forces have not been measured during the experiments, thus the physical hydrodynamic mechanisms underlying the onset of motion is still unclear. Moreover, the experimental data in terms of critical water depth and velocity are extremely scattered because the vehicle weight and geometry plays an important role in the flow-vehicle interaction.

2.2.2 Experiments on people instability in flood flows

Human safety is generally the primary objective in any flood risk management strategy. In section 2.1.6 the existing studies on people fatalities have illustrated that the main cause of death for drowning is related to vehicles (Maples & Tiefenbacher 2009; Meridith et al. 2010; Fitzgerald et al. 2010; Jonkman & Kelman 2005). However many casualties occur also when people try to move in floodwaters (Di Mauro et al. 2012; Milanesi et al., 2015; Chanson et al. 2014). Thus, understanding the safest way to face a flood might be of crucial importance for management strategies (Franklin et al. 2014; Di Mauro et al. 2012). Two hydrodynamic mechanisms that can cause human instability have been usually distinguished in previous studies: moment instability (toppling) and friction instability (sliding). Toppling occurs when the mobilising moment caused by the incident flow exceeds the resisting moment caused by the resultant weight of the body (Abt et al.,

1989; Jonkman & Penning-Rowsell 2008). Sliding occurs if the drag force induced by the flow is larger than the frictional resistance between the person's feet and the substrate surface (Keller & Mitsch, 1993). Foster & Cox (1973) tested the stability of children with different height and mass combinations in a laboratory flume and found that human stability to water flow is affected by a wide set of physical, emotional and dynamic factors. They observed that failure was mainly caused by slipping, since the tests were performed with high flow velocities and low water depths. Further tests by Abt et al. (1989) showed that toppling should also be accounted. More recently, several experimental analyses were performed on real adults and children (Takahashi et al., 1992; Keller and Mitsch, 1993; Karvonen et al. 2000; Yee, 2003; Russo et al. 2013) considering different training, wearing, environmental conditions and definitions of instability (Figure 2.8, Figure 2.9). These studies provide an experimental basis for an inversely proportional linear relationship between mean flow velocity and depth (Shand et al., 2011), that are often introduced as a reference in several national regulations on flood hazard zoning. These empirical approximating functions are however purely regressive and do not allow to establish an effective link between hazard level and physical effect. In order to overcome some of the limitations of experimental activities and to provide an interpretative framework, some conceptual models (Pan & Chanson, 2015) were introduced in the last decades to describe the human stability as a function of flow velocity and water depth. These models are based on different assumptions regarding the shape of the body, the involved forces and the failure mechanisms. Love (1987) modelled a rectangular monolith and recognized the role of the buoyancy force and of toppling instability. Lind et al. (2004) tested both conceptual and empirical formulae finally calibrating a relation based on the concept of the product number (i.e. water depth multiplied by flow velocity Eq. 2.14). They modelled the human body as a rigid circular cylinder of diameter a and height H . They proposed an equation for toppling instability, which yields the critical depth speed product number $(h \cdot v)_{cr}$ as

$$(h \cdot v)_{cr} = \left[\frac{\pi g}{C} adH \left(1 - \frac{h}{H} \right) \right]^{\frac{1}{2}} \quad (2.14)$$

where C is the drag coefficient assumed equal to 1.2 and d (m) is the moment arm about the pivot of toe.

Walder et al. (2006), studying a tsunami induced by a debris flow, developed a simplified approach (Eq. 2.15) to predict critical velocity U_{cr} for slipping to occur, disregarding toppling instability and the role of the buoyancy force

$$U_{cr} \approx \sqrt{\frac{\mu mg}{\rho C_D D_l D_a}} \quad (2.15)$$

where m (kg) is the person mass, D_a (m) is the distance from the sole of the foot to the ankle and D_l (m) is the average diameter of the leg. Walder et al. (2006) also supposed that, in waters of some sufficient depth people couldn't stand even if the flow velocity is negligible. They proposed a simple criterion of the form

$$\bar{h}_c \approx 10 D_a \left(1 - \frac{U_{\max}}{UC} \right) \quad (2.16)$$

where the factor 10 is equal to a selected selected maximum water depth divided by D_a , U_{ref} is set equal to 2.5 m/s, which is about 50% of U_a . They also identified depth thresholds for adult men, women and children evaluated from typical average mass and physical characteristics. More advanced approaches were pursued by Jonkman &

Penning-Rowsell (2008) and, recently, by Xia et al. (2014), who coupled experimental and theoretical analyses. Jonkman & Penning-Rowsell (2008) tested an adult stuntman in



FIGURE 2.8: Experiments on human instability: water depth 1.07 m and velocity 1.0 m/s (from Karvonen et al., 2000)

real channel conditions of low depth and significant velocity. Moreover, they calibrated a simplified model for adults accounting for both slipping and toppling but neglecting the buoyancy force. The resulting equations were calibrated on the basis of Abt et al. (1989) and Karvonen et al. (2000)(Figure 2.8) data sets and fitted well the experimental points by Jonkman & Penning-Rowsell (2008), that actually are related to low depths where buoyancy force plays a minor role for slipping instability. Recently, Xia et al. (2014) conducted experiments on a human body model with geometric scale 1:5.54 (Figure 2.9). They developed a strongly parametric scheme, introducing buoyancy force and considering both toppling and slipping failure mechanisms. They derived two formulae for the critical velocity for slipping and toppling instability mechanism. The model was then extensively calibrated by experimental data from the literature, disregarding the slipping failure mechanism on the ground that it is considered of rare occurrence. The comparison between experimental data of real humans and those of the human model illustrates that the latter is more unstable than real humans under the same flow conditions. In fact, the human model could not adjust its standing posture according to the flow conditions and therefore became unstable for lower velocities. The effect of the local bottom slope on human stability was accounted for by Abt et al. (1989) and Jonkman & Penning-Rowsell (2008), who considered values of slope steepness in a limited range below 1.5%. Milanese, et al., (2015) recently introduced a conceptual model for people instability in a fluid flow also considering the effect of the local bottom slope and the effect of the density of the fluid.

Cox & Shand (2010) and Russo et al. (2013) reviewed all the experimental data on people instability from 1989 to 2008. They proposed hazard regimes for adults and children collecting all the previous experimental data on people instability (Figure 2.10). The proposed hazard regimes (Cox & Shand 2010) are function of the product of water depth H and velocity U ,

$$U \cdot H = 0.4 \quad (2.17)$$

is the hazard threshold proposed for children for water depth lower than 0.5 m, which is considered a limiting value.

$$U \cdot H = 0.6 \quad (2.18)$$



FIGURE 2.9: Human model (scale 1:5.54) tested by Xia et al. 2014

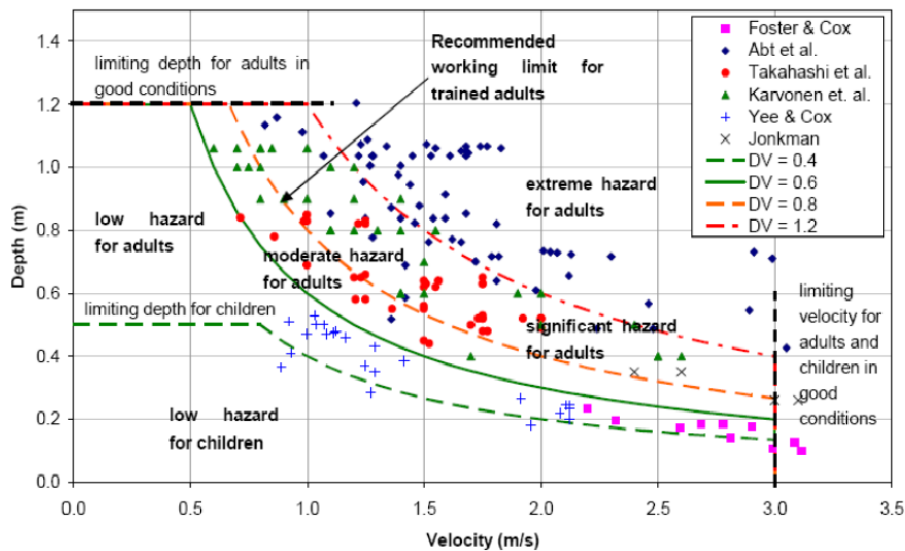


FIGURE 2.10: Proposed hazard regimes for people (from Russo et al., 2013)

is the threshold between low and moderate hazard for adults.

$$U \cdot H = 0.8 \quad (2.19)$$

is the recommended working limit for trained adults.

$$U \cdot H = 1.2 \quad (2.20)$$

is proposed as the limit for extreme hazard for adults. The above criteria (Eqs. 2.17, 2.18, 2.19, 2.20) are currently used in Australia to develop safety guidelines for pedestrians in flood. The criteria Eqs. 2.17, 2.18, 2.19, 2.20 are usually called product number curves. They are empirical thresholds which attempt to interpret the large variability of critical pairs of water depth and velocity observed in the experiments. For their empirical definition the product number curves do not allow assessing the physical consequences of

flow properties on human subjects. Moreover, they do not account for the type of instability mechanism involved (e.g. toppling or sliding) and are not defined for flow velocity higher than 3.0 m/s, i.e. for supercritical flows. These characteristics make the product number curves a simplified tool for people's hazard mapping, which is the main advantage justifying their large use. However a better understanding of instability mechanisms for pedestrians in floodwaters would help defining physically based curves instead of empirical ones with interesting benefits for flood risk mapping and educational purposes. Over the last four decades, a number of laboratory-based experimental studies have been undertaken to define the limits of stability under different flow regimes. Moreover, different conceptual models have been developed to derive formulae for these stability limits. Human stability within floodwaters has been found to be dependent on many factors. The two most important factors are flow depth and velocity, with the depth dictating whether loss of stability is by sliding (friction) or toppling (moment) failure. Large water depths increase buoyancy and reduce friction underfoot typically resulting in tumbling failure while low depth-high velocity flows may cause sliding instability (Cox & Shand 2010). The main evidence of the experimental data plotted in Figure 2.10 in terms of critical pairs of water depth and flow velocity is that they are extremely scattered. This occurs within an individual data sets and, to a more significant degree, when all data sets are combined. In fact, instability conditions are strongly affected by diverse external parameters, including the physical characteristics of the subjects (i.e. weight and height), their level of training, clothing and experimental conditions (i.e. flume characteristics). Thus, a precise identification of hazard regimes in dimensional terms is quite difficult.

The literature on people instability under water flows is sparse and existing datasets are affected by a large scatter, which depends on the large variability of human characteristics, such as weight and height. Conceptual models identified two instability mechanisms, namely toppling and sliding. Only a few recent laboratory tests, carried out to detect the critical pairs of water depth and velocity, have investigated the incipient motion of small scale model vehicles. However, instability diagrams suffer again from a large scatter depending on vehicles characteristics. Moreover the transferability of these findings to prototype vehicles and the role of hydrodynamic forces has not been studied so far.

2.3 Numerical modelling

2.3.1 Effects of an obstacle in a fluid flow

In a natural environment, the presence of a bluff body immersed in a fluid affects the flow around it (Bearman & Morel 1983; Rodi, 1997). The mechanics of the flow around a bluff body and the interaction between fluids and objects is a subject mostly studied in aerodynamics for its implications on the design of structures and infrastructures (i.e. vibrations). In free surface flows, such as in rivers, a common case is the presence of boulders on the bed, which affect the water flow as an increased roughness (Olsen & Stokseth, 2010), while in an urban environment, for instance, a building is an obstruction affecting the propagation of a flood (Syme, 2008). The main effects of the interaction between fluids and structures are:

- flow separation and generation of complex vortices and wakes
- non-uniform 3D flow in the near field around the body

- hydrodynamic solicitation of the body

The prominence of these effects depends on the characteristic of the flow and on the geometry of the body. A vehicle or man immersed in floodwaters behave as obstacles to the flow, thus interact with the flow field. The immersed body is affected by hydrodynamic forces generated by non-uniform pressure distribution around the body (drag and lift forces). The study of flow around an obstacle is of large importance in many fields starting from industrial applications (e.g. aerodynamics of vehicles) up to environmental applications (e.g. dispersion of pollutants, scour evaluation around submerged structures) (Zhang et al. 2006; Campana et al. 2006; Tseng et al. 2006; Teruzzi et al. 2006; Ataie-Ashtiani & Aslani-Kordkandi 2013; Malavasi & Guadagnini 2003). Given the complexity of such problems, the common approach is to describe the flow considering three dimensions in order to capture all the effects (e.g. turbulence) and evaluating the consequent stresses. Starting from the 1960s the analysis of systems involving fluid flow has been carried out through Computational Fluid Dynamics (CFD) (Ferziger, J.H., Peric 2002; Anderson, 1995).

2.3.2 CFD numerical modelling

First works on CFD solutions appeared during 1950's and 60's as an attempt to solve the high velocity and temperature re-entry problem (Anderson, 1995). The introduction of the time averaging technique provided an important advance on the CFD solutions, making practical the use of this tool for several applications (Anderson, 1995). CFD models based on solutions of the Navier-Stokes (NS) equations can provide accurate and detailed solutions of the flow around a bluff body. The NS equations are a set of non-linear partial differential equations that can describe the fluid motion. Several numerical models are based on the solution of these equations but assumptions and considerations are normally implemented to simplify the NS equations (e.g., time and volume averaging techniques). The Reynolds Averaged Navier-Stokes equations (RANS), the Volume-Averaged RANS equations (VARANS) are some of the set of equations derived by simplification of the original NS equations in order to solve practical problems. The decomposition allows the separation of the time-averaged and time-fluctuating quantities: the time averaged quantities are calculated directly through the set of equations, while the fluctuating components are modelled by the turbulence models, as closure of the RANS equations (Ferziger, J.H., Peric 2002). Considerable research efforts have been dedicated to the development of numerical methods to capture the effects due to turbulence. These methods can be grouped into the following three categories:

- Turbulence models for Reynolds-averaged Navier-Stokes equations (RANS): the attention is focused on the mean flow and the effects of turbulence on mean flow properties. Prior to the application of numerical methods the Navier Stokes equations are time averaged (or ensemble averaged in flows with time-dependent boundary conditions). Extra terms appear in the time-average flow equations due to the interactions between various turbulent fluctuations. These extra terms are modelled with classical turbulence models: among the most common ones are the $k - \epsilon$ model and the Reynolds stress model (Lumley, 1977; Speziale, 1991; Nagata et al., 2005). The most common RANS turbulence model are classified according to the number of additional transport equations that need to be solved (e.g. zero for the mixing length model, two for $k - \epsilon$ model). These models form the basis of standard turbulence calculation procedures in currently available commercial CFD codes (Ferziger, J.H., Peric 2002).

- Large eddy simulation (LES): this is an intermediate form of turbulence calculations, which tracks the behaviour of the larger eddies. The method involves space filtering of the unsteady Navier-Stokes equations prior to the computations, which passes the larger eddies and rejects the smaller eddies. The effects on the resolved flow (mean flow plus large eddies) due to the smallest, unresolved eddies are included by means of a so-called sub-grid scale model. The method starts with the selection of a filtering function and a certain cut-off width with the aim of resolving in an unsteady flow computation all those eddies with a length scale greater than the cut-off width. In the following step, the spatial filtering operation is performed on the time-dependent flow equations. During the spatial filtering, information related to the smaller filtered-out turbulent eddies is destroyed (John, 2004; Tseng et al., 2006; Kim et al., 2015).
- Direct numerical simulations (DNS): these simulations compute the mean flow and all turbulent velocity fluctuations. The unsteady Navier–Stokes equations are solved on spatial grids that are sufficiently fine that they can resolve the Kolmogorov length scales at which energy dissipation takes place and with time steps sufficiently small to resolve the period of the fastest fluctuations. These calculations are highly costly in terms of computing resources, so the method is generally not used for industrial flow computations (Moser et al. 1999; Scardovelli & Zaleski 1999).

Vehicles are commonly studied with aerodynamics purposes, in order to improve their design with a decrease in the aerodynamic resistance (Zhu et al. 2012). The numerical modelling approach to the problem of incipient motion of vehicles/people glances at the study of free surface flows past bluff bodies (Arrighi et al. 2015). The flow around a fully submerged rectangular cylinder and other simple-shape bodies has been studied by many researchers so far both numerically (Vickery 1966; Zou et al. 2008) and experimentally (Malavasi & Guadagnini 2003). There are only a few references for partly submerged conditions and subcritical flow conditions (Malavasi & Guadagnini 2003; Arslan et al. 2013) and references can hardly be found for partially submerged complex objects leaning on a channel bed under both subcritical and supercritical flows. The most used approaches to model the flow around bluff bodies are RANS equations with $k - \epsilon$ or $k - \omega$ closures (Olsen & Stokseth; Nagata et al., 2005) and LES simulations (Kim et al., 2015). Transition to supercritical conditions may substantially alter the pressure distributions and the resulting drag and lift forces, as already observed in the study of hydrodynamics of marine vehicles (Chapman, 1972; Savitsky & Ward-Brown 1976; Faltinsen, 2006). Therefore, the choice of an appropriate numerical framework to study the hydrodynamics of a partly submerged vehicle is not straightforward.

2.3.3 CFD codes

CFD codes are structured around the numerical algorithms that can tackle fluid flow problems. In order to provide easy access to their solving power, commercial CFD packages include sophisticated user interfaces to input problem parameters and to examine the results. Hence, all codes contain three main elements: (i) a pre-processor, (ii) a solver and (iii) a post-processor. Pre-processing consists of the input of a flow problem to a CFD program by means of an operator-friendly interface and the subsequent transformation of this input into a form suitable for use by the solver. The user activities at the pre-processing stage involve:

- Definition of the geometry of the computational domain

- Grid generation i.e. the subdivision of the domain into a number of smaller, non-overlapping sub-domains (cells)
- Definition of fluid properties
- Specification of appropriate boundary conditions at cells in the domain boundary

The solver is identified by the numerical solution technique adopted. The numerical algorithm consists of the following steps:

- Integration of the governing equations of fluid flow over all the finite control volumes of the domain
- Conversion of the resulting integral equations into a system of algebraic equations
- Solution of the algebraic equations by an iterative method

The post-processing phase allows to:

- Display domain geometry and grid
- Plot results

One of the most promising open source code for CFD analysis is OpenFOAM®, other well-known commercial packages are ANSYS Fluent (<http://www.ansys.com>) and FLOW-3D (www.flow3d.com). The OpenFOAM®(Open Field Operation and Manipulation) CFD Toolbox is a free, open source CFD software package produced by OpenCFD Ltd (OpenFoam, 2013). It has a large user base across most areas of engineering and science, from both commercial and academic organizations (Lindmeier et al. 2010; Campbell & Paterson 2011; Liu & Ph 2013). OpenFOAM has an extensive range of features to solve any complex fluid flow problem involving chemical reactions, turbulence and heat transfer, but also solid dynamics and electromagnetics. It includes tools for meshing, a parallelized mesher for complex CAD geometries, and for pre- and post-processing. Almost all tools (including meshing, and pre- and post-processing) runs in parallel as standard, enabling users to take full advantage of computer hardware at their disposal. By being open, OpenFOAM offers users complete freedom to customize and extend its existing functionality, either by themselves or through support from Open CFD (OpenFoam, 2013). OpenFOAM includes many solver applications (Bohorquez 2008; Deshpande et al. 2012; Lee et al. 2014) that simulate specific problems in engineering mechanics and many utility applications that perform pre- and post-processing tasks (e.g. meshing, data visualization). Among the standard libraries, it provides forces and force coefficients calculations (*libforces.so*) and post-processing. For simulating flows around complex geometries the *snappyHexMesh* utility is usually considered as optimal for refining the mesh cells around the objects.

Bluff bodies immersed in fluids generate complex 3D flows, with vortices and wakes. The study of the hydrodynamic forces acting on bluff bodies is often carried out using Computational Fluid Dynamics analysis (CFD). CFD codes allow discretizing the geometry of the domain and integrating the governing equations of fluid flow over all the finite control volumes, through the specification of appropriate boundary conditions and fluid properties. Among the existing codes OpenFOAM® is an open source package capable of handling complex meshes and forces calculation, widely used for many engineering applications.

2.4 Summary and implications for the research

Figure 2.11 summarizes the conceptual link between the topics addressed in this chapter. Following the definition of flood risk, the current flood hazard and damage assessment methodologies have been reviewed. Among the common categories of flood damages defined in the Floods Directive (European Parliament, 2007), the potential adverse consequences on human health have been selected. The available loss of life models (Aboelata & Bowles 2005; Mauro et al. 2008; de Bruijn et al. 2014) and reports on the causes of people fatalities have been reviewed. Two main causes of death have been identified in the literature (Jonkman et al. 2002; Jonkman 2007; Maples & Tiefenbacher 2009; Fitzgerald et al. 2010). The first cause of drowning is vehicles-related and the second occurs as pedestrian. In fact, vehicles can be easily swept away during a flood also for very low water depths and high velocity, and people awareness is very limited (Franklin et al. 2014; Arrighi et al. 2015). Therefore, the available studies on vehicles instability and people instability in floodwaters have been discussed. The critical threshold conditions for vehicle safety adopted for the design of road drainage systems (Russo et al. 2005) are empirical and mostly consider only water depth as relevant parameter. Existing flume experiments on the incipient motion conditions of fully and partly submerged vehicles (Xia et al., 2011; Shu et al. 2011; Teo et al. 2012; Xia et al. 2013) have been carried out on small scale models. The derived instability diagram show a large scatter in incipient motion conditions expressed in terms of water depth and flow velocity, because the characteristics of the tested vehicles (i.e. weight, height, height of the planform) strongly differ. The conceptual models so far elaborated, do not account for the actual three-dimensional geometry of the human body (Abt et al. 1989; Lind et al. 2004; Milanesi et al., 2015). Experiments on human instability in floods (Abt et al. 1989; Karvonen et al. 2000; Jonkman & Penning-Rowsell 2008; Xia et al. 2014) carried out both on real people and on human scale models exhibit again large scatters within individual data sets and, to a more significant degree, when all data sets are combined (Cox & Shand 2010). Thus, they allow introducing purely regressive hazard criteria (Cox & Shand 2010; Russo et al. 2013). Advanced hydrodynamic models may be capable of describing the flow around partially submerged bodies of complex shapes under different free surface flow regimes, thus allowing to calculate the pressure distribution, forces and moments on these bodies. Complex 3D geometries can be handled by recent mesh generation algorithm (OpenFoam, 2013). Therefore, the OpenFOAM CFD toolbox is considered in the present study since it is a 3-dimensional open-source software capable to perform free surface (or two-phase) simulations around 3D obstacles as well as to calculate hydrodynamic forces. Moreover, its meshing tools are optimal to refine computational cells around bodies with complex 3D geometries and the solvers capabilities have been validated thanks to the extensive use of the code in many engineering problems so far.

2.5 Specification of objectives and methodology

Human health is the primary objective in flood risk management strategies. The current knowledge about the instability of people and vehicles under water flow is not adequate to propose hazard criteria to be applied in flood mapping and to support people education. Based on the results of the analysis of the current knowledge and on the identified gaps of knowledge, the objectives and the methodology of the PhD study are specified more precisely in this section.

2.5.1 Specification of objectives

The objective of this research is to deepen the knowledge of the instabilization phenomenon of vehicles and people under water flow. The investigation of motion mechanisms aims at identifying some parameters capable of supporting the introduction of new hazard criteria for flood risk mapping. The specific objectives are listed below.

(i) Introduction of a new dimensionless mobility parameter able to account both for flood and vehicles/people characteristics:

- Analysis of the hydrodynamic forces acting on a partly immersed body (i.e. vehicles and people).
- Identification of a new dimensionless parameter to describe the threshold of instability for vehicles and pedestrians reducing the large scatter of experimental datasets.
- Representation of existing experimental data about people and vehicles with the new parameter.
- Validation of the mobility parameter.

(ii) Numerical modelling of incipient motion conditions in OpenFOAM to better understand the underlying mechanisms and the most relevant parameters affecting incipient motion:

- Reproduction of existing physical flume experiments on the incipient motion of scale models of vehicles and human bodies described as a function of the mean flow properties (H , U).
- Simulation of Froude-scaled incipient motion conditions.
- Mean flow description around the immersed vehicles and human bodies, and evaluation of hydrodynamic forces/moments.
- Identification of most relevant parameters and scaling numbers.
- Validation of the numerical model against the result of the stability analysis based on the new mobility parameter.

(iii) Application of the new hazard criteria to real case studies:

- Demonstration of the feasibility of the application of the new mobility parameter in flood maps.
- Generation of new hazard maps for vehicles and people to support risk management strategies.
- Qualitative validation through comparison between reconstructed floods and pictures taken during the events.

2.5.2 Specification of methodology

The main tasks of the present research are illustrated in Figure 2.12 and the phases of the works are described below.

(i) In phase I, a comprehensive analysis of the current knowledge is conducted with the aim of identifying knowledge gaps, missing approaches and other limitations in the

literature. This phase also includes the review of published experimental data and conceptual models. In addition, the capabilities of available CFD codes are analysed for the simulation of the flow around a partially immersed bluff body. As a result of this first step, the objectives and methodology of the research are specified more precisely.

(ii) In phase II, the equilibrium conditions for the onset of motion are analysed. The hydrodynamic forces on a flooded vehicle and on a person standing in floodwaters are described. The obtained limit state equation is manipulated in order to identify relevant dimensionless groups of variables. The physical characteristics of the flow and the geometric characteristics of vehicles and people are considered accordingly in order to reduce the scatter of existing experimental data. As a result, a new mobility parameter is developed, which is capable of accounting both for flood and object characteristics.

(iii) In phase III, a numerical model in OpenFOAM is set up considering vehicles and people and focusing on the mean flow properties for which the data are available from previous experiments. First, a 3D detailed geometry of a medium passenger vehicles and the appropriate tool for mesh generation are selected. A sensitivity analysis of the mesh resolution is performed to choose the adequate level of the mesh refinement. A sensitivity analysis with respect to the choice of the turbulence model is carried out to find a compromise between accuracy and computational time. Then boundary conditions are specified in order to reproduce the existing flume experiments. Froude similarity is applied to scale the experimental data in order to simulate prototype vehicles. Similarly, the simulations reproducing the experimental instability conditions of people are carried out.

(iv) In phase IV, the numerical results are analysed and represented through graphs in order to allow the proper description of the main findings. The numerical results are compared with the mobility parameter introduced in phase II to validate the model. The main underlying assumption of the numerical model are analysed and discussed.

(v) In phase V, new hazard criteria are defined starting from the dimensionless relationships found in phase II. The applicability of the introduction of the new approach proposed for the instability of vehicles and people in flood maps is demonstrated for two case studies.

(vi) In phase VI, the key findings are summarized and critically discussed. Finally, the limitations of the study are identified. Implications for future research are drawn.

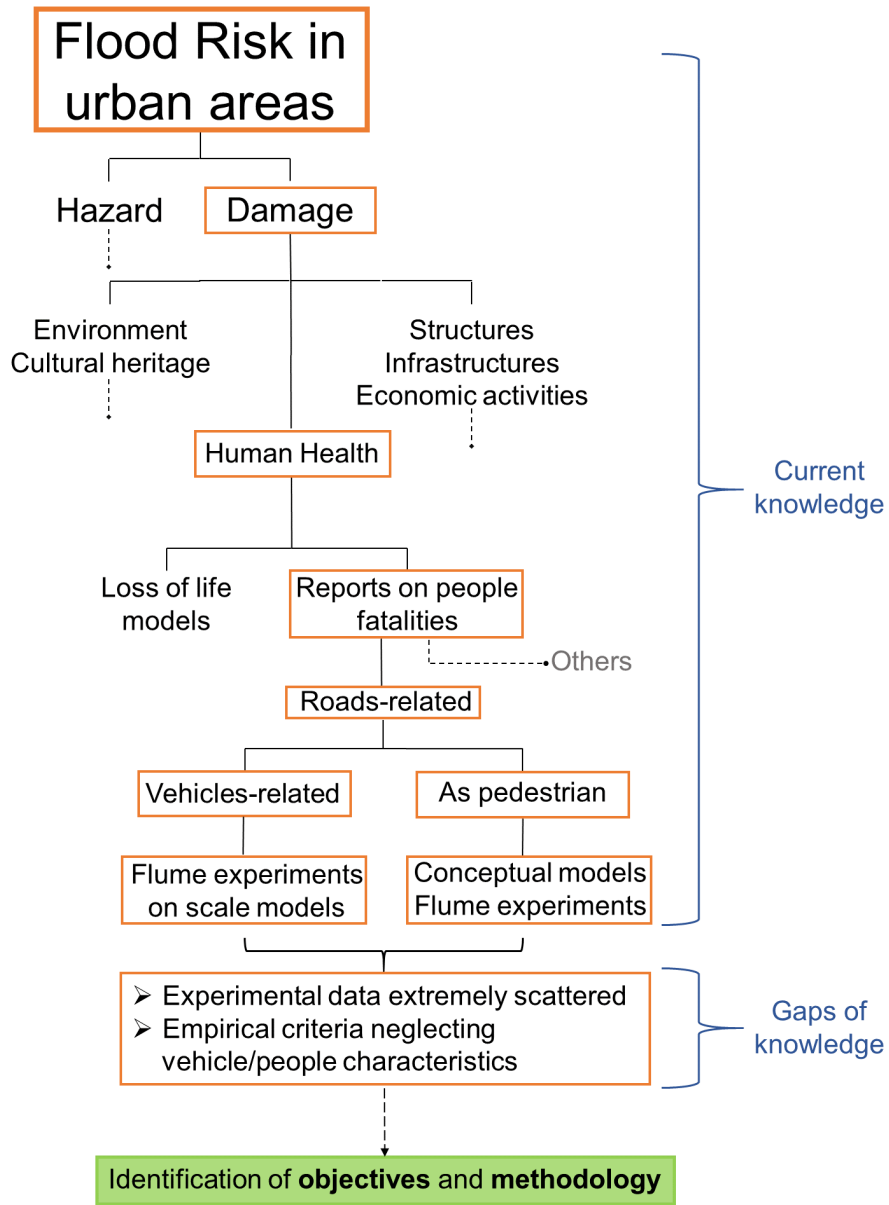


FIGURE 2.11: Summary of the topics described in the review of the current knowledge.

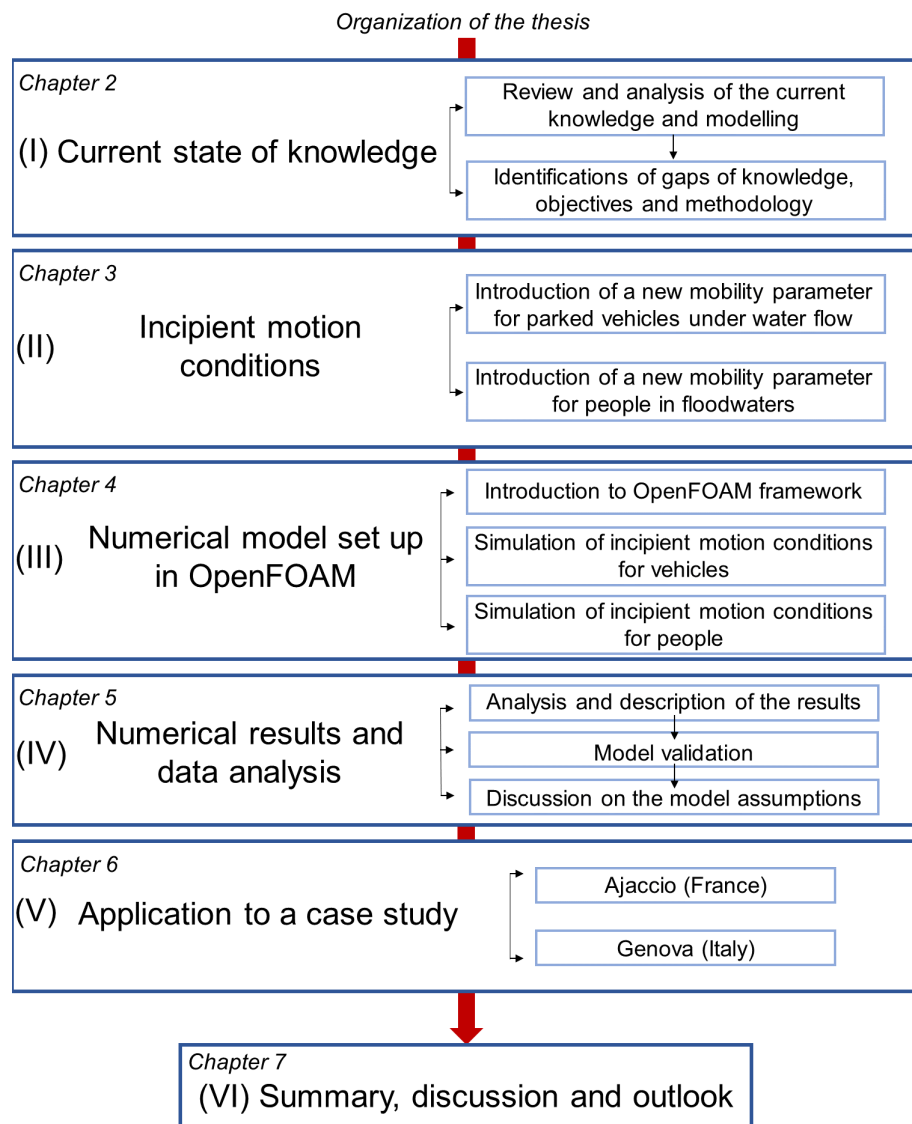


FIGURE 2.12: Methodology of the research and structure of the PhD thesis.

Chapter 3

Incipient motion of parked cars and pedestrians under water flow

3.1 Incipient motion of parked cars

3.1.1 Mobility parameter of parked cars

The two recognized hydrodynamic mechanisms by which the stability of a stationary vehicle (i.e. parked) is lost are floating and sliding. Assuming that a car cannot be filled quickly by floodwater, its density is much smaller than water density and most of the weight is usually distributed in the lower front part (close to the engine in the majority of modern cars). The floating instability occurs when the buoyancy and lift effects exceed the weight of the car. The sliding instability occurs when the drag force exceeds the resistance force (i.e. tyre/road friction). These two mechanisms interact as the effect of buoyancy and lift reduce the normal component of the weight thus promoting sliding conditions even for very low water depths. The incipient motion of flooded vehicles can be approached with some similarity to the study of sediment transport in rivers, also taking into account the peculiar features of the vehicles. The main parameters of a vehicle, which influence its incipient motion are: shape, specific weight, weight distribution, elevation of the chassis over the channel bed, degree of submergence. Vehicles, when not filled with water, have a lower density than sediments so they can float, i.e. even under still water conditions they may become unstable for water depths lower than their height (partial submergence). Moreover, the weight distribution of a common modern car is not homogeneous as most of the weight is concentrated in the frontal lower part where the engine is placed. The car cockpit instead is almost empty. Regarding the position, a car body is not directly placed on the ground, but it leans on the tyres, allowing water to pass under the vehicle. The forces on a parked vehicle under water flow are, as shown in Figure 3.1, weight, buoyancy, drag, lift and friction.

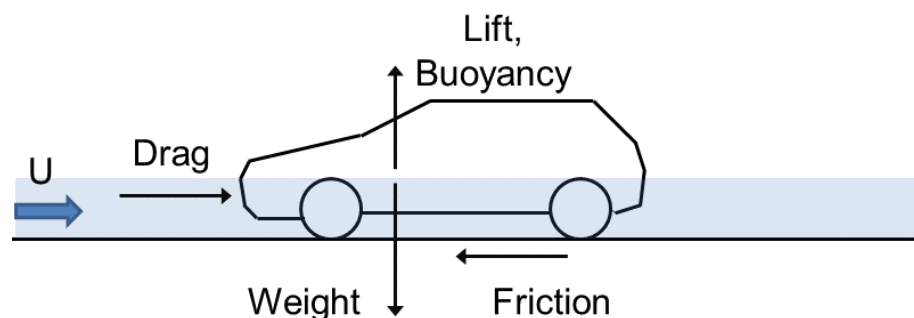


FIGURE 3.1: Forces acting on a parked vehicle under water flow.

Following the assumptions by Xia et al. (2011) and Shu et al. (2011), the bottom of the channel is horizontal, the gravity force (weight) is orthogonal to the bottom, and the instability mechanism considered is sliding (i.e. the wheels are locked). The car is considered as a rigid body and the friction coefficient is assumed as constant for all the types of vehicles and all hydraulic conditions considered. Values in the range 0.3-0.5 for the static friction coefficient are generally adopted for tyres on a wet surface (Bonham & Hattersley, 1967; Gordon & Stone, 1973; Cox & Ball, 2001). The onset of motion by sliding of a vehicle is modelled using the parameters defined in Figure 3.2, where H_V is the height of the vehicle, h_c is the height of the planform, L is the length and l is the width of the vehicle while U is the undisturbed mean flow velocity and H the water depth. We

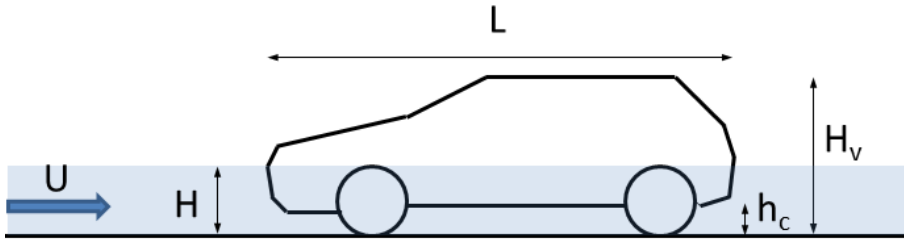


FIGURE 3.2: Definition of geometric parameters of the vehicle and water flow parameters.

considered as reference area for forces calculations the area of the vehicle above the level of the chassis since it is assumed that the motion occurs for water depths higher than the planform. Incipient sliding on a horizontal bed occurs when drag force D on the car body just exceeds the friction force of the tyres on the bottom (Eq. 3.1). The friction force is commonly defined as the product of the friction coefficient μ and the resultant normal force, which is the weight of the car (W) minus buoyancy B and lift force Li

$$D > (W - B - Li) \cdot \mu \quad (3.1)$$

where:

$$D = \frac{1}{2} \cdot \rho \cdot C_D \cdot (H_v - h_c) \cdot l \cdot U^2 \quad (3.2)$$

$$W = \rho_c \cdot g \cdot (H_v - h_c) \cdot l \cdot L \quad (3.3)$$

$$B = \rho \cdot g \cdot (H - h_c) \cdot l \cdot L \quad (3.4)$$

$$Li = \frac{1}{2} \cdot \rho \cdot C_L \cdot L \cdot l \cdot U^2 \quad (3.5)$$

Here ρ_c is the car bulk density estimated as total weight divided by body volume, ρ is the water density, g is the gravity acceleration, H_V is the height of the vehicle, h_c is the distance of the chassis from the ground, l and L are the frontal width and the length of the vehicle, respectively. H is the undisturbed water depth, U is the mean flow velocity, C_D is the drag coefficient, C_L is the lift coefficient defined with respect to the planform area $L \cdot l$ while for the drag coefficient the total frontal area is used. For partly submerged conditions, the reference area for the drag force could be also assumed equal to the wet

area in undisturbed conditions $(H - h_c) \cdot l$, but since the flow-object interaction generates possible backwater effects and local changes to the water profile, the determination of the actual wet area is not straightforward. Thus a reference area not affected by local flow effects is preferred. The selection of the reference area for the hydrodynamic forces is arbitrary, so the use of the wetted area is optional. Drag and lift coefficients are derived from dimensional analysis and the reference area is an arbitrary scale factor with dimensions of $(length)^2$. Thus, wetted area and full frontal area are commonly used in engineering practice (Fox and McDonald, 1978; Hoerner, 1965; Bertin and Smith, 1979). Obviously, consistency between reference area and force coefficients possibly evaluated through numerical simulations must be ensured. After substitution of the single forces from Eqs. 3.2, 3.3, 3.4, 3.5 in Eq. 3.1 and after some meaningful rearrangements of the terms and variables, Eq. 3.1 yields:

$$\left(\frac{C_D}{\mu} + C_L \cdot \frac{L}{H_v - h_c} \right) \cdot \frac{U^2}{g(H - h_c)} = 2L \cdot \frac{\rho_c(H_v - h_c) - \rho(H - h_c)}{\rho(H - h_c)(H_v - h_c)} \quad (3.6)$$

which can be written in a more condensed dimensionless form as

$$C \cdot Fr_v^2 = \theta_V \quad (3.7)$$

with

$$Fr_v^2 = \frac{U^2}{g(H - h_c)} \quad (3.8)$$

where Fr_v is the Froude number of the flow adjusted for the height of the chassis of the car.

$$C = \frac{C_D}{\mu} + C_L \cdot \frac{L}{H_v - h_c} \quad (3.9)$$

C includes the coefficients for drag C_D , for lift C_L and for friction μ . It can be noticed that drag and lift coefficients are weighted respectively by the friction coefficient μ and $\frac{L}{H_v - h_c}$. The latter refers to a shape factor representing the relevance of the lift force on the overall equilibrium, in fact the more the vehicle is long the higher is the contribution of lift effect.

$$\theta_V = \frac{2L}{(H_v - h_c)} \cdot \left(\frac{\rho_c \cdot (H_v - h_c)}{\rho \cdot (H - h_c)} - 1 \right) \quad \text{for } H > h_c \quad (3.10)$$

θ_V is the mobility parameter of the vehicle composed of two terms. The first term $\frac{2L}{(H_v - h_c)}$ accounts for the shape of the vehicle, the second term $\frac{\rho_c \cdot (H_v - h_c)}{\rho \cdot (H - h_c)} - 1$ for the relative immersed weight of the car. The mobility parameter θ_V is defined for water depths larger than the height of the chassis of the vehicle ($H > h_c$).

According to Eq. 3.7, the incipient motion conditions are essentially governed by the ratio of inertial and gravitational forces (i.e. Froude number), the geometry of the vehicle and the immersed weight. The mobility parameter θ_V increases quadratically with the Froude number of the vehicle. An aerodynamic vehicle shape (i.e. $L \gg H_v - h_c$) increases the shape factor and consequently θ_V . The mobility parameter θ_V can be estimated from the experimental mean flow data H, U once the geometry of the vehicle model is known. Also the adjusted Froude number Fr_v is easily assessed, but the three coefficients (C_D, C_L and μ) determining parameter C are unknown. Drag and lift coefficients C_D and C_L , in Eq. 3.9 quantify the effect of the immersed body in the fluid flow in terms of mobilizing hydrodynamic forces. C_D and C_L can be separately assessed through numerical simulations (or with flume experiments). The analysis of the forces acting on a partly submerged object hints the dependence of θ_V on the parameter Fr_v , which will

be used for the validation of the coefficients estimated with the numerical model (see 5.1.3). However since the use of Froude number of the flow, is practically handier for most engineering applications (i.e. inundation mapping), also the dependence of θ_V on $Fr = \frac{U}{(gH)^{0.5}}$ is tested. In fact, the available flood maps provide information on water depth and flow velocity, thus allowing the calculation of the spatial distribution of Froude number Fr in the inundated area, which will be used for the urban scale application (see chapter 6). The use of Froude number Fr instead of Froude number adjusted for the height of the car planform Fr_v does not significantly affect the correlation with the mobility parameter θ_V as shown in Figure 3.3 and Figure 3.5.

3.1.2 Application of the mobility parameter to available experimental data

In order to represent the incipient motion conditions the Froude number of the undisturbed flow $Fr = \frac{U}{(gH)^{0.5}}$, and the mobility parameter θ_V are chosen. The experimental data by Xia et al. (2011) and Shu et al. (2011) on six different vehicle models are re-analyzed using θ_V and Fr to determine the threshold for vehicle motion. The bulk density of the cars (Table 3.1) is evaluated through a graphic method to calculate the volume (confirmed by the author Xia, personal communication). The six tested vehicle models differ in scale, geometry and specific weight. The 1:43 scaled car models tested by Xia et al., 2011 were filled by water thus, their density was larger than water density (Table 3.1). 4WD vehicles have higher planform and thus higher values of the ratio h_c/H_V than the other car types. The results of the re-analysis of the data are shown in Figure 3.3.

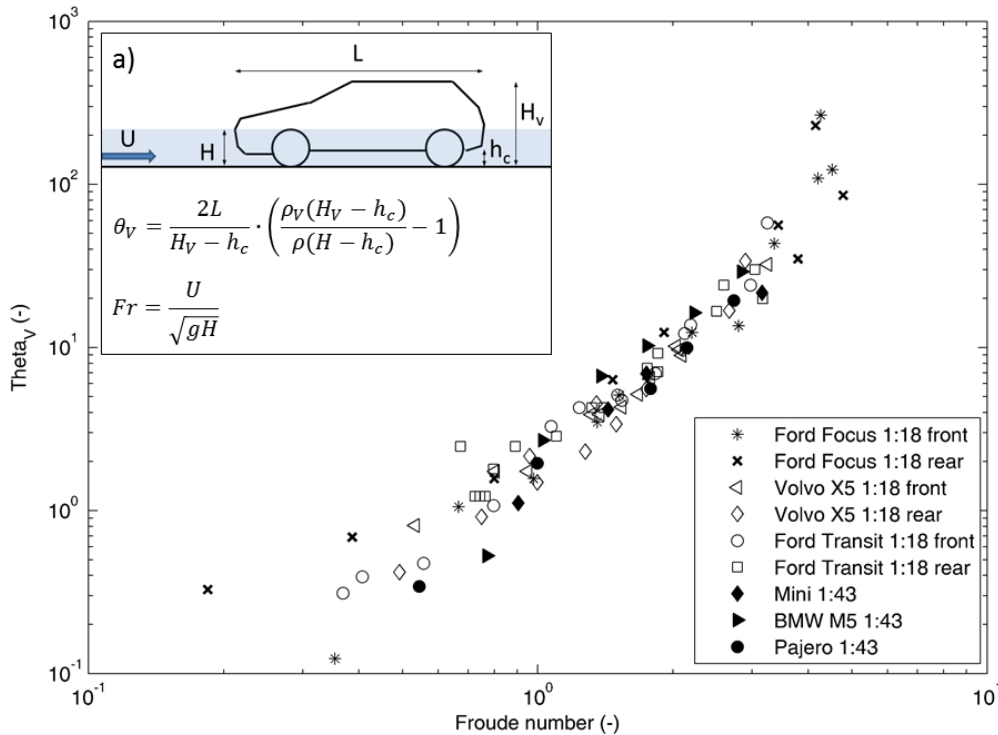


FIGURE 3.3: Mobility parameter θ_V versus Froude number Fr of undisturbed flow using the experimental data of Xia et al. (2011) and Shu et al. (2011).

All the experimental data points in Figure 3.3 (logarithmic scale on Fr and θ_V axes), both for the vehicles scale 1:43 models filled by floodwater (Xia et al., 2011) and for the vehicles scale 1:18 waterproof models (Shu et al., 2011), lie on the same curve $\theta_V = f(Fr)$.

TABLE 3.1: Characteristics and mobility parameter of the car models for different submergence $H/H_V = 0.25 - 1.0$

Vehicle type	Pajero jeep	BMW M5	Mini Cooper	Ford Focus	Volvo X5	Ford Transit
Model scale	1:43	1:43	1:43	1:18	1:18	1:18
Car height H_V (m)	0.042	0.038	0.032	0.082	0.099	0.109
Chassis height h_c (m)	0.004	0.003	0.003	0.007	0.01	0.008
Car bulk density (kg/m ³)	1241	1480	1544	254	198	165
θ_V (for $H/H_V = 1$)	1.48	3.30	3.24	-5.01	-5.28	-4.80
θ_V (for $H/H_V = 1/2$)	13.60	18.17	16.72	-2.72	-3.24	-3.49
θ_V (for $H/H_V = 1/3$)	36.86	42.91	39.30	0.65	0.57	-1.50
θ_V (for $H/H_V = 1/4$)	90.38	86.15	79.24	5.48	8.85	1.53

This curve represents the critical threshold of incipient vehicle motion: stable vehicle in the zone above the curve and unstable vehicle below the curve. The value of the mobility parameter changes significantly for different bulk density and for different submergence H/H_V of the vehicles (Table 3.1). Froude number Fr ranges from 0.1 (subcritical flow) to 5 (supercritical flow) and mobility parameter θ_V from 0.1 (buoyancy prevails) up to 275 (drag force prevails). No discontinuity appears in the diagram at the transition from subcritical to supercritical flow ($Fr = 10^0$). Table 3.1 shows the value of θ_V for the different car models and relative water depths (submergence). The waterproof car models (Focus, Volvo and Transit) can have a negative value of θ_V also for partially submerged conditions since their density is lower than the water density. Thus, they start floating before the water submerges the vehicle and the incipient motion occurs for buoyancy instability before sliding. Figure 3.4 shows the experimental data by Shu et al. (2011) and by Xia et

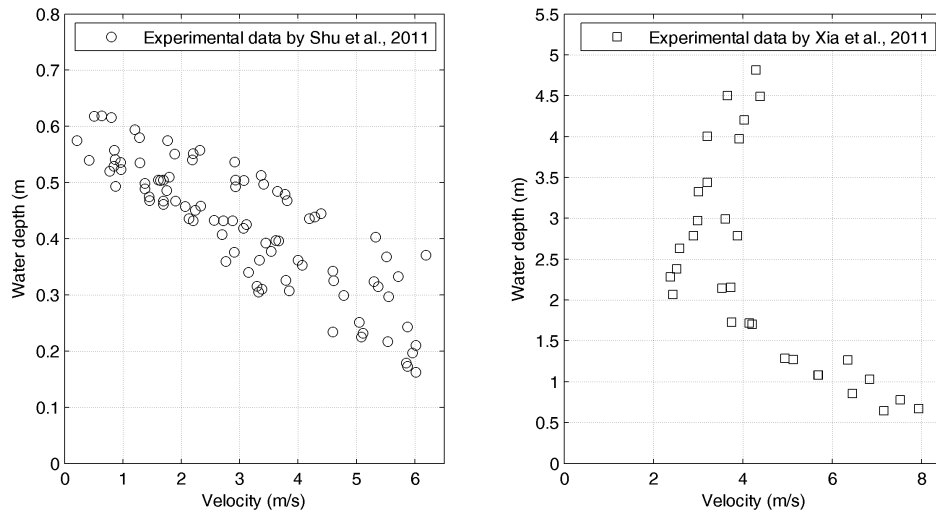


FIGURE 3.4: Experimental data by Shu et al. 2011 (left panel) and by Xia et al. 2011 (right panel) scaled to prototype values.

al. (2011) scaled to prototype values using Froude's similarity law. For waterproof scale 1:18 vehicles (left panel), the range of prototype-scaled critical velocity is 0.15-6 m/s and the range of water depths is 0.16-0.62 m. For scale 1:43 vehicles (right panel), the range of prototype-scaled velocity is 2.1-8 m/s and the range of water depths is 0.5-4.85 m. Using the same data in Figure 3.3, the scatter reduces significantly and a unique curve is able to represent both experimental datasets, which cover different ranges of water depth and flow velocity. If Froude number of the vehicle Fr_v (Eq. 3.8) is used, Figure 3.5 is obtained. In this case the values in the horizontal axis range from 0.2 up to 26. Although there is a

higher correlation between θ_V and Fr_v , with a determination coefficient of 0.97 instead of 0.83 (see Fig. 3.14) the dimensionless diagram θ_V versus Froude number of the flow Fr_v has the advantage of being more easily related to the properties of flow regime and thus it is preferred for practical use, comparison with pedestrians' stability (Fig. 3.14) and hazard mapping (see chapter 6).

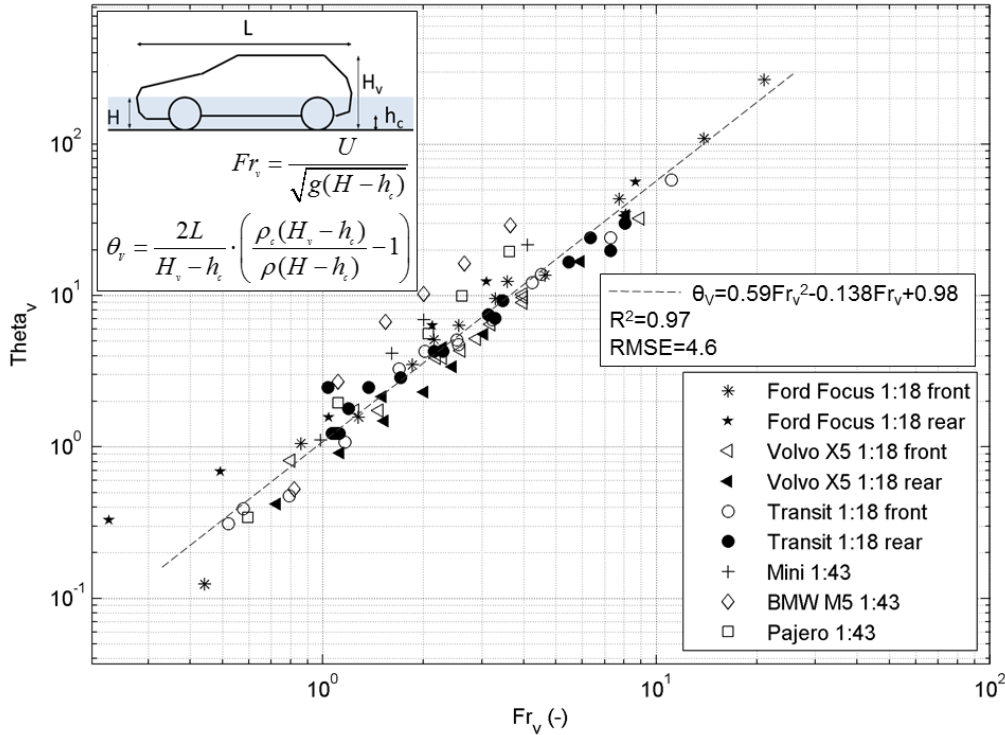


FIGURE 3.5: Mobility parameter θ_V versus Froude number Fr_v of the vehicle using the experimental data of Xia et al. (2011) and Shu et al. (2011).

3.1.3 Effect of flow orientation on the mobility parameter

Parked cars can be parallel to the longitudinal axis of the street or may have different orientations depending on the geometry of the parking lot. Thus, the effect of flow orientation has to be taken into account in order to better understand the mechanisms underlying incipient motion of vehicles. The mobility parameter in Eq. 3.10 has to be modified to include the orientation of the vehicle with respect to the flow direction. The most relevant effect of the angle of incidence is a change in the area of the vehicle, which faces the flow and thus contributes to the drag force (Figure 3.6). Figure 3.6 shows that frontal and rear areas (A_0 green bar) are smaller than lateral area (A_{90} yellow bar) and the latter is even smaller than the area corresponding to the angle of flow incidence 65° (red bar). To account for the angle of flow incidence, the reference area for the drag force in Eq. 3.2 is modified. Eq. 3.1 describes the incipient sliding on a horizontal bed of a vehicle in floodwater. For any given flow orientation the drag force D is referred to the full area projected normally to the flow and given by Eq. 3.11:

$$D = \frac{1}{2} \cdot \rho \cdot C_D \cdot U^2 \cdot (l \cdot \cos \beta + L \cdot \sin \beta) \cdot (H_v - h_c) \quad (3.11)$$

where β is the angle of flow incidence (see Figure 3.7). Lift force is given by Eq. 3.12

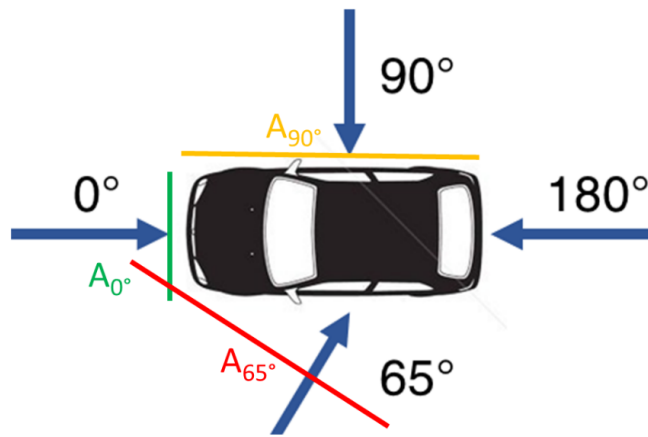


FIGURE 3.6: Plan view of the surfaces affected by drag force according to the angle of flow incidence.

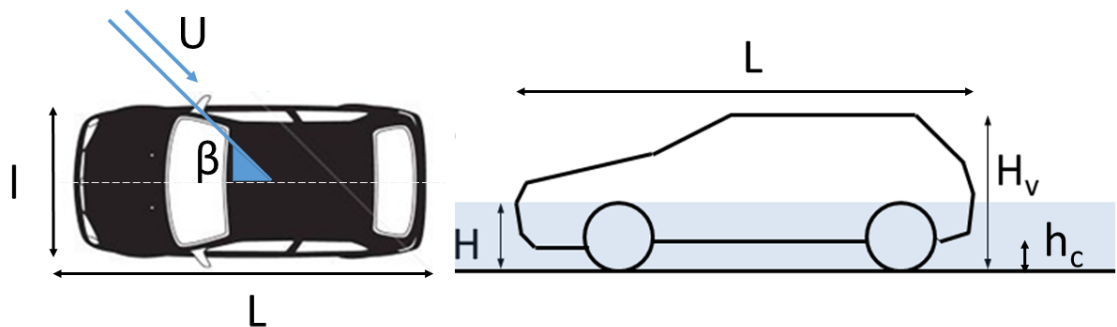


FIGURE 3.7: Geometric scheme for a vehicle with angle of flow incidence β .

TABLE 3.2: Characteristics of Honda Accor (prototype and scale 1:14)(Xia et al., 2013)

Vehicle	Length (m)	Width (m)	Height (m)	Kerb weight (kg)
Honda Accor prototype	4.95	1.845	1.480	1631
Honda Accor 1 : 14	0.353	0.134	0.062	0.107

$$Li = \frac{1}{2} \cdot \rho \cdot C_L \cdot U^2 \cdot (l \cdot L) \quad (3.12)$$

Where C_L is defined as referred to the actual area of the lift force which is the planform area $l \cdot L$ (as in Eq. 3.5). Substituting Eqs. 3.11 and 3.12 in Eq. 3.1 and after some manipulations to separate the geometric characteristics from the dynamic characteristics, the relationship in Eq. 3.7 is obtained again. The mobility parameter θ_V is now obtained by introducing correction factor for $0^\circ < \beta < 90^\circ$ in Eq. 3.10:

$$\theta_V = \frac{2L}{(H_v - h_c)} \cdot \alpha \cdot \left(\frac{\rho_c \cdot (H_v - h_c)}{\rho \cdot (H - h_c)} - 1 \right) \quad \text{for } H > h_c \quad (3.13)$$

where

$$\alpha = \frac{l}{l \cdot \cos \beta + L \cdot \sin \beta} \quad (3.14)$$

is the dimensionless parameter accounting for the flow orientation (i.e. $0^\circ < \beta < 90^\circ$) assuming the hypothesis of the existence of two axis of symmetry of the car. The assumption is based on the experimental results by Shu et al., (2011) and Xia et al. (2013), that demonstrated the equivalence of frontal and rear impact (i.e. 0° and 180°) for the incipient motion. For $\beta = 0^\circ$ (or the equivalent 180°) the absolute value of parameter α is equal to 1, so that Eq. 3.13 transforms to Eq. 3.10. In order to verify Eq. 3.13, which accounts for the angle of incidence of the flow, the experimental data by Xia et al. (2013) on the threshold of vehicle instability for three orientation angles have been selected. Two types of die-cast model vehicles (Honda Accor and Audi Q7) were tested. The experimental data regarding the Honda Accor model have been used to calculate Froude number Fr and mobility parameter. The geometric characteristics of Honda Accor are shown in Table 3.2.

Three angles of flow incidence are considered in the study (0° , 180° , 90°) (Figure 3.8). The experiments show that for the same water depth, the incipient velocity for the orientations of 0° and 180° are slightly greater than for the 90° orientation for the Honda model, due to the larger projected area (Xia et al., 2013). The verification in Figure 3.8 could benefit of the use of other experimental data if available. However this preliminary test is pretty good to extend the use of the mobility parameter to $0^\circ < \beta < 90^\circ$.

Figure 3.8 shows the dimensionless diagram θ_V versus Fr calculated with Eq. 3.13, including the experimental data on the Honda Accor model for the 90° angle of flow incidence. Therefore, the mobility parameter θ_V modified with the parameter α is able to identify the instability threshold of incipient motion also for the new dataset (Xia et al., 2013). In fact, the Honda Accor incipient motion points compare well with the existing incipient motion threshold, since the regression curve is not significantly altered by their presence. A few points, for supercritical conditions, appear under the threshold. This can be due to the fact that lift effect might be negative for those conditions, thus contributing to the car stability as demonstrated by laboratory experiments (Bonham & Hattersley, 1967). Eq. 3.14 allows calculating the orientation factor α of the mobility parameter. For angles of flow orientation in the range $0^\circ < \beta < 90^\circ$, α is lower than one, with a minimum

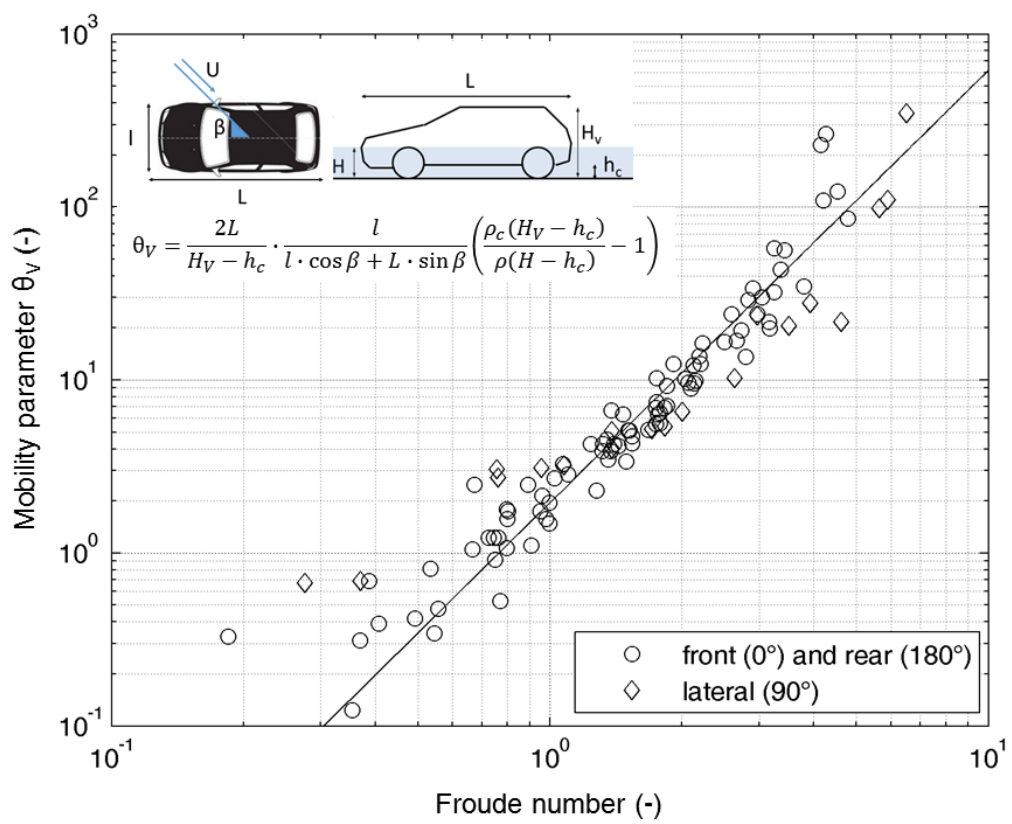


FIGURE 3.8: Mobility parameter accounting for the angle of flow incidence (experiments with 90° angle represented with diamonds, Xia et al., 2013)

TABLE 3.3: RMSE of the perturbed data over the original regression obtained with different multipliers for the standard deviation of the noise

Multipliers	U	1.0	0.7	0.5	0.3	0.2	0.1	0.01	0.001
H									
1		2.14	1.82	1.65	1.52	1.48	1.45	1.44	1.44
0.7		1.99	1.64	1.44	1.30	1.25	1.22	1.21	1.21
0.5		1.89	1.51	1.30	1.13	1.07	1.03	1.02	1.02
0.2		1.79	1.38	1.14	0.94	0.87	0.82	0.81	0.81
0.3		1.74	1.31	1.05	0.83	0.75	0.70	0.68	0.68
0.1		1.69	1.24	0.96	0.72	0.62	0.55	0.53	0.53
0.01		1.67	1.21	0.92	0.66	0.55	0.55	0.53	0.53
0.001		1.69	1.24	0.96	0.72	0.62	0.55	0.53	0.53

corresponding to 65° (orientation which maximizes the area). For 65° , is approximately 0.4, while $\alpha = 0.45$ for 90° . This means that for a given Froude number of the undisturbed flow $Fr = U/(g \cdot H)^{0.5}$ (i.e. for a given pair (H, U) of water depth and flow velocity) the mobility parameter for any lateral orientation ($0^\circ < \beta < 90^\circ$) is lower than the mobility parameter for frontal and rear impact. In fact, it can be reduced up to 60%. Thus, lateral flow orientations are more favourable for incipient motion, confirming the experimental results (Xia et al., 2013).

3.1.4 Sensitivity analysis of θ_V to uncertainties in H and U

In order to avoid the introduction of a spurious correlation between the two dimensionless parameters Fr and θ_V , the experimental data of water depth and velocity (i.e. 192 couples) are perturbed. The perturbations are obtained by summing to the original data an artificial random gaussian noise with a standard deviation equal to the product of a multiplier and the standard deviation of the original set of data. The multipliers used are [1.0, 0.7, 0.5, 0.3, 0.2, 0.1, 0.01, 0.001] both for water depth and velocity. Froude number Fr and mobility parameter θ_V are calculated using the perturbed data, then the root mean square error ($RMSE$) and the coefficient of determination (R^2) are evaluated as an average after 105 iterations, with respect to the original regression curve. The procedure is applied to all the different car models and all the possible couples of multipliers (i.e. 64 cases). The results are presented in Table 3.3 and Table 3.4 for $RMSE$ and R^2 , respectively. The $RMSE$ and the determination coefficient R^2 of the original set of experimental data are 0.53 and 0.89, respectively. The introduction of a random gaussian noise with a standard deviation of one order of magnitude lower than the standard deviation of the original data doesn't alter the $RMSE$ and R^2 . The original regression still explains the data with a 20% error. The results of this analysis allow to exclude a spurious correlation between the two dimensionless groups adopted to describe the incipient motion conditions. If a significant spurious correlation was present, a large perturbation over the experimental data would have shown a high determination coefficient similar to the original one.

Figure 3.9, 3.10 show the effect of the addition of the Gaussian random noise to the experimental pairs (H, U) on the mobility parameter. In both graphs, the multipliers for the standard deviation of water depth H ($mult_{stdH}$) and velocity U ($mult_{stdV}$) are specified on the top of the picture as well as the $RMSE$ and R^2 obtained from the regression on the perturbed data. If the perturbation is small as in Figure 3.9, the law for the original unperturbed experimental data describes the data with the noise. If the perturbation is larger,

TABLE 3.4: Determination coefficient R^2 of the perturbed data over the original regression obtained with different multipliers for the standard deviation of the noise

Multipliers	U	1.0	0.7	0.5	0.3	0.2	0.1	0.01	0.001
H									
1		-0.86	-0.34	-0.10	-0.07	0.12	0.15	0.16	0.16
0.7		-0.68	-0.14	0.12	0.29	0.35	0.38	0.39	0.39
0.5		-0.53	0.02	0.28	0.46	0.51	0.55	0.56	0.56
0.2		-0.35	0.2	0.46	0.63	0.68	0.72	0.73	0.73
0.3		-0.25	0.29	0.55	0.72	0.77	0.80	0.81	0.81
0.1		-0.17	0.37	0.62	0.79	0.85	0.88	0.89	0.89
0.01		-0.21	0.36	0.63	0.81	0.87	0.88	0.89	0.89
0.001		-0.08	0.41	0.65	0.81	0.85	0.88	0.89	0.89

although unrealistic, (Figure 3.10), the mobility parameter is not anymore correlated to Froude number (i.e. the determination coefficient R^2 is negative). The hypothesis on the presence of a spurious correlation is thus rejected. In fact if a spurious correlation was present a large perturbation on the pairs H, U would not have decreased the R^2 between Fr and θ_V .

3.2 Incipient motion of pedestrians standing in floodwaters

3.2.1 Mobility parameter of pedestrians

The two mechanisms by which the stability of people is lost in floodwaters are sliding and toppling (see section 2.2). Therefore, the equilibrium conditions for both instability mechanisms are separately analysed. Similarly to vehicles, incipient sliding on a horizontal bed occurs when drag force D on the human body just exceeds the friction force of the feet on the bottom (Eq. 3.15). The friction force is equal to the effective weight (weight W minus buoyancy B and lift force Li) multiplied by the friction coefficient μ

$$D > (W - B - Li) \cdot \mu \quad (3.15)$$

where both drag and lift forces are referred to the full area of a prism of height H_P and width l (see Figure 3.11)

$$D = \frac{1}{2} \cdot \rho \cdot U^2 \cdot C_D \cdot H_P \cdot l \quad (3.16)$$

$$W = \rho_P \cdot g \cdot (H_P \cdot d \cdot l) \quad (3.17)$$

$$B = \rho \cdot g \cdot (H \cdot d \cdot l) \quad (3.18)$$

$$Li = \frac{1}{2} \cdot \rho \cdot U^2 \cdot C_l \cdot H_P \cdot l \quad (3.19)$$

C_D and C_l are the drag and lift coefficient respectively and ρ_P is the density of human body. Referring to Figure 3.11, the human body is modelled as a rectangular prism so that the projected area normal to flow direction is equivalent to prism area $H_P \cdot l$ (Figure 3.11, panel b). The streamwise length is assumed equal to d , which is the lever arm of the effective weight (Figure 3.11, panel a). The lever arm of drag force is assumed equal to

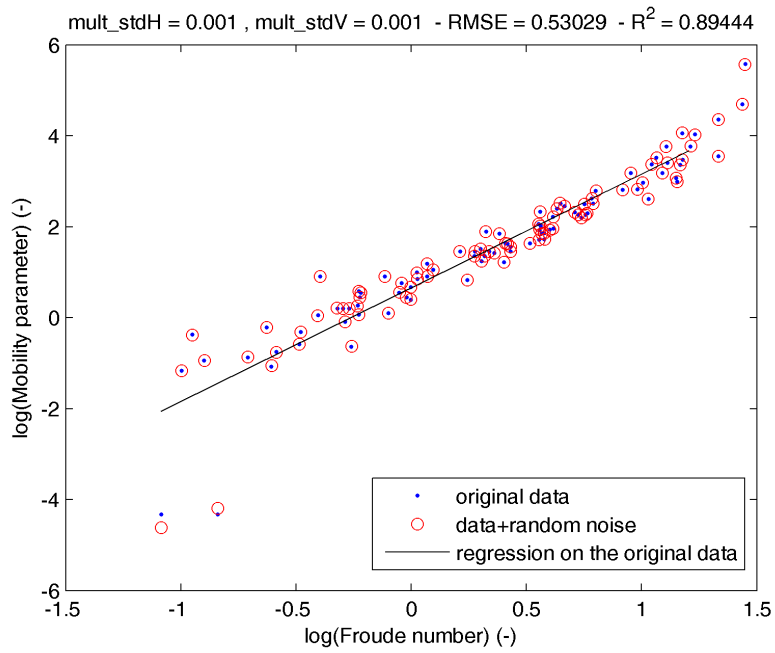


FIGURE 3.9: Effect of addition of a small random noise to the pairs (H, V) on the mobility parameter.

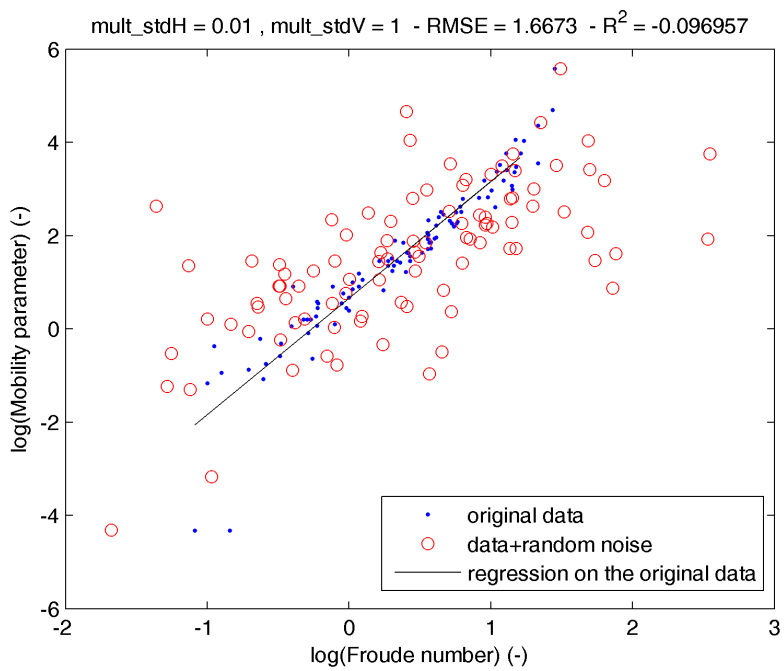


FIGURE 3.10: Effect of addition of a large random noise to the pairs (H, V) on the mobility parameter.

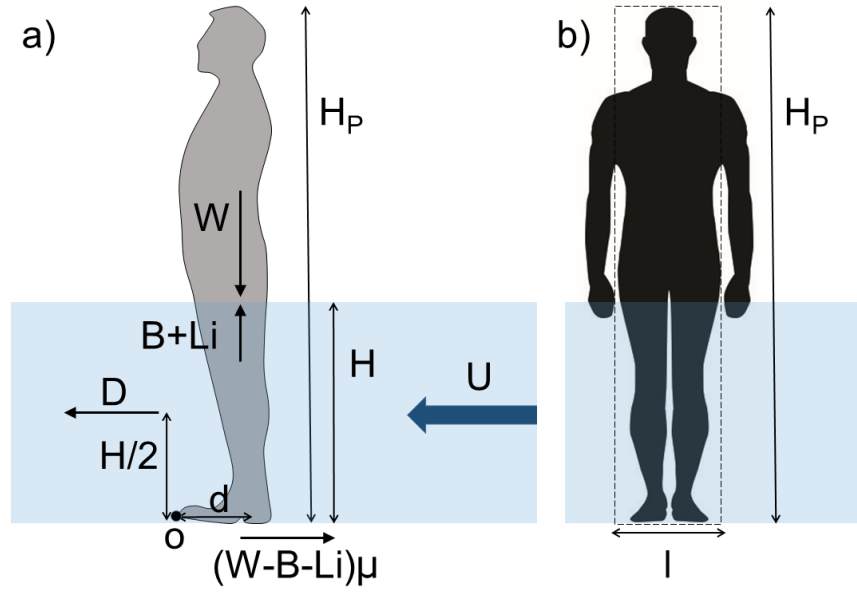


FIGURE 3.11: Mobilising and resisting forces on a human body in floodwater (a) lateral view, frontal view (b).

$H/2$. The use of the same reference area for drag and lift force, may appear physically not meaningful for lift force, since its reference area should be the projection of an horizontal surface normal to the vertical axis. However, the determination of the actual area where the lift force acts is difficult since the projection of the human body on the horizontal plane varies with the submergence. This justifies the use of a simplified reference area for lift force as in the existing conceptual models (Milanesi et al., 2015). The average density of the human body ($\rho_P = 1062 \text{ kg/m}^3$) is generally assumed equal to the density of water (a difference of 6% is usually considered negligible as in Lind et al., 2004 and Milanesi et al. 2015), thus ρ_P is substituted with ρ in Eq. 3.17. Substituting the Eqs. 3.16, 3.17, 3.18, 3.19 in Eq. 3.15 the following equation is obtained

$$\frac{1}{2} \cdot \rho \cdot U^2 \cdot C_D \cdot H_P \cdot l = \left(\rho \cdot g \cdot (H_P \cdot d \cdot l) - \rho \cdot g \cdot (H \cdot d \cdot l) - \frac{1}{2} \cdot \rho \cdot U^2 \cdot C_l \cdot H_P \cdot l \right) \cdot \mu \quad (3.20)$$

The variables l and ρ appear in the terms of the Equation, thus they can be simplified. Separating the dynamic terms from the static terms Eq. 3.20 is simplified as

$$\frac{1}{2} \cdot U^2 \cdot C_D \cdot H_P + \left(\frac{1}{2} \cdot U^2 \cdot C_l \cdot H_P \right) \cdot \mu = [(g \cdot H_P \cdot d) - (g \cdot H \cdot d)] \cdot \mu \quad (3.21)$$

Collecting U^2 in the left term and d in the right term, then dividing both terms for $0.5 \cdot \mu \cdot H \cdot g$ the equilibrium condition yields

$$\frac{U^2}{gH} \cdot \left(C_l + \frac{C_D}{\mu} \right) = \frac{2d}{H_P} \cdot \frac{H - H_P}{H} \quad (3.22)$$

where

$$Fr^2 = \frac{U^2}{gH} \quad (3.23)$$

is the square of Froude number of the flow,

$$C_s = \frac{C_D}{\mu} + C_l \quad (3.24)$$

and where C_s includes the coefficients for drag C_D , for lift C_l and for friction μ ,

$$\theta_P = \frac{2d}{H_P} \cdot \frac{H_P - H}{H} \quad (3.25)$$

is defined as the dimensionless mobility parameter for sliding instability of people standing in floodwaters. θ_P is composed by two factors: the shape factor $2d/H_P$ and the relative dry surface of the body $(H_P - H)/H$. θ_P depends on Froude number and on the forces coefficient similarly to θ_V which was introduced for vehicles.

Toppling instability occurs when the moment induced by the drag force around a pivot point (i.e. the toe as in Figure 3.11, panel a) just exceeds the moment from the resultant vertical force (body weight W minus buoyancy B and minus lift force Li)

$$(W - B - Li) \cdot d > D \cdot \frac{H}{2} \quad (3.26)$$

Substituting the forces in Eq. 3.26 according to previous definitions, the following threshold condition for incipient toppling is obtained

$$\left[(\rho \cdot g \cdot l \cdot H_P \cdot d) - (\rho \cdot g \cdot l \cdot H \cdot d) - \frac{1}{2} \rho \cdot U^2 C_l \cdot H_P \cdot l \right] \cdot d = \left(\frac{1}{2} \cdot \rho \cdot U^2 \cdot C_D \cdot H_P \cdot l \right) \cdot \frac{H}{2} \quad (3.27)$$

ρ and l can be dropped on both side of Eq. 3.27 which after some manipulations and simplifications yields:

$$\frac{U^2}{gH} \cdot \left(\frac{H}{2d} \cdot C_D + C_l \right) = \frac{2d}{H_P} \cdot \frac{H_P - H}{H} \quad (3.28)$$

This represents a relationship between the square of Froude number together with dimensionless parameter C_t on the left hand side

$$C_t = \left(\frac{H}{2d} \cdot C_D + C_l \right) \quad (3.29)$$

which also accounts for the ratio $H/2d$ (water depth to moment lever of resisting forces) and on the right hand side a mobility parameter for toppling instability conditions for a person in floodwaters θ_{Pt}

$$\theta_{Pt} = \frac{2d}{H_P} \cdot \frac{H_P - H}{H} \quad (3.30)$$

The mobility parameter θ_{Pt} obtained for toppling is equal to the mobility parameter θ_P introduced for sliding (Eq. 3.25). However, the difference is in coefficients C_s (Eq. 3.24) and C_t (Eq. 3.29). In fact, for toppling instability conditions, C_D is multiplied by $H/2d$ in Eq. 3.29, which can be interpreted as a measure of the relevance of the moment induced by the drag force for larger water depths H . For smaller water depths H , sliding is more likely to occur than toppling. Therefore, although there are two different incipient motion mechanisms, a unique parameter θ_P accounting for human body parameters and flow characteristics is able to represent both mechanisms. It should be noticed that the

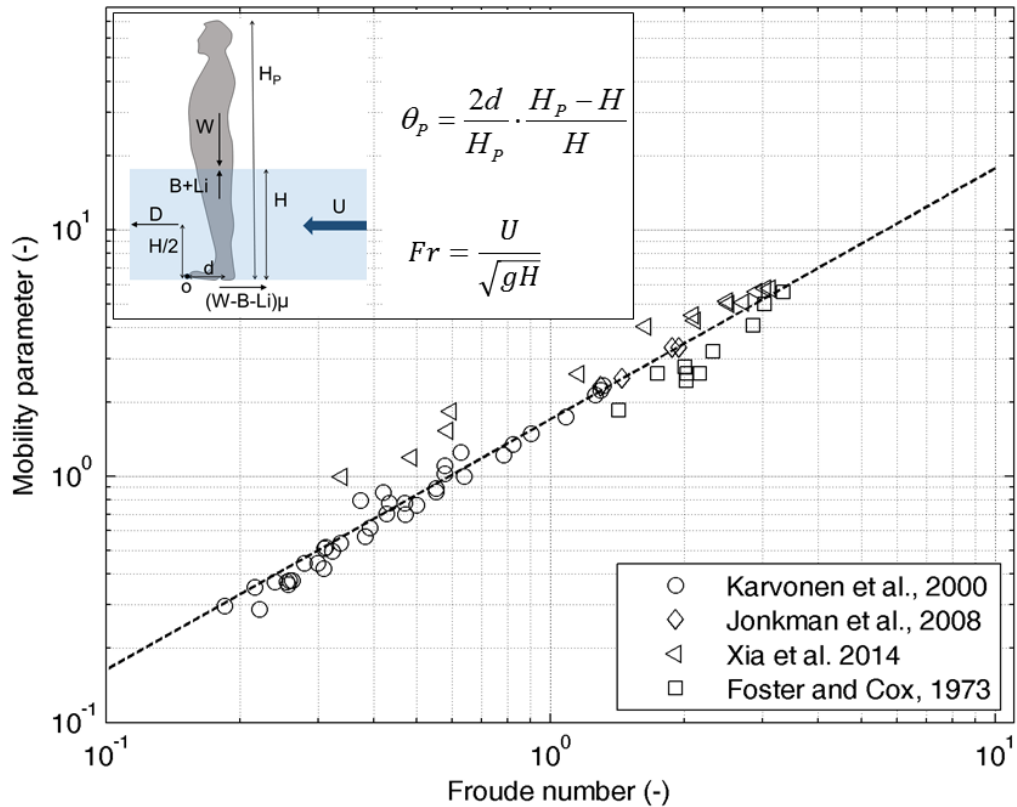


FIGURE 3.12: Mobility parameter θ_P versus Froude number Fr for the experiments from published selected studies.

mobility parameter for people could be also obtained from Eq. 3.10 considering a human body as a ‘special’ vehicle model with elevation of the planform h_c equal to zero, length equal to d and density ρ_c equal to water density ρ .

3.2.2 Application of the mobility parameter to existing experimental data

The mobility parameter introduced in the previous section is calculated for four different experimental datasets available in the literature (Foster & Cox, 1973; Karvonen et al., 2000; Jonkman et al., 2008 and Xia et al., 2014). These datasets cover a wide range of flow regimes and human body characteristics (i.e. different H_P) and include the experiments made on a human scale model (Xia et al., 2014). Figure 3.12 shows the mobility parameter θ_P versus the Froude number of the undisturbed flow calculated for the pairs (H, U) from published selected studies (Foster & Cox, 1973; Karvonen et al., 2000; Jonkman et al., 2008 and Xia et al., 2014). The threshold curve $\theta_P = f(Fr)$ of incipient motion separating stable conditions (above the curve) from unstable conditions (below the curve) is capable of describing the instability conditions of different bodies subject to water flow, overcoming the scatter of the existing experimental data. However, the data from the experiments with a human body model by Xia et al., (2014) appear above the curve, thus in stable conditions. In fact also in the dimensional diagrams, the instability conditions for human body models are more conservative (i.e. lower) than conditions tested on real humans, because people react to face the loss of stability.

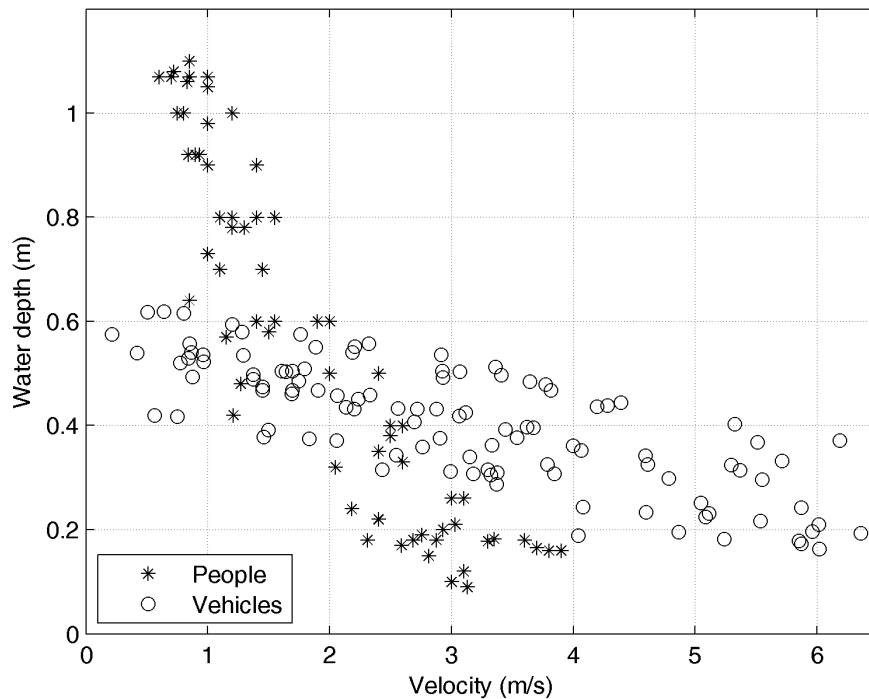


FIGURE 3.13: Instability diagram “water depth H versus flow velocity U ” scaled to prototype for vehicles (Xia et al., 2011; Shu et al., 2011; Xia et al., 2013) and people (Foster and Cox, 1973; Karvonen et al., 2000; Jonkman et al., 2008; Xia et al. 2014).

3.3 Comparison between mobility parameters for vehicles and people

As highlighted in section 2.2, the available datasets for the instability of vehicles and people subject to flow in floodwaters are extremely scattered and show large variability within the same dataset if represented dimensionally. In fact, such variability depends on the characteristic of the geometry and density of the object in floodwater, which are not accounted for in common graphs considering only water depth vs velocity. Figure 3.13 represents such a graph obtained from the experimental data scaled to prototype according to Froude similarity for people and vehicles used to calculate the mobility parameters in sections 3.2.1 and 3.1.1. Experimental data about people instability (Foster & Cox, 1973; Karvonen et al., 2000; Jonkman et al., 2008; Xia et al. 2014) are represented with black stars. Experimental data about partly submerged cars (Shu et al., 2011; Xia et al., 2013) are represented with black circles. It can be noticed that, for low velocities, people can remain stable for water depth higher than cars. Moreover, for very low water depths, vehicles can resist to higher velocities. In fact, a threshold for velocities equal to 3.0 m/s has been set as limiting velocity for adults and children in good training conditions by Cox & Shand (2010). Plotting mobility parameters θ_P for persons and θ_V for vehicles together in the same graph, Figure 3.14 is obtained. The dimensionless instability diagram represented in Figure 3.14 describes both people and vehicles threshold of instability. Since the mobility parameters θ_P and θ_V are dimensionless and account for object characteristics (i.e. geometry and density), and together with the Froude number Fr , also for the flood characteristics (i.e. water depth and velocity), they are capable of identifying two instability threshold curves, which are critical for the onset of instability

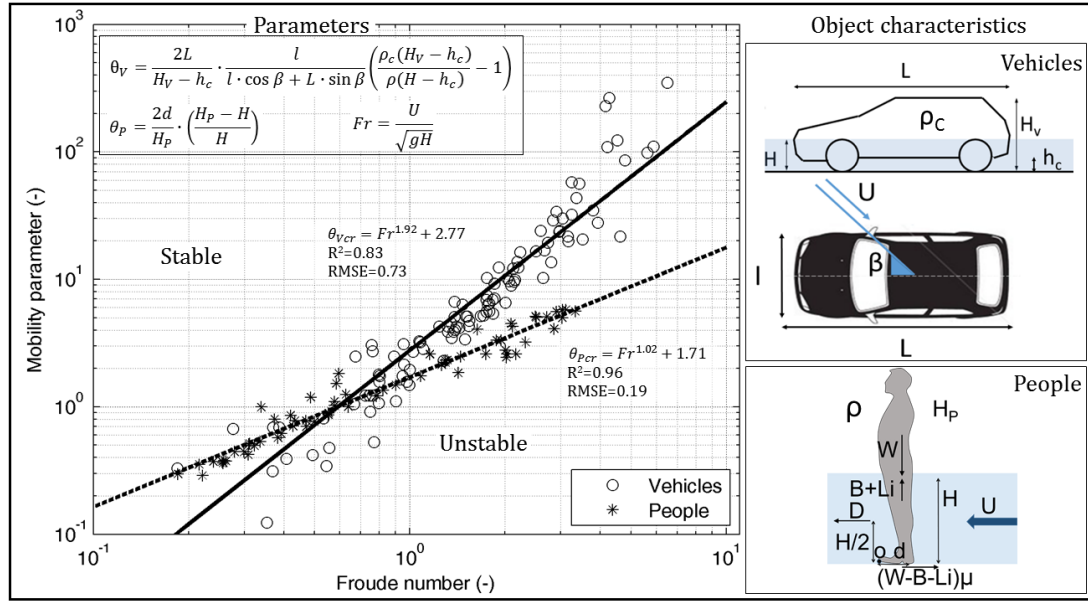


FIGURE 3.14: Dimensionless instability diagram as mobility parameter versus Froude number for vehicles and people.

conditions

$$\theta_{Vcr} = Fr^{1.92} + 2.77 \quad \text{for vehicles} \quad (3.31)$$

$$\theta_{Pcr} = Fr^{1.02} + 1.71 \quad \text{for people} \quad (3.32)$$

Eq. 3.31 is the instability curve for vehicles θ_{Vcr} represented with a black continuous line in Figure 3.14. The $RMSE$ and determination coefficient R^2 for the regression are equal to 0.73 and 0.83 respectively. Eq. 3.32 describes the instability curve for people under water flow and is represented with a black dashed line in Figure 3.14. The $RMSE$ and determination coefficient R^2 for the regression are equal to 0.19 and 0.96 respectively. The pairs (H, U) , which fall in the area of the diagram above the curve are stable combinations of water depth and velocity, while pairs (H, U) , which fall in the area of the diagram below the curve are unstable. Since the two critical curves in Eqs. 3.31, 3.32 intersect each other, some pairs (H, U) can be stable for people and unstable for vehicles and viceversa. Referring to Figure 3.14, the intersection between the curves corresponds to Froude number equal to about 0.6. At the left of the intersection point, the area between the curves is safe for vehicles and dangerous for people. At the right of the intersection point (i.e. supercritical flows), the area between the curves is safe for people and dangerous for vehicles. $Fr = 0.6$ corresponds to a water depth of about 0.4 m in incipient motion condition of vehicles, which is about the critical threshold for buoyancy instability.

3.4 Summary of key results and implications

In this chapter, the instability conditions for vehicles and people under water flow have been analysed. The different forces acting on partly/fully immersed objects have been explicited for the equilibrium conditions accounting for the mean flow properties. For the vehicles, the sliding instability has been analysed. For people, both sliding and toppling have been considered. In order to overcome the large scatter of existing experimental data, two mobility parameters have been defined: θ_P for people and θ_V for vehicles. The mobility parameters are dimensionless and are dependent on Froude number

of the undisturbed mean flow. They can provide a suitable tool to identify dimensionless hazard criteria for vehicles and people in flood mapping to support risk managers. The mobility parameter for vehicles θ_V is defined for sliding instability as the product of a shape factor of the object, an angle of flow incidence factor and the relative immersed weight (Eq. 3.13). Existing experimental data (i.e. pairs of water depth and velocity) (Xia et al., 2011; Shu et al., 2011; Xia et al., 2013) have been used to calculate Froude number Fr and θ_V . The relation $\theta_V = f(Fr)$ is capable of identifying a threshold of incipient motion for different vehicle models with different flow orientation, geometry, density and scale. The hypothesis of the existence of a spurious correlation between mobility parameter and Froude number has been rejected after having tested the effect of the addition of a random noise to the experimental pairs on the determination coefficient of the regression. The mobility parameter for people θ_P is defined as the product of a shape factor of the object and the relative dry height of the subject (Eq. 3.25) for both sliding and toppling instability mechanisms. Existing experimental data (i.e. pairs of water depth and velocity) (Foster & Cox, 1973; Karvonen et al., 2000; Jonkman et al., 2008; Xia et al. 2014) have been used to calculate Froude number Fr and θ_P . The relation $\theta_P = f(Fr)$ is capable of identifying a threshold of instability for different human characteristics (including a scale human model), thus reducing the scatter of experimental datasets. The two mobility parameters have been plotted together (Figure 3.14) to identify regions of the diagram where the instability of people and vehicles behaves differently in floodwaters. Two critical curves θ_{Pcr} and θ_{Vcr} have been defined (Eq. 3.31, 3.32), which separate safe conditions (above the curves) from dangerous conditions (below the curve). Since the two critical curves intersect for Froude number $Fr = 0.6$ some areas of the diagram where people are stable while vehicles are unstable, and vice versa, have been identified. Figure 3.15 summarizes the outline and results of this chapter. The most important result of the first part of the research is the introduction of two new mobility dimensionless parameters for vehicles and pedestrians. The instability diagrams obtained using the new mobility parameters as a function of the Froude number of the undisturbed mean flow (which summarize flood depth H and flow velocity U) are capable of describing the instability conditions more accurately than the common instability diagrams based only on flood depth H and flow velocity U . This is made possible through the introduction of relevant characteristics related to the geometry and density of the considered object in floodwater, thus substantially reducing the very large scatter generally observed in the current $H - U$ diagrams. In the new dimensionless $\theta - Fr$ diagrams, however, the relative contribution of the buoyancy, drag and lift forces on the instability people and vehicles is still not clear. For this purpose, a 3D numerical model, in which a detailed car/human geometry is simulated under different mean flow characteristics might be appropriate. Moreover, a numerical model might also state the validity of Froude's similitude for scaling the hydrodynamic effects from scale to prototype objects.

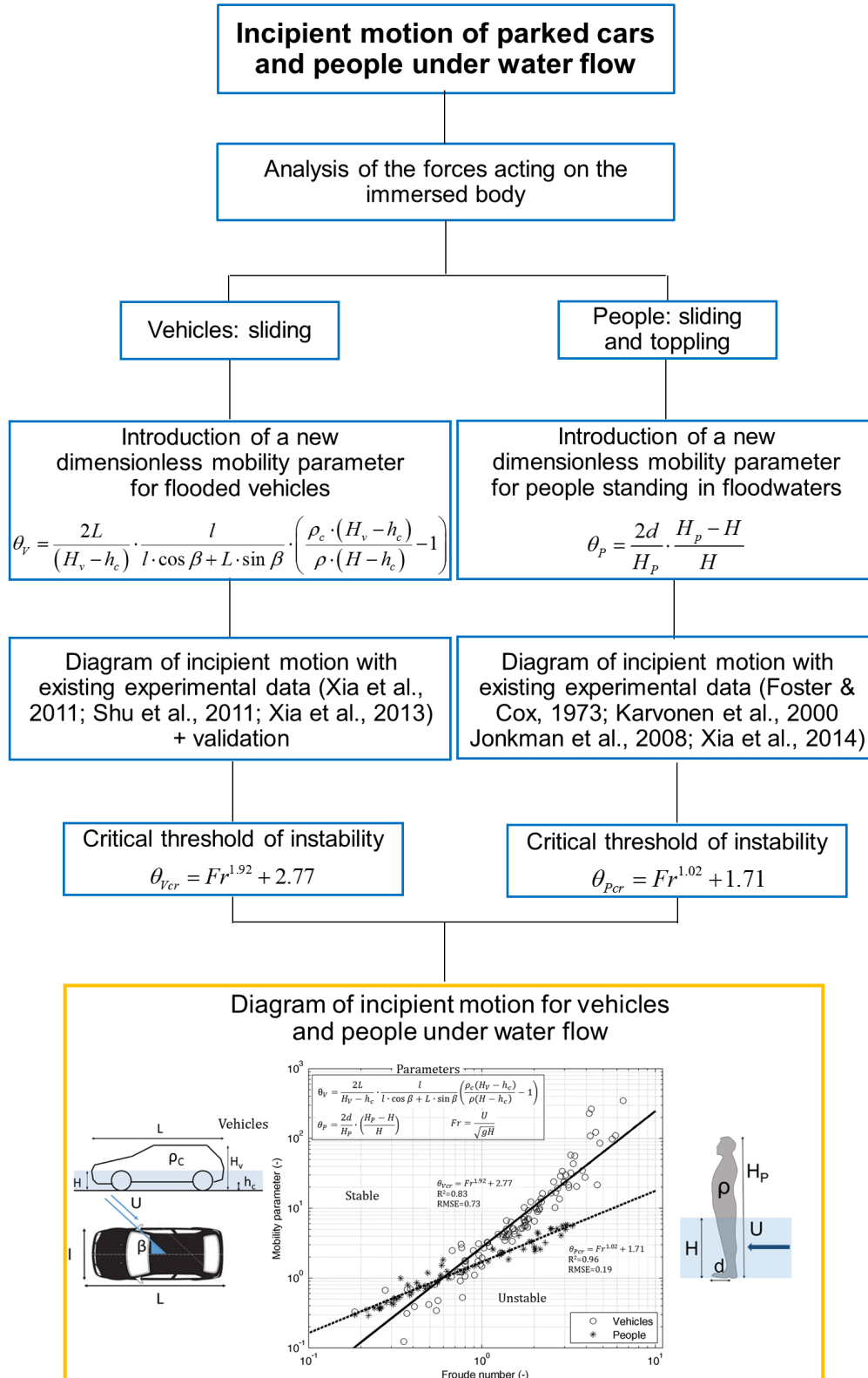


FIGURE 3.15: Graphical summary of chapter 3.

Chapter 4

Numerical model set-up in OpenFOAM

In the first part of the research, a review of the current knowledge about vehicles and pedestrians instability has been carried out. Two dimensionless mobility parameters have been introduced, which depend on Froude number and dimensionless force coefficients. No numerical models have yet been used to understand the conditions of instability of vehicles or pedestrians subject to flow in floodwaters. In the last two decades, many experiments have been carried out on human subjects in hydraulic flumes (e.g. Karvonen et al., 2000; Jonkman et al., 2008; Xia et al., 2014). More recently, a few experiments on the incipient motion conditions of scale vehicle models have been conducted (e.g. Xia et al., 2011; Shu et al., 2011). Thus, although the hydrodynamic forces are accounted for in some conceptual models, a numerical parameter study was never carried out. Therefore, and in order to clarify the relative contribution of drag and lift forces exerted by water on flooded cars and people, a numerical study is performed. The numerical modelling of cars/people facing a flood flow may provide crucial help in better understanding the conditions for incipient motion of objects partially submerged in flowing water and thus, in evaluating and managing flood risk in urban areas. For this purpose, a 3-dimensional numerical model is required in order to: i) describe the mean fluid motion around vehicles/human body, which may induce their instability, ii) reproduce laboratory tests for validation and extension of the available data at the laboratory scale to field scale, iii) estimate the forces acting on the object, including drag (C_D) and lift (C_L) coefficients and relating them to controlling parameters of the mean flow such as Froude and Reynolds numbers. OpenFOAM is an adequate tool to perform 3D hydrodynamic simulations for its meshing capabilities, available solvers and forces calculation libraries. Different combinations of water depth and flow velocity are simulated in the parameter study, reproducing the existing physical flume experiments on partially submerged vehicles scaled models and people. In this chapter, a brief overview of the OpenFOAM framework is outlined first. Second, the governing equations used for the CFD modelling of an object subject to water flow are summarized. Third, the model setup for the parameter study, including mesh generation, solver and boundary conditions, is described. Fourth, a study is performed on the sensitivity of the mesh resolution and the turbulence model on the evaluation of hydrodynamic forces. This is required to achieve a good compromise between computational time and accuracy. The tests program of the parameter study is then described and the assumptions and limitations of the study are discussed. Finally, a summary of the chapter is provided.

4.1 The OpenFOAM framework

OpenFOAM was developed by OpenCFD Ltd. at ESI Group. Its advantage over other numerical frameworks is that it consists in a free open source library of C++ classes for

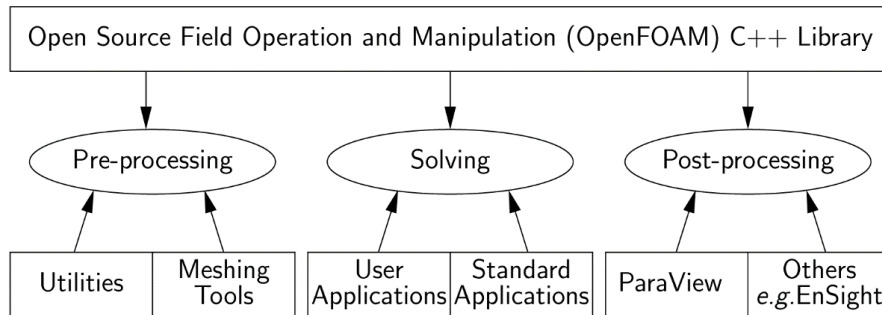


FIGURE 4.1: OpenFoam Structure (OpenFOAM User Guide, 2013)

which the user can have complete access to improve/modify the current codes. Moreover, a large still growing web community is constantly updating and reporting issues and solutions, which constitute a fundamental support for researchers. The OpenFOAM applications fall into two categories: solvers, that are each designed to solve a specific problem in continuum mechanics, and utilities, which are designed to perform tasks that involve diverse types of data manipulations. OpenFOAM is supplied with pre- and post-processing environments. The interface to the pre- and post-processing are themselves OpenFOAM utilities, thereby ensuring consistent data handling across all environments. The overall structure of OpenFOAM is shown in Figure 4.1. The OpenFOAM distribution contains numerous solvers and utilities covering a wide range of problems. For the use of OpenFOAM in engineering applications problems, solvers for incompressible and multiphase flows are available using the RANS equations coupled with a finite volume discretization method (VOF). The CFD model construction consists of six main steps:

- the geometry (physical bounds) of the problem is defined
- the volume occupied by the fluid is divided into discrete cells
- the physical model is defined
- boundary and initial conditions are defined
- the equations are solved iteratively
- a postprocessor is used for the analysis and visualization of the results

For the mesh generation, OpenFOAM includes the *blockMesh* utility, which builds structured meshes. It also allows the generation of sub-meshes with different cell size by considering the ratio cell size between adjacent sub-meshes. Moreover, very complex geometries can be handled by the supplied utility *snappyHexMesh*, which automatically generates 3-dimensional meshes containing hexahedra (hex) from triangulated surface geometries in Stereolithography (.stl) format (OpenFOAM, 2013). Several alternatives for turbulence modelling are available and supplied by OpenFOAM: more than 15 models of RAS type (Reynolds Average Simulation: e.g., $k - \epsilon$, $k - \omega$, SST); more than 18 models of LES type (Large Eddy Simulation) and 2 DES type (Detached Eddy Simulation).

4.2 Governing equations of the CFD model

At the core of all unsteady flow routing computer simulations are the Navier-Stokes equations for an incompressible fluid:

$$\frac{\delta v_i}{\delta x_i} = 0 \quad \text{continuity equation} \quad (4.1)$$

$$\frac{\delta v_i}{\delta t} + \frac{\delta v_i v_j}{\delta x_j} = -\frac{1}{\rho} \cdot \frac{\delta p}{\delta x_i} + \nu \cdot \frac{\partial^2 v_i}{\partial x_j \partial x_j} \quad \text{momentum conservation} \quad (4.2)$$

Where v is the vector (u, v, w) of the velocity components in the three directions x (i.e. x, y, z in Cartesian coordinates), i, j indicate the i -th and j -th components, t is the time, p is the pressure, ρ is the fluid density, ν is the kinematic viscosity. Reynolds Averaged Navier Stokes equations (RANS) are obtained replacing the instantaneous velocity with the sum of the mean U_i and the fluctuating part u_i in Eqs. 4.1 and 4.2 respectively

$$\frac{\delta u_i}{\delta x_i} = \frac{\partial (U_i + u_i)}{\delta x_i} = 0 \quad (4.3)$$

$$\frac{\delta (U_i + u_i)}{\delta t} + \frac{\delta (U_i + u_i)(U_j + u_j)}{\delta x_j} = -\frac{1}{\rho} \cdot \frac{\delta (P + p)}{\delta x_i} + \nu \cdot \frac{\partial^2 (U_i + u_i)}{\partial x_j \partial x_j} \quad (4.4)$$

Then the average $\overline{U_i + u_i}$ is calculated for Eqs. 4.3 and 4.4 and since the average of the fluctuating component is null $\overline{u_i} = 0$ the continuity equation reads

$$\frac{\delta \overline{U_i}}{\delta x_i} = 0 \quad (4.5)$$

And the conservation of momentum becomes

$$\frac{\delta U_i}{\delta t} + \frac{\delta U_i U_j}{\delta x_j} = -\frac{1}{\rho} \cdot \frac{\delta P}{\delta x_i} + \nu \cdot \frac{\partial^2 U_i}{\partial x_j \partial x_j} - \frac{\overline{\delta u'_i u'_j}}{\delta x_j} \quad (4.6)$$

Where an extra term (Reynolds stress tensor) is present, which represents an additional transfer of momentum through fluctuating velocities. Such extra term originates the closure problem, which is addressed by the turbulence models (see section 2.3.2). Closure refers to finding expressions for terms that arise in averaged and filtered versions of the NS equations and for which there are no fundamental equations. In OpenFOAM the effects of the turbulence are included through the turbulent viscosity (OpenFOAM, 2013). The discretisation method used in OpenFOAM is the finite volume method (FVM) which is a common approach used in CFD codes for representing and evaluating partial differential equations in the form of algebraic equations (Toro, 2009). In the finite volume method, the governing partial differential equations (i.e. RANS equations, the mass and energy conservation equations, and the turbulence equations) are recast in an integral conservative form, and then solved over discrete control volumes. This discretisation guarantees the conservation of fluxes through a particular control volume. In the finite volume method, volume integrals in a partial differential equation that contain a divergence term are converted to surface integrals, using the divergence theorem. These terms are then evaluated as fluxes at the surfaces of each finite volume. Because the flux entering a given volume is identical to that leaving the adjacent volume, these methods are conservative. Another advantage of the finite volume method is that it is easily formulated to allow for unstructured meshes (Toro, 2009). Hydrodynamic forces (i.e. drag D

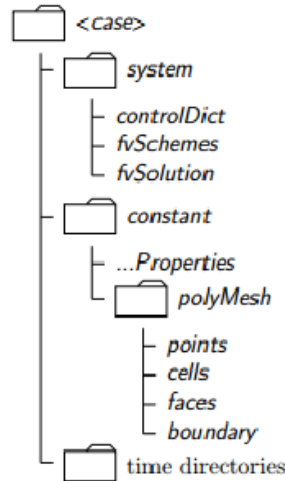


FIGURE 4.2: File structure of OpenFOAM cases (OpenFOAM, 2013)

and lift L_i) are calculated in OpenFOAM during the simulations through direct integration of the pressures over a specified surface. Forces coefficients C_D and C_L are obtained as the ratio between the force and a reference undisturbed velocity U_{ref} and area A_{ref}

$$C_D = \frac{D}{0.5 \cdot \rho A_{ref} U_{ref}^2} \quad (4.7)$$

$$C_L = \frac{L_i}{0.5 \cdot \rho A_{ref} U_{ref}^2} \quad (4.8)$$

4.3 Numerical model set up

4.3.1 Structure of a simulation in OpenFOAM

The structure of a case in OpenFOAM is built around three folders: 0 folder (time directory), constant folder and system folder (OpenFOAM, 2013). Each folder contains the necessary files (called dictionaries) for setting the properties of the computational domain and of the fluids (Figure 4.2). The 0 folder (i.e. time directory) contains individual files of data for particular fields. The data can be either initial values and boundary conditions that the user must specify to define the problem or results written to file by OpenFOAM. The name of each time directory is based on the simulated time at which the data is written. The constant directory contains a full description of the case mesh in a subdirectory called *polyMesh* and files specifying physical properties of the fluid for the application concerned, such as the viscosity. The system directory allows setting parameters associated with the solution procedure itself. It contains at least the following 3 files: *controlDict* where run control parameters are set including start/end time, time step and parameters for data output; *fvSchemes* where discretisation schemes used in the solution may be selected at run-time; and, *fvSolution* where the equation solvers, tolerances and other algorithm controls are set for the run.

4.3.2 Solver

Among the available solvers for incompressible flows, *interFoam* has been selected. *interFoam* is a solver for two incompressible, isothermal, immiscible fluids which uses

a VOF (volume of fluid) phase-fraction based interface capturing approach. It is suitable to simulate partly submerged objects where part of the surface is wet by a mixture of air and water (Desphande, 2012). *interFoam* uses the volume fraction α as an indicator function (*alpha* in OpenFOAM code) to define which portion of the cell is occupied by the fluid (Jasak, 1996)

$$\alpha(x, y, z, t) = \begin{cases} 1 & \text{for a place occupied by fluid 1} \\ 0 < \alpha < 1 & \text{at interface between 1 \& 2} \\ 0 & \text{for a place occupied by fluid 2} \end{cases} \quad (4.9)$$

The transport of α is expressed by an advection function and the local fluid properties are a weight mixture of the physical properties of both fluids (Jasak, 1996). *interFoam* has been improved with a library called *waves2Foam*, which is a toolbox used to generate and absorb free surface water waves and currents (Jacobsen et al., 2011). The method applies the relaxation zone technique (active sponge layers) which covers the method of removing reflected or internally generated wave components adjacent to vertical boundaries. The explicit relaxation technique is performed before the momentum equation as follows

$$U = (1 - \omega)U_{target} + \omega U_{computed} \quad (4.10)$$

$$\alpha = (1 - \omega)\alpha_{target} + \omega\alpha_{computed} \quad (4.11)$$

Where $\omega \in [0, 1]$ is a weighting function, U_{target} and α_{target} are the desired velocity and water content in a cell at the boundary respectively while $U_{computed}$ and $\alpha_{computed}$ are the velocity and water content in a cell as calculated by the momentum and continuity equations. Since the relaxation zone can assume different arbitrary shapes, the choice of the waveFoam solver will also affect the shape of the computational mesh (section 4.3.3).

4.3.3 Mesh generation

Three different meshes are generated to reproduce three different angles of flow incidence for the simulations of a selected car model. The Ford Focus used for the experiments by Shu et al. (2011) has been chosen because it is representative of a class of common small passenger vehicles. The computational mesh describes a rectangular channel with a vehicle inside it. As a starting point, the mesh with the longitudinal axis of the car parallel to the y-axis is created, then the car geometry is rotated to generate the new meshes. Five meshes are generated around a human body to account for the different geometric characteristics of the experimental subjects (Karvonen et al., 2000; Jonkman et al., 2008; Xia et al., 2014). Given the simple geometry of the channel and the complex geometry of the car/human body both utilities *blockMesh* and *SnappyHexMesh* are used for the discretization of the domain. The *blockMesh* tool is used to enter the geometry of the channel and the *SnappyHexMesh* tool is used to build the refined mesh around the 3D surface. The geometry of the channel is entered as a list of vertices of a box in the International System of Units after specifying a possible scaling factor. The pieces of information needed for the mesh generation are included in the constant folder of the case directory in the *blockMeshDict* text file. Since a reduction of possible reflection effects is needed without generating cumbersome computational domains, the geometry of the channel is set to be a cylinder (Figure 4.7) with maximum height of 1 m for the maximum water depth to be modelled for the car (i.e. 0.5 m) and 1.5 for the human subjects. This is made possible thanks to the *waveFoam* solver which supports a cylindrical shape of the relaxation zones (see section 4.3.4). The operations needed to create the channel mesh and

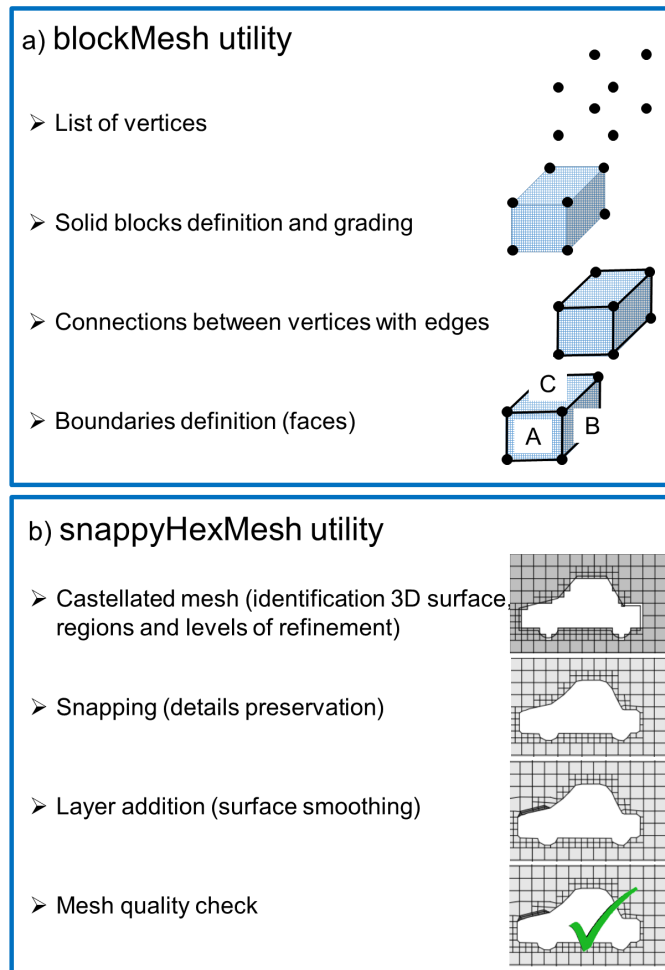


FIGURE 4.3: Mesh generation procedure in OpenFOAM (exemplarily for a car).

proceed with the refinement around the selected 3D surface are summarized in Figure 4.3, panel a and b, respectively. To define a cylindrical channel, 15 vertices are entered. Then five blocks are defined as a list of their boundary vertices and the number of cells in which dividing each direction of each block is set (e.g. grading). The list of the edges specify how two vertices are linked. To generate a cylinder, the edges must be set to arcs defining the two connecting vertices and the interpolation points. The boundary is broken into patches (regions), where each patch in the list has its name as a keyword selected by the user. The name is used as an identifier for setting boundary conditions in the field data files. The patch information is then contained in sub-dictionary with type and faces (defined by four vertices). Three boundary patches are introduced in our configuration: the atmosphere, the bottom of the channel and the bounding ring-shaped surface (named inlet). When the *blockMeshDict* is completed (Figure 4.3, a) the command *blockMesh* is run from the terminal window in the case directory and the channel computational mesh is created. Once the channel is generated by running *blockMesh* the tridimensional surface of the car/human body is added and the mesh is adjusted and refined through the *snappyHexMeshDict* file located in the system folder in the case directory. The procedure consists of three consecutive phases (Figure 4.3, b):

- Generation of the castellated mesh
- Snapping

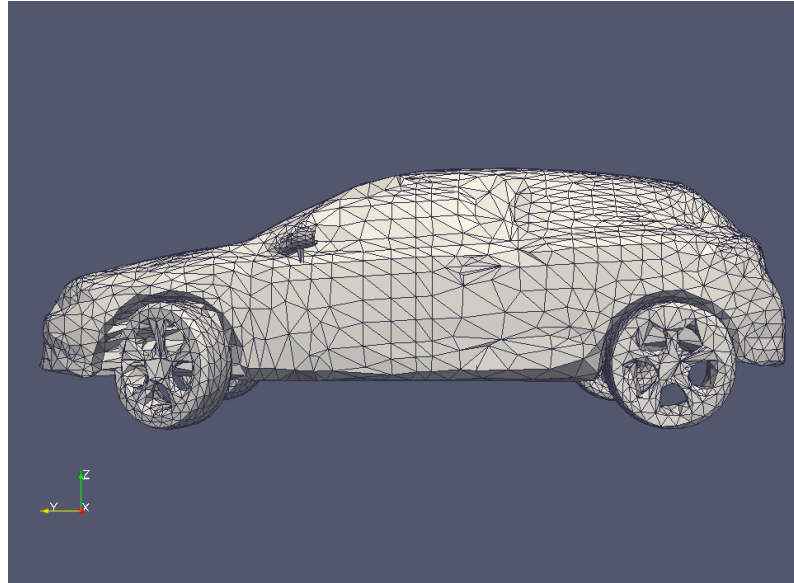


FIGURE 4.4: Triangulated surface .stl of the car Opel Astra used for the mesh generation

TABLE 4.1: Characteristics of Honda Accor (prototype and scale 1:14)(Xia et al., 2013)

Dimensions	Ford Focus	Opel Astra
Length (cm)	435	440
Width (cm)	182	181
Height (cm)	148	151
wheelbase (cm)	264	268

- Addition of layers
- Quality check

The first three operations can be switched on/off at the top of the dictionary. The tridimensional surface in .stl format (e.g. a car in Figure 4.4, or a human body in Figure 4.5) included in the constant/tri-surface folder is specified in the dictionary and it is used to specify the refinement for any mesh cell intersecting it or for any mesh cell inside/outside/near and to 'snap' the mesh boundary to the surface. The crucial condition for the consistent use of the triangulated surface is that it must be closed, if not *snappyHexMesh* does not remove the cells inside the surface and the object is not captured by the mesh generation procedure. To represent the geometry of the Ford Focus model the triangulated geometry of an Opel Astra is used (Figure 4.4). The geometry is provided by LaSIS laboratory at the University of Florence (<http://www.lasis.unifi.it>). Although the car model is different, the lower part, which is accounted for in the simulation for partially submerged conditions (e.g. the chassis and the lower bodywork) is considered as commutable for our purposes. In fact, the vehicle category, the shape and the geometric dimensions are approximately the same (Table 4.1).

To check the quality of the triangulated .stl surface the program *ADMESH* (<http://www.varlog.com/admesh-htm>) can be used. *ADMESH* is a program for processing triangulated solid meshes, it reports the number of the disconnected facets and allows the user to remove unconnected parts and fill holes. Given the bad quality of our geometry and the number of holes, the geometry is first processed with some mesh manipulation tools

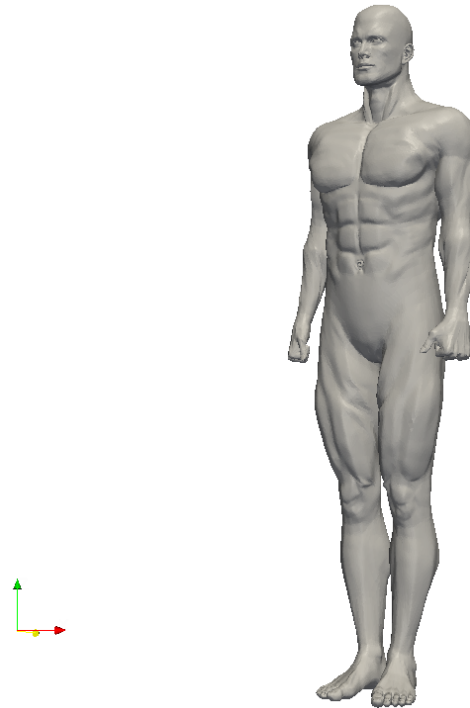


FIGURE 4.5: Triangulated surface .stl of a human body used for the mesh generation

available in OpenFOAM, then it is manually closed, fixing edge by edge through the program Blender (<http://www.blender.org/>). The OpenFOAM tools used are:

- *collapseEdges*: collapse short edges and combines edges that are in line
- *surfacePointMerge*: merges points on surface if they are within absolute distance
- *surfaceClean*: Removes baffles - collapses small edges, removing triangles.

In the Blender environment the .stl file is imported and all the unconnected edges are highlighted by the command select non-manifold edges and the vertices are connected pressing F. Once the pre-processing of the .stl geometry is completed, the geometry is exported from Blender and it is ready to be imported in the OpenFOAM dictionary. In the first section of the dictionary, the settings for the castellated mesh are added and the type of refinement is set around the car surface. The surface based refinement requires two levels (minimum and maximum). The first is the minimum level, every cell intersecting a surface gets refined up to the minimum level. The second level is the maximum level. The region-wise refinement requires specifying levels for cells in relation to a surface with three modes: distance, inside, outside. A point, which should never be on a face, must be set inside the mesh to define the refinement area. The choice of the mesh size is based on the results of a mesh sensitivity analysis (section 4.4.1). The second part of the dictionary is about the snap settings. This part allows identifying particular or sharp details, which should be kept realistic, and which could be smoothed by the generation of the castellated mesh (e.g. the mirrors of the car). The third part of the dictionary is about the layer addition that removes the cubic grid aspect and restores the natural curve shape of the surface adding a layer of specified thickness. Some advanced setting may be added, and finally the quality of the mesh is checked. For specific details of the mesh generation procedure, we refer to the OpenFOAM User Guide (OpenFOAM, 2013). The software

generates a new folder called *polyMesh* containing the information run with *blockMesh* together with the new refinement done with *SnappyHexMesh*. To represent the human body geometry, a free .stl file has been used (www.stlfinder.com) and scaled according to the physical characteristics of the simulated subjects (Figure 4.5). The mesh generation follows an identical procedure as for the car (Figure 4.3).

4.3.4 Relaxation zones, boundary and initial conditions

To initialize the flow field inside the computational domain the dictionary *waveProperties* is required by the *waveFoam* solver. The dictionary is located in the constant folder and contains the current (or wave) characteristics and identifies the source of the field and the relaxation zones with their geometry. In the *waveProperties* dictionary, the initial water depth in the computational domain is specified, as well as the name of the relaxation zone, which corresponds to the boundary named in the *blockMesh* dictionary. The relaxation zone is a bounding ring of assigned thickness of the cylinder created for the computational mesh. The thickness of the relaxation zone was set equal to one meter. For steady simulations, also the desired flow velocity is set up in the *waveProperties* text file. To initialize the flow field inside the domain before the simulation the dictionary *setFields* located in the system folder is set for both phases (air and water). The initial conditions of the case study represent the solution at the instant zero and are located in the 0 folder. The initial conditions are set for velocity U , pressure p_{rgh} and phase $alpha1$. For the velocity the initial condition at the inlet refers to the wave/current set in the *waveProperties* file, at the water surface the atmospheric pressure is set and at the bottom of the channel and around the investigated 3D surface, the non-slip condition is set. All the pairs (i.e. critical water depth H and flow velocity U) used as boundary conditions for the numerical simulations of the car and human body are specified in section 4.5.

4.3.5 Control of the simulation and forces calculation

Before running the simulations, the details about the type of solver, the simulation time, time steps, the details on the frequency for writing the output folders and the additional libraries to be recalled are specified in the *system/controlDict* file. The time step is set to be adjustable according to a specified maximum value of Courant number equal to 0.7. The resulting observed order of magnitude of the time step is 10^{-4} s. Approximately 30 s are used as simulation time in order to guarantee a steady oscillation of the calculated forces coefficient. A wall function available in the code (i.e. *nutkWallFunction*) is used to model the flow velocity close to the bottom boundary. The additional library *libforces.so* is included in the *controlDict* file in order to calculate the pressure and viscous forces for each time step. For the forces calculation, the surface around which the pressure field is integrated is specified as a patch (e.g. the surface of the car/human body). For the drag and lift coefficients, the reference undisturbed flow velocity (*magUInf*) and an area of reference are set (*Aref*) (see Eqs. 4.7 and 4.8). The reference flow velocity is set equal to undisturbed flow velocity. The reference area for the drag coefficient is the total normal area of the partly immersed object projected normally to the flow. The reference area for the lift force is the planform area of the car. The drag and lift coefficients of every simulation are calculated as the time average of the instantaneous coefficients computed during the simulation once they reach a steady oscillation (see also Figure 4.6). Forces and forces coefficients are calculated and saved in a text file inside the PostProcessing folder in the case directory during the simulations.

TABLE 4.2: Total number of cells and execution time for 1 s of simulation for the three analysed meshes (one core)

Mesh size (m)	0.03	0.015	0.0075
Computational cells (n°)	$1.5 \cdot 10^6$	$5 \cdot 10^5$	$2.8 \cdot 10^6$
Simulation time for 1 s (s)	$4.8 \cdot 10^3$	$4.8 \cdot 10^4$	$2.3 \cdot 10^5$

TABLE 4.3: Percent variation of the estimated force coefficients for the three analyzed meshes

Mesh size (m)	0.03	0.015	0.0075
C_D	0.3766	-0.2%	+2.6%
C_L	0.4548	-6.2%	-2.1%

4.4 Sensitivity analysis to the applied mesh size and turbulence model

4.4.1 Sensitivity of the results to the mesh size

In order to choose an appropriate size of the mesh for the numerical simulations, the sensitivity of the evaluated forces coefficients with respect to the size of the cells is examined. Three cell sizes around the car surface are considered. The aim of the mesh sensitivity analysis is to choose a spatial discretization, which

- (i) is capable of describing the detailed 3D surface of the car,
- (ii) ensures an evaluation of the hydrodynamic forces with an accuracy comparable to the accuracy of the experimental data,
- (iii) allows running simulations with a reasonable computational time according to the available resources.

The mesh sensitivity analysis is performed with the default settings (laminar flow) of the code (see section 4.4.2) for one of the numerical simulations on the Ford Focus (water depth 0.46 m and velocity 2.1 m/s). Three different mesh sizes around the car surface are tested: 0.03 m, 0.015 m, 0.0075 m. The differences in the estimated drag and lift average coefficients are of the order of a few percent (Table 4.3) and smaller than the standard deviation of the instantaneous values computed during the simulation (Figure 4.6). Thus, the 0.03 m mesh is preferred for the associated shorter computational time (Table 4.2). The total number of cells is around $5 \cdot 10^5$ (Figure 4.7). The *snappyHexMesh* tool allows to refine the mesh close to the car surface (cell size is set to 0.03 m) while in the whole mesh domain the maximum size is 0.25 m. The refinement close to the vehicle boundary can be observed in Figure 4.7 where the 3-dimensional view of the mesh (panel a), a longitudinal cross section (panel b) and a detail of the refinement close to the surface (panel c) are shown. The time step is automatically adjusted during the simulation according to the maximum Courant number set to 0.7. The time step was around $10^{-3} - 10^{-4}$ s to ensure stability. With a time step of $2 \cdot 10^{-4}$ s and with $5 \cdot 10^5$ cells, one second of simulation takes approximately 70 minutes without running in parallel (i.e. one core).

Similarly, for the computational mesh of the simulations around a human body, the number of cells is kept around $4.5 \cdot 10^5$ in order to preserve the details of the human geometry and ensure a reasonable computational time. In Figure 4.8, a cross section of the

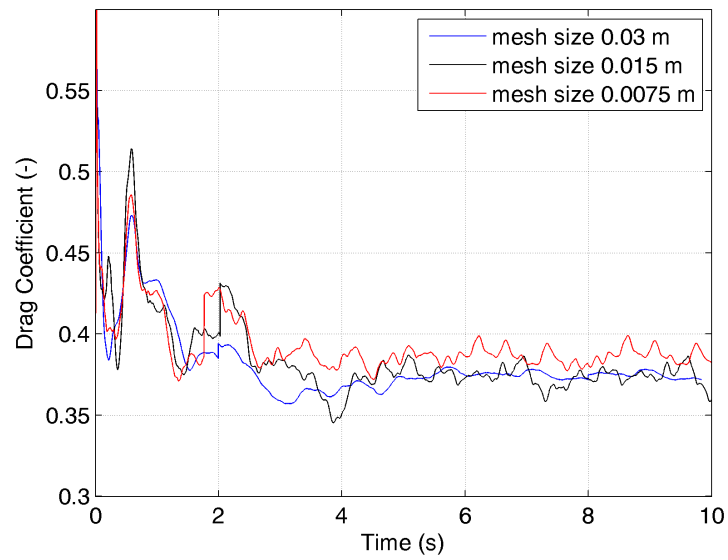


FIGURE 4.6: Instantaneous values of drag coefficient C_D for the three analysed meshes

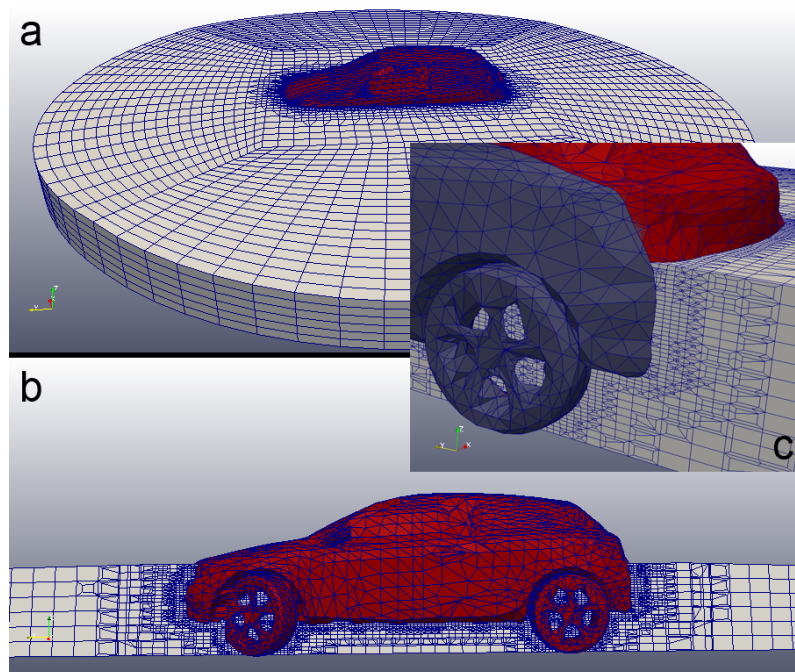


FIGURE 4.7: Computational mesh for the simulation of a car: 3D view of the whole mesh (a), longitudinal cross section (b) and detail of the mesh around the car surface (c).

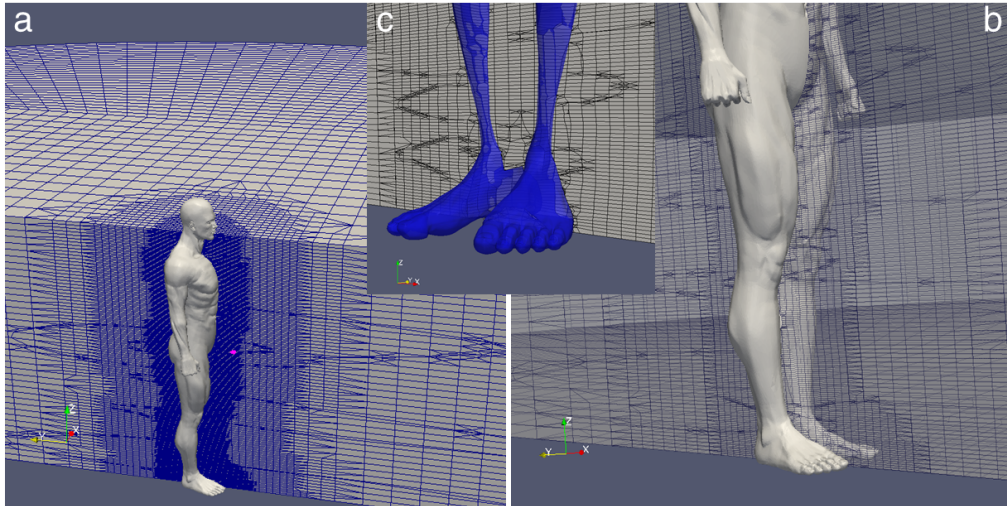


FIGURE 4.8: Computational mesh for the simulation of a human body: cross section (a) and detail of the legs (b) and of the feet (c)

whole mesh orthogonal to the x axis is depicted (panel a) and a detail of the refinement close to the legs and the feet is shown in panel b and c. The cell size close to the body is set to 0.015 m and the maximum cell size is 0.25 m.

4.4.2 Sensitivity of the results to the turbulence model

The main aim of the numerical simulations carried out in this part of the research is to understand how different mean flow regimes (from which the data are available from previous experiments) affect the contribution of drag and lift components in the overall balance of forces on a flooded object, which may cause its incipient motion. Thus, the focus is to assess the physical dependencies among the involved parameters (e.g. force coefficients, Reynolds number, Froude number) for the mean flow. Given that the study is focused on the estimation of integral quantities such as forces considering the mean flow, rather than on the detailed description of the flow properties in terms of local distributions, simulations were performed using the default settings (i.e. laminar) of the numerical code, avoiding the calibration of the turbulence model coefficients (OpenFOAM, 2013). Different turbulence (closure) models are adopted in the literature for the study of air flows past bluff bodies (e.g. Eriksson, 2007; Mansoorzadeh et al., 2014; Papadakis et al., 2014) and for simulating free-surface flows around structures (e.g. Losada et al., 2005; Prasad et al., 2015) or flood waves (e.g. Ozmen-Cagatay et al., 2014). Moreover, the lack of detailed experimental data does not allow an ad hoc calibration of the coefficients. In any case, some short preliminary tests have shown the substantial independence of the results on the particular choice of the closure model, in terms of selected (local) testing flow velocity profiles and even better in terms of force coefficients (Arrighi et al., 2015). The sensitivity analysis is carried out using the mesh size selected in section 4.4.1, i.e. 0.03 m around the car surface. The results in terms of estimated average forces coefficients obtained by default (laminar), $k - \epsilon$ and $k - \omega$ closure models for both subcritical and supercritical flows are compared. The results of these tests (Table 4.4) show a negligible variation of force coefficients for the different closure models in subcritical flow conditions. Moreover, Table 4.4 shows a maximum variation of the order of 10% for supercritical flow conditions, which is comparable with the standard deviation of the instantaneous force coefficients and negligible with respect to the overall variation

TABLE 4.4: Percent variation of the force coefficient with the three tested turbulence model for subcritical ($Fr < 1$) and supercritical ($Fr > 1$) flow conditions.

Turbulence model	Fr<1			Fr>1		
	Default (laminar)	$k - \epsilon$	$k - \omega$	Default (laminar)	$k - \epsilon$	$k - \omega$
C_D	0.3766	+5.8%	-0.9%	0.0871	-8.1%	-9.2%
C_L	0.4548	+3.2%	-1.4%	0.4548	-10.2%	-7.3%

of the coefficients values on the analyzed range of Froude numbers (see Chapter 5). Furthermore, the over/under-estimation of drag and lift coefficients is very similar, thus the ratio between the coefficients bears a difference of the order of 1 – 2%.

4.5 Test programme for the parameter study

4.5.1 Test programme for the Ford Focus

The simulations of the flow around the Ford Focus model consider two different scales (i.e. 1:1 and 1:18) and four angles of flow incidence (0° , 180° , 90° , 65°). The numerical simulations on the scale 1:18 are the close reproduction of the experiments by Shu et al. (2011). The simulations on the Ford Focus prototype scale are scaled using a Froude similarity, thus they reproduce the experimental pairs of water depth and velocity for a car at full scale. The four angles of flow incidence considered are defined as follows (see Figure 3.6):

- 0° : the flow affects the frontal part of the vehicle
- 180° : the flow affects the rear part of the vehicle
- 90° : the flow affects the lateral side of the car
- 65° : the flow affects both front and lateral side of the car (maximized affected area)

Shu et al. (2011) have tested the frontal and rear impacts (i.e. 0° and 180°) in the laboratory flume (Tables 4.5, 4.6). These experimental conditions, i.e. pairs of water depth H and flow velocity U , have been determined during laboratory tests as incipient motion conditions for sliding. The simulations with an angle of flow incidence of 90° and 65° have not yet been studied experimentally. The objective of these simulations is to investigate at prototype scale the effect of different angles of flow incidence with a selection the same pairs (U , H) in table 4.5 (Table 4.7). A total of 26 simulations are carried out for 0° at scales 1:1 and 1:18 (Table 4.5), 10 simulations for 180° at scale 1:1 (Table 4.6), and 22 simulations for both 90° and 65° at scale 1:1 (Table 4.7). Thus, the total number of numerical simulations for the car is 58.

4.5.2 Test programme for human subjects

Three experimental datasets on the instability of people are considered (Karvonen et al., 2000; Jonkman et al., 2008; Xia et al., 2014) because they cover a wide range of flow regimes (i.e. Froude numbers) and include different physical characteristics and a human body model (scaling up to prototype). All simulations account for a frontal impact of the water flow on the human body. The experimental pairs (H , U) recognized as critical in the laboratory tests and used for the numerical simulations are summarized in Tables 4.8-4.13 for the different datasets. The total number of numerical simulations is 33.

TABLE 4.5: Simulated pairs of water depth H and flow velocity U for prototype and scale 1:18 model for the frontal impact (0°)

H 1:1 (m)	U 1:1 (m/s)	H 1:18 (m)	U 1:18 (m/s)
0.171	5.855	0.010	1.380
0.198	5.940	0.011	1.400
0.209	6.020	0.012	1.419
0.234	5.091	0.013	1.200
0.299	4.794	0.017	1.130
0.306	4.073	0.017	0.900
0.326	3.810	0.018	0.898
0.360	3.309	0.020	0.780
0.378	2.927	0.021	0.690
0.408	2.715	0.023	0.640
0.459	2.078	0.026	0.490
0.477	1.442	0.027	0.340
0.529	0.806	0.029	0.190

TABLE 4.6: Simulated pairs of water depth H and flow velocity U for prototype and scale 1:18 model for the rear impact (0°)

H 1:1 (m)	U 1:1 (m/s)
0.162	6.020
0.180	5.855
0.225	5.091
0.243	5.855
0.306	3.309
0.360	2.758
0.459	1.697
0.491	0.849
0.522	0.976
0.540	0.424

TABLE 4.7: Simulated pairs of water depth H and flow velocity U for angle of flow incidence 90° and 65°

H 1:1 $\beta = 90^\circ$ (m)	U 1:1 $\beta = 90^\circ$ (m/s)	H 1:1 $\beta = 65^\circ$ (m)	U 1:1 $\beta = 65^\circ$ (m/s)
0.17	5.85	0.17	5.85
0.20	5.94	0.20	5.94
0.23	5.09	0.23	5.09
0.28	4.79	0.28	4.79
0.31	3.81	0.31	3.81
0.31	4.07	0.31	4.07
0.36	3.30	0.36	3.30
0.39	2.71	0.39	2.71
0.44	2.08	0.44	2.08
0.48	1.44	0.48	1.44
0.51	0.81	0.51	0.81

TABLE 4.8: Simulated pairs of water depth and flow velocity for Subject 2 tested by Karvonen et al. (2000)

Subject 2 (Karvonen et al., 2000)		
Water depth H (m)	Velocity U (m/s)	Froude number Fr (-)
0.40	2.60	1.31
0.50	2.40	1.08
0.60	2.00	0.82
0.80	1.55	0.55
0.90	1.40	0.47
1.00	1.20	0.38
1.05	1.00	0.31

TABLE 4.9: Simulated pairs of water depth and flow velocity for Subject 4 tested by Karvonen et al. (2000)

Subject 4 (Karvonen et al., 2000)		
Water depth H (m)	Velocity U (m/s)	Froude number Fr (-)
0.6	1.4	0.58
0.8	1.1	0.39
1	0.75	0.24
1	0.8	0.26

TABLE 4.10: Simulated pairs of water depth and flow velocity for Subject 5 tested by Karvonen et al. (2000)

Subject 5 (Karvonen et al., 2000)		
Water depth H (m)	Velocity U (m/s)	Froude number Fr (-)
0.40	2.50	1.26
0.60	1.90	0.78
0.80	1.40	0.50
1.07	1.00	0.31

TABLE 4.11: Simulated pairs of water depth and flow velocity for the stuntman tested by Jonkman and Penning-Rowse et al. (2008)

Stuntman (Jonkman et al., 2008)		
Water depth H (m)	Velocity U (m/s)	Froude number Fr (-)
0.26	3.00	1.88
0.26	3.10	1.94
0.33	2.60	1.45
0.35	2.40	1.30

TABLE 4.12: . Simulated pairs of water depth and velocity (scaled to prototype) for the human model tested by Xia et al. (2014) classified as sliding instability

Sliding instability (Xia et al., 2014)		
Water depth H (m)	Velocity U (m/s)	Froude number Fr (-)
0.21	3.03	2.11
0.20	2.93	2.09
0.18	3.35	2.51
0.18	3.30	2.50
0.18	3.60	2.71
0.17	3.70	2.91
0.16	3.80	3.03
0.16	3.90	3.11

TABLE 4.13: Simulated pairs of water depth and velocity (scaled to prototype) for the human model tested by Xia et al. (2014) classified as toppling instability

Toppling instability (Xia et al., 2014)		
Water depth H (m)	Velocity U (m/s)	Froude number Fr (-)
0.64	0.85	0.34
0.57	1.15	0.49
0.48	1.27	0.59
0.42	1.21	0.60
0.32	2.05	1.16
0.22	2.40	1.63

4.6 Applicability and limitations of the CFD simulations

Different factors may affect the accuracy and validity of the results of numerical simulations, including for instance:

- Simplifications/assumptions required to reduce the complexity of the model (i.e. complex governing equations).
- Specification of inappropriate initial and boundary conditions
- Selection of an inappropriate turbulence model.
- Mesh resolution, possibly resulting in inaccuracies of the results if the mesh is too coarse, and in too high computational time if the mesh is too fine.

Therefore, the limitations of the applied numerical model are briefly described in this section. The major simplification in the numerical simulations of the instability conditions of vehicles and people under water flow is the rigid body assumption. More specifically, the hydrodynamic forces on the car model simulated are calculated by assuming the entire car model as fully rigid. However, the vertical displacement of the vehicle platform, due to the presence of the suspensions may affect the level of submergence and consequently the value of the hydrodynamic forces. When a car is immersed in flowing water, we expect that an equilibrium exists between the force exerted by the suspensions and the lift force, thus resulting in an equilibrium elevation of the chassis, which is different from the equilibrium elevation in non-submerged conditions. Since this assumption may introduce inadmissible errors in the numerical results, the effect of the suspensions is analysed in Chapter 5. For people instability conditions, the rigid body assumption is even more crucial than for vehicles. In fact, a person standing in flowing water may adjust its position in order to resist to the destabilizing effect of the flow. These limitations for vehicles and pedestrians could be overcome by using a fully-coupled CFD-CSD numerical model, which, for its complexity, would constitute a topic on its own for a next PhD research. In the experiments carried out on real people instability, the human subjects were allowed to behave naturally in order to oppose themselves to the loss of stability. In contrast, the numerical simulations of people in flowing water only account for the hydrodynamic forces on fully rigid and fixed human bodies, ignoring any adjustment to improve their stability. A further limitation is due to the absence of clothing of the numerical human body model, which consists of a naked body. The presence of clothing is recognised as extremely important (e.g. Abt et al., 1989; Karvonen et al., 2000; Xia et al., 2014), because it can significantly affect the drag and lift coefficients. Only one type of body structure for humans (i.e. thin and tall) is considered, although scaled according to heights of the subjects tested in experimentally in previous studies. The quality of the mesh in terms of cell size adopted in this numerical study might be considered as too coarse for other purposes associated with a very detailed description of the flow field. However, as specified in the section about the sensitivity analysis (section 4.4.1), the numerical simulations are rather intended to identifying and understanding the mechanisms underlying the incipient motion of vehicles and pedestrians in flowing water referring to mean flow field as well as the relevant influencing parameters. As shown in tables 4.3, the mesh sensitivity analysis shows very small differences in terms of estimated force coefficients, which are negligible if compared with the range of forces analysed (Chapter 5). The boundary conditions set in the numerical simulations are taken from the corresponding experimental studies, which may have intrinsic uncertainties and errors. It must be also noticed that the onset of motion is instantaneous, while a force coefficient is obtained as an average over the simulated time. In section 3.1.4, it was shown that an error of about 10% on

the water depth H and velocity U pairs inducing vehicle incipient motion does not significantly alter the correlation between mobility parameter θ_V and Froude number Fr . Furthermore, as shown in section 4.4.2, the effect of applying different turbulence models may cause a maximum variation up to 10% in the calculated drag and lift coefficients. The above described assumptions and limitations of the numerical model might indeed seriously affect the reliability of the numerical results. Therefore, the implications of the main assumptions will be critically analysed and discussed in Chapter 5.

4.7 Summary of the chapter

This chapter describes the setup of the numerical model used to simulate the mean flow conditions for the onset of the instability of vehicles and pedestrians as observed in physical experiments. The aim of the numerical simulations is to clarify the conditions under which incipient motion of parked vehicles and those of people in flowing floodwater may occur. The results are expected to substantially improve the understanding the mechanisms and most relevant parameters underlying this incipient motion. An overview of the contents of this chapter is shown in Figure 4.9. The description of the model setup is addressed in different sections describing the numerical solver, the mesh generation, the turbulence model, the boundary and initial conditions and the sensitivity analysis. The numerical solver adopted to simulate a steady flow around partly submerged people and vehicles is *waveFoam*. The latter solves two incompressible and immiscible fluids (i.e. water and air) using a parameter α , which describes the relative content of the fluids within a computational cell. The main advantage of the solver is that it uses special absorbing boundary conditions, which allows to substantially reduce the computational domain (i.e. number of cells). The procedure of the mesh generation consists of two main steps described in section 4.3.3. First, the bounding channel is generated using the *blockMesh* tool, then the mesh is refined around a 3D object, whose geometry is represented with a .stl triangulated surface, using the *snappyHexMesh* tool. The sensitivity analysis is carried out to understand the effect of the selected mesh size and turbulence model on the calculated hydrodynamic forces (sections 4.4.1 and 4.4.2 respectively). The results allow one to achieve a good compromise between accuracy and computational time.

The boundary and initial conditions and the control settings of the simulations, such as the time step are finally described. The programme of the numerical tests for vehicles and people is provided in Tables 4.5- 4.13. For the tests with vehicles, a Ford Focus is selected by considering two scales (1:1 and 1:18) and four angles of flow incidence (0° , 180° , 90° , 65°). The experimental data carried out by Shu et al. (2011) are reproduced. The simulations about pedestrians instability take into account three different datasets (Karvonen et al., 2000; Jonkman et al., 2008; Xia et al., 2014) for which the human geometry is scaled according to the physical characteristics of the human subjects and model. Finally, the applicability and limitations of the model are discussed, highlighting the implications of the main assumptions.

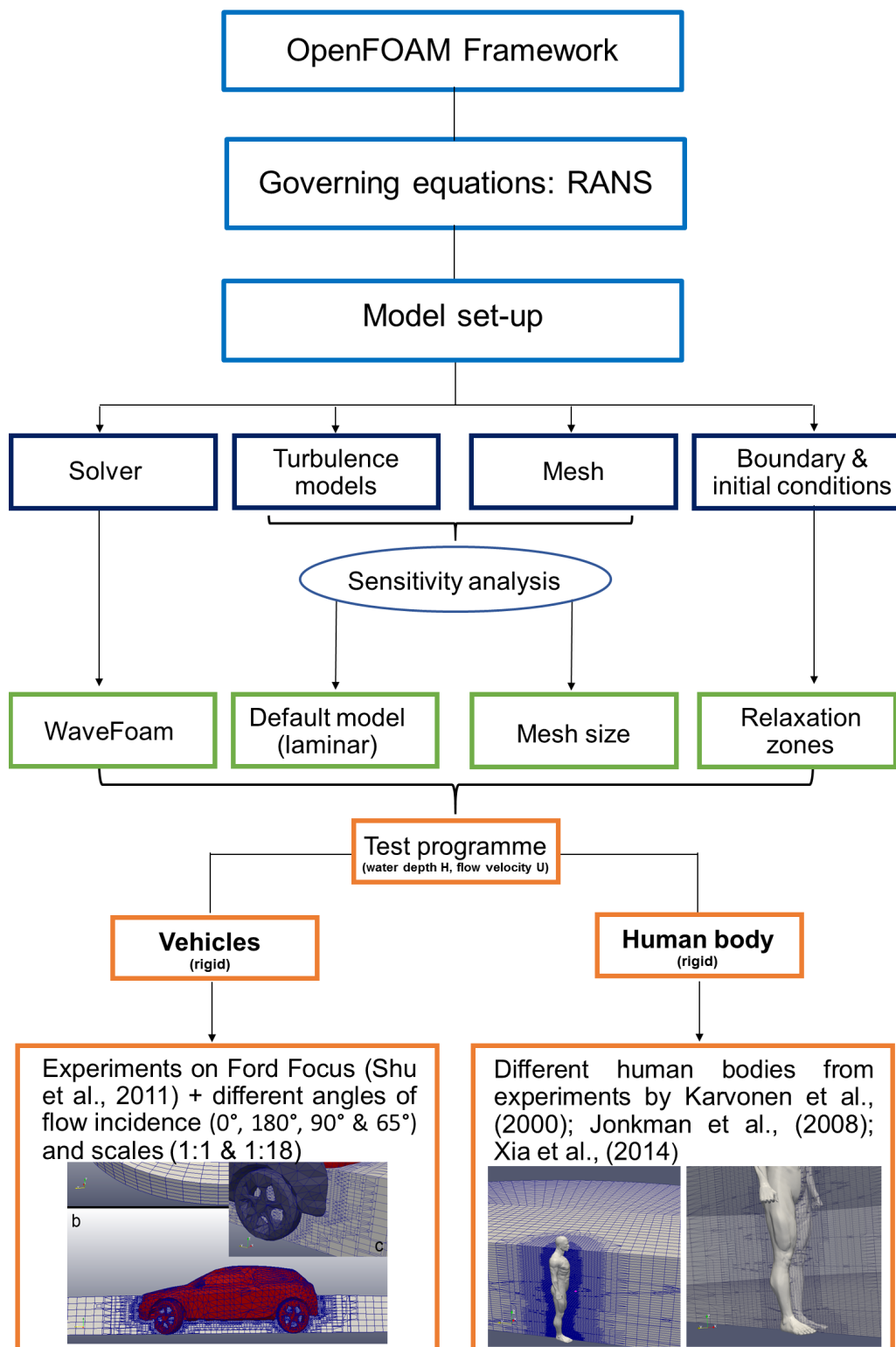


FIGURE 4.9: Graphical summary of the chapter

Chapter 5

Numerical results and data analysis

First, the conditions of incipient motion of a partly submerged Ford Focus car determined in previous laboratory experiments are analysed based on the hydrodynamic forces obtained from numerical simulations performed in this study (section 5.1). Second, the instability mechanism of pedestrians under water flow are analysed based on the numerical reproduction of laboratory experiments on different human subjects (section 5.2). In both cases, the focus of the analysis is put on the mean flow properties for which the data are available from previous studies and on the relationship between the dimensionless parameters governing the incipient motion and on possible scale effects, which are however not expected for the analysed range of Reynolds number.

5.1 Numerical results of the simulations of the Ford Focus car

5.1.1 Flow around the Ford Focus

After the simulations, it is possible to check qualitatively the results through the Paraview utility. ParaView is an open-source, multi-platform data analysis and visualization application embedded in OpenFOAM (www.paraview.org). The most intuitive control is conducted by visualizing the flow around the vehicle in the simulated flow conditions in terms of both water depth and flow velocity. Qualitatively, the presence of the car partially immersed in the water flow generates waves similar to those induced by a sailing ship. For supercritical conditions, the flow is undisturbed upstream. The water depth increases immediately before reaching the impacted side of the car and the velocity decreases close to and behind the tyres. Figure 5.1 shows the streamlines in the top-left panel, which highlights the complex interaction between the flow and the tyres. The bottom-left panel represents the pressures around the surface of the car. Particularly in the case where the impacted side is the front part of the vehicle, the highest pressures are located in the engine area. In the right panel of Figure 5.1, it is possible to see the waves generated by the obstacle and the decrease of the velocity behind the tyres. For subcritical flow conditions, the increase of the water depth in the impact zone is less marked. The flow velocity behind the tyres is still very low but in this case, the flow is also perturbed in the upstream area (Figure 5.2). Figure 5.3 shows the streamlines of the velocity field generated for 0.5 m water depth and 0.8 m/s velocity. The streamlines close to the tyres are particularly interesting where we see the vorticity due to the presence of the obstacle. As shown in Figure 5.1, the pressure on the surface of the vehicles is not uniformly distributed. This is due to the perturbation of the flow field by the car (Figure 5.3). This perturbation depends on the Froude number of the incident flow, thus the pressure field is expected to change according to Froude number. Figure 5.4 shows a 3D view of the pressure distribution on the car surface for sub-critical flow (top panel) and super-critical flow (bottom panel). The same colour scale is used for the two panels and the car geometry is represented as a semi-transparent surface in order to better visualize the pressures

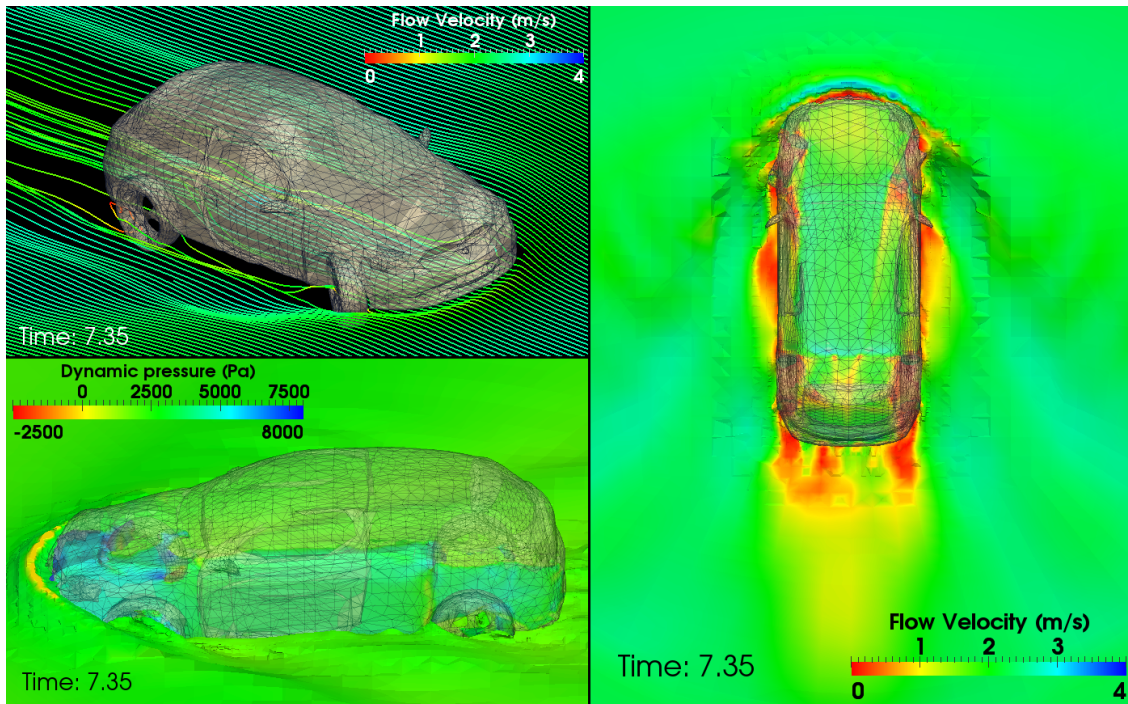


FIGURE 5.1: Streamlines, flow velocity and pressures around the car for super-critical flow conditions with 0.4 m water depth and 2.7 m/s velocity (angle of flow incidence $\beta = 0^\circ$).

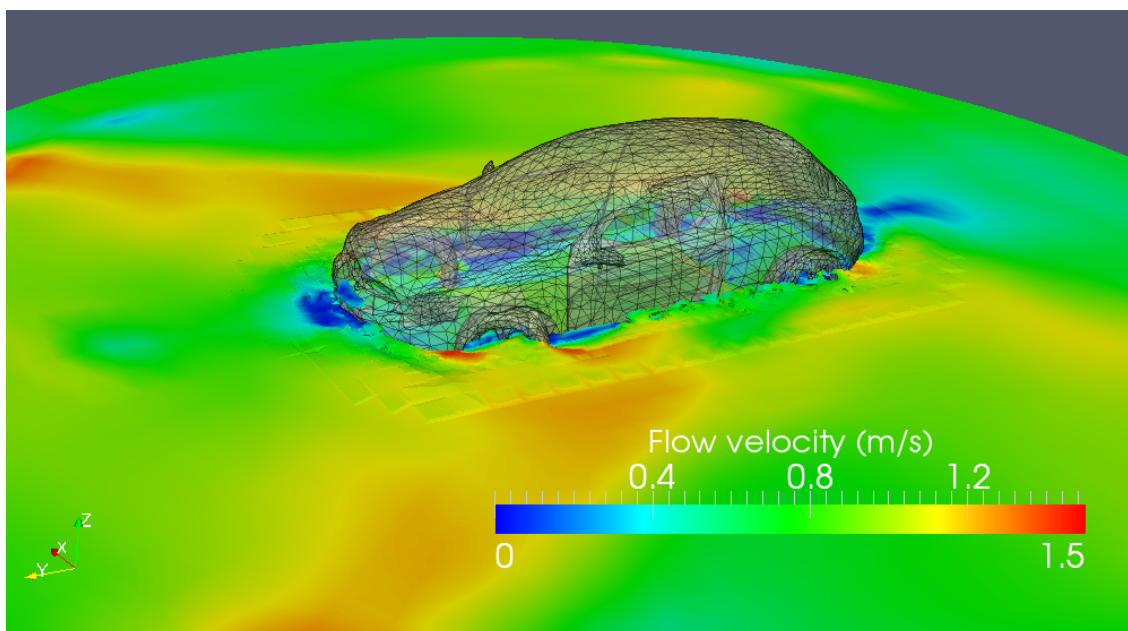


FIGURE 5.2: Flow around the Ford Focus for sub-critical flow conditions, 0.5 m water depth and 0.8 m/s velocity (angle of flow incidence $\beta = 0^\circ$).

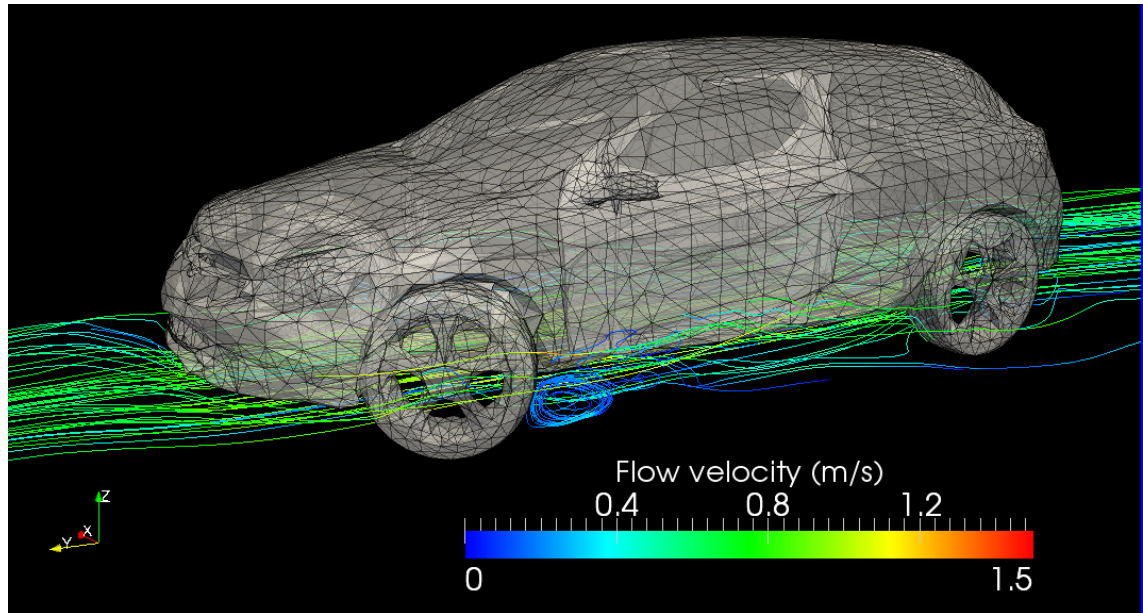


FIGURE 5.3: Streamlines for 0.5 m water depth and 0.8 m/s velocity, angle of flow incidence $\beta = 0^\circ$.

on the planform. The angle of flow incidence is 0° , i.e. the impact, is frontal, so the flow goes from left to right in the figure. For sub-critical flow conditions, the pressure distribution on the car planform is uniform, in fact, in the top panel the planform is represented with a uniform light blue colour. In super-critical flow conditions, the highest pressures represented with green to red shades are located in the impacted side of the car, which is the lower frontal area of the vehicle.

5.1.2 Forces and force coefficients for scale and prototype Ford Focus for angles of flow incidence $\beta = 0^\circ$ and $\beta = 180^\circ$

The hydrodynamic forces on the vehicle are computed at each time step by integrating the dynamic pressures on the vehicle surface. According to the settings in the controlDict file (section 4.3.5) the drag coefficient C_D and lift coefficient C_L are also calculated. The reference area for the calculation of drag coefficient (Eq. 4.7) is the total frontal area of the Ford Focus. It is set to be equal to $A_{Dn} = 2.21m^2$ and $A_{Dm} = 0.0068m^2$ for prototype and scale 1:18 respectively, after a graphical evaluation. The reference area for the calculation of lift coefficient (Eq. 4.8) is the planform area of the Ford Focus. It is set to be equal to $A_{Ln} = 7.81m^2$ and $A_{Lm} = 0.0241m^2$ for prototype and scale 1:18, respectively. For each simulation, the forces and the coefficients can oscillate according to the modification of the water surface and flow field during the simulation (e.g. waves), thus the time average is calculated for both drag and lift coefficients in order to have a representation of the mean flow effect. The drag and lift coefficients are plotted against Froude number and Reynolds number. Figure 5.5 shows the variation of the drag coefficient with Froude number for the numerical simulation of the Ford Focus scale model 1:18 and its prototype, for angles of flow incidence $\beta = 0^\circ$ and $\beta = 180^\circ$. Drag coefficient C_D varies from 0.1 up to 0.8 and decreases exponentially with the Froude number Fr . No substantial difference is found between the drag coefficients obtained for the two angles of flow incidence, i.e. for the impact on the front and on the rear part of the car (as in Shu et al., 2011). This is due to a quasi-symmetry of the car with respect to the axis perpendicular to the longitudinal one, in fact, the reference areas A_{Dn} , A_{Dm} for the angles

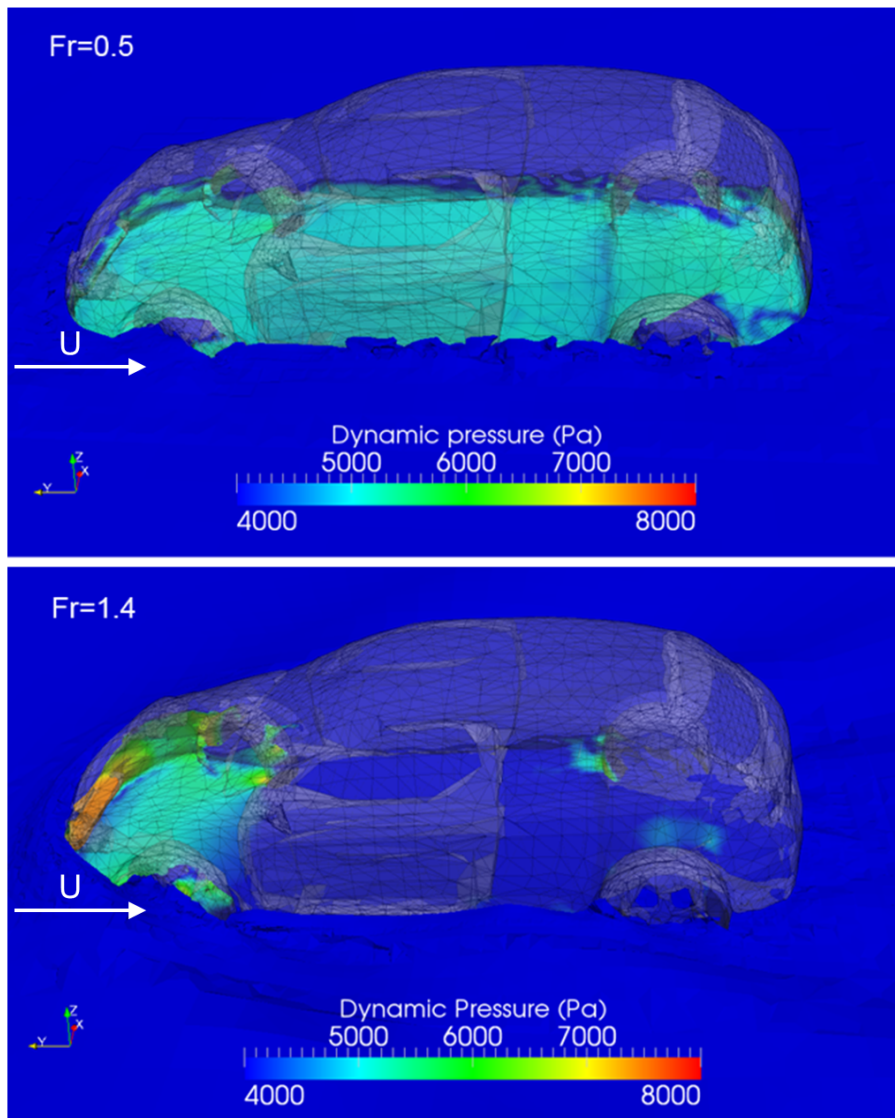


FIGURE 5.4: Pressure distribution on the Ford Focus surface for sub-critical (top) and super-critical (bottom) flow conditions (angle of flow incidence $\beta = 0^\circ$).

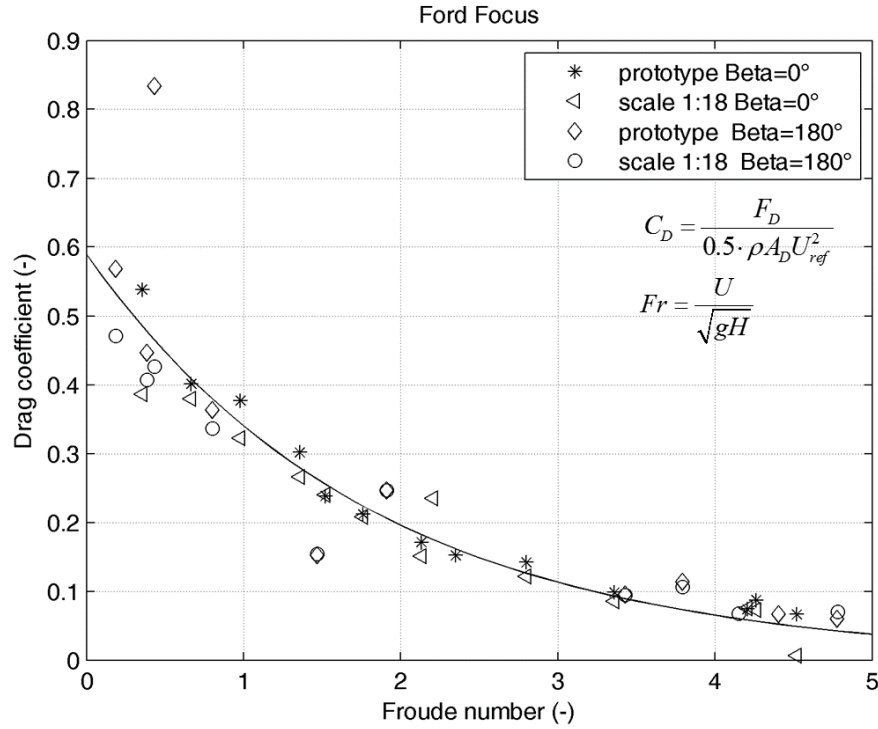


FIGURE 5.5: Drag coefficient versus Froude number for incipient motion conditions of a Ford Focus in scale 1:18 and prototype subject to incoming flow with angles of incidence $\beta = 0^\circ$ and $\beta = 180^\circ$.

of flow incidence $\beta = 0^\circ$ and $\beta = 180^\circ$ are the same. Moreover, despite the different Reynolds number (in the order of 10^6 for scale 1:18 simulations and 10^8 for prototype simulations), prototype and scale 1:18 car models have the same drag coefficients for the same Froude-scaled flow conditions. Thus, as expected, scale effects are negligibly small in terms of drag coefficient since both prototype and scaled pairs of water depth and velocity lie in a fully turbulent flow as shown by the very high Reynolds number (Hoerner, 1965). This confirms the substantial validity of Froude similarity for scaling drag force from scale models to prototype vehicles in fully turbulent conditions (Shu et al., 2011). Figure 5.6 shows the variation of the lift coefficient C_L with Froude number for the numerical simulation of the Ford Focus scale model 1:18 and its prototype for the angles of flow incidence equal to $\beta = 0^\circ$ and $\beta = 180^\circ$. Lift coefficient C_L varies from 0.009 (water depth lower than the chassis) up to 12 and decreases exponentially with the Froude number Fr . The logarithmic scale of the vertical axis in Figure 5.6 allows identifying two distinct zones separated at $Fr = 1$ (critical flow): the decrease of C_L with decreasing Fr is much more pronounced in the subcritical flow zone ($Fr < 1$) than in super-critical flow zone ($Fr > 1$). No substantial difference is found between the lift coefficients obtained by a flow impacting on the front ($\beta = 0^\circ$) and the rear part of the car ($\beta = 180^\circ$). Moreover, despite the different Reynolds number, prototype and scale 1:18 car models have the same lift coefficients for the same (Froude-scaled) flow conditions. This again confirms the validity of a Froude similarity. Drag coefficients cover one order of magnitude ($10^{-1} - 10^0$) for the simulated conditions ($Fr = 0.2 - 4.5$), while lift coefficients cover four orders of magnitude ($10^{-2} - 10^2$). Moreover, while the relationship between C_D and Fr remains the same for both sub-critical and super-critical flow regimes (Fig. 5.5), the relationship between C_L and Fr greatly differs in the two flow regimes (Fig. 5.6). The two different slopes of the regression curves in Fig. 5.6 for C_L reflect the different pressure distribution shown in Figure 5.4 for the two different flow regimes. In fact, since

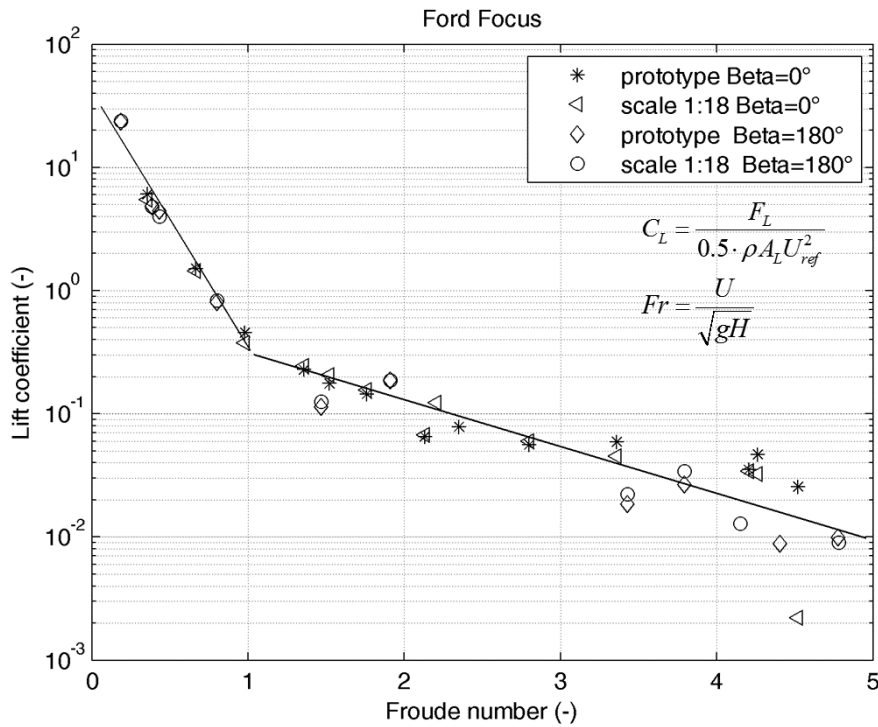


FIGURE 5.6: Lift coefficient versus Froude number for incipient motion conditions of a Ford Focus in scale 1:18 and prototype subject to incoming flow with angles of incidence $\beta = 0^\circ$ and $\beta = 180^\circ$.

for sub-critical flow the car-induced pressure affects a larger portion of the planform, the global dependency of the lift coefficient, which accounts for the vertical forces acting on the Ford Focus, is more relevant for sub-critical conditions. As Froude number decreases (i.e. water depth increases), lift coefficient increases faster for subcritical flow conditions than for supercritical flows. This behaviour is interpreted as a direct consequence of the different pressure distribution on the vehicle chassis shown in Figure 5.4. Figure 5.7 confirms a change in the physical mechanism leading to the onset of motion due to the flow regime. In the figure, Froude number decreases from left to right and the dashed red line indicates the critical flow condition. Both drag and lift coefficients (Figures 5.5, 5.6) increase with decreasing Froude number, thus they increase with increasing water depth and decreasing velocity. Since Froude number $Fr = U/(\sqrt{gH})$ is inverse proportional to the square root of the water depth H and proportional to the velocity U , this behaviour is not obvious. The fact that both force coefficients increase with decreasing Froude number can be explained if considering the relative submergence. In fact, the reference area for calculating the force coefficients is constant for all the simulations, but when the velocity increases the water depth decreases. As a consequence, in partly submerged conditions, the area affected by the flow (and by the drag force) for higher Froude numbers decreases, with a limited pushing efficiency.

The change in the motion mechanism due to the flow regime can be explained looking at the hydrodynamic forces in dimensional terms. Figure 5.8 shows the drag and lift force against Froude number for prototype (top panel) and scale 1:18 Ford Focus (bottom panel). Lift force decreases exponentially with increasing Froude number, while drag force first increases then decreases with increasing Froude number and has a maximum around $Fr = 3$. Forces are scaled according to Froude similarity, thus leading to 18^3 times larger forces in prototype than those at scale 1:18. Since the incipient motion for

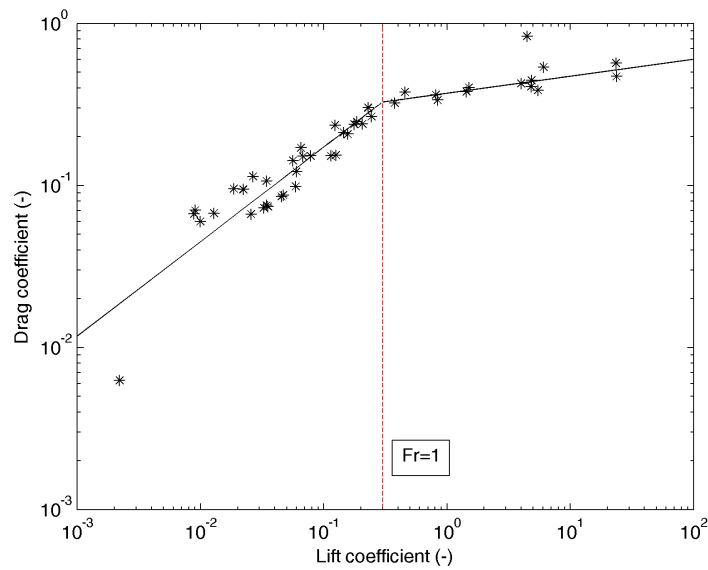


FIGURE 5.7: Drag coefficient against lift coefficient for scale 1:18 and prototype ($\beta = 0^\circ$ and $\beta = 180^\circ$).

TABLE 5.1: Drag and lift coefficients for Ford Focus at prototype scale (1:1) and at scale 1:18 for angle of flow incidence $\beta = 0^\circ$

Water depth H 1:1(m)	Velocity U 1:1 (m/s)	Drag coeff. C_D (-)	Lift coeff. C_L (-)	Water depth H 1:18(m)	Velocity U 1:18 (m/s)	Drag coeff. C_D (-)	Lift coeff. C_L (-)
0.171	5.855	0.067	0.026	0.010	1.380	0.006	0.002
0.198	5.940	0.087	0.047	0.011	1.400	0.073	0.033
0.209	6.020	0.074	0.035	0.012	1.419	0.075	0.034
0.234	5.091	0.098	0.059	0.013	1.200	0.086	0.045
0.299	4.794	0.142	0.056	0.017	1.130	0.122	0.060
0.306	4.073	0.152	0.078	0.017	0.900	0.235	0.123
0.326	3.810	0.171	0.065	0.018	0.898	0.151	0.068
0.360	3.309	0.212	0.144	0.020	0.780	0.208	0.156
0.378	2.927	0.238	0.176	0.021	0.690	0.240	0.205
0.408	2.715	0.302	0.228	0.023	0.640	0.266	0.244
0.459	2.078	0.377	0.455	0.026	0.490	0.322	0.375
0.477	1.442	0.401	1.506	0.027	0.340	0.380	1.436
0.529	0.806	0.538	6.058	0.029	0.190	0.386	5.464

sliding occurs when the drag force equals the friction force (see chapter 3), the lift force is multiplied by the friction coefficient μ , which is about 0.2-0.4 according to Bonham and Hatterseley, 1967, Gordon and Stone, 1973; Cox and Ball, 2001. Since the drag force is much smaller than the lift force for sub-critical flow conditions, the right term of Eq. 3.1 is small. As a consequence, a smaller drag force is sufficient to induce the onset of motion. Therefore, for sub-critical flow conditions, the onset of motion is induced by a reduced resistance of the car to the flow, due to higher lift forces. On the other hand, for super-critical flow conditions the left term of Eq. 3.1 is more relevant. In fact, as shown in Figure 5.8, the magnitudes of drag and lift forces are in the same range for larger Froude number Fr . Therefore, for super-critical flow conditions the onset of motion is induced by higher drag forces. Tables 5.1, 5.2 show the computed drag and lift coefficients for the Ford Focus car at prototype scale and 1:18 scale for $\beta = 0^\circ$ and $\beta = 180^\circ$ respectively.

A common practice is to analyse the force coefficients as a function of Reynolds number, since the study of drag and lift is usually carried out in aerodynamics (e.g. design of vehicles shape to reduce the resistance to flow) for objects fully immersed in air flow.

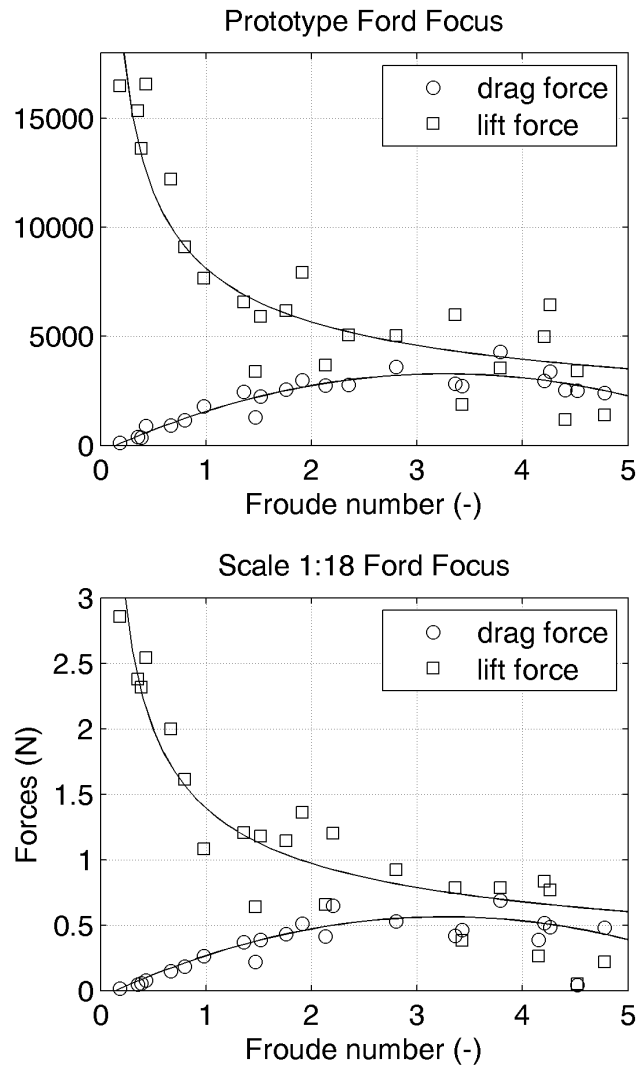


FIGURE 5.8: Drag and lift forces for prototype (top panel) and scale 1:18 Ford Focus (bottom panel).

TABLE 5.2: Drag and lift coefficients for Ford Focus at prototype scale (1:1) and at scale 1:18 for angle of flow incidence $\beta = 180^\circ$

Water depth H 1:1(m)	Velocity U 1:1 (m/s)	Drag coeff. C_D (-)	Lift coeff. C_L (-)	Water depth H 1:18(m)	Velocity U 1:18 (m/s)	Drag coeff. C_D (-)	Lift coeff. C_L (-)
0.162	6.020	0.060	0.010	0.009	1.420	0.070	0.009
0.180	5.855	0.067	0.009	0.010	1.300	0.067	0.013
0.225	5.091	0.095	0.019	0.013	1.200	0.095	0.022
0.243	5.855	0.114	0.027	0.014	1.380	0.107	0.034
0.306	3.309	0.247	0.186	0.017	0.780	0.247	0.186
0.360	2.758	0.152	0.114	0.020	0.650	0.154	0.125
0.459	1.697	0.363	0.809	0.026	0.400	0.337	0.836
0.491	0.849	0.446	4.847	0.027	0.200	0.407	4.802
0.522	0.976	0.834	4.457	0.029	0.230	0.426	3.986

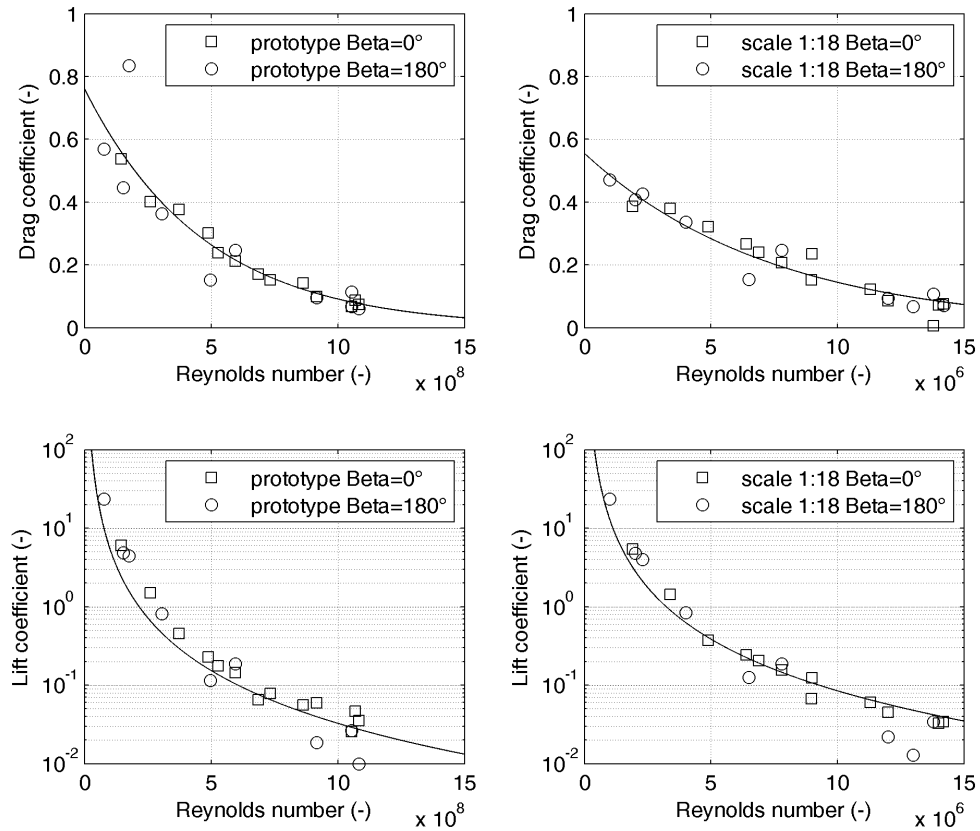


FIGURE 5.9: Drag coefficient versus Reynolds number for prototype and 1:18 scaled Ford Focus (top left and top right panels) and lift coefficient versus Reynolds number for prototype and 1:18 scaled Ford Focus (bottom left and bottom right panels).

In fact, Reynolds number governs some physical mechanisms such as flow separation and turbulent wakes, which affect the resistance of a body to flow. Reynolds number Re represents the ratio between inertial and viscous forces and is defined as

$$Re = \frac{U \cdot l}{\nu} \quad (5.1)$$

where U (m/s) is the characteristic velocity here assumed equal to the mean flow velocity, l (m) is the characteristic length scale assumed equal to the width of the vehicle and ν (m^2/s) is the kinematic viscosity of the fluid. Figure 5.9 shows the variation of force coefficients with Reynolds number. The two top subplots show the drag coefficient versus Reynolds number for the prototype and 1:18 scaled Ford Focus in left and right panels, respectively for flow incidence angles $\beta = 0^\circ$ and $\beta = 180^\circ$. The drag coefficient decreases exponentially with Reynolds number. For the simulations with the prototype car, Reynolds number is of the order of magnitude of 10^8 while for the scale 1:18 cars the order of magnitude is 10^6 . The two bottom subplots show the lift coefficient versus Reynolds number Re for prototype and scale Ford Focus in left and right panels, respectively for $\beta = 0^\circ$ and $\beta = 180^\circ$. Like the drag coefficient, the lift coefficient also decreases exponentially with Reynolds number Re , but at a higher rate.

In order to evaluate the relative importance of the effect of Froude number Fr and

TABLE 5.3: Partial correlation of x over y , given z .

partial correlation (x,y,z)	$x=C_D$ $y=Fr$ $z=Re$	$x=C_D$ $y=Re$ $z=Fr$	$x=C_L$ $y=Fr$ $z=Re$	$x=C_L$ $y=Re$ $z=Fr$
	-0.607	-0.003	-0.68	0.2

Reynolds number Re on both drag and lift coefficients C_D and C_L , the partial correlation of C_D and C_L with respect to Fr and Re is performed. In probability theory and statistics, partial correlation measures the degree of association between two random variables, with the effect of a set of controlling random variables removed. The partial correlation between X and Y given a set of n control variables $Z = \{Z_1, Z_2, \dots, Z_n\}$, written $\rho(XY\Delta Z)$, is the correlation between the residuals RX and RY resulting from the linear regression of X with Z and of Y with Z , respectively (Kendall & Stuart, 1973). If once the dependence on Z is removed, the correlation between X and Y is high the importance of Y and Z are comparable. Vice versa if once the dependence on Z is removed, the correlation between X and Y is low the importance of Z is higher than Y . The results in Table 5.3 show that the main control variable for both drag coefficient C_D and lift coefficient C_L is Froude number, since the correlation coefficient between C_D and C_L and Froude number once the dependency on Reynolds number is removed, is very high. The contribution of Reynolds number is small for C_L and negligible for C_D . This confirms again the validity of a simple Froude similarity in order to scale the incipient motion conditions found in flume experiments to full scale (i.e. prototype).

5.1.3 Comparison of numerical results with experiments

In order to verify the non-dimensional groups found in analyzing the experimental data on the incipient motion, the force coefficients estimated numerically are substituted in the dimensionless variable C , which has been introduced in Chapter 3 (Eq. 3.9). The variable C groups lift coefficient, drag coefficient and friction coefficient, the latter assumed constant and equal to 0.3. Since the mobility parameter θ_V evaluated from the experiments (Xia et al., 2011; Shu et al., 2011) is equal to the product of the square of Froude number Fr_v^2 and C (Eq. 3.7), which is evaluated from the numerical simulations, the validation of the results of the numerical model is performed by comparing these two quantities in a scatter plot (Figure 5.10). Figure 5.10 shows the comparison between the non-dimensional mobility parameter for incipient motion of the Ford Focus derived from the experimental data by Shu et al. (2011) and the forces coefficients estimated with the 3D numerical model. Friction coefficient μ is assumed as constant and equal to 0.3. The numerical results agree relatively well with the experimental data, in fact the determination coefficient of the regression curve R^2 is 0.89 and the RMSE 7.35. Although globally there is a good accordance between experiments and numerical model, some points in the right hand side of the scatter plot show large deviations. These points correspond to higher values of mobility parameter and thus, higher Froude numbers. A water depth almost equal to the height of the car planform characterizes the experimental pairs of water depth and velocity, which correspond to these values of the mobility parameter. Moreover, the height of the planform h_c is an important parameter to be considered for the occurrence of the onset of motion. Since the Ford Focus is assumed as a rigid body in the numerical simulations, the height of the planform is assumed as constant for every simulated flow condition. However, real cars are not rigid bodies, since vertical displacements are allowed by the presence of the suspensions. The effect of the suspensions is analyzed in section 5.1.4.

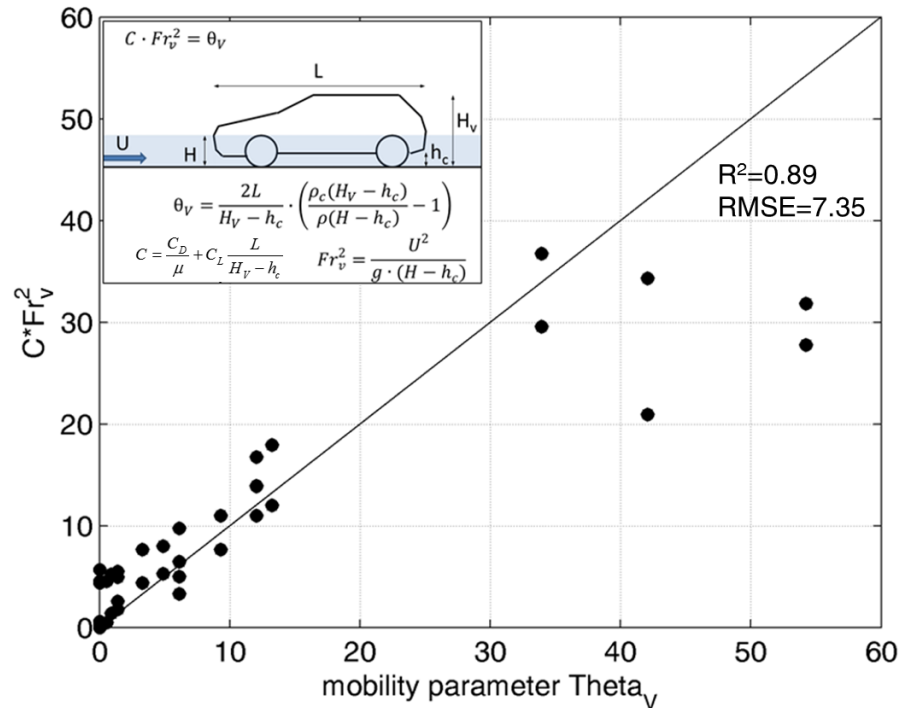


FIGURE 5.10: Comparison between numerical results and mobility parameter evaluated from the experiments of Shu et al. (2011) .

5.1.4 Discussion of the assumptions "rigid body and constant friction coefficient"

The results of the numerical simulations compared with the laboratory experiments highlight that the incipient motion conditions of a vehicle defined by the mobility parameter θ_v are very sensitive to the height of the chassis. In the numerical simulations, the 3D geometry of the car is rigid, so a strong assumption on the characteristics of the vehicle is introduced. Real vehicles and scale models instead are not rigid, so during a flood at full scale or in the hydraulic flume the car can move vertically due to the presence of the suspensions, which are an elastic device. The suspension travel refers to the distance that the axle can move up and down in relation to the frame before becoming fully extended or fully compressed. If the water moves up the chassis, this can significantly decrease the lift forces and buoyancy for low water depths. To verify this hypothesis, assuming that for a common car at full scale, the maximum wheel vertical travel is lower than 0.1 m, three simulations of the Ford Focus with the same hydraulic conditions but different heights of the chassis are carried out. To simulate the increased height of the chassis, the geometry is scaled only in the vertical (z) direction to reproduce a suspension travel of 0.02, 0.04 and 0.7 (Table 5.4). Since the x and y directions are not scaled and the car is partially submerged, the error on the modified geometry is very limited and only the height of the car appears stretched. Figure 5.11 compares the real geometry (yellow surface) with the stretched mesh obtained with a scaling along the z direction. The hydraulic conditions used to verify this hypothesis are 0.23 m water depth and 5.06 m/s velocity, which are critical because the water depth is in the same range as the height of the chassis. The results obtained are summed up in Table 5.4. The zero suspension travel is equivalent to the hypothesis of rigid body. As expected, if the car is lifted up by the water, the lift force strongly decreases while the drag force decreases at a lower rate.

Furthermore, the variation of the hydrodynamic forces due to the deformability of the

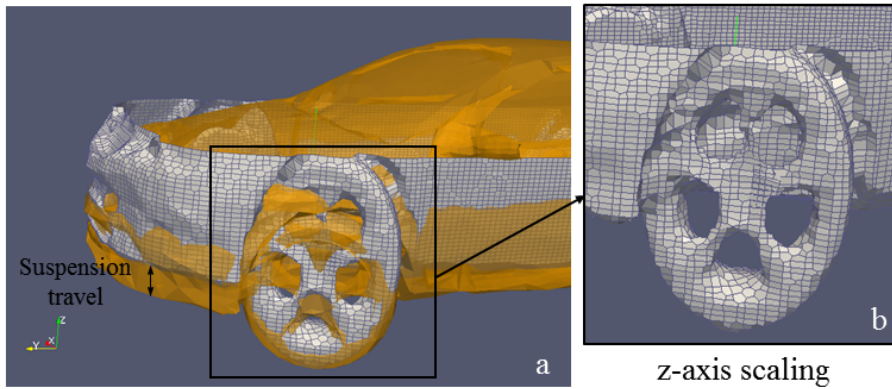


FIGURE 5.11: Vertical scaling of the Ford Focus to reproduce the suspension travel (a) and detail of the stretched tyre (b).

TABLE 5.4: Effect of the suspension travel on the forces exerted by water for 0.23 m water depth and 5.09 m/s velocity.

Suspension travel (m)	0 (rigid)	0.02	0.04	0.07
Weight (N)	13641	13641	13641	13641
Drag Force (N)	2840	2829	2819	2719
Lift force (N)	5984	4299	4218	2751
Buoyancy (N)	3379	2298	0	0
Friction coefficient (-)	0.66	0.40	0.30	0.25

tyres yields another important issue about the estimation of the friction coefficient. The experimental incipient motion conditions found by Shu et al. (2011) are again compared with the numerical results to understand the effect of the friction coefficient. The mobility parameter θ_V , evaluated from the flume experiments and the coefficient C estimated numerically multiplied by the square of Froude number (Eq. 3.7), are plotted against the square of Froude number for assigned values of friction coefficient from 0.01 to 0.6 (Figure 5.12). Figure 5.12 shows that the incipient motion conditions are highly sensitive to the assigned friction coefficient. Moreover, the hypothesis of constant friction coefficient is clearly not justified. When the Froude number increases, lower values of the friction coefficient are required to fit the flume experiments. These results suggest that a more detailed analysis of the friction coefficient is required. To better understand the role of the friction, the friction coefficient for incipient motion conditions is estimated for the numerical simulations reproducing the 1:18 Ford Focus experiments by Shu et al. 2011 and for the prototype simulations. The static friction coefficient is defined as the ratio between driving forces (i.e. drag force) and the resisting forces (e.g. friction force), as described in Eq. 3.1. For some of the simulated flow conditions (those with higher water levels), the friction coefficient appears to be negative, meaning that the effective weight is null. This should lead to incipient motion conditions due to floating and not to sliding, which is in contrast with the main assumption of the experiments by Shu et al. (2011). If only the physically meaningful friction coefficient (positive values only) are considered, it is found that the friction coefficient seems to decrease from 0.7 to 0.1 when Froude number increases. Equalling weight and buoyancy, the static limit for floating (i.e. for zero velocity), for the Ford Focus prototype model, is obtained for a water depth around 0.38 m. Considering the experimental data this means that for a Froude number smaller than 2.2, the car moves due to its null effective weight. Since most of the assessment of the static limit for floating is based on the height of the chassis, this particular result suggests

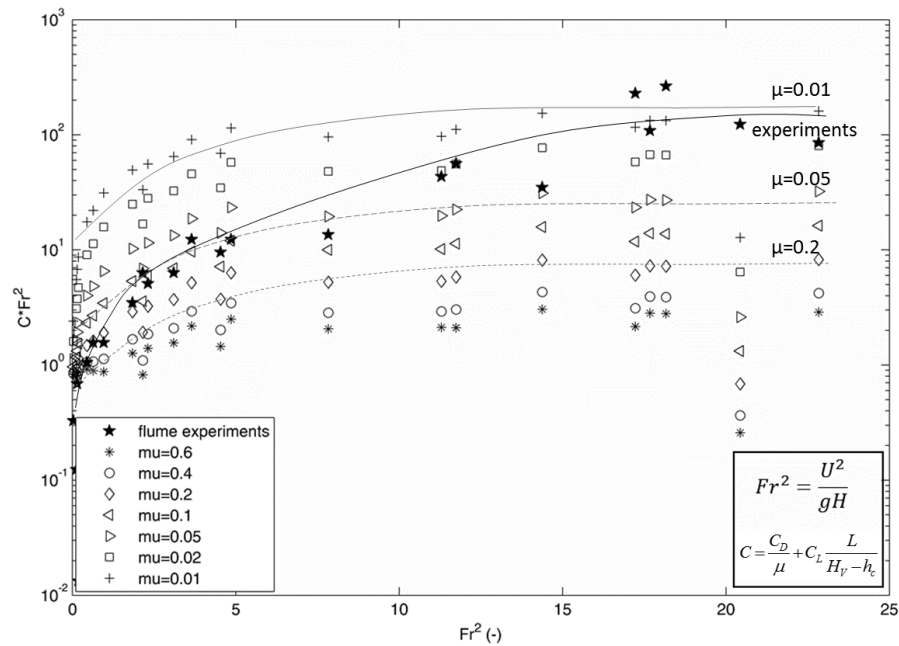


FIGURE 5.12: Vertical scaling of the Ford Focus to reproduce the suspension travel (a) and detail of the stretched tyre (b).

that a variation of the height of the chassis may alter significantly the friction coefficient as shown in Figure 5.13. The values in Figure 5.13 refer to the forces evaluated assigning different values of suspension travel for the same pair of water depth and velocity as in Table 5.4. In conclusion, the assumption of the rigid body introduces some uncertainties on the forces estimation and on the calculation of the friction coefficients. Both issues should require a separate and further investigation, which is not undertaken in this study. These limitations could be overcome by using a coupled CFD-CSD numerical model, which could constitute on its own a topic for a PhD, thus is left for a future research.

5.1.5 Effect of the angle of flow incidence

Numerical simulations have been carried out for a selection of pairs of water depth and velocity of the experimental dataset on the incipient motion of a Ford Focus (Shu et al., 2011) to investigate the effect of the angle of flow incidence only on the hydrodynamic forces. Thus, this set of simulations (see section 4.5.1) does not necessarily represent incipient motion conditions. The new set of numerical simulations accounts for two different angles of flow incidence $\beta = 90^\circ$ and $\beta = 65^\circ$ (see Figure 3.6). Since no significant scale effects have been found in the previous set of simulations, this new set of numerical simulations involves only the prototype geometry of the Ford Focus. The angles of flow incidence $\beta = 90^\circ$ and $\beta = 65^\circ$ change the flow pattern and the hydrodynamic forces on the vehicle as compared to $\beta = 0^\circ$ and $\beta = 180^\circ$ flow orientations. In fact, as the cars are designed to reduce the resistance to the air flow during the motion, the angles of flow incidence $\beta = 0^\circ$ and $\beta = 180^\circ$ are those meeting aerodynamic requirements. Thus, it is expected that for the same simulated pairs of water depth and velocity, the drag force will be higher for lateral impacts of the flow. Figure 5.14 shows flow velocity for the super-critical simulated pair $H=0.23$ m and $U=5.09$ m/s and $\beta = 90^\circ$. The flow is in x-direction and accelerates when passing under the vehicle chassis and suddenly decelerates at the end of the chassis causing a hydraulic jump, which is underlined by the colour scale as indicated in Figure 5.14. Moreover, the flow velocity tends to zero

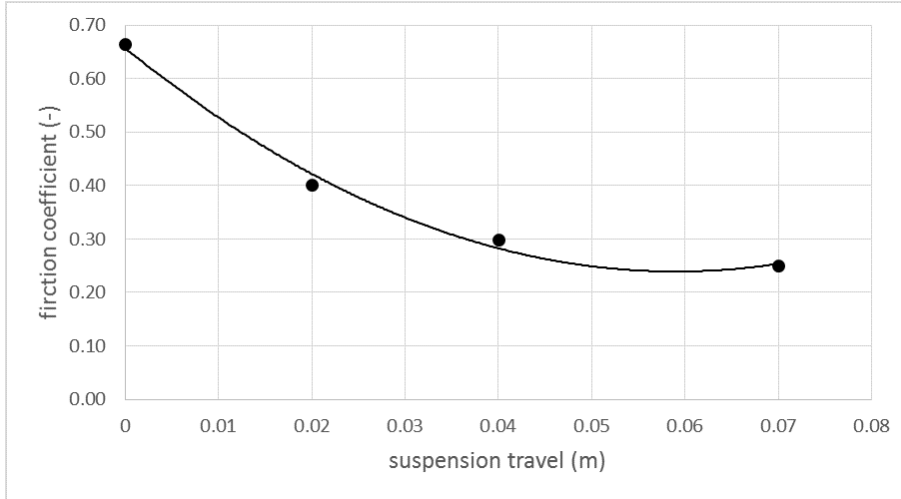


FIGURE 5.13: Friction coefficient versus suspension travel for water depth 0.23 m and velocity 5.06 m/s.

behind the right side tyres (right hand side of the figure). As for the $\beta = 0^\circ$ and $\beta = 180^\circ$ numerical simulations, the pressure distribution on the vehicle chassis changes according to Froude number. When the flow regime is subcritical the pressure is uniform on the vehicle planform. However, for supercritical flow as shown in Figure 5.15, the pressure suddenly increases in the impact area and then decreases afterwards. This flow behaviour has an important implication for the forces, which can be explained through Bernoulli's principle. Bernoulli's principle states that for an inviscid flow, an increase in the speed of the fluid occurs simultaneously with a decrease in pressure or a decrease in the fluid's potential energy. The principle can be derived as a direct consequence of the energy conservation

$$\frac{U^2}{2g} + z + \frac{p}{\rho g} = \text{constant} \quad (5.2)$$

Where U (m/s) is the flow velocity, g (m/s^2) is the acceleration of gravity, z (m) is the elevation above a reference plane, p (Pa) is the pressure and ρ (kg/m^3) is the density of the fluid. For the assumption of energy conservation, if two points A and B, which are respectively upstream the impact zone (undisturbed velocity) and below the car planform, are considered, Bernoulli's Principle yields

$$\frac{U_A^2}{2g} + z_A + \frac{p_A}{\rho g} = \frac{U_B^2}{2g} + z_B + \frac{p_B}{\rho g} \quad (5.3)$$

Where $\frac{U^2}{2g}$ is the dynamic pressure head and $z + \frac{p}{\rho g}$ is the hydraulic head. Since the left and right terms are equal, when U_B increases below the car planform the hydraulic head decreases and both z_B and p_B decrease. This lead to a suction effect (Bonham & Hattersley, 1967), which affects the lift force as shown in Figures 5.17 and 5.19.

5.1.6 Forces and forces coefficients for different angles of flow incidence

This section presents the effect of the angle of flow incidence on the forces and force coefficients calculated in the numerical simulations. The reference area for C_D , which has been evaluated graphically, is equal to $A_{90^\circ} = 4.32\text{m}^2$ and $A_{65^\circ} = 4.85\text{m}^2$ for $\beta = 90^\circ$ and $\beta = 65^\circ$, respectively. The reference area for C_L is the same planform area equal to 7.81m^2 , used in all the simulations. The largest reference area for C_D is $A_{\beta = 65^\circ}$ as

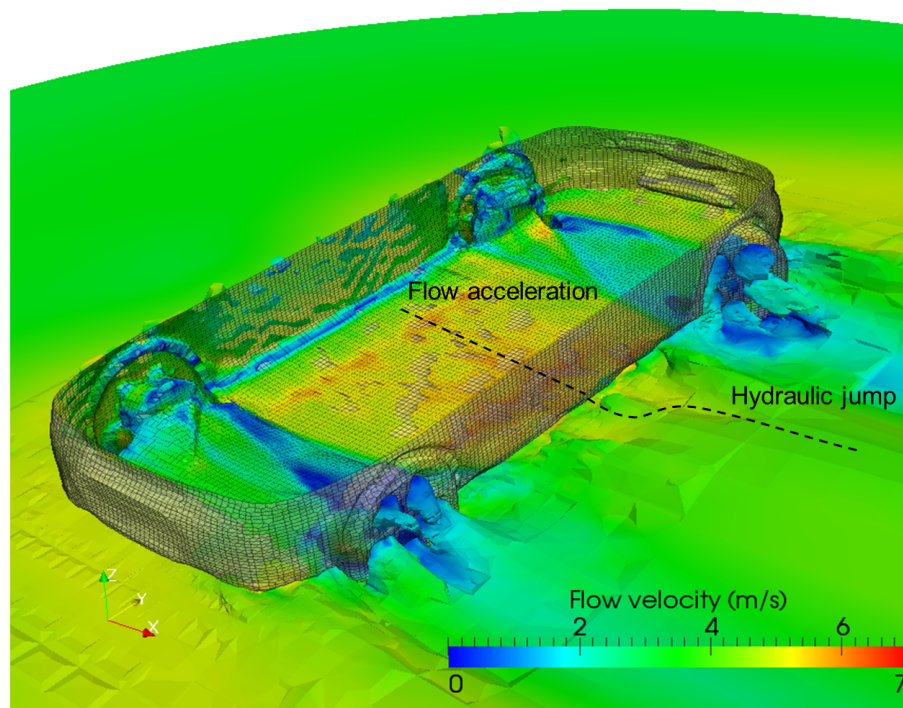


FIGURE 5.14: Flow velocity for a prototype Ford Focus with 0.23 m water depth and 5.09 m/s velocity, $\beta = 0^\circ$.

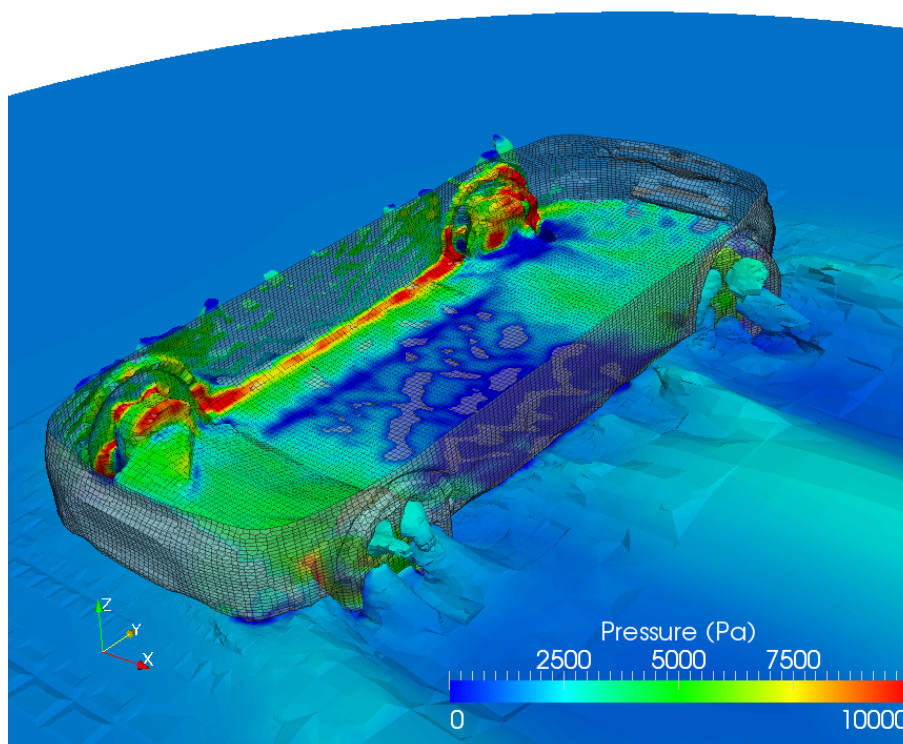


FIGURE 5.15: Pressure for a prototype Ford Focus with 0.23 m water depth and 5.09 m/s velocity $\beta = 90^\circ$.

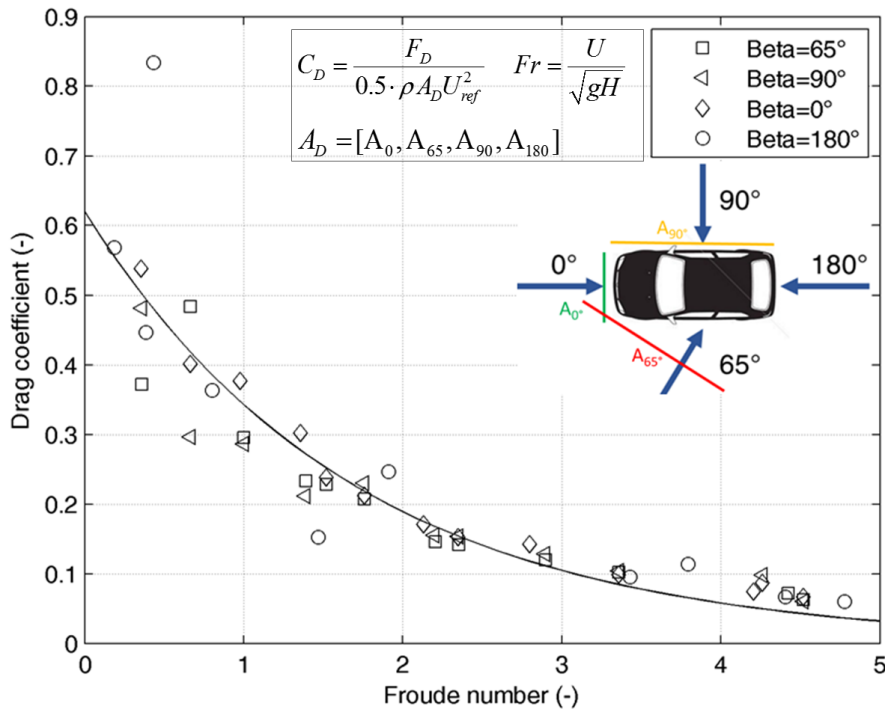


FIGURE 5.16: Comparison of drag coefficient for all the investigated angles of flow incidence.

depicted in the embedded sketch in Figure 5.16. Figure 5.16 shows the drag coefficients versus Froude number, evaluated for the four angles of flow incidence investigated in the numerical simulations, which are $\beta = 0^\circ$, $\beta = 65^\circ$, $\beta = 90^\circ$ and $\beta = 180^\circ$. The value of drag coefficient ranges from 0.06 (for high Froude number) to 0.8 (for low Froude number). The drag coefficient decreases exponentially with decreasing Froude number. For the different angles of flow incidence, the values of the drag coefficient are very similar for the same Froude numbers, i.e. for the same simulated pairs of water depth and velocity. This means that, since C_D is a dimensionless measure of the 'efficiency' of the drag force over a reference surface, the average force exerted on a unitary surface of the car for the same pairs of water depth and velocity is similar. However, the dimensional drag force will be different since the reference areas are different. Figure 5.17 shows the lift coefficient versus Froude number, calculated for different flow orientations. Unlike the drag coefficient, the lift coefficients for $\beta = 90^\circ$ and $\beta = 65^\circ$ (left panel) are very different from those for the $\beta = 0^\circ$ and $\beta = 180^\circ$ simulated cases (right panel). Lift coefficients for $\beta = 90^\circ$ and $\beta = 65^\circ$ are lower than lift coefficients evaluated for $\beta = 0^\circ$ and $\beta = 180^\circ$ for the same simulated pairs of water depth and velocity. In particular, lift coefficients are negative for Froude number in the range 1.6-4 for $\beta = 90^\circ$ and $\beta = 65^\circ$ (left panel in Figure 5.16). This means that the vertical force is directed downward for the mentioned flow conditions and thus it contributes to the global stability of the vehicle. This also confirms the suction effect due to the velocity pattern qualitatively described in section 5.1.5. This effect is more relevant for super-critical flows since the flow is undisturbed upstream and the flow acceleration occurs under the planform (Figure 5.14), while for a sub-critical regime the flow perturbation is less pronounced and thus no suction effect occurs. The representation of the dimensional forces on the vehicle underlines the large difference in terms of impact for the different flow orientations. Figure 5.18 shows that the drag force for $\beta = 0^\circ$ and $\beta = 180^\circ$ is smaller than the drag force for $\beta = 90^\circ$ and $\beta = 65^\circ$. While for sub-critical flow conditions the drag forces are in the same range for

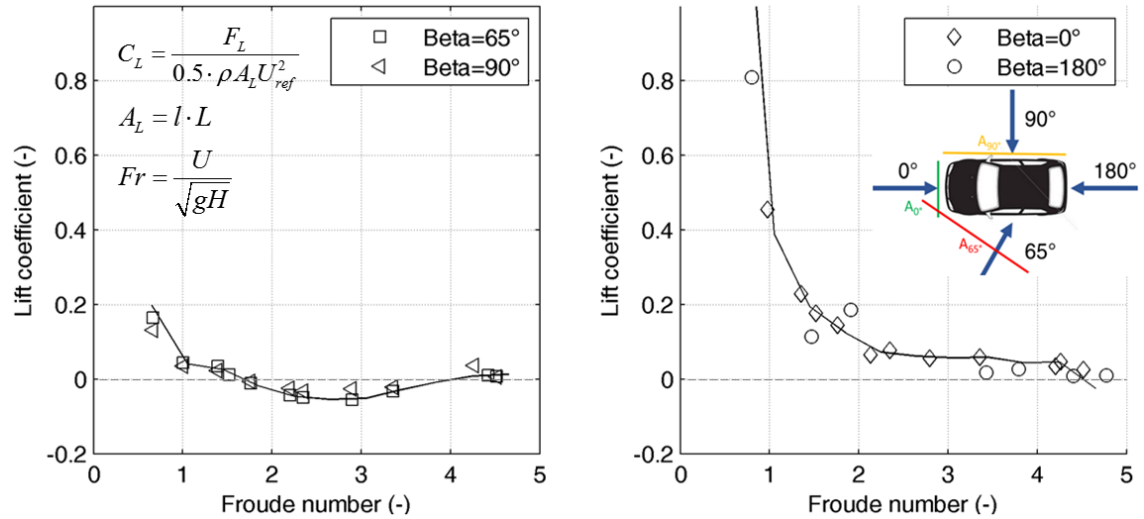


FIGURE 5.17: Comparison of the lift coefficients for all the investigated angles of flow incidence, $\beta = 90^\circ$, $\beta = 65^\circ$ and $\beta = 0^\circ$, $\beta = 180^\circ$ in the left and right panel respectively.

all the flow orientations considered, for super-critical flows the drag force for $\beta = 90^\circ$ and $\beta = 65^\circ$ reaches twice the value for the same simulated conditions (H,U) and flow orientation $\beta = 0^\circ$ and $\beta = 180^\circ$. This means that a lateral flow impact can be more critical for the onset of vehicle motion.

Figure 5.20 shows the ratio between the horizontal forces acting on the vehicle (i.e. drag and friction) versus Froude number. Since the incipient motion for sliding occurs when the drag force exceeds the friction force the ratio in Eq. 5.4 is often used as safety coefficient, in fact $R > 1$ means stability and $R < 1$ means instability

$$R = \frac{(W - Li) \cdot \mu}{D} \quad (5.4)$$

The friction coefficient μ is assumed equal to 0.3. As shown by the continuous and dashed lines in Figure 5.20, R is lower for $\beta = 65^\circ$ than for $\beta = 0^\circ$. Thus for the same simulated Froude number Fr a lateral flow impact is more critical for the onset of motion. This also means that the incipient motion conditions for $\beta = 65^\circ$ will occur for lower water depth (or lower velocity) compared to $\beta = 0^\circ$ as demonstrated by Xia et al. (2013).

5.1.7 Summary of the numerical results of the Ford Focus

In order to better understand the effect of the hydrodynamic forces on the incipient motion of a parked vehicle, a Ford Focus scaled 1:18 for flume experiments (Shu et al., 2011), is considered for a numerical parametric study. A set of numerical simulations reproducing the experimental incipient motion conditions observed in the hydraulic flume are carried out for two angles of flow incidence, $\beta = 0^\circ$ and $\beta = 180^\circ$. Then, using a Froude similarity, the experimental conditions derived for the 1:18 Ford Focus model are scaled up to prototype and simulated in order to identify possible scale effects. The results of the first set of numerical simulations show that:

- No significant scale effect exist for forces coefficients

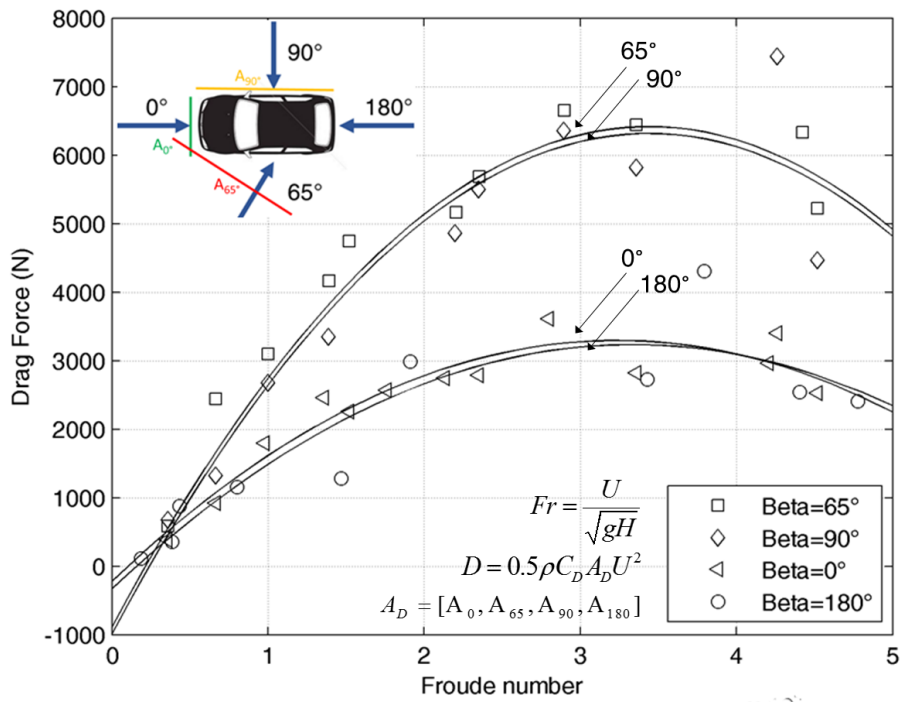


FIGURE 5.18: Drag force versus Froude number for the analysed flow orientations

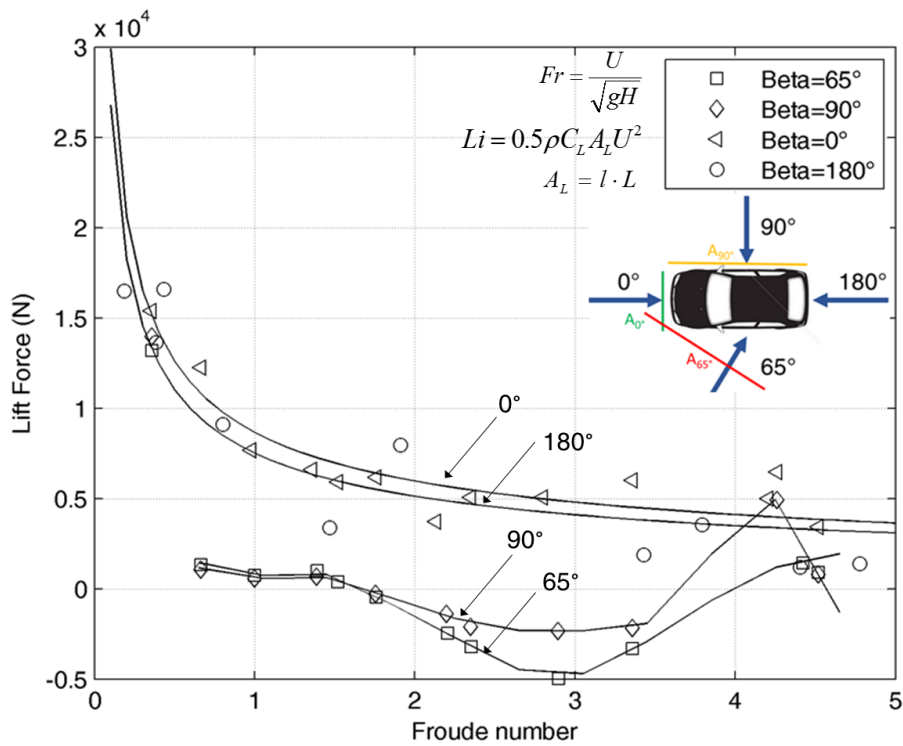


FIGURE 5.19: Lift force versus Froude number for the analysed flow orientations

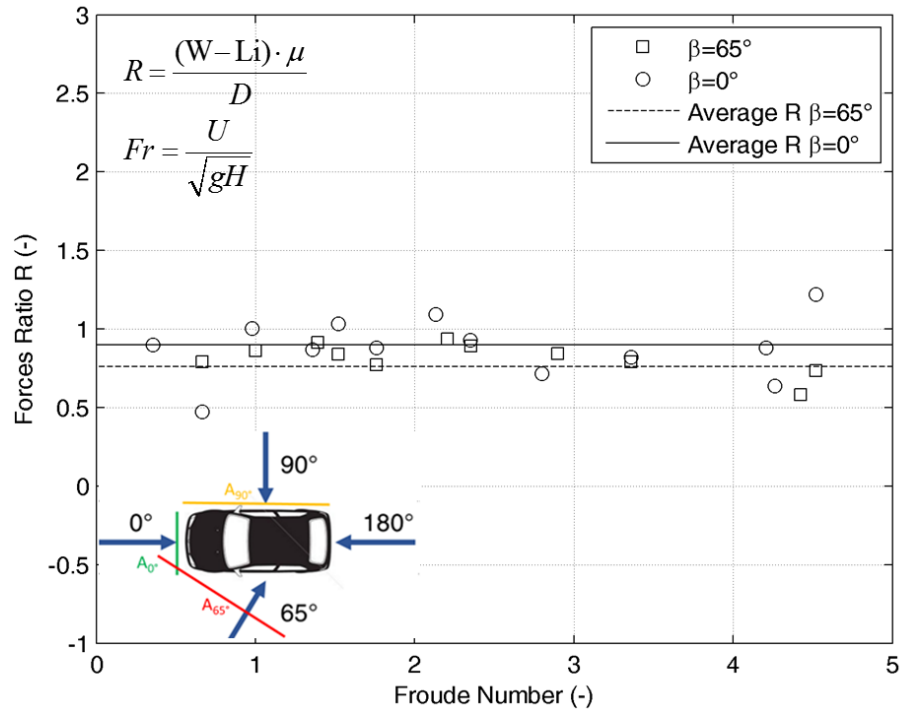


FIGURE 5.20: Ratio between resisting and drag forces for $\beta = 65^\circ$ and $\beta = 0^\circ$, values of the ratio R above 1 represent stable conditions

- Froude similarity is valid for scaling the dimensional forces on the vehicle, so the results of the 1:18 scaled model tests in the laboratory can be transferred to prototype scale
- No significant difference is found in terms of force and force coefficients for flow incidence angles $\beta = 0^\circ$ and $\beta = 180^\circ$
- Two incipient motion mechanisms are identified for sub-critical and super-critical flow regimes, where respectively the lift force and the drag force dominate
- As also confirmed by the results of a partial correlation analysis, Froude number is the most relevant parameter governing the conditions for the onset of motion
- The numerical results show a relatively good agreement with the experimental results in terms of mobility parameter θ_V
- Constant friction and rigid body represent both strong but necessary assumptions for the numerical model, thus requiring further research.

Another set of numerical simulations considers the effect of the angle of flow incidence by accounting for two lateral impacts $\beta = 90^\circ$ and $\beta = 65^\circ$. These conditions have not been tested experimentally as incipient motion conditions, so that they only aim at a better understanding of the effect of flow direction on a parked car. The results of this set of numerical simulations show that:

- The flow direction significantly alters the flow pattern and a suction effect may occur for some super-critical flow conditions
- Drag and lift coefficients do not change with flow direction for the same Froude number Fr

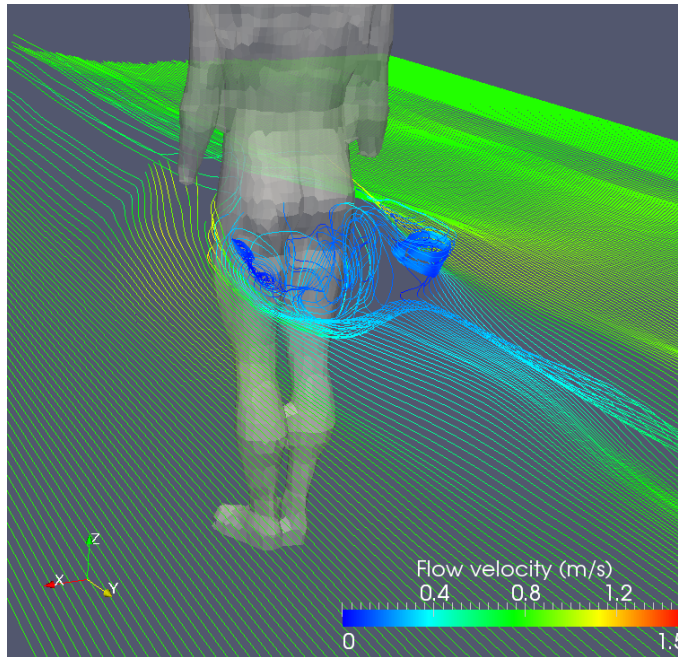


FIGURE 5.21: Streamlines around human body for subject 4 considered by Karvonen et al. (2000) at 0.87 m elevation for $H=1.0$ m and $U=0.8$ m/s

- Drag and lift forces change significantly with flow direction, in particular the drag force for $\beta = 90^\circ$ and $\beta = 65^\circ$ is larger than for $\beta = 0^\circ$ and $\beta = 180^\circ$ while lift force is smaller or even negative
- The analysis of the global balance of forces shows that lateral flow directions (e.g. $\beta = 90^\circ$ and $\beta = 65^\circ$) are more critical for the onset of motion than frontal impact ($\beta = 0^\circ$) and rear impact ($\beta = 180^\circ$).

5.2 Numerical results of the simulations of pedestrians

5.2.1 Flow characteristics around an upright standing human body

The numerical simulations of people instability under water flow are carried out by considering the four human subjects tested by Karvonen et al., 2000, Jonkman & Penning-Rowsell, 2008 as well as the human model tested in a physical flume by Xia et al., 2014. A selection of water depths and velocities covering a wide range of Froude numbers are simulated. The flow impact considered is frontal as in the experiments by Karvonen et al., 2000 and Xia et al., 2014. For sub-critical flow conditions the flow is disturbed upstream the human body, where a slight deceleration occurs and vortices occur downstream (Figure 5.21). The latter shows the streamlines at vertical elevation 0.87 m for the human subject 4 tested by Karvonen et al. (2000) (see Table 4.9) for water depth $H=1.00$ m and flow velocity $U=0.8$ m/s. The flow velocity decreases significantly behind the body where a vortex is generated as a consequence of the flow separation around the body. For the same simulated pair of water depth and velocity (H,U) and lower elevation 0.62 m (Figure 5.22), the velocity increases when the streamlines surround the knees, then decreases again behind the obstacle without any vortex.

For super-critical flows, a significant splash is generated in the impact zone (Figure 5.23, panels a, c). Figure 5.23 depicts the simulation on the subject tested by Jonkman & Penning-Rowsell (2008) (see Table 4.11) for $H=0.35$ m and $U=2.40$ m/s. For this flow

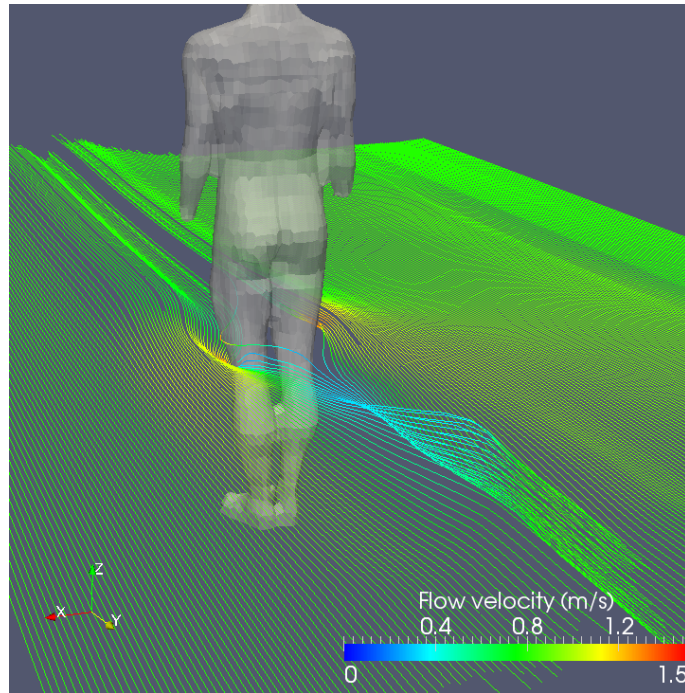


FIGURE 5.22: Streamlines around human body for subject 4 considered by Karvonen et al. (2000) at 0.62 m elevation for $H=1.0$ m and $U=0.8$ m/s.

TABLE 5.5: Reference frontal areas A_{ref} , height and weight of the human subjects and human body model considered for force coefficient calculation.

Subject	N ^o 2 Karvonen et al., 2000	N ^o 4 Karvonen et al., 2000	N ^o 5 Karvonen et al., 2000	Jonkman and Penning-Rowcell, 2000	Model scale 1:5.54 Xia et al., 2014
A_{ref} (m ²)	0.49	0.42	0.46	0.43	0.014 (0.43 prototype)
Height H_P (m)	1.95	1.62	1.82	1.7	0.31 (1.71 prototype)
Weight (kg)	100	57	94	68.2	0.334 (57 prototype)
d (m)	0.28	0.24	0.27	0.27	0.043 (0.24 prototype)

condition the free surface decreases downstream after passing the ankles where the flow accelerates, then a sudden energy dissipation occurs (behind the ankles, panel b) and the free surface is restored (panel c).

5.2.2 Forces and force coefficients

Drag and lift forces are integrated over the human body surface during the simulations and the force coefficients are calculated using the frontal reference areas A_{ref} in Table 5.5, which are evaluated graphically. Force coefficients are the time average of the instantaneous force coefficients once steady conditions are established. The reference area for lift coefficient calculation coincides with the reference area for drag coefficient calculation as in Milanese et al., 2015 (see also 3.2.1).

Figure 5.24 shows the drag coefficient and lift coefficient versus Froude number in the top and bottom panels, respectively. Drag coefficient ranges from 0.1 for high Froude numbers, up to approximately 1 for low Froude numbers. Drag coefficients decrease exponentially with increasing Froude number, i.e. with decreasing submergence. The drag coefficients of all the human subjects (Karvonen et al., 2000; Jonkman & Penning-Rowcell, 2008) are very similar for the same simulated flow regimes. Drag coefficients for the human scale model (Xia et al., 2014) in the range of Froude number 0.4-1.5 are

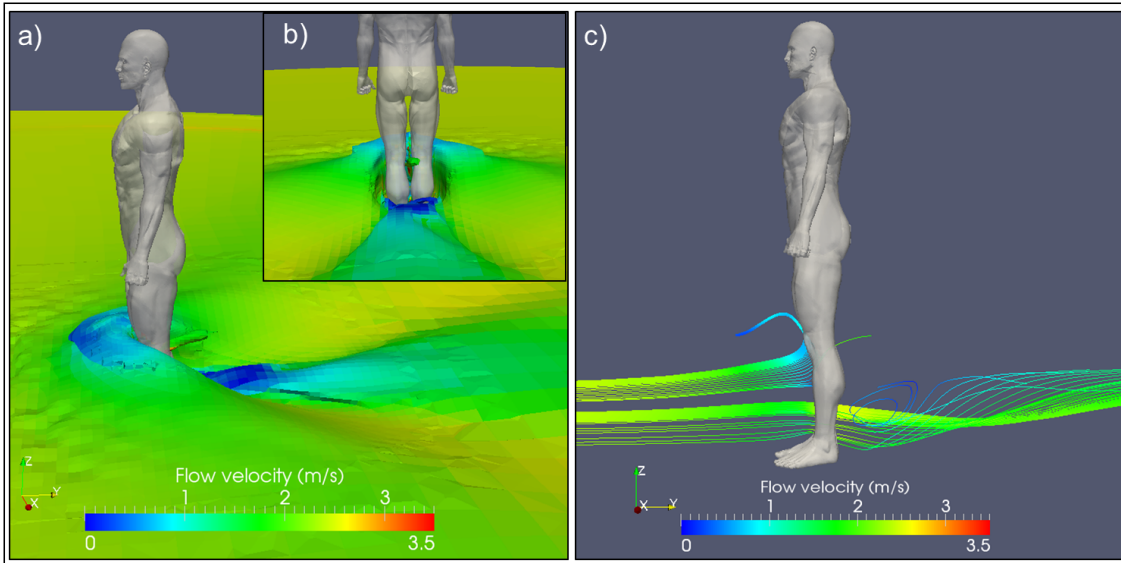


FIGURE 5.23: Splashing effect for super-critical flows shown as flow velocity (a), streamlines (c) and inset view parallel to flow direction upstream-oriented (b), for the subject considered by Jonkman & Penning-RowSELL (2008), $H=0.35$ m, $U=2.40$ m/s.

lower than the coefficients evaluated for the human subjects. In fact the human model is ‘weaker’ than the real human subjects in facing the water flow, as demonstrated by the comparison between dimensional threshold of instability for the model and real human subjects (Xia et al., 2014). For Froude numbers above 1.5, the drag coefficient for the human model remains almost constant. Lift coefficients range from -0.49 up to 0.06. Except for subject 4, which is represented with a diamond symbol in the bottom panel of Figure 5.24, the lift coefficients are negative. This means that the lift force contributes to stability because is directed downward. The two positive value for subject 4 (Karvonen et al., 2000) are due to the relative submergence of the subject H/H_P , which is higher than 0.6 (see Figure 5.25, bottom panel). For this level of submergence, the water reaches the lower part of the body trunk and thus can exert its action pushing it upward. The negative lift coefficients are the result of the downward directed force acting on the feet. Figure 5.25 depicts drag and lift coefficients versus relative submergence H/H_P , in the top and bottom panels respectively. Drag coefficient increases quadratically as the relative submergence H/H_P increases since a larger portion of body surface is affected by the water flow, thus increasing the lever arm of the destabilizing moment. Lift coefficient linearly decreases with increasing relative submergence since a larger water depth results in a larger hydraulic head, and thus in a higher pressure. In fact, the only surface, which is affected by a vertical force is that of the feet, while legs only contribute to horizontal (i.e. drag) forces. Once a threshold level of relative submergence is reached (i.e. around 0.55), the water also surrounds the body trunk, which contributes to the pressure integration.

Figure 5.26 depicts the drag force versus Froude number for all the simulated subjects and the human body model. For human subjects, which have been tested in the range of Froude numbers Fr 0.2-2, drag force increases for $0.2 < Fr < 1$, reaching a peak for Fr 1, then it decreases. The values of drag force for human subjects range from 100 N up to 350 N. Subject 2 tested by Karvonen et al., (2000), which is the tallest and heaviest subject of the dataset, is able to face the highest forces with respect to the other subjects. Subjects 4 and 5 are weaker according to the diagram, subject 4 is a woman and subject 5 is a 60 years old man. The estimated forces for the human model (Xia et al., 2014) have been

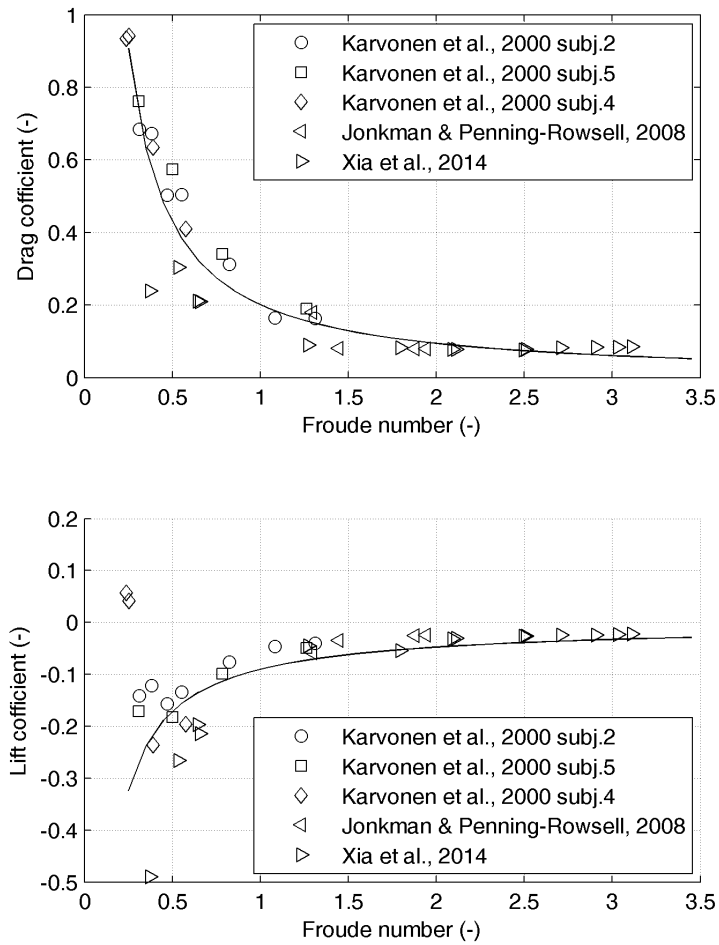


FIGURE 5.24: Drag (top panel) and lift (bottom panel) coefficients versus Froude number for the four human subjects considered in (Karvonen et al., 2000; Jonkman & Penning-Rowse, 2008) and the human body model considered in (Xia et al., 2014). Reference area A_{ref} for both force coefficients shown in Tab. 5.5

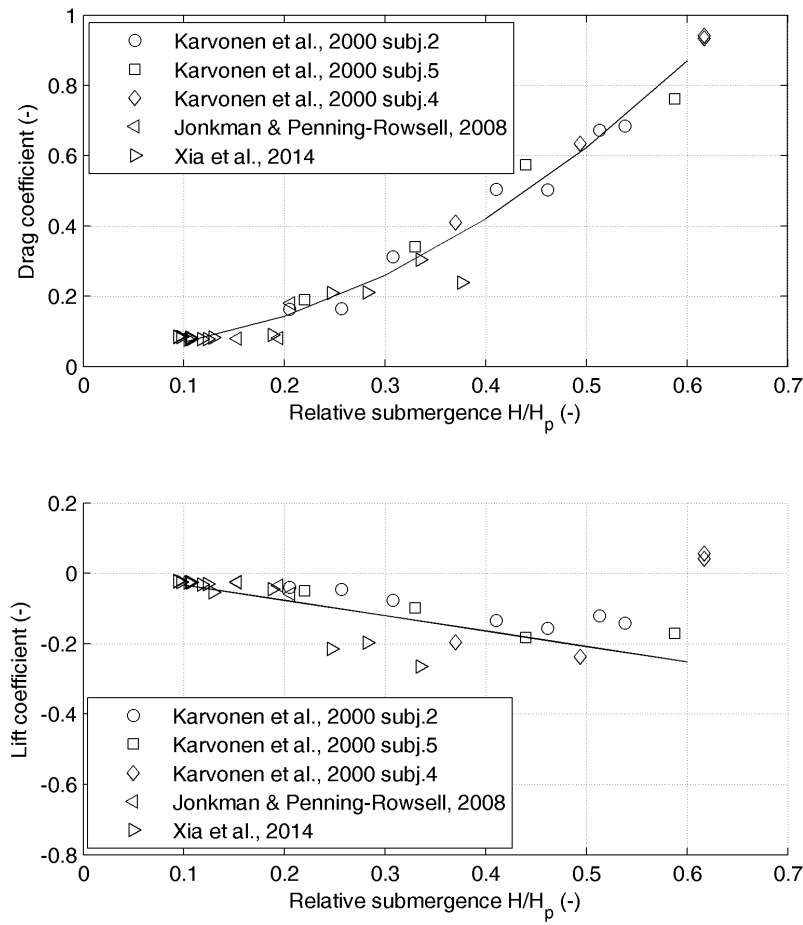


FIGURE 5.25: Drag (top panel) and lift (bottom panel) coefficients versus relative submergence H/H_p for the four human subjects considered in (Karvonen et al., 2000; Jonkman & Penning-Rowse, 2008) and the human body model considered in (Xia et al., 2014). Reference area A_{ref} for both force coefficients shown in Tab. 5.5

scaled using the scale ratio 5.54 (Table 5.5). This allows comparing the dimensional forces of the human body model with the forces acting on the human subjects. The behaviour of the human body model, whose drag force values are represented in Figure 5.26 with right-oriented triangles, are basically different from the human subjects. In fact, drag force values increase almost linearly with Froude number (without any a peak for Froude around 1). The peak of drag force observed for human subjects for Froude around 1 is the result of a balance between drag-induced moment and immersed weight, including the ability of real subjects to actively react to the action of the water flow. Moreover, for $Fr = 1$, where the peak of drag force occurs, the lift force reaches its maximum absolute value (Figure 5.27). Therefore, since the stabilizing effect of the lift force increases the effective weight, the change of position of real human subjects, with a consequent change of lever arm d (Eq. 3.15), increases the resisting moment. Thus, a larger drag force can be faced. This is not possible for the human model, since it behaves passively in the water flow without adjusting its posture. Figure 5.27 represents the lift force plotted against Froude number; again, the forces on the human body model are up-scaled to prototype conditions in order to ease the comparison. For Froude number between 0.5 and 1 there is a trough of the lift force, which reaches about -90 N for subject 2. For low Froude number and relative submergence equal to 0.62 (see Figure 5.25, bottom panel), subject 4 (Karvonen et al., 2000) experiences positive lift force since a portion of the lower body trunk is immersed in water. These values correspond in fact, to low values of drag force in Figure 5.27. For higher Froude numbers, the human body model is subject to an increasing absolute value of lift force, which allows resisting to increasing drag forces (Figure 5.26). Unfortunately, no human subjects have been tested for highly super-critical flows so that a direct comparison between human subjects and human body model is not possible for those regimes. While for sub-critical flow regimes, it is clear that the ability of human subject to actively resist to the flow adjusting its position is an advantage in terms of safety as compared to the human body model. However, the passive behaviour of the human body model can be seen as representative of the weakest class of human subjects such as elderly or sick people. A further research could overcome the limits of the rigid body assumption, by adopting a coupled CFD-CSD model where the adjustment of the body posture can be fully taken into account.

5.2.3 Identification of motion mechanisms

Since literature distinguishes two motion mechanisms, namely sliding and toppling (see Chapter 3), the identification of these mechanisms is addressed. The normalized moment is defined as the ratio of drag induced moment and resisting moment

$$Norm.moment = \frac{D \cdot (H/2)}{(W - Li) \cdot d} \quad (5.5)$$

Where the effective weight of the subject is calculated subtracting (adding) the lift force to the weight. The normalized moment is represented against Froude number in Figure 5.28. As can be seen from Figure 5.28 there are two regions identified by the normalized moment. As Froude number increases, submergence (depth H) decreases. In the left side of the diagram the normalized moment decreases with Froude number until approximately $Fr = 1.5$. Then, for Froude number higher than 1.5 the normalized moment increases slowly. The region with $Fr < 1.5$ is interpreted as a toppling instability zone and the region with $Fr > 1.5$ as a sliding instability zone with a transition zone around $Fr = 1.5$ where both instability mechanisms may occur. For lower Froude numbers (i.e. high relative submergence) toppling instability is rather expected while for high Froude

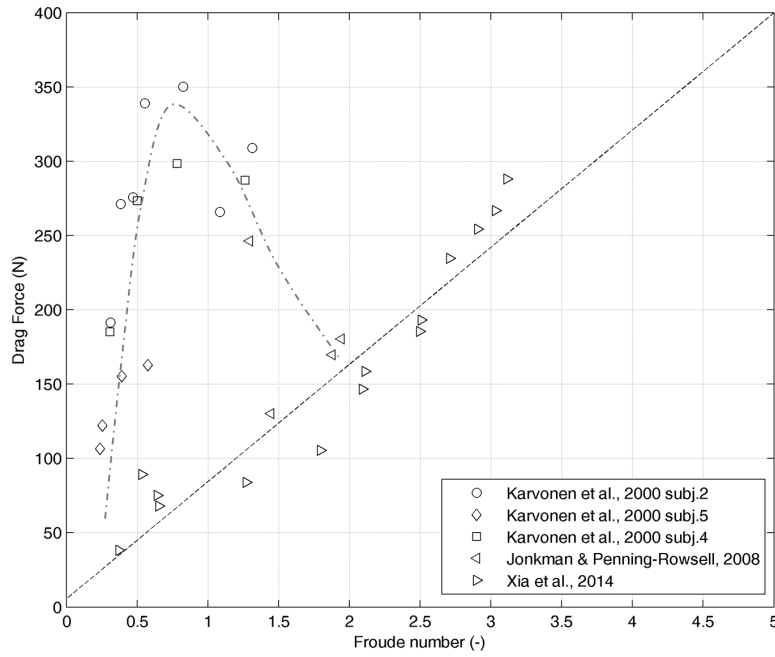


FIGURE 5.26: Drag force versus Froude number for the four human subjects considered in Karvonen et al., 2000; Jonkman & Penning-Rowse, 2008 and the human body model considered in Xia et al., 2014.

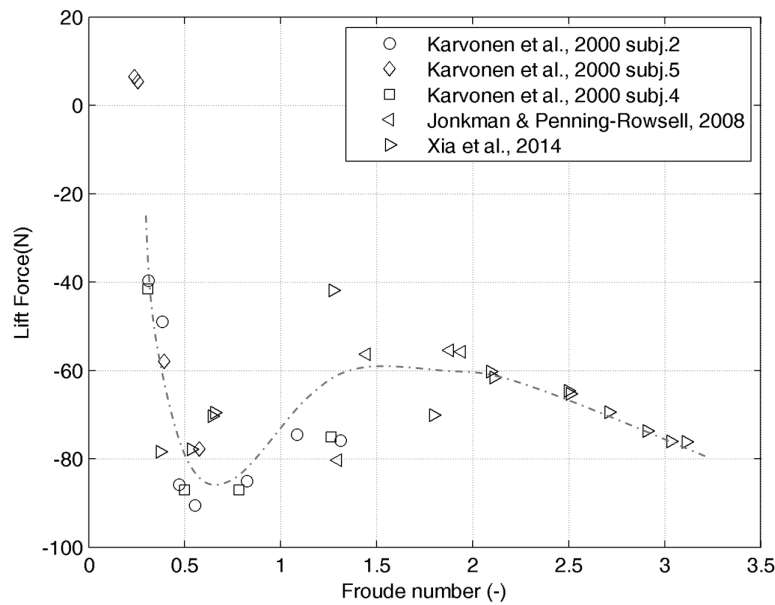


FIGURE 5.27: Lift force versus Froude number for the four human subjects considered in Karvonen et al., 2000; Jonkman & Penning-Rowse, 2008 and the human body model considered in Xia et al., 2014.

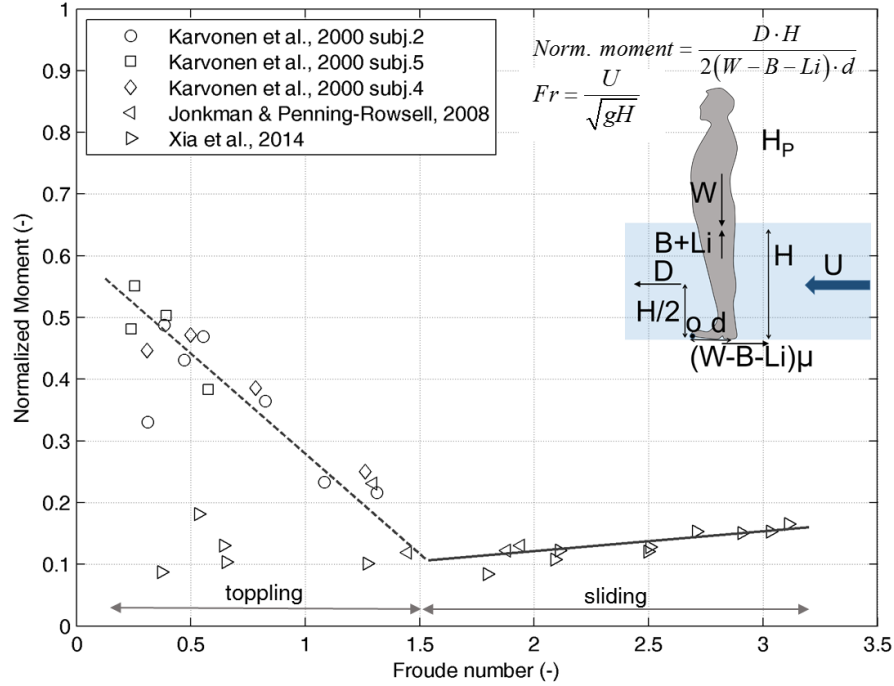


FIGURE 5.28: Normalized moment against Froude number for the four human subjects (Karvonen et al., 2000; Jonkman & Penning-RowSELL, 2008) and the human body model considered in Xia et al., 2014.

numbers a sliding instability is more likely (Jonkman & Penning-RowSELL, 2008). In fact, Froude number equal to 1.5 corresponds to a simulated water depth approximately equal to 0.45 m, which is about $2 \cdot d$. If $H = 2 \cdot d$ the coefficient $H/2d$ multiplying the drag coefficient C_D in C_t (Eq. 3.29) is equal to one, thus becoming equal to the variable C_s obtained for sliding equilibrium in Eq. 3.24. The identification of the two motion mechanisms helps in defining the dimensionless groups C_t (Eq. 3.29) and C_s (Eq. 3.24), which are used for the comparison between experiments and numerical results (section 5.2.4).

5.2.4 Comparison with experimental data and discussion

The numerical results obtained from the simulations are compared to the experimental datasets of (Karvonen et al., 2000; Jonkman & Penning-RowSELL, 2008; Xia et al., 2014) using the analytical relation between the mobility parameter θ_P , Froude number and coefficients C_s (for sliding, Eq. 3.24) or C_t (for toppling, Eq. 3.29) (Chapter 3). Since the Froude zones relevant for the sliding and toppling mechanisms have been identified in Figure 5.28, C_s is calculated for Froude number $Fr \geq 1.5$ and C_t for $Fr < 1.5$. Friction coefficient is assumed constant and equal to 0.3, which is in the range used in literature (Milanesi et al., 2015). The mobility parameter θ_P and Froude number Fr is calculated with the experimental water depths H flow velocity U pairs (H, U). The length of the foot d assigned for the different subjects and human body model is shown in Table 5.5. Figure 5.29 shows the scatter plot of experimental (x-axis) and numerical results (y-axis) for product $C_s \cdot Fr^2$ (for sliding) or $C_t \cdot Fr^2$ (for toppling) versus mobility parameter θ_P . With $R^2 = 0.76$ and an RMSE=0.63, the agreement is not full satisfying. In fact, most of the data points for super-critical flow regimes are below the 1:1 line. Therefore in Figure 5.30, the datasets related to human subjects are separated from the data of the human body model, which have shown a different behaviour in terms of hydrodynamic forces. If the dataset on the human body model is removed the determination coefficient increases

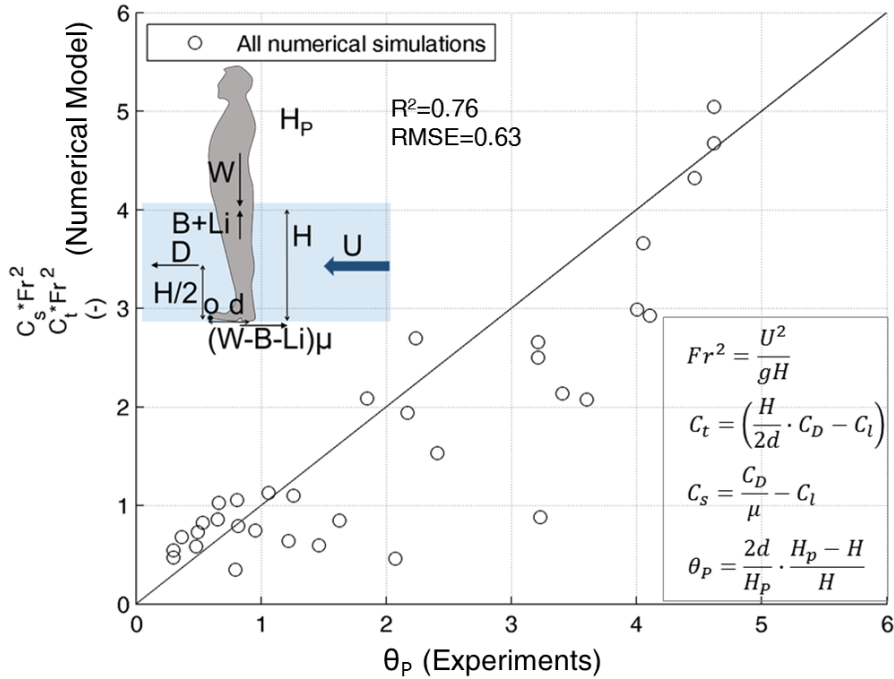


FIGURE 5.29: Comparison between experiments in terms of mobility parameter and numerical results for all the simulated human subjects and human body model defined in Table 5.5.

($R^2 = 0.84$) and the RMSE decreases to 0.29, implying an improved agreement between numerical and experimental results. As expected the numerical results of the human body model are generally below the 1:1 line except for the two data point corresponding to the two highest tested Fr -values.

5.2.5 Summary and discussion of the results of the numerical simulations of people

A selection of experimental data about the instability conditions of pedestrians under water flow has been simulated with a 3D numerical model. The human geometry is represented with a real 3D rigid body geometry facing the flow defined in terms of experimental pairs of water depth and velocity (i.e. mean flow). The experimental data have been selected in order to cover the widest range of flow regimes, i.e. Froude number from 0.2 to 3.1 and to consider both body real human subjects and a scaled human body model. Four human subjects (Karvonen et al., 2000; Jonkman & Penning-Rowell, 2008) and a 1:5.54 scaled human body model (Xia et al., 2014) have been simulated. The main findings of the numerical simulations show that:

- Drag coefficient C_D increases with submergence depth H and decreases with Froude number.
- The hydrodynamic forces for human subjects and human body model basically differ. The human body model is fully rigid and thus unable to adjust its position like real human subjects in order to resist to the flow, thus the drag force for the human model is lower than the drag force for the human subject. Lift forces are quite similar instead.
- Lift force is negative for relative submergence $H/H_p < 0.6$, since the body trunk is not immersed, thus contributing to the stabilisation of the body.

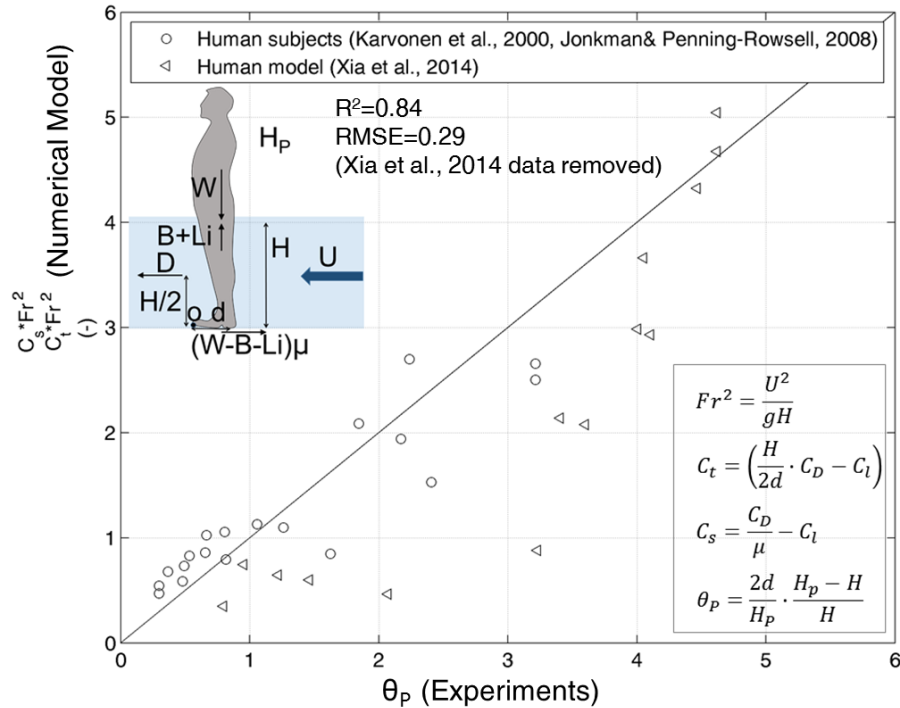


FIGURE 5.30: Comparison between experiments in terms of mobility parameter and numerical results separating the human subjects (circles) and human model (triangles).

- According to the literature, there are two incipient motion mechanisms, namely toppling and sliding, which occur for different flow regimes and levels of relative submergence depth H/H_P . In particular, for low submergence and high Froude number Fr , sliding is more likely to occur. The numerical simulations confirm the existence of these two motion mechanisms (toppling for higher H -values and lower Fr -values; sliding for lower H -values and higher Fr -values Fr) with a transition zone around $Fr=1.5$ where both mechanisms may occur.
- Froude number Fr and relative submergence depth H/H_P are the most relevant dimensionless parameters governing both sliding and toppling mechanisms. Particularly Froude number describes the flow regime (critical, sub-critical and supercritical flow) and hydrodynamic effects, while relative submergence drives the portion of wet surface and lever arm of drag force.
- The comparison between experiments and numerical results indicates that the human body model performs less well if compared with the mobility parameter θ_P , while the comparison is pretty good for the human subjects with $R^2 = 0.84$.

The human body is modelled as a fully rigid upright standing body facing a flow with a frontal impact, introducing a strong assumption. In the experiments, the human subjects were in fact allowed to adjust their position in order to face and better resist the water flow. This justifies the use of the full length of the foot d to calculate the lever arm of the resisting moment induced by the weight. Moreover, the stuntman used by Jonkman & Penning-Rowsell was crossing the water stream, so the impact was lateral. However, for the low submergence levels tested in their experiments (i.e. sliding instability) the differences in the wet area and forces are considered very small. For the human body model, the assumption on the full length of the foot is not consistent as shown by the differences in the estimated forces. The human body geometry used in the numerical simulations

is naked. However, some authors (Karvonen et al., 2000; Xia et al., 2014) stress that the clothes and other equipment may play an important role for drag effects, which could not be included in this study. Nevertheless, the numerical results demonstrate that the use of a constant drag coefficient equal to 1, which was assumed in many studies (Love, 1986; Walder et al., 2006; Milanesi et al., 2015) is not realistic. The friction coefficient is an important parameter for the sliding mechanisms and is difficult to calibrate in the experiments. Here a value of 0.3 is used, which is a conservative value in the range available in literature (Milanesi et al., 2015). Therefore, a more detailed study on the effect of friction and on the non-rigidity of the body is required in future research.

5.3 Summary of the chapter

This chapter analyses the numerical results of the simulations about vehicles and people under water flow. Both for vehicles and people, the numerical simulations adequately reproduce the experimental pairs of water depth and flow velocity in which the stability is lost in the hydraulic flume tests. Both vehicles and people are assumed as rigid bodies. The numerical results for the Ford Focus (section 5.1) and for four human subjects and a human body model (section 5.2) have clarified the incipient motion mechanisms and the related hydrodynamic forces and force coefficients of the objects. Moreover, the most relevant dimensionless parameters are identified, which are Froude number $Fr = U/(gH)^{0.5}$ for both vehicles and people, and relative submergence H/H_p for people. The comparison between numerical results and experiments for vehicles has been considered pretty good. The comparison between numerical results and experiments for pedestrians has been considered pretty good once the data on the scale human model have been removed. The rigidity of the body and the constant friction coefficient are strong but necessary assumptions for the numerical simulations of vehicles and pedestrians, which have been discussed but could require a future study. The numerical model here adopted is simplified since the mesh has been selected to reduce the computational time and a laminar approach has been used. A future study should investigate finer meshes and should also identify an appropriate turbulence model to be validated with new adequate experimental data. Vehicles and human bodies behave differently under water flow. Particularly they differ in shape and density, thus leading to different motion mechanisms and different hydrodynamic interactions. Froude similarity has been demonstrated as appropriate for transferring the forces from scale models to prototype cars. Therefore, the mobility parameters introduced in Chapter 3 can also be applied for full scale conditions, in order to create hazard maps at inundation scale. Figure 5.31 graphically summarizes the contents of the chapter.

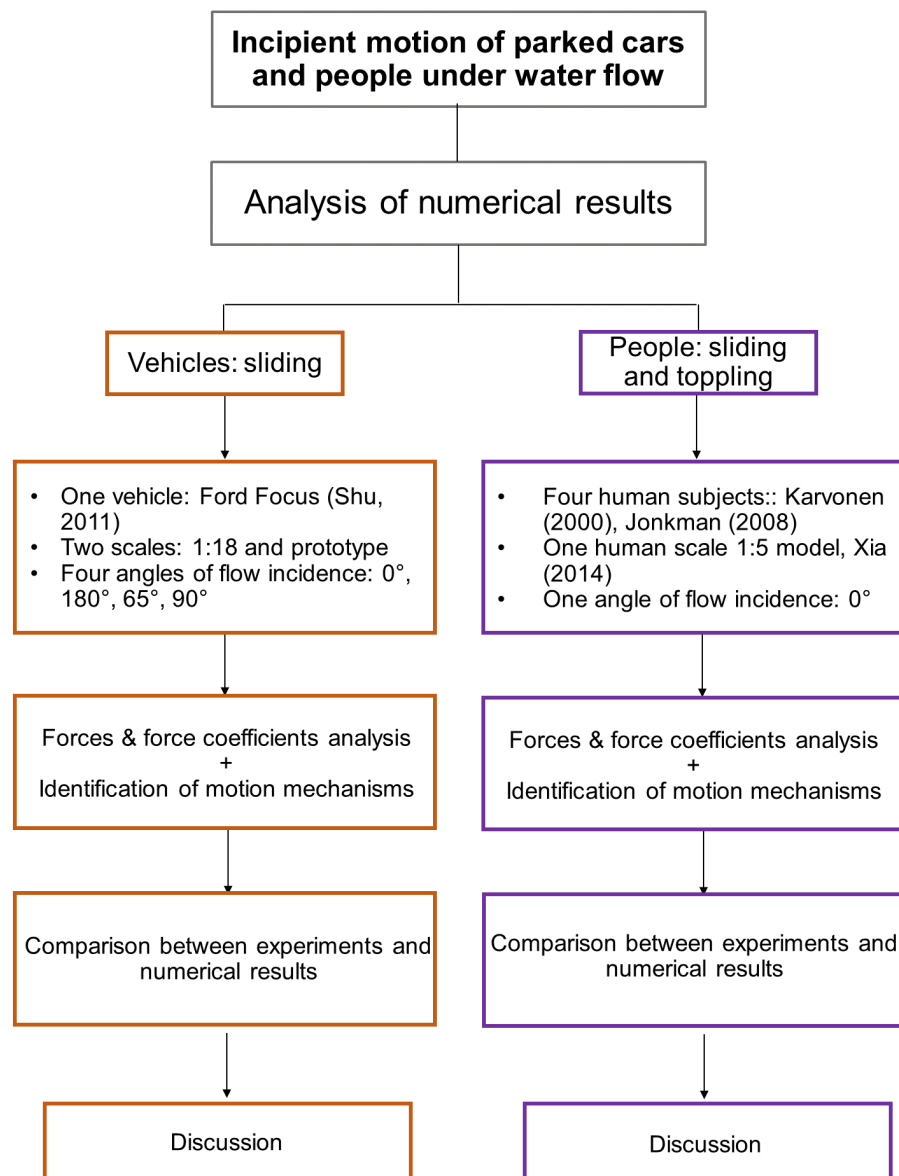


FIGURE 5.31: Graphical summary of the chapter.

Chapter 6

Application to two case studies

Identifying flood prone areas in a hazard map is usually the first step in flood risk studies. This step requires the implementation of hydrologic-hydrodynamic models that enable to quantify the evolution of a flood, which is generally described by representative variables such as flood depth and flow velocity. Hazard maps resulting from hydraulic models usually show potential flood extent, water depth and sometimes velocity for predefined low, medium and high probability levels (e.g. hazard scenarios). The movement of floodwaters through the landscape can be approximated using different methods (see Chapter 2). Describing natural physical phenomena using numerical methods requires making broad assumptions to develop governing equations. While simple hydraulic modeling methods may be sufficient for approximating propagation of flood peaks through river channels, more complex hydraulic analyses may be necessary to incorporate the effects of infrastructure or complex overland flow in urban areas. The evaluation of hazard to people and vehicles under water flow requires a flood map created with a hydrodynamic model representing water depth and flow velocity capable of adequately describing the flow in the streets and thus accounting for the buildings. In the previous chapters, two dimensionless mobility parameters for pedestrians and vehicles under water flow have been developed. Two critical thresholds of instability have been identified by calculating the mobility parameters for the experimental data. Moreover, the numerical model demonstrated that no scale effect exists for the hydrodynamic forces for vehicle models scaled from prototype vehicles using Froude's similitude. Thus, the critical threshold of incipient motion for vehicles can be adopted to floods at prototype scale, to achieve the following objectives:

- i) define hazard criteria for both people and vehicles under water flow
- ii) map the hazard levels for an inundation scenario
- iii) provide a qualitative validation of the critical threshold using reports of past flood events
- iv) demonstrate the potential use of hazard maps

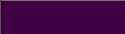






In order to apply the results obtained in this research to a field scale it is necessary to define hazard criteria (section 6.1), then to briefly describe the inundation model (6.2) and finally to present the two case studies namely Ajaccio in France (section 6.3) and Genova in Italy (section 6.4).

6.1 Definition of hazard criteria

6.1.1 Hazard criteria for vehicles

The critical threshold of incipient motion for vehicles $\theta_{V_{cr}}$ has been introduced in chapter 3. The critical mobility parameter $\theta_{V_{cr}}$ resulting from a regression analysis of the mobility

TABLE 6.1: Color scale for hazard classification and mapping

Hazard value (-)	Colour	Description
1.5		Extremely high
1.25		Very high
1.0		High
0.75		Medium
0.5		Low
0.25		Very low
0		No hazard

parameter θ_V obtained from the experiments versus Froude number $Fr = U/(g \cdot H)^{0.5}$ is provided by Eq. 3.31 re-written below (see also Fig. 3.14):

$$\theta_{Vcr} = Fr^{1.92} + 2.77 \text{ (for vehicles) with } R^2 = 0.83 \text{ \& } RMSE = 0.73$$

This regressed curve (Eq. 3.31) accounts for the experimental data of different types of vehicle, whose geometric characteristics are included in the shape factor of θ_V (Eq. 3.13). Typical values of the shape factor are in the range 6.2 – 6.6. Since this equation identifies a threshold, the values of θ_V falling above the curve (see Fig. 3.14) are stable conditions (i.e. low hazard) while the values falling under the curve are unstable (i.e. high hazard), unlike the famous Shield's diagram for sediments incipient motion where the values above the critical curve represent motion conditions. This hazard classification can be written as a hazard criterion Haz_V as

$$Haz_V = \frac{\theta_{Vcr}}{\theta_V} \begin{cases} > 1 \text{ unstable} \\ = 1 \text{ incipient motion} \\ < 1 \text{ stable} \end{cases} \quad (6.1)$$

For values of the ratio Haz_V higher than one, the hazard is very high because a vehicle is very likely to be unstable. For the ratio equal to one, incipient motion is expected, thus the hazard is high. For values lower than one, the hazard can be medium to very low according to the proximity to the threshold. This transition from medium to very low hazard is classified in three categories, which are: medium hazard ($0.75 \leq Haz_V < 1$), low hazard ($0.50 \leq Haz_V < 0.75$), very low hazard ($0.25 \leq Haz_V < 0.5$). A colour scale in hazard maps can easily represent different values of Haz_V as in Table 6.1. The value of θ_V can be calculated either for an average representative car geometry or for a probability distribution of car geometries, once the water depth H and flow velocity U are available from the inundation map. As a conservative hypothesis a representative light vehicle with low chassis height should be considered for the calculation of θ_V . H and U provided by the inundation map are used to calculate Froude number $Fr = U/(g \cdot H)^{0.5}$ and thus the critical threshold θ_{Vcr} . In absence of detailed data about the position and orientation of cars with respect to the longitudinal axis of the streets, a value $\beta = 90^\circ$ for the calculation of the mobility parameter is assumed, since it is the most conservative hypothesis.

6.1.2 Hazard criteria for pedestrians

The critical threshold of instability for people under water flow θ_{Pcr} has been introduced in chapter 3. The critical mobility parameter θ_{Pcr} resulting from a regression analysis of the mobility parameter θ_P obtained from the experiments versus Froude number $Fr =$

$U/(g \cdot H)^{0.5}$ is provided by Eq. 3.25 re-written below (see also Fig. 3.14):

$$\theta_{Pcr} = Fr^{1.02} + 1.71 \text{ (for people) with } R^2 = 0.96 \quad \& \quad RMSE = 0.19$$

Since this equation identifies a threshold, the values of θ_P falling above the curve (see Fig. 3.14) are stable conditions (i.e. low hazard) while the values falling under the curve are unstable (i.e. high hazard). This hazard classification Haz_P can be written as

$$Haz_P = \frac{\theta_{Pcr}}{\theta_P} \begin{cases} > 1 \text{ unstable} \\ = 1 \text{ incipient motion} \\ < 1 \text{ stable} \end{cases} \quad (6.2)$$

For values of the ratio Haz_P higher than one, the hazard is very high because a person is very likely to lose its stability. For the ratio equal to one, the instability threshold is expected, thus the hazard is high. For values lower than one, the hazard can be medium to very low according to the proximity to the threshold. This transition from medium to very low hazard is classified in three categories, which similarly to those of vehicles are medium hazard ($0.75 \leq Haz_P < 1$), low hazard ($0.50 \leq Haz_P < 0.75$), very low hazard ($0.25 \leq Haz_P < 0.5$). A colour scale in hazard maps can easily represent different values of Haz_P (as in Table 6.1). The value of θ_P can be calculated either for an average representative person with typical physical characteristics (i.e. person height and foot length) or for a probability distribution of human body characteristics, once the water depth H and flow velocity U are available from the inundation map. A conservative hypothesis is to assume as reference human subjects a short man with small feet. H and U provided by an inundation map are used to calculate Froude number and thus the critical threshold θ_{Pcr} .

6.2 The TELEMAC-MASCARET suite

The TELEMAC-MASCARET suite of free surface flow solvers has been selected for both the case studies described below. Through its wide and diverse applications in the context of numerous studies worldwide, it has become one of the major standard CFD codes in hydraulic and coastal engineering. TELEMAC-MASCARET (www.opentelemac.org) is an integrated suite of FEM solvers for free-surface flow. TELEMAC-MASCARET is managed by a consortium of core organisations: Artelia (formerly Sogreah, France), Bundesanstalt für Wasserbau (BAW, Germany), Centre d'Etudes Techniques Maritimes et Fluviales (CETMEF, France), Daresbury Laboratory (United Kingdom), Electricité de France R&D (EDF, France), and HR Wallingford (United Kingdom). TELEMAC-MASCARET is an open source code used for design and impact studies, where safety is prevailing and, for this reason, reliability, validation and a worldwide recognition are of utmost importance. TELEMAC-2D is a software package used to simulate free-surface flows in two dimensions of horizontal space. At each point of the mesh, the program calculates the water depth and the two flow velocity components. Space is discretised in the form of an unstructured grid of triangular elements, which means that it can be refined particularly in areas of special interest. The governing equations of TELEMAC-2D are the non-conservative form of the shallow water equations, written with depth and velocity as unknowns (Galland et al., 1991). The bottom friction obeys the Manning-Strickler's formula or Chezy's formula (see section 2.1.3). A semi-implicit time and a finite element space discretization are used. A TELEMAC-2D hydrodynamic simulation requires a minimum of three input files:

- Geometry File (.slf)

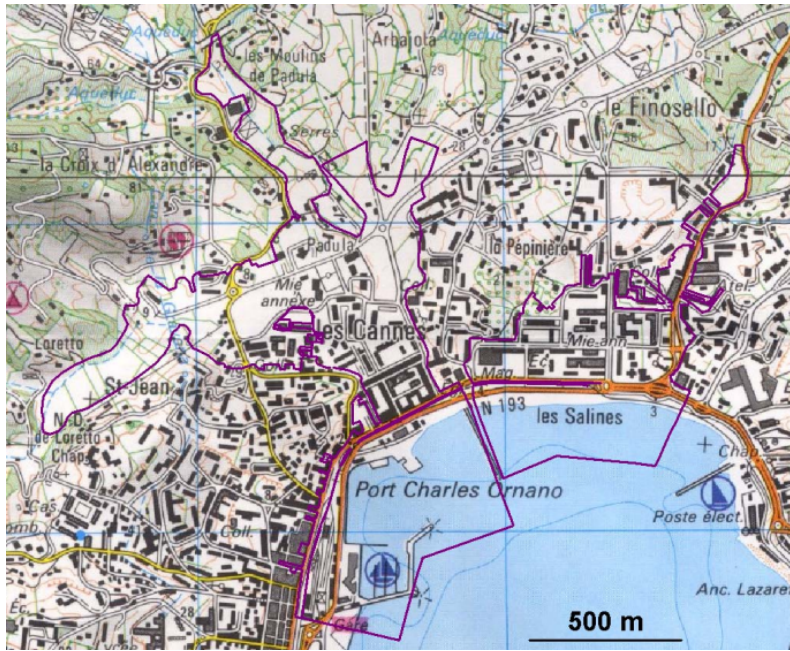


FIGURE 6.1: Detail of les Cannes district in the eastern part of Ajaccio (violet polygon on the left) (Sogreah, 2006).

- Boundary Conditions File (.cli)
- TELEMAC-2D simulation parameters file (.cas)

Items 1 and 2 are prepared with, Blue Kenue developed by the National Research Council of Canada (<http://www.nrc-cnrc.gc.ca>) (CHC, 2011; Gifford-Mears and Leon, 2013). The geometry file contains the unstructured mesh of triangle elements, which can be edited using GIS data, such as buildings polygons or river sections. The boundary conditions file contains the list of nodes to which the conditions are assigned (e.g. the inflow hydrograph). FUDAA Pre-Processor (<http://prepro.fudaa.fr/>), which is developed by the department of Simulation informatique et Modélisation of DTecEMF in the CEREMA Institution is used to set up the TELEMAC-2D parameters file.

6.3 The case study of Ajaccio in Corsica (France)

6.3.1 Case study description

The first case study area considered to show the application of the hazard criteria for people and vehicles, as described above in Section 6.1, is the Cannes district in Ajaccio (Figure 6.1), situated in southwestern Corsica (France). The results of the simulations have been provided by CEREMA (Centre d'études et d'Expertise sur les Risques, l'Environnement, la Mobilité et l'Aménagement) in the person of Patrick Chassé and are described in detail in a project report for the Direction Départementale de l'Équipement Corse du Sud, (Sogreah, 2006). From preliminary hydrologic-hydraulic studies, Ajaccio has been classified as a high flood risk area. The Cannes district is located downstream of three small catchments (Arbitrone, Moulins Blancs and Arbajola), whose streams are culverted in the urbanized area up to the sea. The cadastral map 1:5000 has been used to extract the built footprint and a detailed topographic survey has been carried out to measure the terrain elevation (max 30 m.a.s.l.). The mesh is composed of 10511 nodes and 18486 triangular elements, with edge size ranging from one meter to 25 meters in the sea. Although

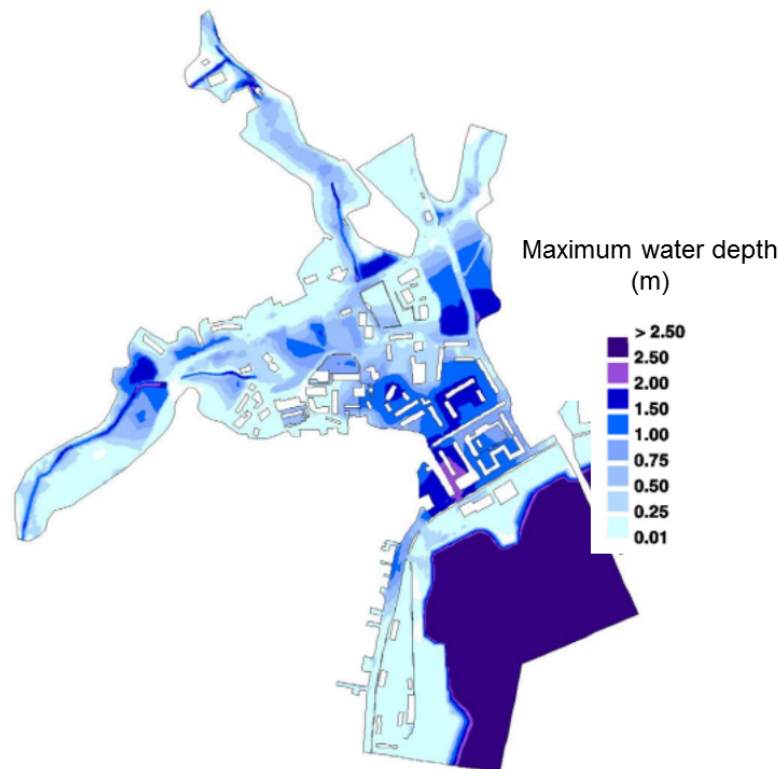


FIGURE 6.2: Temporal maximum of water depth during the flood simulation in the district les Cannes for 100 years recurrence interval (Sogreah, 2006)

the area is not densely urbanized, it hosts two important educational facilities and some commercial activities. It is connected to the port area through an important traffic artery along the coastline, the Cours Jean Nicoli. The numerical simulation is carried out with the TELEMAC-2D suite, imposing the hydrographs and rainfall for a 100 years scenario with 6 hours duration (Sogreah, 2006). The benchmark inundation events of 23 January 2003 and 25-26 November 1990 were used for the validation of the numerical model (Sogreah, 2006).

6.3.2 Inundation characteristics and hazard maps for vehicles and pedestrians

The simulated 100 years scenario in les Cannes district has the characteristics of a flash flood since its timescale is approximately 5 hours. This recurrence interval is used as a reference in French legislation for hydraulic constructions. The maximum water depth reached in les Cannes district for the 100 years scenario, extracted from the simulated time steps and is 2 m (Figure 6.2) and the maximum velocity is up to 2.5 m/s (Figure 6.3). The dark blue area in the bottom of Figure 6.2 represents the sea level used as a southern boundary condition. The flood depth map allows recognising the three small creeks (Arbajola on the top right side, Moulins blancs top and Arbitrone top left side of the figure), which become culverts close to the urbanized area. In the flood conditions shown in the figure, both vehicles and people are likely to be highly vulnerable. Hazard levels H_{azp} and H_{azp} are calculated in the Blue Kenue workspace using a cell calculator tool capable of combining in each computational cell, for each time step, the variables obtained during the simulation (i.e. water depth and velocity) and of performing simple statistical analysis.

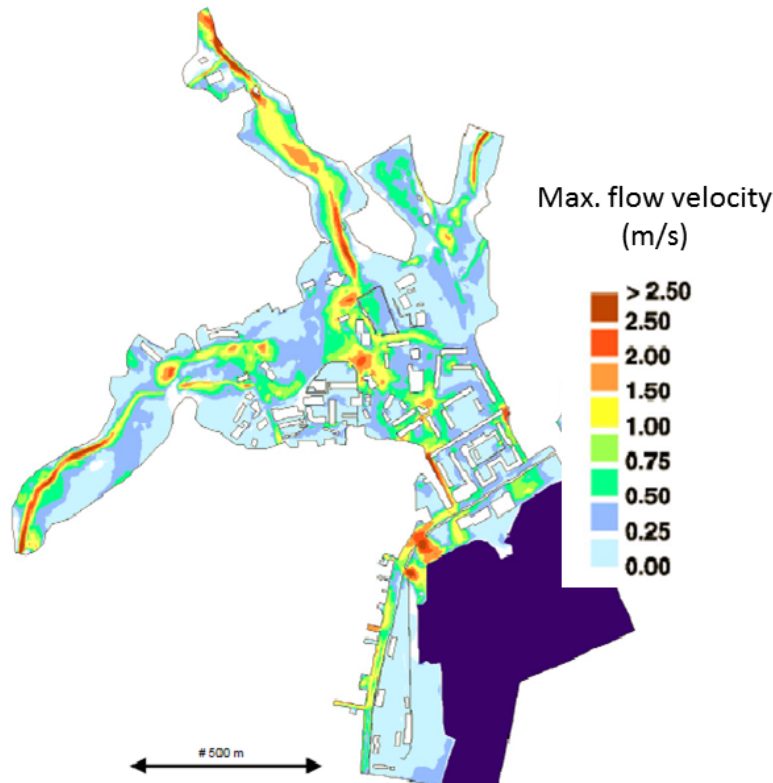


FIGURE 6.3: Temporal maximum of flow velocity during the flood simulation in the district les Cannes for 100 years recurrence interval (Sogreah, 2006)

Figure 6.4 shows the extraction of the maximum value of the vehicle hazard (Eq. 6.1) over the simulation time. The colour scale goes from 0.25 (green colour, very low hazard) up to 1.5 (dark violet, very high hazard). Red areas are those likely to be prone to incipient motion of vehicles (high hazard) and violet areas can be considered as extremely dangerous for parked vehicles since the hazard level Haz_v is higher than one. Moreover, since many open areas are used as car parking for the commercial areas, it is likely that they can be swept away by floodwaters for a similar scenario. Much more interesting is Figure 6.5 showing the hazard to people. The hazard scale as defined in Table 6.1 ranges from 0.25 (green colour, very low hazard) up to 1.5 (dark violet, very high hazard). The most dangerous area for pedestrians is Rue Pierre Bonardi (violet area in the centre of the picture) and the seaside Cours J. Nicoli, which is moreover the most important traffic artery of the city. Furthermore, Rue P. Bonardi allows the access to the primary school, which is a further high vulnerability factor. For these study area and flood characteristics, the comparison between the two maps hints that driving a vehicle is much more hazardous than a pedestrian walking in floodwater. This is mostly because water depths on average are around 0.75 m, so vehicles can easily float. A video taken during the 2003 flood in les Cannes district (available at <https://www.youtube.com/watch?v=fuOiVNrAA-o>) follows a man walking in flood waters through cars which are randomly distributed along the street after being mobilized. The video qualitatively confirms the results of the hazard maps. Another document (<https://www.youtube.com/watch?v=e0HeU3qUJyE>) shows many people walking on the railway line on one of the sides of the flooded Cours J. Nicoli after the 2008 rainfall event, whose recurrence interval is not known. The maps shown in Figures 6.4 and 6.5 are interesting because they allow a risk estimation if

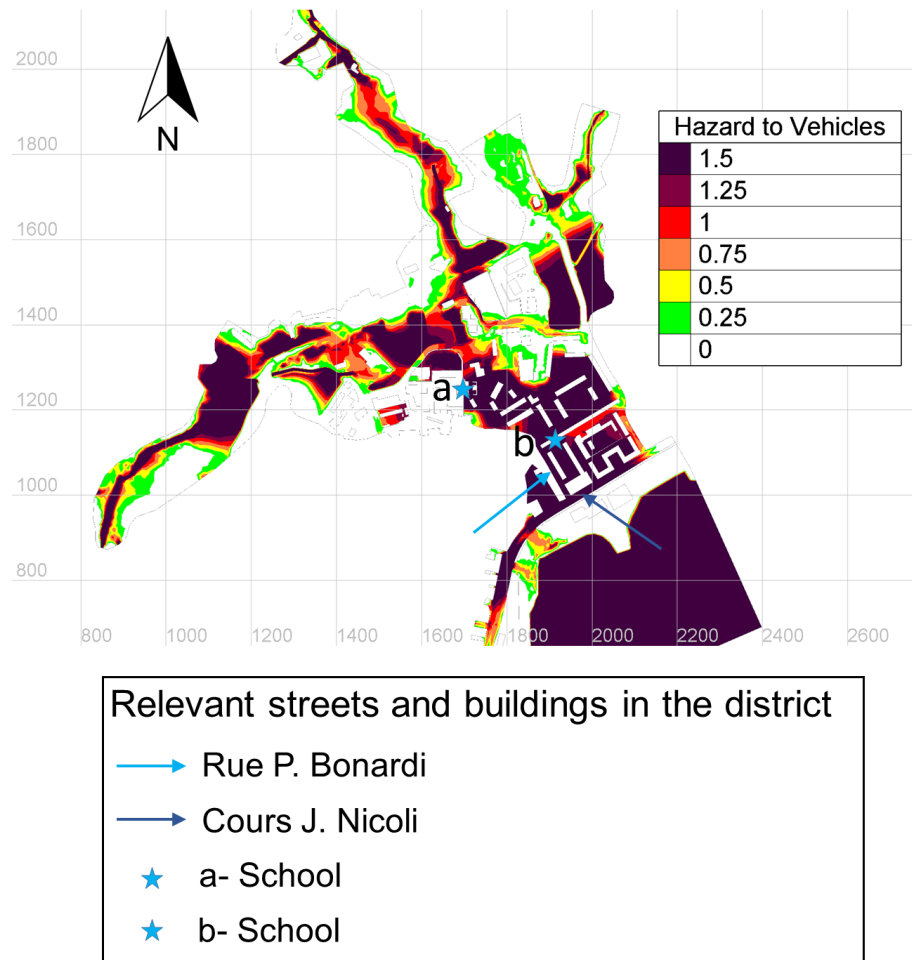


FIGURE 6.4: Hazard to vehicles for the 100 years scenario and relevant streets and buildings in Les Cannes district based on the proposed Hazard criterion (see Eq. 6.1)

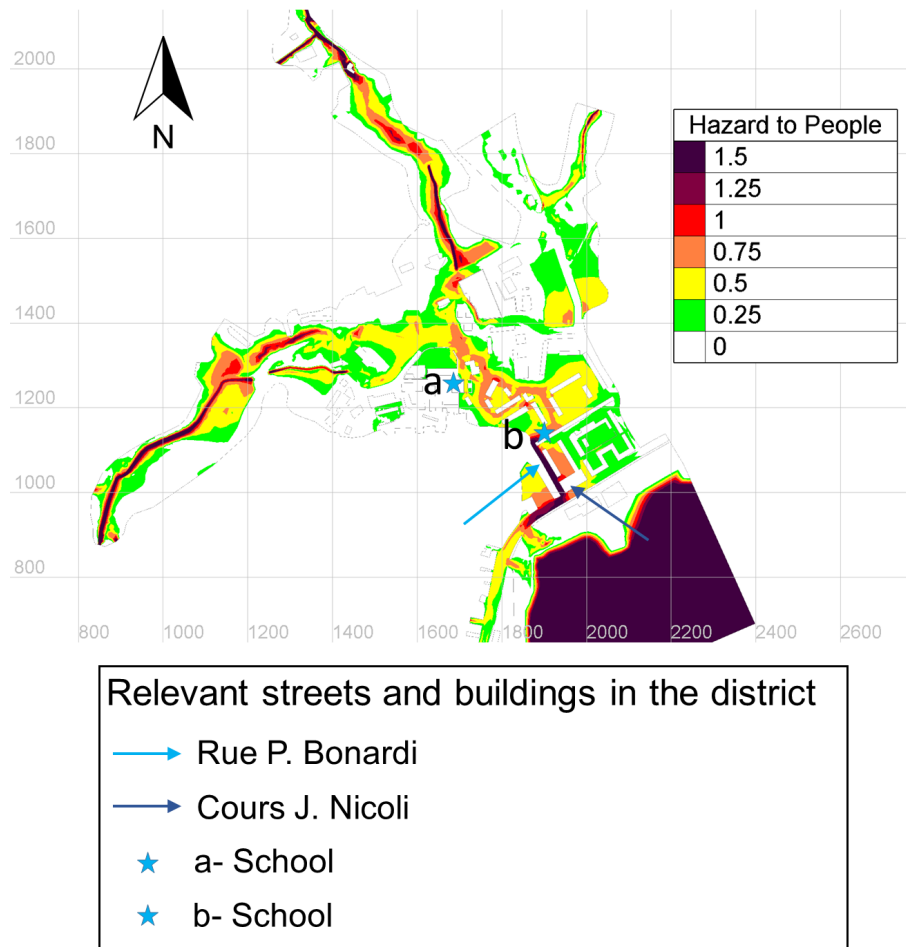


FIGURE 6.5: Hazard to pedestrians for the 100 years scenario and relevant streets and buildings in Les Cannés district based on the proposed Hazard criterion (see Eq. 6.2)

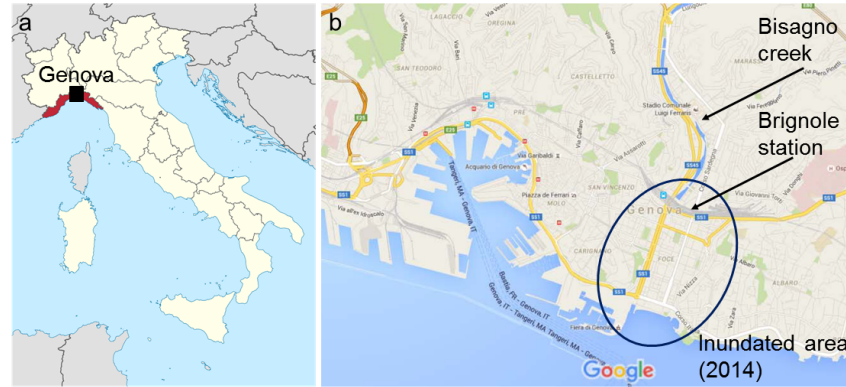


FIGURE 6.6: City of Genova (a) Location in Italy (www.wikipedia.it) and (b) port area (Google Maps) with indication of the Bisagno creek and the inundated area in 2014.

compared to the vulnerability data (i.e. about the actual parking density or traffic). Furthermore, some buildings with special use (such as schools represented with stars a and b in Figures 6.4 and 6.5) may be equipped with some informative panels to suggest emergency behaviours in case of flood. This kind of non-structural mitigation measures can be very effective to educate people and pupils, thus reducing the probability of injuries in case of flood events.

6.4 The case study of Genova (Italy)

6.4.1 Case study description

The second case study in the city of Genova in North-western Italy (Figure 6.6) is considered exemplarily for vehicle incipient motion during urban floods (see Figure 2.5). It hosts the most important port in Italy and has approximately 870000 inhabitants. Genova was hit by two severe floods in 2011 and 2014 (see blue ellipse in Figure 6.6, panel b), which caused damages to buildings and commercial activities and 7 fatalities. In 2014 the Bisagno creek, whose last reach flows culverted in the urban area in correspondence of Brignole station (Figure 6.6, panel b) was responsible for the flood, after heavy rains. Silvestro et al., (2015) reconstructed the hydrological event. During the 8th and the morning of 9th of October 2014 a series of regenerating storms affected the central and eastern parts of the Region. Several showers of rainfall created peak flows in the basins in the area, but the intensities and persistence of the rainfall were not high enough to have any notable impact. On the Bisagno Creek about 130 mm of rainfall was recorded at basin scale in 36 h, produced by three main events of 3–6 h duration. During the evening of 9th of October, after some hours of very light rain, there was a new, strong and intensified storm; approximately 4 h of very intense rainfall affected the central part of the catchment causing a very fast response of the basin. A local rainfall amount of 250 mm in four hours was recorded. This rainfall event led to a peak flow of about 1100–1200 m^3/s that corresponds to a return period of approximately 100–200 years. Dolia (2015) carried out the hydraulic reconstruction of the flood event using the hydrologic data by Silvestro et al. (2015) and the results are currently under publication (Silvestro et al. 2016, in press). The 2014 flood event in Genova has been simulated with TELEMAC-2D. The digital elevation model (DEM, 1 m resolution) and buildings data have been used for the mesh generation (min cell size 1.5 m). The culverted reach of Bisagno creek has been modelled with a sub-routine in the code.

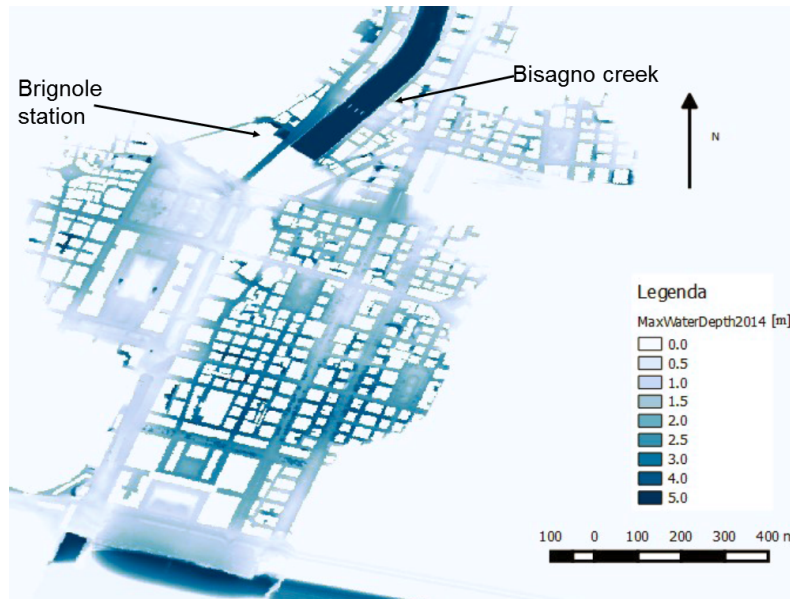


FIGURE 6.7: Maximum simulated water depth for the 2014 Genova flood (Dolia, 2015).

6.4.2 Inundation characteristics and hazard maps for vehicles and pedestrians

Figure 6.7 shows the results of the numerical reconstruction of the 2014 flood event (Dolia, 2015) in terms of temporal maximum of water depth. The Bisagno creek on the top of the figure is represented with dark blue colour (i.e. high water depth) and the opening of the culvert, close to Brignole station is easily recognizable. Flood depth range from 0.15 m up to 3 m in the inundated urban area and the flow velocity up to 4 m/s. The maximum simulated Froude number values reach 3.0 in many inundated areas (Figure 6.8). The hydraulic simulation run with TELEMAC-2D model was validated through comparison of the calculated water levels with the watermarks of the flood event (Dolia, 2015), showing a relatively good performance of the model in terms of water depths. The results of the model (i.e. pairs of water depth and velocity) have been kindly provided by Simone Gabellani from CIMA Research Foundation (International Centre of Environmental Monitoring, Savona, Italy). Hazard levels for pedestrians and vehicles have been calculated according to Eqs. 6.2 and 6.1 respectively in the Blue Kenue environment, which is compatible with the TELEMAC output files. A temporal statistical analysis on the mesh elements is performed within Blue Kenue and the temporal maximum is extracted. The results are shown in Figures 6.9 and 6.10 for the hazard to people and vehicles, respectively. The hazard to people is shown for a detail of the Brignole station area located in the top left side of Figure 6.9. Hazard to people is on average very high, especially in some major roads and squares near the station (purple colour). On the right hand side of Figure 6.9, the hazard values are lower (yellow-green colours) since those areas, farer from the Bisagno creek, are characterised by a water depth of the order of 1 m and low velocities in the order of 0.4 m/s.

The hazard to parked vehicles is shown for a detail of the Brignole station in Figure 6.10. Hazard to vehicles is extremely high for most of the selected area, with very few exceptions. As in the Ajaccio case study, vehicles are more likely to be mobilized than people. The advantage of maps like those in Figures 6.9 and 6.10 over a classical flood depth map (Figure 6.7) is that it is easier to assess the potential adverse consequences of the flood on people and vehicles. Thus, management strategies for traffic circulation, especially for decision making on road closures can be supported more efficiently.

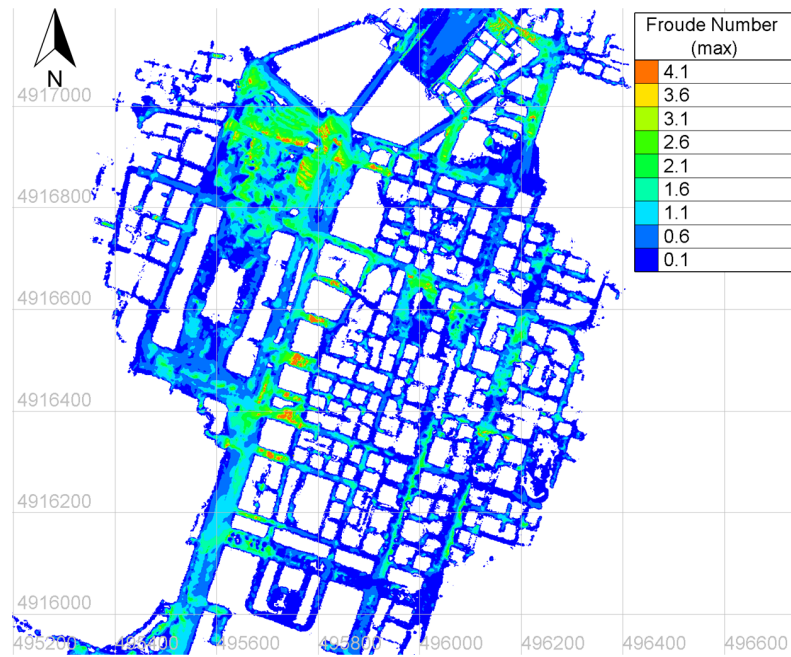


FIGURE 6.8: Maximum Froude number for the 2014 Genova flood.

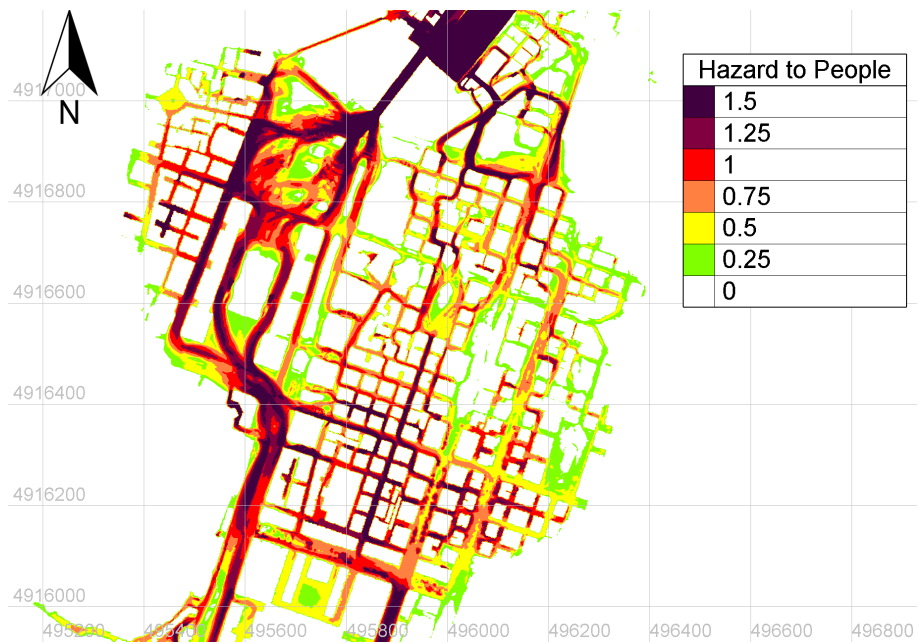


FIGURE 6.9: A detail of hazard to people (temporal maximum) close to Brignole station for the reconstructed 2014 Genova flood event

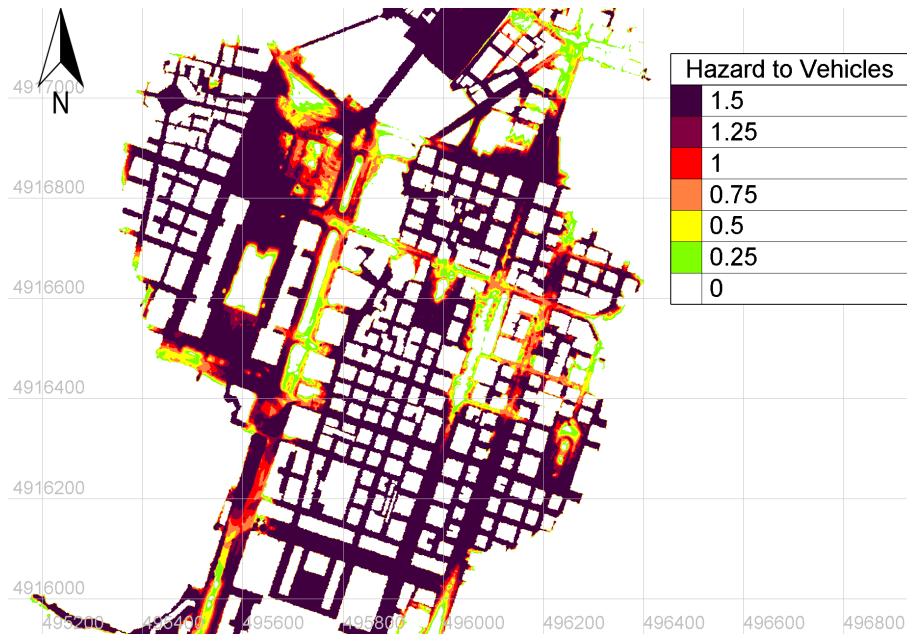


FIGURE 6.10: A detail of hazard to vehicles (temporal maximum) close to Brignole station for the reconstructed 2014 Genova flood event.

6.4.3 Comparison of proposed hazard criteria with photos of the flood event

Recent flood events such as the 2014 Genova flood are usually very well-documented by pictures and movies, often taken by witnesses with their mobile phones. Based on the comparison with such documentation, an attempt is made to partially assess the performance of the hazard criteria for people and vehicles. First, a selection of pictures is made, then the location of the shoot (georeferencing) is reconstructed using Google Maps and street view tools and finally the hazard maps for vehicles are compared with the pictures in order to detect whether incipient motion occurred or not. The map in Figure 6.11 shows the shooting points named a, b, c, d of the photos reported in figures 6.12, 6.13, 6.14, 6.15, 6.16. The description of the shooting locations is provided in the following list:

- a) Via Fiume/Via XX settembre, two vehicles mobilised during the flood event are deposited in the footpath and are blocked by the railing of a pedestrian underpassage (Fig. 6.12)
- b) Via Malta/Via Brigata Liguria, many cars are scattered in the street with different orientations (Fig. 6.13)
- c) Corso Torino/Corso Buenos Aires, cars are deposited in the crossroad after the mobilization occurred upstream (picture d) (Fig. 6.14)
- d) Corso Torino in front of the railway, cars are entrained by the water (Fig. 6.15)
- e) Via A. Canevari, firemen found the body of Antonio Campanella the night of the 9th october (Fig. 6.16)

Both pictures in Figures 6.12 and 6.13 taken the day after the event show the mobilized cars after the deposition and confirm the very high hazard levels in those location shown at locations *a* and *b* in Figure 6.11. Particularly Figure 6.12 indicates that the entrainment of cars can be stopped by urban furniture like trees or artifacts such as rails and fences.

The photo in Figure 6.14 is taken at the end of the flood event, floodwater is lowering and many cars are deposited in the crossroad Corso Torino/Corso Buenos Aires. The

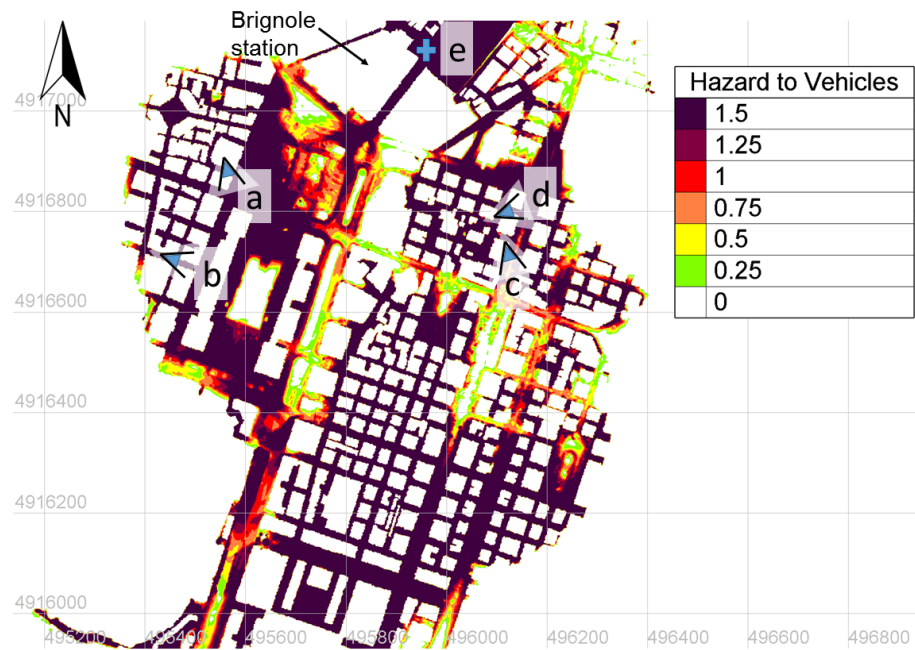


FIGURE 6.11: Hazard to vehicles and locations a, b, c, d of the photos in Figs. 6.12, 6.13, 6.14, 6.15 taken during and after the 2014 Genova flood event. Location where the body of A. Campanella was found (e), Fig. 6.16



FIGURE 6.12: The day after the flood, photo taken at location a (Figure 6.11, from: www.ilsecoloXIX.it).



FIGURE 6.13: The day after the flood, photo taken at location b (Figure 6.11, from: www.ilsecoloXIX.it).

white wagon in Figure 6.15 can be also recognized in Figure 6.14 (bottom right side). In correspondence of this crossroad location, the hazard map in Figure 6.11 shows $H_{azV} \leq 0.75$, which is consistent with the deposition zone since the incipient motion conditions do not occur.

The picture in Figure 6.15 taken at location d (Figure 6.11) is one example of photos taken during the flood event. Three cars and a white wagon are swept away by the flood. They are directed parallel to the flow (from left to right in the picture) with the frontal heaviest part of the bodywork almost completely immersed. This location corresponds in fact, to very high hazard levels for vehicles in Figure 6.11 (purple colour, $H_{azV} \geq 1.5$), confirming the indications of the map. The four vehicles are directed towards the location of Figure 6.14 (c, Figure 6.11). The 2014 flood in Genova also caused one fatality. It was a 57 years old man, Antonio Campanella, who said to some friends that he wanted to check the conditions of Bisagno creek after the rains of the day. He was swept away by the outflowing waters of the Bisagno creek in Via Canevari and his body was found in the same street (location e, Figure 6.11) stopped by a pole of the bus stop sign (Figure 6.16). The hazard map for people in Figure 6.9 shows that location e in Figure 6.16 corresponds to very high hazard levels for pedestrians H_{azP} where walking in floodwaters is extremely hazardous. The observations from the pictures reported above are in agreement with the hazard maps for vehicles based on the proposed hazard criteria (see Eqs. 6.1, 6.2) using the mobility parameter θ_V for the pairs of water depth and velocity characterising the reconstructed flood event. The good agreement between hazard level and photos of the event is promising. However, some local alterations of the flow field (e.g. due to artifacts, urban furniture), which are not captured by the hydrodynamic models can significantly affect the probability of a parked vehicle starting to move. Many factors might be responsible of the actual destabilization of parked vehicles such as:

- Congestion of vehicles
- Duration and persistency of mobilization conditions (i.e. $H_{azV} > 1$)
- Presence of artifacts or other immovable obstructions
- Local turbulent flow effects.



FIGURE 6.14: The night of the flood, photo taken at location c (Figure 6.11, courtesy of S. Gabellani, CIMA Research Foundation).



FIGURE 6.15: The night of the flood, photo taken at location d (Figure 6.11, from:www.adnkronos.it).



FIGURE 6.16: The night of the flood, photo taken at location d (Figure 6.11, from: www.meteoweb.eu./2014)

Nevertheless, the hazard to vehicles, tentatively and qualitatively validated using photos during and after the flood event, might represent a crucial information to be added to the current hazard maps in order to improve the support to flood risk management strategies.

6.5 Summary

In this chapter, two cases studies to illustrate the application of the mobility parameter introduced for vehicles and pedestrians are presented. Hazard criteria have been defined as ratios between critical mobility parameters (θ_{Vcr} for vehicles and θ_{Pcr} for people) as a function of Froude number and mobility parameters (θ_V for vehicles and θ_P for people). The hydraulic study provided by CEREMA about the city of Ajaccio in Corsica and the hydrologic-hydraulic reconstruction of the 2014 flood in Genova provided by CIMA Research Foundation demonstrate the applicability of the proposed hazard criteria over existing flood maps representing water depth and velocity. The differences found between hazard levels for vehicles and people confirm the reports on the flood-related fatalities since both the case studies show higher hazard levels for vehicles than for people. The qualitative comparison between hazard maps and pictures taken during the flood event for the case of Genova allow to partially and tentatively validate the proposed hazard criteria. However, many local variables such as congestion of vehicles, presence of artifacts and local turbulent flow effects, beside the duration in time of a certain hazard level may significantly affect the results. The hazard maps are a static and simplified representation of the phenomenon and other applications could further help in evaluating the reliability of the method. Nevertheless, the results of the preliminary applications in the two case studies are promising. The contents of the chapter are graphically summarized in Figure 6.17.

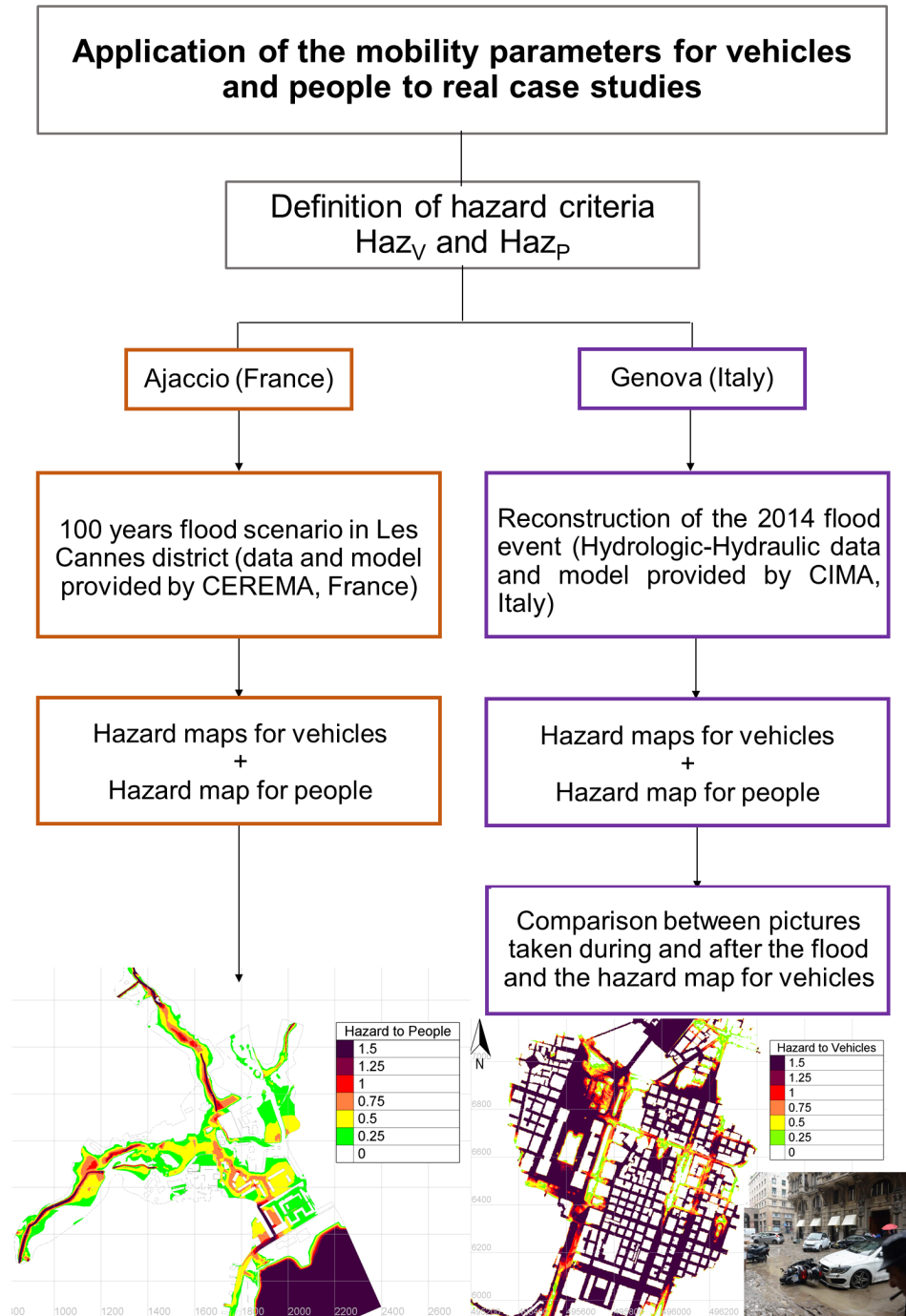


FIGURE 6.17: Graphical summary of chapter 6.

Chapter 7

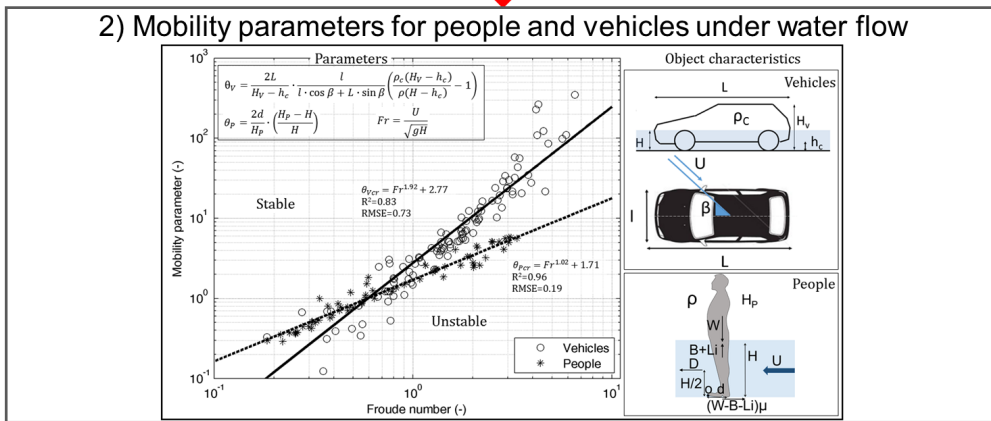
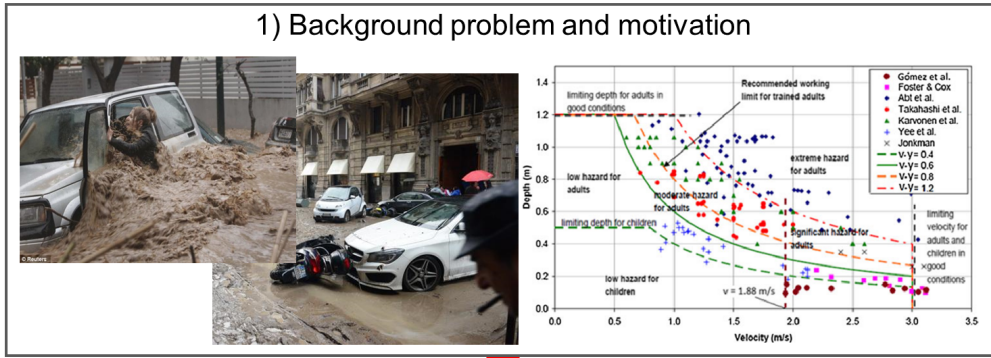
Summary, conclusions and outlook

7.1 General summary

The European flood directive 60/2007/EC requires to identify the areas prone to floods and the significant hazard to people, environment (both natural and anthropic) and cultural heritage. As often reported on people fatalities by floods, people are exposed to high risk when they attempt to drive or move on foot in floodwaters. As a matter of fact, often the casualties are due to inappropriate and high-risk behaviours. Instability mechanisms for parked vehicles and people have been investigated so far through conceptual models and through experiments on scale car models and human subjects. However, the existing experimental datasets are extremely scattered because the results are presented in terms of dimensional critical pairs of water depth H and flow velocity U averaged over H . For vehicles, two characteristics, namely chassis elevation and vehicle weight, are crucial and strongly affect the onset of motion; thus each vehicle model starts to move for different H - U pairs. The existing hazard criteria for people, which are mostly based on the product number $H \cdot U$, are associated with a significant scatter of the experimental data. Moreover, they suffer from a limited connection between flow regimes and physical consequences on people. Thus, this study is aimed at describing the instability conditions for flooded vehicles and pedestrians using a new approach based on dimensionless parameters, which can account for both flood and object characteristics. Moreover, this approach is easier to apply to real urban floods (at full scale) in order to support flood risk management strategies, particularly non-structural mitigation measures such as people education in flood prone areas. The direct transfer of the approach from laboratory scale to full scale was made possible thanks to the absence of scale effects using Froude scaling, which was clearly demonstrated using a 3D hydrodynamic model (CFD). The overall structure as well as the key milestones of this research study, starting from the motivations up to the field scale application of the findings, are graphically summarised in Figure 7.1.

7.2 Mobility parameters and numerical modelling

The analysis of the forces on a partly submerged flooded vehicle was carried out in chapter 3. The manipulation of the equation for sliding equilibrium allowed identifying a dimensionless mobility parameter θ_V , which can describe the incipient motion conditions for different vehicles geometries, densities, scales and angles of flow incidence. The mobility parameter calculated for the experimental H & U -pairs allows us to identify a unique threshold of incipient motion depending on the flow regime described by the Froude number. The results of a sensitivity analysis of the mobility parameter with respect to the variation of water depth H and average flow velocity U confirmed the absence of a spurious correlation between θ_V and Froude number. For people instability, two motion mechanisms were considered, namely sliding and toppling. Similarly to vehicles, the



balance of forces on a human body has been considered. Despite the consideration of two different motion mechanisms, the obtained dimensionless mobility parameters θ_P , which depend on water depth, height of the subject and length of the foot, are the same for both sliding and toppling. The mobility parameter calculated for a selection of existing experiments on human instability in floods allowed us to overcome the significant scatter associated with the common use of the dimensional critical H&U-pairs and to achieve a unique critical threshold of instability. As both mobility parameters describing people and vehicle incipient motion are dimensionless, the critical conditions for people and vehicles can be compared. Since the threshold curves intersect each other, the mobility diagram is divided into four portions, highlighting the flow regimes under which moving on foot is safer than driving a car and vice versa. Such a diagram provides a new insight for developing behavioural rules and supporting urban flood risk mitigation measures and civil defence actions. In order to better understand the role of hydrodynamic forces in the onset of motion, a set of CFD simulations have been carried out in OpenFOAM using a detailed 3D geometric representation of a Ford Focus and of a human body. Simplifications of the model construct was necessary and in order to reduce the computational effort, the mesh size was kept as coarse as feasible without affecting the estimated forces. Moreover, the turbulence is not considered in order to avoid calibration/validation phase of the turbulence coefficients, which anyway could not have been possible with the existing experimental data. For the vehicles, two scales (i.e. 1:18 and prototype) and different angles of flow incidence (0° , 180° , 90° , 65°) were considered in the numerical simulations. Forces and force coefficients calculated by the numerical code after a direct integration of pressures on the affected surface have shown a strong dependence on the flow regime, confirming the high relevance of the Froude number. The comparison between numerical results and experimental data have shown a relatively good agreement despite the simplifications of the numerical model. For the people, four human subjects and a human scale model were considered in the numerical simulations. Forces and forces coefficients calculated from the simulations allowed identifying the two motion mechanisms described in the literature and the two most relevant dimensionless parameters, namely Froude number and relative submergence. The evaluation of the forces also quantitatively demonstrates the importance of the ability of people to react to instability adjusting the body position, which of course cannot be achieved by a human model. The comparison between experiments and numerical model showed generally a relatively good agreement and even a better performance of the CFD model, when considering only the results on human subjects. Since the numerical model confirmed the absence of scale effects, it allowed extending the use of the mobility parameters to field scale. Two case studies have been shown: Ajaccio (France) and Genova (Italy). Hazard criteria have been developed and applied to the existing inundation maps. For the case study of Genova, a partial verification of the hazard maps was possible through the comparison with the picture taken during the 2014 flood event. The agreement between hazard maps and pictures is very promising for the applications to further case studies where more quantitative information and data are available for a final validation of the approach.

7.3 Limitations of the results

The following limitations of this research study are particularly addressed below:

- Limitations of the mobility parameters for vehicles and pedestrians
- Limitations of the numerical model

- Limitations of the applicability of the mobility parameters to urban flood scale

The mobility parameters for both vehicles and people have been introduced to overcome the scatter of dimensional datasets, thus they rely on some crucial parameters of the movable bodies. The mobility parameter for vehicles is sensitive to the elevation of the chassis of the car, which composes the shape factor of the parameter. The numerical model showed that assuming the car as a rigid body may lead to some errors in the determination of the instability conditions since a vehicle can move vertically due to the presence of the suspensions. The effect of the variability of the chassis elevation should be further investigated both in the dimensional analysis and in the numerical simulations. The mobility parameter for people depends on the length of the foot of the subjects, which is a very sensitive parameter. The length of the foot is usually derived from standard ratios with respect to the height of the subject. However, this parameter, assumed equal to the lever arm of resisting forces, can vary according to the displacement of the center of mass of the human body, which usually tends to resist against flow destabilization. A proper account for the changes of the posture depending on the flow would also require a consideration of the psychological and physical reactions of the subjects. Regarding numerical modelling, the main limitations reside in the simplifications in the model and in the model set up without consideration of a finer mesh, local turbulence effects and actual detailed geometry of the semi-submerged bodies. In fact, it was not the intention of this research to investigate local small-scale turbulent effects, the objectives of the numerical simulations were mostly the identification of the most relevant dimensionless parameters and scaling numbers associated with the mean flow for which experimental data for validation are available from previous studies. Further studies could properly investigate the flow around vehicles/people with a very fine mesh capable of capturing small-scale phenomena. This would consequently require more computational resources. Also an appropriate selection of a turbulence model would require some *ad hoc* experimental studies to record water depths and velocities in a laboratory flume in order to carry out a calibration/validation study. Finally, different vehicles models should be studied. In fact, the results of the forces evaluation for a Ford Focus do not apply to other types of vehicle, which can differ in shape and elevation of the chassis. Similarly, for people the effect of further parameters on the forces, such as body type and build, clothing, posture etc., should also be investigated. The reliability of the flood hazard maps generated in the two case studies is affected by the type of the inundation model used. As the focus was put on the mean flow to map the water depths and the mean flow velocities over large flood prone areas, the state of the art model TELEMAC-2D was selected as the most appropriate available open source code for this purpose. As expected and as finally shown in chapter 6, many local effects, which may affect the results, can neither be captured by the available inundation models as the latter generally focus on the mean flow over larger areas nor can they be accounted for by the proposed hazard criteria which are solely based on mean flow parameters. Among these non-considered effects, there are local turbulent flow effects and the effect of natural or man-made obstacles in urban areas, which deeply affect the flow field and are usually not properly considered in large-scale urban flood models. The velocity profile in a real urban flood would not be as regular as in TELEMAC-2D, which is based on 2D depth averaged equations. Moreover, the hazard criteria do not account for congested conditions and hiding effects due to the presence of many cars parked in the streets.

7.4 Outlook

The mobility parameters for vehicles and people have proved to be a valuable tool for hazard mapping, overcoming the scatter of existing experimental datasets. The numerical model, although simplified, clarified the role of the mean flow regime in the mechanisms of incipient motion. Future studies could deepen and extend the numerical part of the work by considering the effects of more refined turbulence approaches. Numerical simulations representing the car/person as a six degrees of freedom movable body could also be very interesting in order to dynamically model at the urban scale the vehicles entrainment. On the side of social and communication sciences, the work could be extended in order to develop safety manuals providing behavioural rules and possibly designing traffic signs and emergency protocols. Finally, borrowing the widely used definition of flood risk as product of hazard, vulnerability and exposure, a risk assessment methodology for street networks could be introduced, based on hazard maps for vehicles and people generated for different flood scenarios.

References

- Aboelata, M. & Bowles, D.S. 2005. LIFESim : A Model for Estimating Dam Failure Life Loss. , Report to Institute for Water Resources, US Army Corps of Engineers and Australian National Committee on Large Dams.
- Aboelata, M. & Bowles, D.S., 2008. LIFESim : A Tool for Estimating and Reducing Life-Loss Resulting from Dam and Levee Failures. *Proceedings of the Association of State Dam Safety Officials "Dam Safety 2008" Conference*.
- Abt, S.R., Wittler, R.J., Taylor, A., Love, D.J., 1989. Human Stability in a High Flood Hazard Zone1. *JAWRA Journal of the American Water Resources Association*, 25(4), pp.881–890. Available at: <http://dx.doi.org/10.1111/j.1752-1688.1989.tb05404.x>.
- Alcrudo, F., 2004. Mathematical modeling techniques for flood propagation in urban areas. *Impact Project Report*, available at: http://www.impact-project.net/AnnexII_DetailedTechnicalReports/AnnexII_PartB_WP3/Modelling_techniques_for_urban_flooding.pdf
- Anderson, J., 1995. Computational Fluid Dynamics: The Basics with Applications. 1995. *McGrawhill Inc*, pp.1–547. Available at: <http://scholar.google.com/scholar?hl=en&btnG=Search&q=intitle:Computational+Fluid+Dynamics+the+Basics+With+Applications#2>.
- Apel, H., Aronica, G., Kreibich, H., Thielen, A., 2009. Flood risk analyses - How detailed do we need to be? *Natural Hazards*, 49(1), pp.79–98.
- Arrighi, C., Alcèrreca-Huerta J.C., Oumeraci, H., Castelli, F., 2015. Drag and lift contribution to the incipient motion of partly submerged flooded vehicles. *Journal of Fluids and Structures*, 57, pp.170–184. Available at: <http://www.sciencedirect.com/science/article/pii/S0889974615001498>.
- Arrighi, C., Brugioni, M., Franceschini, S., Castelli, F., Mazzanti B., 2013. Urban micro-scale flood risk estimation with parsimonious hydraulic modelling and census data. *Natural Hazards and Earth System Science*, 13(5), pp.1375–1391. Available at: <http://www.nat-hazards-earth-syst-sci.net/13/1375/2013/>.
- Arslan, T., Malavasi, S., Pettersen, B., Andersson, H., 2013. Turbulent Flow Around a Semi-Submerged Rectangular Cylinder. *Journal of Offshore Mechanics and Arctic Engineering*, 135(4), p.041801. Available at: <http://offshoremechanics.asmedigitalcollection.asme.org/article.aspx?doi=10.1115/1.4025144>.

- Ataie-Ashtiani, B. & Aslani-Kordkandi, A., 2013. Flow field around single and tandem piers. *Flow, Turbulence and Combustion*, 90(3), pp.471–490.
- Barredo, J.I., 2009. Normalised flood losses in Europe: 1970–2006. *Natural Hazards and Earth System Science*, 9(1), pp.97–104.
- Bates, P.D. & De Roo, a P.J., 2000. A simple raster based model for flood inundation simulation. *Journal of Hydrology*, 236(1-2), pp.54–77.
- Bearman, P.W. & Morel, T., 1983. Effect of free stream turbulence on the flow around bluff bodies. *Progress in Aerospace Sciences*, 20(2-3), pp.97–123. Available at: <http://www.sciencedirect.com/science/article/pii/0376042183900027> [Accessed November 26, 2015].
- Beckers, J.V.L., De Bruijn, K.M. Riedstra, D., 2011. Life safety criteria for flood protection standards. *5th International Conference on Flood Management*, p.2600.
- Begnudelli, L., Sanders, B.F., Bradford, S.F., 2008. Adaptive Godunov-Based Model for Flood Simulation. *Journal of Hydraulic Engineering*, 134(6), pp.714–725.
- Bertin, J.J. and Smith, M.L. 1979. *Aerodynamics for Engineers*, Prentice-Hall, Englewood Cliffs, New Jersey, 410pp.
- Bohorquez, P., 2008. Computational continuum mechanics for sediment transport in free-surface flow. *Open Source CFD International Conference 2008*, p.17. Available at: http://powerlab.fsb.hr/ped/kturbo/openfoam/Berlin2008/Papers/OSCIC-08_BohorquezPatricio.pdf.
- de Bruijn, K.M., Diermanse, F.L.M. & Beckers, J.V.L., 2014. An advanced method for flood risk analysis in river deltas, applied to societal flood fatality risk in the Netherlands. *Natural Hazards and Earth System Science*, 14(10), pp.2767–2781. Available at: <http://www.nat-hazards-earth-syst-sci.net/14/2767/2014/>.
- Büchle, B., Kreibich, H., Kron, A., Thieken, A., Ihringer, J., Oberle, P., Merz, B., Nestmann, F., 2006. Flood-risk mapping: Contributions towards an enhanced assessment of extreme events and associated risks. *Natural Hazards and Earth System Sciences*, 6(4), pp.483–503.
- Burzel, A., Dassanayake, D.R. and Oumeraci, H. (2015): Spatial Modelling of Tangible and Intangible Losses in Integrated Coastal Flood Risk Analysis. *Coastal Engineering Journal* Vol. 57, No. 01, 154000.
- Campana, E.F., Peri, D., Tahara, Y., Stern, F., 2006. Shape optimization in ship hydrodynamics using computational fluid dynamics. *Computer Methods in Applied Mechanics and Engineering*, 196(1-3), pp.634–651. Available at: <http://www.sciencedirect.com/science/article/pii/S0045782506001927> [Accessed November 26, 2015].
- Campbell, R.L. & Paterson, E.G., 2011. Fluid-structure interaction analysis of flexible

- turbomachinery. *Journal of Fluids and Structures*, 27(8), pp.1376–1391. Available at: <http://dx.doi.org/10.1016/j.jfluidstructs.2011.08.010>.
- Canadian Institute of Hydraulics (CHC), 2011. Blue Kenue Reference Manual.
- Chakraborty, J., Tobin, G. a. & Montz, B.E., 2005. Population Evacuation: Assessing Spatial Variability in Geophysical Risk and Social Vulnerability to Natural Hazards. *Natural Hazards Review*, 6(1), pp.23–33.
- Chanson, H., Brown, R. & McIntosh, D., 2014. Human body stability in floodwaters: the 2011 flood in Brisbane CBD. *Hydraulic structures and society - Engineering challenges and extremes*, (January 2011), pp.1–9. Available at: <http://espace.library.uq.edu.au/view/UQ:329775>.
- Chapman, R.B., 1972. Hydrodynamic Drag of semisubmerged ships. *J. Fluids Eng.* 94 (4), 879-884.
- Chen, A.S., Evans, B., Djordjevic, S., Savic, D.A., 2012. A coarse-grid approach to representing building blockage effects in 2D urban flood modelling. *Journal of Hydrology*, 426-427, pp.1-16.
- Cobby, D.M., Mason, D.C. & Davenport, I.J., 2001. Image processing of airborne scanning laser altimetry data for improved river flood modelling. *ISPRS Journal of Photogrammetry and Remote Sensing*, 56(2), pp.121–138.
- Correia, F. & Rego, F., 1998. Coupling GIS with hydrologic and hydraulic flood modelling. *Water Resources*, pp.229–249.
- Cox, R.J. & Ball E.J., 2001. Stability and safety in flooded streets. Proceedings of the 6th Conference on hydraulics in Civil Engineering. The institution of Engineers, Australia.
- Cunge, J. A., 1969. On The Subject Of A Flood Propagation Computation Method (Muskingum Method). *Journal of Hydraulic Research*, 7(2), pp.205–230.
- Dassanayake, D.R., Burzel, A. and Oumeraci, H. 2015. Methods for the Evaluation of Intangible Flood Losses and their Integration in Flood Risk Analysis. *Coastal Engineering Journal Vol. 57, No. 01, 1540007*
- Deckers, P., 2010. Geospatial Techniques in Urban Hazard and Disaster Analysis. , pp.51–69. Available at: <http://link.springer.com/10.1007/978-90-481-2238-7>.
- Deshpande, S.S., Anumolu, L. & Trujillo, M.F., 2012. Evaluating the performance of the two-phase flow solver interFoam. *Computational Science & Discovery*, 5(1), p.014016. Available at: <http://iopscience.iop.org/1749-4699/5/1/014016/article/>
- Dolia D., 2015. Flooding scenarios in urban area with an open source 2D hydraulic model: the case of the Bisagno creek in Genoa. Master thesis submitted to the Genoa University, Italy.

- Elmer, F., Hoymann, J., Duethmann, D., Vorogushyn, S., Kreibich, H., 2012. Drivers of flood risk change in residential areas. *Natural Hazards and Earth System Science*, 12(5), pp.1641-1657.
- EM-DAT, 2012. Disasters in numbers. , (October 2012).
- Eriksson, P., 2007. The Zimont TFC Model Applied to Premixed Bluff Body Stabilized Combustion Using Four Different RANS Turbulence Models. Proceedings of ASME GT2007, 2.
- Ernst, J., Dewals, B., Detrembleur, S., Archambeau, P., Ercicum, S., Piroton, M., 2010. Micro-scale flood risk analysis based on detailed 2D hydraulic modelling and high resolution geographic data. *Natural Hazards*, 55(2), pp.181-209.
- Falter, D., Vorogushyn, S., Lhomme, J., Apel, H., Gouldby, B., Merz, B., 2013. Hydraulic model evaluation for large-scale flood risk assessments. *Hydrological Processes*, 27(9), pp.1331-1340.
- Faltinsen, O.M., 2006. Hydrodynamics of high speed marine vehicles. Cambridge University Press.
- Ferziger, J.H., Peric, M., 2002. *Computational Methods for Fluid Dynamics.pdf*, Springer.
- Finaud-Guyot, P., Delenne, C., Guinot, V., Llovel, C., 2011. 1D-2D coupling for river flow modeling. *Comptes Rendus Mécanique*, 339(4), pp.226-234. Available at: <http://www.sciencedirect.com/science/article/pii/S163107211100026X>.
- Fitzgerald, G., Du, W., Jamal, A., Clark, M., Hou, X., 2010. Flood fatalities in contemporary Australia (1997-2008): Disaster medicine. *EMA - Emergency Medicine Australasia*, 22(2), pp.180-186.
- Fox, R.V. and McDonald, A.T.: Introduction to Fluid Mechanics, 2nd ed. John Wiley & Sons, N.Y. 684 pp.
- Franklin, R.C., King, J., Aitken, P., Leggat, P., 2014. "Washed away"-assessing community perceptions of flooding and prevention strategies: A North Queensland example. *Natural Hazards*, 73(3), pp.1977-1998.
- Galland, J.C., Goutal, N. & Hervouet, J.M., 1991. {TELEMAC}: A new numerical model for solving shallow water equations. *Adv. Water Resources*, 14(3), pp.138-148.
- Genovese, E., 2006. A methodological approach to land use-based flood damage assessment in urban areas: Prague case study. *European Communities, DG-JRC, Ispra, EUR*. Available at: http://www.preventionweb.net/files/2678_EUR22497EN.pdf.
- Gifford-Miears, C. and A.S. Leon, 2013. Tutorial on the use of TELEMAC-2D Hydrodynamics model and Pre-/Post-processing with BlueKenue for flood-inundation mapping in unsteady flow conditions. [online].

- Gilles, D. & Moore, M., 2010. Review of Hydraulic Flood Modeling Software used in Belgium , The Netherlands , and The United Kingdom. *Europe*.
- Helmiö, T., 2002. Unsteady 1D flow model of compound channel with vegetated floodplains. *Journal of Hydrology*, 269, pp.89–99.
- Hervouet, J.M., Samie, R. & Moreau, B., 2000. Modelling urban areas in dam-break flood-wave numerical simulations. *Proceedings the International Seminar and Workshop on Rescue Actions Based on Dambreak Flow Analysis*, p.14.
- Hoerner, S.F.: Fluid dynamic drag: theoretical, experimental and statistical information. Hoerner Fluid Dynamics ISBN-10: 9993623938, 1965.
- Horritt, M.S. & Bates, P.D., 2002. Evaluation of 1D and 2D numerical models for predicting river flood inundation. *Journal of Hydrology*, 268(1-4), pp.87–99.
- Huang, S., Rauberg, J., Apel, H., Lindenschmidt, K.E, 2007. The effectiveness of polder systems on peak discharge capping of floods along the middle reaches of the Elbe River in Germany. *Hydrology and Earth System Sciences Discussions*, 4(1), pp.211–241.
- Hunter, N.M., Bates N., Neelz, P., Pender, G., Villanueva I, Wright, N., Liang, D., Falconer, R., Lin, B., Waller, S., Crossley, A., Mason D., 2008. Benchmarking 2D hydraulic models for urban flooding. Available at: <http://dx.doi.org/10.1680/wama.2008.161.1.13>.
- Hunter, N.M. , Bates, P., Horritt, M., Wilson, M., 2007. Simple spatially-distributed models for predicting flood inundation: A review. *Geomorphology*, 90(3-4), pp.208–225.
- Jacobsen, N.G., Fuhrman, D.R., Fredsoe, J., 2011. A Wave Generation Toolbox for the Open-Source CFD Library: OpenFoam. *International Journal of Numerical Methods in Fluids*, 70-9, 1073-1088.
- Jasak, H., 1996. Error Analysis and Estimation for the Finite Volume Method with Applications to Fluid Flows. PhD Thesis Imperial College, London, UK.
- Jonkman, S.N., 2007. *Loss of life estimation in flood risk assessment - theory and applications*. PhD thesis, available at: <http://library.wur.nl/ebooks/hydrotheek/1875249.pdf>
- Jonkman, S.N., Gelder, P.H. a J.M. Van & Vrijling, J.K., 2002. Loss of life models for sea and river floods. *Public Works*, 2000, pp.196–206.
- Jonkman, S.N. & Kelman, I., 2005. An analysis of the causes and circumstances of flood disaster deaths. *Disasters*, 29(1), pp.75–97.
- Jonkman, S.N., Kok, M. & Vrijling, J.K., 2008. Flood risk assessment in the Netherlands: A case study for dike ring South Holland. *Risk Analysis*, 28(5), pp.1357–1373.

- Jonkman, S.N. & Penning-Rowsell, E., 2008. Human instability in flood flows. *Journal of the American Water Resources Association*, 44(5), pp.1208–1218.
- Karvonen, R.A., Hepojoki, H.K., Huhta, H.K. and A. Louhio, 2000. The use of physical models in dam-break analysis. *RESCDAM Final Report*, Helsinki University of Technology, Helsinki, Finland.
- Kendall, M.G., & Stuart, A., 1973. *The Advanced Theory of Statistics, Volume 2* (3rd Edition), ISBN 0-85264-215-6.
- Kim, H.S., Nabi, M., Kimura, I., Shimizu, Y. 2015. Computational modelling of flow and morphodynamics through rigid-emergent vegetation. *Advances in Water Resources*, 84, 64-86.
- Kreibich, H., Piroth, K., Seifert, H., Maiwald, H., Kunert, U., Schwarz, J., Merz, B. and A. H. Thielen, 2009. Is flow velocity a significant parameter in flood damage modelling? *Natural Hazards and Earth System Science*, 9(5), pp.1679–1692.
- Lee, A.H., Campbell, R.L. & Hambric, S. A., 2014. Coupled delayed-detached-eddy simulation and structural vibration of a self-oscillating cylinder due to vortex-shedding. *Journal of Fluids and Structures*, 48, pp.216–234. Available at: <http://dx.doi.org/10.1016/j.jfluidstructs.2014.02.019>.
- Lehner, B., Doll, P., Alcamo, J., Henrichs, T., Kaspar, F., 2006. Estimating the impact of global change on flood and drought risks in Europe: A continental, integrated analysis. *Climatic Change*, 75(3), pp.273–299.
- Lind, N., Hartford, D. & Assaf, H., 2004. Hydrodynamic models of Human Stability in a Flood. *Journal of the American Water Resources Association*, 8, pp.89 – 96.
- Lindenschmidt, K.E., Herrman, U, Pech, I., Suht, U., Apel, H., Thielen, A., 2006. Risk assessment and mapping of extreme floods in non-dyked communities along the Elbe and Mulde Rivers. *Advances in Geosciences*, 9, pp.15–23.
- Lindmeier, I., Heschl, C., Clauss, G., Heck, U., 2010. Prediction of the flow around 3D obstacles using open source CFD-Software. *The Fifth International Symposium on Computational Wind Engineering*.
- Liu, X. & Ph, D., 2013. Modeling of Earth Surface Dynamics and Related Problems Using OpenFOAM®. A brief introduction of OpenFOAM.
- Losada, I.J., Lara, J.L., Christensen, E.D., Garcia, N., 2005. Modelling of velocity and turbulence fields around and within low-crested rubble-mound breakwaters. *Coastal Engineering*, 52, 887-913.
- Love, D.J., 1987. Analysis of a high hazard flood zone. Technical Report prepared for City of Boulder Public Works Department, Boulder, Colorado.
- Lugeri, N., Genovese, E., Lavallo, C., De Roo, A., 2006. Flood risk in Europe : analysis of exposure in 13 Countries. EUR 22525 EN Report.

- Luino, F., Turconi, L., Petrea, C., Nigrelli, G., 2012. Uncorrected land-use planning highlighted by flooding: The Alba case study (Piedmont, Italy). *Natural Hazards and Earth System Science*, 12(7), pp.2329–2346.
- Lumley, J.L., 1977. Computational modelling of turbulent flows. *Advances in Applied Mechanics*, 18, 124-174.
- Lung, T., Lavelle, C., Hiederer, R., Dosio, A., Bouwer, L., 2013. A multi-hazard regional level impact assessment for Europe combining indicators of climatic and non-climatic change. *Global Environmental Change*, 23(2), pp.522–536. Available at: <http://dx.doi.org/10.1016/j.gloenvcha.2012.11.009>.
- Ma, Q., Abily, M., Vo, N.D., Gourbesville, P., 2015. High Resolution Rainfall-Runoff Simulation in Urban Area: Assessment of Telemac-2D and Fullswof-2D. *E-proceedings of the 36th IAHR World Congress*, (1), pp.1–8.
- Malavasi, S. & Guadagnini, A., 2003. Hydrodynamic Loading on River Bridges. *Journal of Hydraulic Engineering*, 129(11), pp.854–861.
- Mansoorzadeh, S., Javanmard, E., 2014. An investigation of free surface effects on drag and lift coefficients of an autonomous underwater vehicle (AUV) using computational and experimental fluid dynamics methods. *Journal of Fluids and Structures*, 51, 161-171.
- Maples, L.Z. & Tiefenbacher, J.P., 2009. Landscape, development, technology and drivers: The geography of drownings associated with automobiles in Texas floods, 1950-2004. *Applied Geography*, 29(2), pp.224–234. Available at: <http://dx.doi.org/10.1016/j.apgeog.2008.09.004>.
- Mauro, D., Lumbroso, D., 2008. Recent developments in loss of life modelling for flood defence and dam break risk assessments. HR Wallingford.
- Di Mauro, M., De Bruijn, K.M. & Meloni, M., 2012. Quantitative methods for estimating flood fatalities: towards the introduction of loss-of-life estimation in the assessment of flood risk. *Natural Hazards*, 63(2), pp.1083–1113. Available at: <http://link.springer.com/10.1007/s11069-012-0207-4>.
- Meridith K., 2010. The examination of vehicle related flood fatalities, PhD Thesis, pp.1995–2005.
- Merz, B., Kreibich, H., Thielen, A., Schmidtke, R., 2004. Estimation uncertainty of direct monetary flood damage to buildings. *Natural Hazards and Earth System Science*, 4(1), pp.153–163.
- Merz, B., Kreibich, H., Schwarze, R., Thielen, A., 2010. Review article “assessment of economic flood damage.” *Natural Hazards and Earth System Science*, 10(8), pp.1697–1724.
- Messner, F. & Meyer, V., 2007. Evaluating flood damages: guidance and recommendations on principles and methods principles and methods. *Flood*

Risk Management: Hazards, Vulnerability and Mitigation Measures, p.189.

- Meyer, V. N. Becker, V. Markantonis, R. Schwarze, J. C. J. M. van den Bergh, L. M. Bouwer, P. Bubeck, P. Ciavola, E. Genovese, C. Green, S. Hallegatte, H. Kreibich, Q. Lequeux, I. Logar, E. Papyrakis, C. Pfurtscheller, J. Poussin, V. Przyluski, A. H. Thieken, and C. Viavattene. Review article: Assessing the costs of natural hazards-state of the art and knowledge gaps. *Natural Hazards and Earth System Science*, 13(5), pp.1351–1373.
- Meyer, V. & Messner, F., 2005. National flood damage evaluation methods : A review of applied methods in England, the Netherlands, the Czech republic and Germany. , p.49.
- Mignot, E., Paquier, A., Haider, S., 2006. No Title. *Journal of Hydrology*, 2, pp.186–199.
- Milanesi, L., Pilotti, M., Ranzi, R., 2015. A conceptual model of people’s vulnerability to floods. *Water Resources Research*, pp.7206–7230. 10.1002/2014WR016172
- de Moel, H., van Alphen, J. & Aerts, J.C.J.H., 2009. Flood maps in Europe – methods, availability and use. *Natural Hazards and Earth System Science*, 9(2), pp.289–301.
- Moser, R.D., Kim, J. & Mansour, N.N., 1999. Direct numerical simulation of turbulent channel flow up to $Re = 590$. *Physics of Fluids*, 11(4), pp.943–945. Available at: <http://link.aip.org/link/PHFLE6/v11/i4/p943/s1&Agg=doi>.
- Munich RE, 2012. Great natural catastrophes worldwide 1950 – 2011 Number of events with trend.
- Munich Re, 2015a. Loss events worldwide 1980 – 2014 10 costliest events ordered by overall losses. , (January 2015).
- Munich Re, 2015b. Loss events worldwide 2014. , (January 2015).
- Nagata, N., Hosoda, T., Nakato, T. 2005. Three-Dimensional Numerical Model for Flow and Bed Deformation around River Hydraulic Structures. *Journal of Hydraulic Engineering*, 131, 12, 1074-1087.
- Oliveri, E. & Santoro, M., 2000. Estimation of urban structural flood damages: the case study of Palermo. *Urban Water*, 2(3), pp.223–234. Available at: <http://www.sciencedirect.com/science/article/pii/S1462075800000625> [Accessed November 24, 2015].
- Olsen, N.R.B. and S. Stokseth (2010). Three-dimensional numerical modelling of water flow in a river with large bed roughness. *Journal of Hydraulic Research*, 33, 4, 571-581.
- Open V FOAM, (2013). The Open Source CFT toolbox. User Guide.
- Oumeraci, H., Kortenhaus, H., Burzel, A., Naulin, M., Dassanayake, D.R., Jensen, J

- Wahl, T., Mudersbach, C., Gonnert, G., Gerkenmeier, B., Frohle, P. and Ujeyl, G. 2015. XtremRisk - Integrated Flood Risk Analysis for Extreme Storm Surges at Open Coasts and in Estuaries: Methodology, Key Results and Lessons Learned. *Coastal Engineering Journal* Vol. 57, No. 01, 1540001
- Ozmen-Cagatay, H., Kocaman, S., Guzel, H., 2014. Investigation of dam-break flood waves in a dry channel with a hump. *Journal of Hydro-environment Research*, 8, 304-315.
- Papadakis, G., Voutsinas, S., Sieros, G., Chaviaropoulos, T., 2014. CFD aerodynamic analysis of non-conventional airfoil sections for very large rotor blades. *Journal of Physics: Conference Series*, 555, 1-11.
- Pan, D. Z. & Chanson, H. (2015): Physical modelling of tidal bore dyke overtopping: implication on individuals' safety. E-proceedings of the 36th IAHR World Congress 28 June - 3 July, 2015, The Hague, the Netherlands.
- Parlamento Europeo, 2007. Direttiva 2007/60/CE relativa alla valutazione e alla gestione dei rischi di alluvioni. *Gazzetta Ufficiale dell'Unione Europea*, pp.27-34.
- Penning-Rowsell, E., Floyd, P., Ramsbottom, D., Surendan, S., 2005. Estimating injury and loss of life in floods: A deterministic framework. *Natural Hazards*, 36(1-2), pp.43-64.
- Prasad, B., Hino, T., Suzuki, K., 2015. Numerical simulation of free surface flows around shallowly submerged hydrofoil by OpenFOAM. *Ocean Engineering*, 102, 87-94.
- R. J. Cox, T. D. Shand, and M.J.Blacka., 2010. *Australian Rainfall & Runoff; Revision Project 10: Appropriate Safety Criteria for People*,
- Rodi, W., 1997. Comparison of LES and RANS calculations of the flow around bluff bodies. *Journal of Wind Engineering and Industrial Aerodynamics*, 69-71, pp.55-75.
- Russo, B., Gomez, M., Martinez, P., Sanchez, H., 2005. Methodology to study the surface runoff in urban streets and the design of drainage inlets systems. Application in a real case study. *10th International Conference on Urban Drainage*, (August), pp.1-8.
- Russo, B., Gómez, M. & Macchione, F., 2013. Pedestrian hazard criteria for flooded urban areas. *Natural Hazards*, 69(1), pp.251-265.
- Samarasinghe, S., Nandalal, H.K., Weliwitiya, D., Fowze, J., Hazarika, M., K., Samarakoon, L., 2010. Application of Remote Sensing and GIS for Flood Risk Analysis: A Case Study at Kalu - Ganga River, Sri Lanka. *International Archives of the Photogrammetry, Remote Sensing and Spatial Information Science*, XXXVIII(8), pp.110-115.
- Savitsky, D., Ward-Brown, P., 1976. Procedures for Hydrodynamic Evaluation of Planing Hulls in Smooth Rough Water.

- Scardovelli, R. & Zaleski, S., 1999. Direct Numerical Simulation of Free-Surface and Interfacial Flow. *Annual Review of Fluid Mechanics*, 31(1), pp.567–603.
- Silvestro, F., Rebori, N., Giannoni, F., Cavallo, A., Ferraris, L., 2016. The flash flood of the Bisagno creek on the 9th October 2014: An unfortunate combination of spatial and temporal scales. *Journal of Hydrology*, in press.
- Silvestro, F., Rebori, N., Rossi, L., Dolia, D., Gabellani, S., Pignone, F. Masciulli, C., 2015. What if the 25th October 2011 event that stroke Cinque Terre (Liguria) had happened in Genoa, Italy? Flooding scenarios, hazard mapping and damages estimation. Article in preparation.
- Schubert, J.E. & Sanders, B.F., 2012. Building treatments for urban flood inundation models and implications for predictive skill and modeling efficiency. *Advances in Water Resources*, 41, pp.49–64. Available at: <http://dx.doi.org/10.1016/j.advwatres.2012.02.012>.
- Scorzini, A. R. & Frank, E., 2015. Flood damage curves: new insights from the 2010 flood in Veneto, Italy. *Journal of Flood Risk Management*, p.n/a–n/a. Available at: <http://doi.wiley.com/10.1111/jfr3.12163>.
- Shand, T.D., Cox, R.J., Blacka, M.J., Smith, G., 2013. Australian Rainfall and Runoff, Project 10: Appropriate safety design criteria for vehicles, Literature Review, pp.1–20.
- Shu, C., Xia, J., Falconer, R., Lin, B., 2011. Incipient velocity for partially submerged vehicles in floodwaters. Available at: <http://dx.doi.org/10.1080/00221686.2011.616318>.
- Smith, D., 1994. flood damage estimation-A review of urban stage-damage curves and loss function, *Water SA*, 20, pp.231–238.
- Speziale, C.G., 1991. Analytical methods for the development of Reynolds-Stress closures in turbulence. *Annual Reviews of Fluids Mechanics*, 23, 107–157.
- Sogreah, 2006. Direction Départementale de l'Équipement Corse du Sud. Evaluation du risqué pluvial sur la commune d'Ajaccio-Etude hydraulique dans les bassins versant d'Arbitronne, San Remedio at la Madonnuccia, N° 2 74 0190.
- Syme, W.J., 2008. Flooding in Urban Areas-2D Modelling Approaches for Buildings and Fences. *Engineers Australia, 9th National Conference on Hydraulics in Water Engineering, Darwin Convention Centre, Australia, (September)*, pp.23–26.
- Syme, W.J., Pinnell, M.G. & Wicks, J.M., 2004. Modelling Flood Inundation of Urban Areas in the UK Using 2D/1D Hydraulic Models. *8th Natinal Conference on Hydraulics in Water Engineering, (July)*, p.8.
- Tapsell, S.M., Penning-Rowsell, E.C., Tunstall, S.M., Wilson, T., 2002. Vulnerability to flooding: health and social dimensions. *Philosophical Transactions of the Royal Society A: Mathematical, Physical and Engineering Sciences*, 360(1796), pp.1511–

1525. Available at:
<http://rsta.royalsocietypublishing.org/cgi/doi/10.1098/rsta.2002.1013>.
- Teo, F.Y. , Xia, J., Falconer, R., Lin, B., 2012. Experimental studies on the interaction between vehicles and floodplain flows. *International Journal of River Basin Management*, 10, pp.37–41. Available at:
<http://dx.doi.org/10.1080/15715124.2012.674040>.
- Teruzzi, A., Ballio, F., Salon, S., Armenio, V., 2006. Numerical investigation of the turbulent flow around a bridge abutment. *River Flow 2006, Vols 1 and 2*, (2003), pp.667–672. Available at: <Go to ISI>://WOS:000241916500069.
- Thieken, A., Merz, B., Kreibich, H., Apel, H., 2006. Methods for flood risk assessment: concepts and challenges. *International Workshop on Flash Floods in Urban Areas*, (4-6 September), pp.1–12. Available at:
<http://www.rcuwm.org.ir/En/Events/Documents/Workshops/Articles/8/pdf>.
- Toro, E.F. 2009. *Riemann Solvers and Numerical Methods for Fluid Dynamics, a practical introduction*. Springer.
- Tseng, Y.-H., Meneveau, C. & Parlange, M.B., 2006. Modeling flow around bluff bodies and predicting urban dispersion using large eddy simulation. *Environmental science & technology*, 40(8), pp.2653–2662.
- United Nations (UN), 2015. *World Urbanization Prospects The 2014 Revision*.
- US Department of Homeland Security, 2011. *Estimating Loss of Life for Dam Failure Scenarios. Dams Sector*, (September).
- USACE, 2010. *HEC-RAS River Analysis System, Hydraulic reference manual, version 4.1*.
- Van Der Veen, A. & Logtmeijer, C., 2005. Economic hotspots: Visualizing vulnerability to flooding. *Natural Hazards*, 36(1-2), pp.65–80.
- ten Veldhuis, J. A. E., 2011. How the choice of flood damage metrics influences urban flood risk assessment. *Journal of Flood Risk Management*, 4(4), pp.281–287. Available at: <http://onlinelibrary.wiley.com/doi/10.1111/j.1753-318X.2011.01112.x/abstract> \n<http://onlinelibrary.wiley.com/store/10.1111/j.1753318X.2011.01112.x/asset/jfr31112.pdf?v=1&t=hul7o36i&s=4094adf2c702285b7fbb1b11a18667f1cef778e4>.
- Vickery, B.J., 1966. Fluctuating lift and drag on a long cylinder of square cross-section in a smooth and in a turbulent stream. *Journal of Fluid Mechanics*, 25(03), p.481.
- Walder, J.S., Watts, P. & Waythomas, C.F., 2006. Case Study : Mapping Tsunami Hazards Associated with Debris Flow into a Reservoir. *Journal of Hydraulic Engineering*, 132(January), pp.1–11.

- Ward, P.J., Jongman, B., Weiland, F., Bouwman, A., van Beek, R., Bierkens, M., Ligtoet, W., Winsemius, H., 2013. Assessing flood risk at the global scale: model setup, results, and sensitivity. *Environmental Research Letters*, 8(4), p.044019. Available at: <http://stacks.iop.org/1748-9326/8/i=4/a=044019?key=crossref.2ecb02eb38c1de207a81abed549fe415>.
- Ward, P.J., De Moel, H. & Aerts, J.C.J.H., 2011. How are flood risk estimates affected by the choice of return-periods? *Natural Hazards and Earth System Science*, 11(12), pp.3181–3195.
- World Meteorological Organization, 2008. Urban Flood Risk Management: A Tool for Integrated Flood Management. *Risk Management*, (March 2008).
- Xia, J., Falconer, R., Xiao, X., Wang, Y., 2013. Criterion of vehicle stability in floodwaters based on theoretical and experimental studies. *Natural Hazards*, 70(2), pp.1619–1630. Available at: <http://www.scopus.com/inward/record.url?eid=2-s2.0-84891120882&partnerID=tZOtx3y1>.
- Xia, J., Teo, F.Y., et al., 2011. Formula of incipient velocity for flooded vehicles. *Natural Hazards*, 58(1), pp.1–14.
- Xia, J., Falconer, R.A, Wang, Y. and Xiao, X., 2014. New criterion for the stability of a human body in floodwaters. *Journal of Hydraulic Research*, 52(1), pp.93–104. Available at: <http://dx.doi.org/10.1080/00221686.2013.875073>.
- Xia, J., Falconer, R., Lin, B., Tan, G., 2011. Numerical assessment of flood hazard risk to people and vehicles in flash floods. *Environmental Modelling and Software*, 26(8), pp.987–998. Available at: <http://dx.doi.org/10.1016/j.envsoft.2011.02.017>.
- Yan, W.Y., Shaker, A. & El-Ashmawy, N., 2015. Urban land cover classification using airborne LiDAR data: A review. *Remote Sensing of Environment*, 158, pp.295–310. Available at: <http://www.sciencedirect.com/science/article/pii/S0034425714004374> [Accessed November 4, 2015].
- Zerger, A. & Wealands, S., 2004. Beyond modelling: Linking models with GIS for flood risk management. *Natural Hazards*, 33(2), pp.191–208.
- Zhang, Z., Liu, H., Zhu, S.P., Zhao, F., 2006. Application of CFD in ship engineering design practice and ship hydrodynamics. *Journal of Hydrodynamics, Ser. B*, 18(3), pp.315–322. Available at: <http://www.sciencedirect.com/science/article/pii/S1001605806600723> [Accessed November 26, 2015].
- Zhu, L.D., Li, L., Xu, Y.L., Zhu, Q., 2012. Wind tunnel investigations of aerodynamic coefficients of road vehicles on bridge deck. *Journal of Fluids and Structures*, 30, pp.35–50.

Zou, L., Lin, Y.F. & Lam, K., 2008. Large-Eddy Simulation of Flow around Cylinder Arrays at a Subcritical Reynolds Number. *Journal of Hydrodynamics*, 20(4), pp.403–413. Available at: <Go to ISI>://000261614300001.